Title
Damage Assessment and Collapse Simulations of Structures under Extreme Loading Conditions

Author
Do Ngoc, Thanh

Publication Date
2017

Peer reviewed|Thesis/dissertation

Damage Assessment and Collapse Simulations of Structures under Extreme Loading Conditions

by

Thanh Do Ngoc

A dissertation submitted in partial satisfaction of the
requirements for the degree of
Doctor of Philosophy

in

Engineering - Civil and Environmental Engineering

in the

Graduate Division

of the

University of California, Berkeley

Committee in charge:

Professor Filip C. Filippou, Chair
Professor Anil K. Chopra
Professor Panayiotis Papadopoulos

Spring 2017

Damage Assessment and Collapse Simulations of Structures under Extreme Loading Conditions

Abstract

Damage Assessment and Collapse Simulations
of Structures under Extreme Loading Conditions

by

Thanh Do Ngoc

Doctor of Philosophy in Engineering - Civil and Environmental Engineering

University of California, Berkeley

Professor Filip C. Filippou, Chair

This dissertation presents a family of new beam-column element models which are based on damage-plasticity and are suitable for the damage assessment and the collapse simulation of structures.

First, a new 1d hysteretic damage model based on damage mechanics is developed that relates any two work-conjugate response variables such as force-displacement, moment-rotation or stress-strain. The strength and stiffness deterioration is described by a damage variable with continuous evolution. The formulation uses a criterion based on the hysteretic energy and the maximum absolute deformation value for the damage initiation with a cumulative probability distribution function for the damage evolution. The damage evolution function is extended to accommodate the sudden strength and stiffness degradation of the force-deformation relation due to brittle fracture. The model shows excellent agreement with the hysteretic response of an extensive set of reinforced concrete, steel, plywood, and masonry specimens. In this context it is possible to relate the model's damage variable to the Park-Ang damage index so as to benefit from the extensive calibration of the latter against experimental evidence.

The 1d damage model is then extended to the development of beam-column elements based on damage-plasticity. In these models the non-degrading force-deformation relation in the effective space is described by a linear elastic element in series with two rigid-plastic springs with linear kinematic and isotropic hardening behavior. The first model, the series beam element, assumes that the axial response is linear elastic and uncoupled from the flexural response. The second model, the NMYS column element, uses an axial-flexure interaction surface for the springs to account for the inelastic axial response and capture the effect of a variable axial load on the flexural response. A novel aspect of the beam-column formulation is that the inelastic response is monitored at two locations that are offset from the element ends to account for the spread of inelasticity for hardening response and the size of the damage zones for softening response. The plastic hinge offsets account for the response coupling between the two element ends.

The implementation of the damage-plasticity elements with the return-mapping algorithm ensures excellent convergence characteristics for the state determination. The proposed elements compare favorably in terms of computational efficiency with more sophisticated models with fiber discretization of the cross section while achieving excellent agreement in the response description for homogeneous metallic structural components. The excellent accuracy is also confirmed by the agreement with experimental results from more than 50 steel specimens under monotonic and cyclic loading. The models are able to describe accurately the main characteristics of steel members, including the accumulation of plastic deformations, the cyclic strength hardening in early cycles, the low-cycle fatigue behavior, and the different deterioration rates in primary and follower half cycles. With the plastic axial energy dissipation accounted for in the damage loading function, the damage-plasticity column model captures the effect of a variable axial force on the strength and stiffness deterioration in flexure, the severe deterioration under high axial compression, the nonsymmetric response under a variable axial force, and the very large plastic axial and flexural deformations before column failure. The validation studies point out the dependence of the strength and stiffness deterioration on the section compactness, the element slenderness, the axial force history, and the axial shortening of the columns. A regression analysis is then used to establish guidelines for the damage parameter selection in relation to the geometry and the boundary conditions of the structural member.

The proposed damage-plasticity frame elements are deployed in an analysis framework for the large-scale simulation and collapse assessment of structural systems. The capabilities of the modeling approach are demonstrated with the case study of an 8-story 3-bay special moment-resisting steel frame that investigates various aspects of the structural collapse behavior, including the global and local response under strength and stiffness deterioration, the magnitude and distribution of the local damage variables, and the different types of collapse mechanism. The study proposes new local and global damage indices, which are better suited for the collapse assessment of structures than existing engineering demand parameters like the maximum story drift. The incremental dynamic analysis of the 8-story moment frame under a suite of earthquake ground motions confirms the benefits of the proposed damage indices for the collapse assessment of structures. The study shows that an aftershock as strong as the main shock increases the collapse margin ratio by as much as 30% and requires more stringent design criteria for protecting the building from collapse that currently specified.

The study compares different modeling aspects for the archetype building to assess the benefits of the proposed beam-column elements, such as the ability to account for the member damage, the offset location of the plastic hinges, the inelastic axial response, the axial-flexure interaction, and the sudden strength and stiffness deterioration due to brittle fracture of the structural member. The study concludes that the proposed family of beam-column elements holds great promise for the large scale seismic response simulation of structural systems with strength and stiffness deterioration, because of their computational efficiency and excellent accuracy. Consequently, the proposed models should prove very useful for the damage assessment and the collapse simulation of structures under extreme loading conditions.

Contents

Contents **i**

List of Figures **v**

List of Tables **x**

1 Introduction **1**
1.1 Motivation . . . 1
1.2 Literature Review . . . 2
1.2.1 Damage models . . . 2
1.2.2 Beam-column models . . . 4
1.2.3 Damage assessment of structures . . . 7
1.3 Objectives and Scope . . . 9
1.4 Dissertation Outline . . . 9
1.5 Preliminaries . . . 10
1.5.1 Continuum damage mechanics . . . 10
1.5.2 Basic coordinate system for plane frame elements . . . 11

2 Hysteretic Damage Model **12**
2.1 Introduction . . . 12
2.2 Formulation . . . 12
2.2.1 Constitutive relation in effective space . . . 13
2.2.2 Damage loading function. . . . 15
2.2.3 Damage evolution law . . . 17
2.3 Effect of Damage Parameters . . . 19
2.4 Illustrative example . . . 22
2.5 Validation Studies . . . 25
2.5.1 Reinforced concrete columns . . . 25
2.5.2 Steel beam-column joints . . . 27
2.5.3 Low-cycle fatigue of steel components . . . 27
2.5.4 Effect of load histories on plywood shearwalls response . . . 30
2.5.5 Degrading behavior of structural systems . . . 31

2.6 Damage Variables . . . 41
2.6.1 Comparison with Park-Ang index . . . 41
2.6.2 Damage states . . . 44
2.7 Damage Evolution Law for Brittle Failure . . . 46

3 Damage-Plasticity Beam Model 49
3.1 Series Beam Element . . . 50
3.1.1 Formulation . . . 50
3.1.2 Plastic hinge offset . . . 54
3.1.3 State determination: Return-mapping algorithm . . . 55
3.1.4 Model parameters . . . 62
3.2 Examples of Series Beam Element . . . 65
3.2.1 Pushover analysis of portal frame . . . 65
3.2.2 General bending of simply-supported beam . . . 66
3.2.3 Reduced beam section (RBS) connections . . . 70
3.3 Damage-Plasticity Beam Element . . . 80
3.3.1 Effective response . . . 80
3.3.2 Damage loading function . . . 81
3.3.3 Damage evolution law . . . 82
3.4 Examples of Damage-Plasticity Beam Element . . . 83
3.4.1 Simply-supported beam . . . 83
3.4.2 Portal frame . . . 86
3.5 Validation Studies . . . 91
3.5.1 Simulation of steel components . . . 91
3.5.2 Regression analysis for parameter identification . . . 92
3.5.3 Parameter sensitivity . . . 94
3.6 Damage Evolution with Brittle Failure . . . 98
3.6.1 Formulation . . . 98
3.6.2 Validation studies . . . 99

4 Damage-Plasticity Column Element 101
4.1 NMYS Column Element . . . 102
4.1.1 Force-deformation relation . . . 102
4.1.2 Plastic hinge offset . . . 106
4.1.3 Return mapping algorithm . . . 107
4.1.4 Model parameters . . . 110
4.1.5 Example 1: Cantilever column . . . 114
4.1.6 Example 2: Four-story three-bay frame . . . 121
4.2 Damage-Plasticity Column Element . . . 126
4.2.1 Formulation . . . 126
4.2.2 Implementation . . . 129
4.2.3 Model parameters . . . 131

4.3 Illustrative Example . . . 131
4.3.1 Monotonic response . . . 131
4.3.2 Cyclic response . . . 133
4.4 Comparison with Other Column Models . . . 134
4.4.1 Concentrated plasticity without N-M interaction . . . 135
4.4.2 Distributed plasticity . . . 136
4.5 Validation Studies . . . 143
4.5.1 Columns by Lignos [56] . . . 143
4.5.2 Columns by MacRae [59] . . . 147
4.5.3 Columns by Newell and Uang [66] . . . 149
4.5.4 Remarks on parameter C_i . . . 150

5 Case Study: 8-story Steel Moment Frame 152
5.1 Archetype Building . . . 152
5.2 Structural Model . . . 154
5.2.1 Element models . . . 154
5.2.2 Mass, damping, nonlinear geometry . . . 155
5.2.3 Member naming convention . . . 155
5.3 Static Response . . . 155
5.4 Ground motions . . . 156
5.5 Dynamic Response . . . 158
5.5.1 Local damage distribution . . . 158
5.5.2 Collapse mechanism . . . 162
5.5.3 Other response distribution . . . 164
5.5.4 Further remarks . . . 166
5.6 Global Damage Index . . . 167
5.6.1 Formulation . . . 167
5.6.2 Localized Damage Region . . . 169
5.6.3 Comparison with maximum story drift . . . 171
5.6.4 Damage-base limit states . . . 172
5.6.5 Case study: collapse assessment with aftershocks . . . 174
5.7 Effect of Modeling Assumptions . . . 177
5.7.1 Effect of element damage . . . 177
5.7.2 Effect of plastic hinge offsets . . . 179
5.7.3 Axial-flexure interaction . . . 181
5.8 Consideration of Element Brittle Failure . . . 188
5.8.1 Background . . . 188
5.8.2 Calibration of model parameters . . . 190
5.8.3 Pushover analysis . . . 190
5.8.4 Dynamic analysis . . . 190
5.8.5 Further remarks . . . 194

6 Concluding Remarks **196**
6.1 Summary 196
6.2 Conclusions 197
6.2.1 Hysteretic damage model 197
6.2.2 Damage-plasticity beam and column elements 198
6.2.3 Damage assessment of steel moment-frames 199
6.3 Recommendations for Further Study 201

Bibliography **202**

A Alterative Damage Evolution Functions **211**
A.1 Beta Distribution 211
A.2 Lognormal distribution 212

B Mathematical Derivations **215**
B.1 Plastic Consistency Parameter 215
B.2 Algorithmic Tangent 215
B.2.1 Series beam model 215
B.2.2 NMYS column model 216

C Thermodynamics Framework **218**

List of Figures

1.1 Coordinate systems for plane frame elements: (a) global coordinate system, (b) local coordinate system, (c) basic system 11

2.1 Relation between effective and true response 13
2.2 Selected force-deformation relations in effective space 14
2.3 Effect of p_x and p_y on the reloading response of the hysteretic model 15
2.4 Illustration of ψ_t and ψ_c and of the effect of the parameter C_{wc} 16
2.5 Effect of parameters $d_p^{\pm}$ on the damage evolution 18
2.6 FEMA force-deformation envelope 21
2.7 Effect of damage parameters on force-deformation relation 21
2.8 Sample cyclic response of proposed model 22
2.9 Evolution of damage variables $d^{\pm}$ under cyclic loading 23
2.10 Stiffness degradation under cyclic loading with decreasing magnitudes 24
2.11 Simulations of reinforced concrete columns 26
2.12 Simulations of steel beam-column assemblages 28
2.13 Simulation of steel cantilever beams under cyclic loading 29
2.14 Numerical and experimental correlation for plywood shear walls 30
2.15 Simulation of beam-to-column shear tab connections (S1 system) 32
2.16 Simulation of pre-Northridge non-ductile welded steel beam-column connections (system S2) 34
2.17 Simulation of post-Northridge ductile steel beam-column connections (system S3) 35
2.18 Simulation of stiff, non-ductile concentrically braced steel frame (system S4) . . 36
2.19 Simulation of stiff, non-ductile masonry wall with pronounced pinching (system S5) 37
2.20 Simulation of lightly reinforced concrete column with limited-ductility (system S7) 38
2.21 Monotonic response and comparison of Park-Ang damage index with damage variable d^+ 42
2.22 Cyclic response and comparison of damage index d_{PA} with damage variable d^+ . 43
2.23 Effect of parameters C_{wc} and C_{cd} on damage index d_{PA} and damage variable d^+ 43
2.24 Response of steel beam-column subassemblages under cyclic load protocols . . . 44
2.25 Comparison of damage evolution in specimen LS2 45
2.26 Damage evolution with brittle failure 47

2.27 Simulations of steel beam with brittle failure 48

3.1 Series beam element 50
3.2 Equilibrium and compatibility relations of series beam model 51
3.3 Yield envelope of series element 52
3.4 Scenarios of plastic deformation increments: (a) only f_i active, (b) only f_j active, (c) both f_i and f_j active 53
3.5 Series beam element with plastic hinge offset 54
3.6 Moment interpolation between the hinge locations and the element ends 54
3.7 Return-mapping algorithm for series element 59
3.8 Two-step identification of active surfaces 61
3.9 Violation of Kuhn-Tucker condition due to incorrect active β's 61
3.10 Evolution of yield surfaces: (a) kinematic hardening with $H_{kr} > 0$, and (b) isotropic hardening with $H_{ir} > 0$ 63
3.11 Sample cyclic response with linear kinematic and isotropic hardening 64
3.12 Effect of offset on flexural response of a cantilever beam 65
3.13 Structural model of portal frame 65
3.14 Pushover response of portal frame with EPP element behavior 67
3.15 Simply-supported beam with proportional end rotations 68
3.16 Calibration of post-yield hardening parameter: (a) with target deformation v_{target}, (b) with fictitious moment M_p^* 69
3.17 Moment-rotation relation of simply-supported beam under monotonic loading . 70
3.18 Moment-rotation relation of simply-supported beam under cyclic loading 71
3.19 Modeling approaches for reduced-beam sections: (a) 3 linear-elastic beams with 2 zero-length springs, (b) 2 linear-elastic beams with 1 series beam without offset, (c) 1 series beam with offset 72
3.20 Moment-rotation of beam with RBS: (a) $\rho = 0.5$, $\chi = 0.05$, $\lambda = 0.6$, (b) $\rho = -0.5$, $\chi = 0.05$, $\lambda = 0.8$, (c) $\rho = -0.5$, $\chi = 0.1$, $\lambda = 0.6$ 73
3.21 Effect of hinge offset on portal frame response: static response 74
3.22 Structural model of 3-story moment frame 76
3.23 Collapse mechanisms of 3-story 1-bay moment frame: (a) 1-story, (b) 2-story, (c) full 3-story 76
3.24 Response comparison of design alternatives 77
3.25 Response comparison of RBS designs 78
3.26 Member response at the beam-column joint in the 1st story 79
3.27 Equilibrium and compatibility relations of plastic-damage beam model 80
3.28 Degrading moment-rotation relation of simply-supported beam under monotonic loading 85
3.29 Degrading moment-rotation relation of simply-supported beam under cyclic loading 87
3.30 Dynamic response of portal frame 88
3.31 Girder moment-rotation and damage evolution in model M1 89
3.32 Girder moment-rotation and damage evolution in model M2 90

3.33 Moment-rotation relation of steel specimens LS1 and LS3 [111] 92
3.34 Variation in the limit coefficient C_{d1} with the section compactness and member slender 93
3.35 Cyclic load protocols for cantilever beam 94
3.36 Reference cyclic response under different loading histories 95
3.37 Sensitivity analysis: CUREE loading 96
3.38 Sensitivity analysis: NF loading 97
3.39 Moment-rotation relation of steel specimens with brittle failure 100

4.1 NMYS column element 102
4.2 Yield surfaces 104
4.3 NMYS column element with plastic hinge offset 106
4.4 Geometric illustration of return-mapping algorithm at corner point 110
4.5 Effect of yield surface parameters 113
4.6 Effect of hardening parameters on yield envelope 114
4.7 Cantilever column: (a) structure and loading, (b) concentrated plasticity (CP) model, (c) distributed plasticity (DP) model 115
4.8 Monotonic response of cantilever column with EPP behavior 116
4.9 Cyclic response of cantilever column with EPP response 118
4.10 Cyclic response of cantilever column with EPP response (continued) 119
4.11 Cyclic response of cantilever column with hardening behavior, $\chi = 0$ 121
4.12 Cyclic response of cantilever column with hardening behavior, , $\chi = 0.2$ 122
4.13 Four-story three-bay moment-resisting frame 123
4.14 Global dynamic response of four-story three-bay steel moment frame 124
4.15 Local dynamic response of four-story three-bay steel moment frame 125
4.16 Cantilever column: (a) Structure and loading, (b) Idealized model 132
4.17 Monotonic response of cantilever column under different levels of axial force . . 132
4.18 Cyclic response comparison: (a) variable axial force $N/N_p = -0.4 \mp 0.3$, (b) constant axial force $N/N_p = -0.4$ 133
4.19 Modeling approaches for response simulation of a cantilever column: (a) Structure and loading, (b) Model CP, (c) Model CP0, (d) Model DP 134
4.20 Response comparison of model CP and model CP0 136
4.21 Comparison of cyclic response with variable axial compression 137
4.22 Sample stress-strain relation 138
4.23 Comparison of cyclic response of cantilever column 138
4.24 Numbering of fibers in cross-section of DP model 139
4.25 Sample fiber response under $N/N_p = 0$ 140
4.26 Sample fiber response under N/N_p = -0.2 141
4.27 Damage measures of DP model 142
4.28 Comparison of damage variables D_{CP} and D_{DP} 142
4.29 Response under constant axial compression and monotonic lateral displacement 144
4.30 Effect of axial load level on cyclic response of steel column 145

4.31 Effect of variable axial load on cyclic response of steel column 145
4.32 Axial shortening of steel column under constant axial load 146
4.33 Cyclic response of steel columns under constant axial load 147
4.34 Damage evolution of steel column specimens 148
4.35 Cyclic response of steel column under variable axial compression 149

5.1 Archetype eight-story three-bay special moment frame 153
5.2 Typical floor model of the eight-story three-bay moment frame 155
5.3 Pushover response: load distribution and normalized base shear vs roof drift . . 156
5.4 Story drift and shear distribution 157
5.5 Damage distribution at $RD = 0.045$ 157
5.6 Elastic response spectrum of the far-field ground motions, $\xi = 2.5\%$ 159
5.7 Response distribution and deformed shape (FF4, SF = 6.60) 160
5.8 Response of 1st story exterior columns (FF4, SF = 6.60): (a) Flexural response at base, (b) Plastic axial deformation, (c) Damage evolution 161
5.9 Response distribution and deformed shape (FF1, SF = 5.00) 161
5.10 Response of 1st story exterior columns (FF1, SF = 5.0): (a) Flexural response at base, (b) Plastic axial deformation, (c) Damage evolution 162
5.11 Girder response of 1st floor girders (FF4, SF = 6.6) 163
5.12 Deformed shape with weak-story collapse mechanism: (a) FF14, SF = 9.0, (b) FF1, SF = 5.6 163
5.13 Story DR and shear distribution of a one-story mechanism (FF14, SF = 9.0) . . 164
5.14 Time history of the average floor rotations 165
5.15 Distribution of floor acceleration 165
5.16 Dynamic response under FF9 166
5.17 Illustration of column indices, joint indices, and floor indices 168
5.18 Typical configuration of a story mechanism 169
5.19 Damage indices and localized damage region (FF1, SF = 5.6) 170
5.20 Comparison of damage index D_G and maximum story drift 171
5.21 Incremental dynamic analysis curve in terms of story drift and damage index . . 172
5.22 Comparison of max drift ratio DR and damage index D_G at different limit states: (a) Life safety, (b) Collapse prevention, (c) Collapse 173
5.23 Probability of different damage limit states 174
5.24 Acceleration history of FF1 record with aftershock 175
5.25 Collapse probability with and without consideration of aftershocks 176
5.26 Comparison of dynamic response in model R and model A 178
5.27 Dynamic response without element damage (FF14, SF = 12.15) 179
5.28 Comparison of model R and model B: average roof translation 179
5.29 Comparison of model R and model B: 1st story drift 180
5.30 Comparison of model R and model B: collapse mechanisms 181
5.31 Comparison of model R and model B: damage distribution 182

5.32 Comparison of model R and model CA: story drift and deformed shape (FF17, SF = 9.40) . . . 183
5.33 Comparison of model R and model CA: effect of column shortening (FF17, SF = 9.40) . . . 184
5.34 Comparison of model R and model CA: local column response (FF17, SF = 9.40) 185
5.35 Comparison of model R and model CA: damage distribution (FF17, SF = 9.40) 186
5.36 Comparison of model R and model CB: story drift and deformed shape (FF2, SF = 7.92) . . . 187
5.37 Comparison of model R and model CB: local column response and damage distribution (FF2, SF = 7.92) . . . 189
5.38 Pushover analysis response with sudden strength deterioration . . . 191
5.39 Comparison of model R and model D: 1st story drift . . . 192
5.40 Comparison of model R and model D: 1st story column response . . . 193
5.41 1st story drift ratio under FF19, $SF = 6.93$ . . . 194
5.42 Local response and damage distribution under FF19, $SF = 6.93$ . . . 195

A.1 Effect of β_1 and β_2 on the beta CDF . . . 212
A.2 Effect of μ and σ on the lognormal CDF . . . 213
A.3 Simulation of concrete uniaxial response . . . 214

List of Tables

2.1 State determination algorithm of hysteretic damage model 20
2.2 Parameters used in simulations of reinforced concrete columns 25
2.3 Parameters used in simulations of steel beam-column joints 27
2.4 Parameters for the simulations of the degrading hysteretic behavior of structural components 40
2.5 Correlation of damage measures and limit states for specimen LS2 46

3.1 State determination algorithm of series beam model with plastic hinge offset . . 58
3.2 Design alternatives of 3-story frame 79
3.3 State determination algorithm of damage-plasticity beam model 84
3.4 Regression coefficients for parameter calibration 93
3.5 Sensitivity ranking of damage parameters 98
3.6 Parameters for the simulations of steel beams with brittle damage 99

4.1 Elastic predictor algorithm 111
4.2 Plastic correction algorithm: closest point projection 112
4.3 Unit comparison of beam and column models 114
4.4 State determination algorithm of damage-plasticity column model 130
4.5 Comparison of C_i and C_{d1} in column simulations 150

5.1 Member sizes for eight-story three-bay moment resisting frame 153
5.2 Parameters of reduced beam sections 154
5.3 Far-field ground motion information 158

Acknowledgments

First and foremost, I would like to express my deep gratitude to my advisor, Professor Filip Filippou, for the unique opportunity to embark on this challenging and rewarding journey in the last five years at Berkeley. I truly appreciate his constant guidance and encouragement, and especially his incredible energy and patience as he helped me improve my writing. His dedication to high-quality research and teaching is unparalleled. I am also very grateful for the honor to serve as his graduate student instructor in the *Structural Analysis* and *Nonlinear Structural Analysis* courses.

I would like to thank Professor Anil Chopra and Professor Panayiotis Papadopoulos for agreeing to serve on my qualifying exam and dissertation committee and for their valuable comments to improve the thesis. I am also grateful for the other members on my qualifying exam committee: Professor Khalid Mosalam and Professor John Strain.

I would like to thank Ms. Shelley Okimoto for her valuable advice throughout my stay at Berkeley.

I would like to thank my former advisor at University of the Pacific, Dr. Camilla Saviz, for her encouragement, continuous support, and lifelong mentoring. I am very fortunate to have met and worked with such a dedicated and passionate mentor.

I would like to express my gratitude to all my friends, in particular, my friends at University of the Pacific and at University of California, Berkeley. One way or the other, you have made my journey particularly memorable. Your lifelong friendship and warm welcoming makes me truly feel this is my 'home away from home.'

Finally, my deepest appreciation goes to family. I thank you for your infinite patience especially during the preparation of this dissertation and other difficult times. Without your unconditional love and support, it would be impossible for me to become who I am today. I would like to dedicate my accomplishments to you. You have been, and forever will be, a crucial part of my journey.

Chapter 1

Introduction

1.1 Motivation

Over the last decades, we are continuously reminded of the lack of resilience in the built-environment by earthquakes, tsunamis, hurricanes, that cause intolerable structural damage, economic loss, and significant loss of lives. These hazards pose a constant threat to the resilience of our community. In particular, the seismic hazard has caused severe damage to a wide variety of structural types, ranging from reinforced concrete (RC), masonry, wood, to steel, which is widely believed to exhibit superior performance during earthquakes. Damage in steel structures, even though not as severe as in other structural types such as RC structures, also results in significant economic loss and thus deserves more attention. One example of serious damage in steel structures is the Cordova building during the Prince William Sound, Alaska earthquake in 1964. Damage to this six-story steel frame was concentrated in the first story where a number of wide flange columns buckled due to the high axial forces. Another example of a severely damaged steel structure is the Pino Suarez Complex during the Mexico City earthquake in 1985. In this case, the large brace forces induced axial overstress in the columns and lead to column buckling, and in turns, the collapse of a 21-story building. A detailed discussion on past performance of steel moment-frame buildings in earthquake can be found in the FEMA 355E report [107].

To prevent structural collapse and enhance the community resilience in a multi-hazard environment, it is critical to understand the deterioration in structures so that proper prevention and/or mitigation practices can be undertaken. For the purpose, often times a numerical model is employed to simulate the structural response and quantify the level of damage. However, as will be discussed in detail in the remaining of this dissertation, many existing models have serious limitations in the accuracy and the efficiency.

Due to the above limitations, the major challenge in this generation is two-fold: first, to establish an accurate, efficient, and reliable analytical framework to quantify the performance of existing and new structures under extreme loading conditions both predictively and retrospectively; and second, to develop the design and retrofit guidelines to improve the

system resilience against the effect of manmade and natural hazards. The framework consists of several critical components: (1) a damage model to predict the structural response and assess the damage states and collapse fragility, (2) a probabilistic model to evaluate the multi-hazard risks, and (3) a financial model to estimate the repair/replacement cost as well as the necessary recovery time for the structure to be fully operational. The analysis permits a resilient design for a new building or an economical retrofitting scheme for an existing structure with optimal use of available resources.

This dissertation addresses the first major component of this interdisciplinary framework: to develop efficient and accurate damage models for the response simulation and damage assessment of structural systems in a multi-hazard environment.

1.2 Literature Review

The following review of relevant literature is presented in three parts: the first addresses the existing deterioration models, the second reviews some notable beam and column element models, and the third discusses the engineering demand parameters commonly used in damage evaluation of components and structures.

1.2.1 Damage models

The assessment of structural resilience depends on the analytical description of the damage evolution under a sequence of extreme cyclic loading conditions. Existing models of material damage fall into three broad categories:

(a) Rigorously formulated 3d material constitutive models based on continuum damage mechanics (CDM) that describe the evolution of the strength and stiffness deterioration. These models focus on local response simulations of structural components, which however, make their high computational cost unsuitable for the simulation of structural systems under multi-hazard scenarios.

(b) Hysteretic models with strength and stiffness deterioration rules. These models can, in turn, be divided into polygonal and smooth response description models. The first type assumes piece-wise linear response between events corresponding to cracking, yielding and ultimate capacity. The second type uses algebraic or differential equations to generate a smooth hysteretic response with a gradual transition from the elastic to the inelastic range. These models are simpler than the ones in the first category and are widely used in practice. However, they exhibit some limitations in the damage description of components, such as in the degradation in primary and follower half cycles, the unloading stiffness deterioration, the lack of a consistent damage measure, among others.

(c) Damage index models. These models establish a damage index for quantifying component damage. The damage index calibration is based on experimental measurements

and observations or on analytical results with some of the hysteretic models under (b). The models, however, do not explicitly describe the degrading hysteretic response as the models under (a) and (b), and thus, lacks the correlation between the structural response and the damage states.

Examples of CDM models are those by Simo and Ju [91], Lemaitre [54], and Huang [38] for ductile materials, and those by Mazars and Pijaudier-Cabot [62] and Wu and Faria [110] for concrete materials. The cyclic void growth model (CVGM) by Rice and Tracey [83] and the model by Kanvinde and Deierlein [44] also fall in this category. Because these models focus on local response simulations of structural components, their high computational cost makes them unsuitable for the simulation of structural systems under multi-hazard scenarios.

Models in the second category can be further classified into to groups: polygonal models and smooth models. Polygonal hysteretic models are relatively easy to formulate, but oftentimes depend on many rules limiting their generality and making their consistency and numerical robustness challenging. Several such models have been proposed over the years starting with Clough [17] and Takeda et al. [98]. The force-deformation relation of the former represents the stiffness degradation by adjusting the reloading behavior to target the maximum previous displacement in the loading direction and is often referred to as the peak-oriented model. Takeda's model uses a trilinear envelope to distinguish the cracking from the yield moment of a reinforced concrete component and is characterized by a more complex unloading and reloading peak-oriented behavior than Clough's model. The three-parameter model by Park, Reinhorn, and Kunnath [72, 81] uses a pivot rule to describe the stiffness deterioration and includes strength degradation based on the hysteretic energy at unloading. The model by Song and Pincheira [94] relates the strength and stiffness deterioration to the maximum deformation at the most recent inelastic excursion in the opposite direction. Finally, the model by Ibarra et al. [39] uses a piecewise linear monotonic backbone relation and four deterioration modes: strength, post-capping, unloading stiffness, and accelerated reloading stiffness. [57] reports the extensive calibration of this model. Because of their formulation polygonal models accommodate strength and stiffness deterioration as discrete updates at the instant of load or deformation reversal.

Smooth hysteretic models are more computationally involved than polygonal models but are more consistent and numerically robust. A prominent example of this group is the model of Bouc [11] and its extension by Wen [108] and Baber et al. [9, 8]. Sivaselvan and Reinhorn [93] and Ray and Reinhorn [80] demonstrated the ability of smooth hysteretic models to accommodate a continuous strength and stiffness deterioration through the use of rate equations for the strength and stiffness evolution. Sivaselvan and Reinhorn [93] also proposed an elegant framework for combining basic polygonal and smooth hysteretic models in parallel or in series with the intent of assigning one suitable component to a corresponding physical mechanism like plastic yielding, slip, friction, etc.

Park and Ang [73] proposed an early damage model with the damage index as the linear combination of the normalized maximum deformation and the normalized hysteretic energy. In contrast, the model by Krätzig [49] uses the normalized hysteretic energy of each load

cycle to establish the damage index of the component. To account for the dependence of damage on the deformation history, Krätzig distinguishes the energy dissipation of a primary half cycle (PHC) that extends the deformation envelope from a follower half cycle (FHC) that remains within the current extreme deformations. Mehanny and Deierlein [64] adopted the idea of PHC and FHC but based the damage index on the maximum plastic deformations instead of hysteretic energy. Rahnama and Krawinkler [79] proposed a damage index as an exponential function of the normalized energy dissipation in each load cycle. Finally, Bozorgnia and Bertero [12] suggested a modification of the Park-Ang damage index to discount damage in the elastic range. They also introduced a weight coefficient for the contribution of the deformation ductility relative to the energy dissipation.

1.2.2 Beam-column models

The following review of the existing beam and column elements is presented in two parts. First, the element models without strength and stiffness deterioration are discussed. Then, the discussion focuses on the models that account for the deterioration in the response.

1.2.2.1 Element models with nondegrading response

Existing nondegrading beam-column models can be classified into three main categories:

(a) Continuum models: this approach requires a discretization of the structural model and is common in finite element analysis. These models specify a stress-strain relation for the material response and focus on the local behavior of structural components. However, the high computational cost limits their use in large-scale simulations of structural systems.

(b) Distributed plasticity models: the element response is monitored at several sections along the element length. The models permit plastic hinges to form at any section and account directly for the interaction of the element response, such as axial, flexure, shear, torsion, and warping. The section response is determined from a stress-resultant model [24] or a fiber-based model. The latter can, in turn, be divided into elements with a displacement- and a force-based or a mixed formulation.

(c) Concentrated plasticity models: the inelastic behavior is concentrated in the nonlinear plastic hinges typically located at the element ends. The hysteretic behavior of the plastic hinges are given by a moment-rotation relation.

Distributed plasticity elements based on the displacement-formulation adopt a similar approach in standard finite element method and utilize displacement interpolation functions to relate the section deformations to the element deformations [112]. Since the relation is approximate, several elements are required to describe accurately the nonlinear element response. Distributed plasticity elements based on the force- or mixed-formulation, on the

other hand, use force interpolation functions to relate the section forces to the element forces. Since equilibrium is satisfied exactly, the force-based formulation only requires one element to describe accurately the nonlinear behavior and permits fewer degrees of freedom in the structural model. Further discussion on the advantages of the force-based elements can be found in Spacone et al. [95], Neunhoffer and Filippou [65], Taylor et al. [102].

One of the earliest concentrated plasticity models is the two-component element proposed by Clough, Benuska, and Wilson [17]. It consists of a linear elastic-perfectly plastic component in parallel with a linear elastic component and is able to represent a post-yield linear hardening behavior in the flexural response. Another notable model in this category is the one-component element by Giberson [30], which consists of a linear elastic component in series with two nonlinear springs located at the element ends. The springs assume a rigid-plastic with linear hardening behavior and are activated when the moment exceeds the plastic flexural capacity. Both the one-component and the two-component models assume a linear elastic axial response that is uncoupled from the flexural behavior. The models have been extended to accommodate the axial-flexure interaction in the plastic hinge response [37, 76]. Concentrated plasticity models are widely used in response simulations of structural components of different materials, including steel [67, 67, 75, 70, 37, 76], reinforced concrete [100], and concrete-filled steel tubes [34, 48].

Concentrated plasticity models compare favorably to continuum and distributed plasticity models in the numerical efficiency but also exhibit several limitations. First, despite the effort to account for the response interaction, the challenge to capture sufficiently the coupling of complex element response remains. Second, many concentrated plasticity models explicitly specify a zero-length rotational spring element and require additional nodes and degrees of freedom at the interface between the spring and the elastic beam element. This problem can be resolved by specifying the plastic hinges implicitly in the element state determination [77, 48]. Moreover, the approximatation of the rigid-plastic behavior in the plastic hinges with a large elastic stiffness leads to numerical nonconvergence under dynamic loading and unreasonable sensitivity of the dynamic response to the damping models, especially when the initial stiffness is used in Rayleigh damping [15].

1.2.2.2 Element models with degrading response

The element models with degrading response are based on the models with nondegrading response in Section 1.2.2.1 and specify the deterioration in three main manners: (1) in the material stress-strain relation or in the section moment-curvature relation of a fiber-based element, (2) in the zero-length spring's moment-rotation relation of a concentrated plasticity model, and (3) in the force-deformation relation of a concentrated plasticity model.

(1) Degrading material stress-strain and section moment-curvature

A degrading stress-strain relation for the material response is specified in continuum models and distributed plasticity models. The material models are typically based on continuum damage mechanics (CDM), such as those listed in category (a) in Section 1.2.1. These ele-

ments account for the coupling of complex element response and capture the deterioration at the local material level. However, in addition to the high computational cost, the elements are susceptible to mesh inobjectivity [20].

To resolve this issue, many regularization techniques have been proposed, such as by Coleman and Spacone [18], Addessi and Ciampi [2]. Another approach is the *beam with hinge element* by Scott et al. [86, 87], and Ribeiro et al. [82]. The element consists of three segments: an interior elastic beam element and two plastic hinge segments at the element ends with a specified plastic hinge length, and adopts a proper numerical integration scheme. To represent the deterioration in the element response, a degrading stress-strain relation can be specified for the material response in each fiber, or alternatively, a degrading moment-curvature relation can be specified for the section response.

A recent approach to describe the column strength and stiffness deterioration is the *fiber hinge element* by Kasai et al. [46]. The inelastic behavior is localized at the column base and modeled by the zero-length fiber hinge element, which is discretized into fibers with a degrading stress-strain relation.

(2) Degrading spring moment-rotation

One of the most common approaches to simulate strength deterioration is to define a degrading moment-rotation relation for the zero-length rotational springs at the ends of a concentrated plasticity beam-column element. This approach is recommended in ATC-72 guidelines for modeling of tall buildings [61]. The moment-rotation relation can adopt any deterioration hysteretic model summarized in 1.2.1.

Besides the same drawbacks as in the concentrated plasticity models with nondegrading response, these models fail to capture the effect of a variable axial force on the strength deterioration in flexure, which is critical in tall structures where the columns are subjected to high axial forces from the overturning effect.

(3) Degrading element force-deformation

An efficient approach to incorporate deterioration in concentrated plasticity formulation is to adopt the continuum damage mechanics concept [41, 54]. These element models employ a nondegrading force-deformation relation to describe the response without strength deterioration, and define some criteria for damage initiation and growth to represent the strength and stiffness deterioration in the element response.

Some of the earliest models in this category include the work by Cipolina et al. [16], Florez-Lopez [28], and Inglesis et al. [40]. The models adopted a simple bilinear force-deformation with kinematic hardening for the base response and proposed different damage evolution laws for steel and reinforced concrete (RC) components based on experimental measurements of steel and RC cantilever specimens under cyclic loading. Faleiro et al. [26] proposed an element model that uses an energy variable to describe the damage initiation and growth. Kaewkulchai et al. [42] formulated a beam-column element with a multi-linear force-deformation relation that adopted the Mroz's hardening rule and a damage variable resembling the Park-Ang damage index to investigate the progressive collapse of structures.

One limitation of the existing models is in the criteria for damage initiation and growth. Models that adopt an elastic energy variable to govern the damage evolution fail to capture the low-cycle fatigue behavior due to repeated cycles between the same range of deformation values. Other models that are based on the cumulative plastic deformations do not distinguish the two deterioration rates in the primary and the follower half cycles.

1.2.3 Damage assessment of structures

The engineering demand parameters (EDP) commonly used for damage assessment of structures can be classified into two categories: the parameters of the structural response and the damage indices derived from a damage index model. Each category can, in turn, be divided into the local and the global parameters that relate to the local and global response, respectively [21, 109].

1.2.3.1 Structural response

Local parameters are related to the response of each individual member. The most common local response for collapse assessment is the plastic hinge rotation [4]. Krishnan [52] studied the plastic hinge distribution to interpret the collapse mechanisms of tall steel moment-frames. The local plastic rotations are used to define the non-simulated collapse modes of the structures in FEMA P695 [4]. Once the plastic rotation in any member reaches a threshold, the structure triggers a non-simulated mechanism. Other important local damage indicators include the fiber stress-strain and the element force-deformation. These parameters are critical to detect the local limit states, including cracking, yielding, buckling [21].

Global parameters account for the contributions from all members to the behavior of one or several stories/floors. The most widely used global response for collapse assessment is the maximum story drift and residual drift [3]. The maximum drift is typically used as the main EDP to evaluate the structural collapse fragility, often times through an incremental dynamic analysis [105]. Other important global damage indicators include the peak moments and shear forces, and the maximum floor velocity and acceleration [21].

1.2.3.2 Damage indices

Damage indices may be defined locally for an individual member or globally for an entire structure [109]. Many damage models have been proposed up to date to quantify the member's damage state based on the displacement amplitude, the energy dissipation, the number of loading cycles, or a combination thereof. Some representative models for the local damage indices are summarized in Section 1.2.1. The main disadvantages of many existing local damage indices are two-fold [109]: (1) the lack of parameter calibration against different damage states of various structural types, and (2) the ability to address various component failure mechanisms besides the flexural modes, such as the failure of steel columns under the combined axial and flexural effects.

The overall damage state of a structure depends on both the distribution and the severity of the localized damage. The global damage indices may be defined as weighted average of the local damage indices or from the variation in the structural characteristics, such as the modal properties [109]. Different formulation have been proposed to formulate the global damage indices from the local damage indices in Section 1.2.1 across the structure with some weight distributions. Two most widely used approaches to quantify the contribution from each member are based on the local damage itself and the local energy absorption, such as in Park et al. [73, 71], Kunnath et al. [53], Bracci et al. [13]. These weighted average methods are simple to implement; however, they inherit many limitations of the local damage indices [109]. Moreover, a comparison is necessary to assess different weighing alternatives.

The global damage indices can also be evaluated in terms of the local damage indices in the element models that are based on continuum damage mechanics such as those in Section 1.2.2.2(1) and Section 1.2.2.2(3). Faleiro et al. [26] defined a member damage index in terms of a ratio of the damaged and undamaged free energy variables in the element response. To account for the contribution of the member deterioration to the global response, the model evaluated the sum of the damaged free energy among all elements and the sum of the corresponding undamaged free energy, then the global damage index was defined in terms of the ratio of the two quantities. The damage indices were demonstrated in the simulation of a two-story RC frame under quasi-static cyclic loading. Hanganu et al. [35] and Scotta et al. [88] employed a distributed plasticity model with a degrading material stress-strain relation to examine the damage states of RC structures. The damage indices were calibrated against experimental data of RC cantilever columns and compared to the limit states criteria in FEMA 356 [3] through a nonlinear dynamic analysis of a RC frame.

Another approach to detect the damage evolution is to examine the change in the modal properties. DiPasquale and Cakmak [23, 22] proposed thee softening indices to reflect the structural damage state in term of three periods: the period of the undamaged structure, the maximum period, and the period of the damaged structure. The studies showed that the softening indices correlate well with the stiffness deterioration of a structure and are consistent with several other damage indices, such as the Park-Ang damage index [73]. However, the formulation based solely on the fundamental period neglects the critical impact of the higher modes and the distribution of damage within the structure [109]. An alternative approach is to examine the fundamental and the higher mode shapes as well as the variations in the flexibility coefficients, such as in the work by Raghavendrachar and Aktan [78].

The next definition of global damage indices is associated with the economic loss. This methodology does not directly relate to the structural response as the other approaches; however, it has an important implication in damage mitigation practices and resilience assessment of structures. Hasselman and Wiggins [36] used a damage ratio to quantify the global damage state, which is defined as the ratio of the repair cost to the replacement cost. Based on the data from the 1971 San Fernando earthquake, the study proposed a log-log relationship between the damage ratio and the interstory drift. Gunturi and Shah [33] proposed the global damage as a collective measure of three main components: the structural damage, the nonstructural damage, and the content damage, which are dependent on the

Park-Ang damage index, the maximum story drift, and the maximum floor acceleration. A major challenge of the financial damage indices is the need for an extensive validation with data in real events and, to some extent, the subjective nature of the financial loss estimation.

1.3 Objectives and Scope

This dissertation develops new damage models for the response simulation and damage assessment of structures under extreme loading conditions. The main objectives of the study are as follows:

(1) To present a new hysteretic damage model based on damage mechanics to describe better the continuous strength and stiffness deterioration in structural components.

(2) To implement the damage formulation in the development of efficient and accurate beam and column elements for modeling of steel components.

(3) To generalize the concentrated plasticity frame elements with the plastic hinge offsets to describe the coupling of the inelastic zones at the element ends.

(4) To calibrate the model parameters against experimental data of steel beams and columns under various loading scenarios. The calibration permits a regression analysis to establish a set of guidelines for the parameter identification.

(5) To investigate the dynamic response and collapse behavior of steel special moment frames (SMF). The new element models are deployed in the response simulation of an 8-story 3-bay SMF under a suite of ground motions up to collapse.

(6) To highlight the unique features of the proposed element models in the collapse simulations and identify limitations of existing models commonly used in practice.

(7) To examine the brittle failure in the element and how the failure sequence influences the collapse behavior, force redistribution, and the local and global response.

(8) To formulate new global damage indices from the local element damage variables to assist in the damage assessment of structures.

(9) To introduce the concept of Localized Damage Region (LDR) to identify the most probable story collapse mechanisms in SMFs.

1.4 Dissertation Outline

The dissertation is organized into 6 chapters and 3 appendices, each of which addresses one or several objectives outlined in the previous section.

Chapter 1 discusses the motivation for the study and presents a detailed literature review of relevant topics. The chapter concludes with a brief review of continuum damage mechanics and the basic coordinate system of 2d frame elements.

Chapter 2 presents a new hysteretic damage model. The chapter starts with a detailed description of the model formulation and parameters, followed by a series of validation examples to showcase its capabilities to capture a vast range of hysteretic behaviors and damage evolution. The chapter concludes with a comparison of the model's damage variable with an existing damage index model commonly used in practice.

Chapter 3 and 4 present new damage-plasticity beam and column elements, respectively. Each chapter starts with the element formulation and the state determination in a nondegrading configuration, followed by a discussion of the damage formulation in the element response. Simulations of components and structures are presented to validate the model capabilities. To facilitate the parameter identification, detailed guidelines for the parameter calibration are presented at the end of each chapter.

Chapter 5 incorporates the new damage models in a simulation of an 8-story 3-bay steel special moment-resisting frame (SMF). The chapter investigates the static and dynamic response of the archetype building up to collapse. The chapter presents new damage indices and discusses its implementation in damage evaluation and collapse assessment of steel SMFs. Finally, the reference structural model is compared against several alternatives to examine different modeling assumptions.

Chapter 6 summarizes the key findings in the present study, highlights some limitations of the current models, and offers recommendations for future development.

Appendix A offers further discussion on the selection of the statistical function for the damage evolution law, then introduces two useful statistical functions as alternatives. Appendix B presents the mathematical derivations of the return-mapping algorithm and the algorithmic tangent of the element models. Appendix C discusses the thermodynamic framework of the damage formulation.

1.5 Preliminaries

1.5.1 Continuum damage mechanics

The proposed models in this dissertation are based on the theory of effective stress and equivalent strain in continuum damage mechanics (CDM) [41]. The theory relates the material response in the *true* physical configuration to the response in an *effective* undamaged state. With a bar denoting the variables in the effective space, the *equivalent strain hypothesis* postulates the equality of the true strain ϵ with the effective strain $\bar{\epsilon}$:

$$\epsilon = \bar{\epsilon} \tag{1.1}$$

The *effective stress theory* then states that the actual stress σ and the effective stress $\bar{\sigma}$ at a given strain are related through a damage variable d as is the stiffness E and $\bar{E}$ in the two

configurations:

$$\sigma = (1-d)\bar{\sigma} \tag{1.2}$$

$$E = (1-d)\bar{E} \tag{1.3}$$

1.5.2 Basic coordinate system for plane frame elements

In Chapter 3 and Chapter 4, the element force-deformation relation is defined in a basic system to accommodate the nonlinear geometry under large displacements. The study adopts the corotational formulation, which defines a reference rigid coordinate system that rotates with the element as it deforms and distinguishes the element deformations from the rigid body motion. Equilibrium in the element free body is satisfied in the deformed configuration, with the element basic forces defined relative to the chord in its position under large displacements. The static and kinematic variables for a frame element are shown in the global coordinate system $\mathbf{p}-\mathbf{u}$ in Figure 1.1(a), in the local $\bar{\mathbf{p}}-\bar{\mathbf{u}}$ coordinate system in Figure 1.1(b), and in the basic system $\mathbf{q}-\mathbf{v}$ in Figure 1.1(c). Transformation of the basic element forces to the end forces in the global coordinate system is possible with the direction cosines of the chord orientation in the deformed configuration.

This dissertation limits the element formulation to 2d response and neglects the biaxial bending and torsion effect. The element models relate the basic forces $\mathbf{q} = [q_a, q_i, q_j]^T$ to the basic deformations $\mathbf{v} = [v_a, v_i, v_j]^T$. q_a and v_a denote the axial force and axial deformation, while $q_i - v_i$ and $q_j - v_j$ represent the flexural force and flexural deformation at end i and end j, respectively.

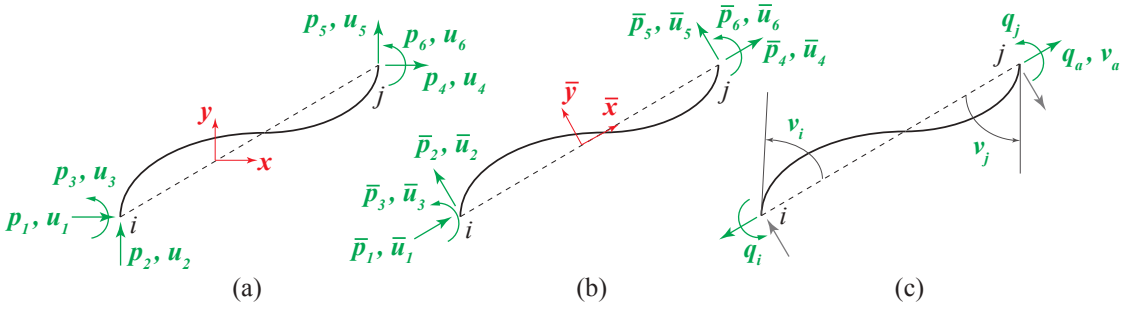

Figure 1.1: Coordinate systems for plane frame elements: (a) global coordinate system, (b) local coordinate system, (c) basic system

Chapter 2

Hysteretic Damage Model

This chapter presents a hysteretic damage model for the response simulation of structural components with strength and stiffness deterioration under cyclic loading. The model is based on 1d continuum damage mechanics and relates any two work-conjugate response variables such as force-displacement, moment-rotation or stress-strain. The strength and stiffness deterioration is described by a continuous damage variable. The formulation uses a criterion based on the hysteretic energy and the maximum absolute deformation value for damage initiation with a cumulative probability distribution function for the damage evolution. A series of structural component response simulations showcase the ability of the model to describe different types of hysteretic behavior. The relation of the model's damage variable to the Park-Ang damage index is also discussed.

2.1 Introduction

2.2 Formulation

The continuum damage mechanics (CDM) theory uses damage as an internal variable d to describe the stress-strain relation at the material level and provides a physical motivation for this choice [41]. For the modeling of structural components, Cipolina [16], Florez-Lopez [40] and Faleiro et al. [26] extended the formulation to stress resultants by showing that a damage-based model for stress resultants is thermodynamically consistent with the CDM material model and gives results that are consistent with experimental observations [26].

Consequently, the proposed hysteretic damage model is presented in the general context of any two work-conjugate variables s and e, where s denotes the stress or stress resultant and e the corresponding strain or deformation. The following description refers to s as *force* and e as *deformation*, but the model can be used for force-displacement, moment-rotation, moment-curvature, or stress-strain hysteretic relations.

The formulation consists of three independent parts: (1) the force-deformation relation in the effective space defining a boundary to serve as the upper bound of the true response

under positive deformations and as the lower bound of the true response under negative deformations; (2) the damage loading function describing the trigger and the accumulation of the energy dissipation, which is then used in the third component, the damage evolution law, to establish the damage variable d. The latter controls the strength and stiffness deterioration of the force-deformation relation by reducing the effective force $\bar{s}$ to the true force s.

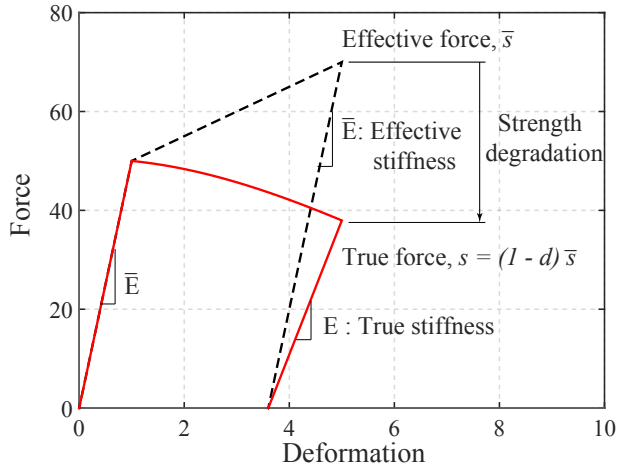

Figure 2.1: Relation between effective and true response

Figure 2.1 illustrates the interplay of the model components: first the relation between the effective force $\bar{s}$ and the deformation is defined, as represented by the long dash line in the figure. Given the effective force-deformation relation the damage loading function serves as the criterion for damage growth. It is defined in terms of the energy dissipation in the effective force-deformation space. Finally, the damage evolution law relates the value of the damage loading function to the damage variable d which is used to reduce the effective force $\bar{s}$ to the true force s and the effective unloading stiffness $\bar{E}$ to the true unloading stiffness E. A solid red line depicts the resulting relation between the deformation and the true force in Figure 2.1. The threshold of damage initiation coincides with the yield point of the effective force-deformation relation in the figure, but can it be set to any value, since it is an independent parameter of the damage evolution law.

The following subsections describe each component of the hysteretic damage model in detail.

2.2.1 Constitutive relation in effective space

The force-deformation relation in effective space serves as the boundary of the degrading response. While any suitable relation can be used for the purpose, the following discussion focuses on two representative relations: (i) the Giuffré, Menegotto, Pinto (GMP) model with isotropic hardening [27], and (ii) a simple bilinear model with elastic unloading and a bilinear reloading path that describes either "pinching" or the Bauschinger effect of the

hysteretic relation. The GMP model is suitable for metallic components with symmetric hysteretic behavior under positive and negative deformations and with pronounced Bauschinger effect in the reloading response, while the simple bilinear model is suitable for components with asymmetric monotonic behavior in tension and compression, and for components with bilinear reloading following an elastic unloading, particularly those exhibiting "pinching".

The first model in effective space describes a smooth hysteretic relation with a gradual transition from the elastic to the plastic behavior. The model requires the following parameters: the elastic stiffness E, the yield strength s_y, the hardening ratio b, the parameter r controlling the transition from the elastic to the plastic branch, two parameters c_{R1} and c_{R2} controlling the evolution of parameter r, and four parameters a_1, a_2, a_3, a_4 describing the isotropic hardening behavior, two for the response under positive forces and two under negative forces. [27] presents details of the formulation and the numerical state determination of the model. Here, the model is extended to accommodate asymmetric hardening and reloading behavior with different values for parameters b, r, c_{R1}, c_{R2} for the response under positive and negative forces. Figure 2.2(a) shows the force-deformation relation of the model for two and a half cycles with one incomplete load reversal under negative deformation. Units are not displayed since these are not pertinent to the discussion. The hardening modulus E_h in Figure 2.2(a) is the product of the elastic stiffness E and the hardening ratio b [27].

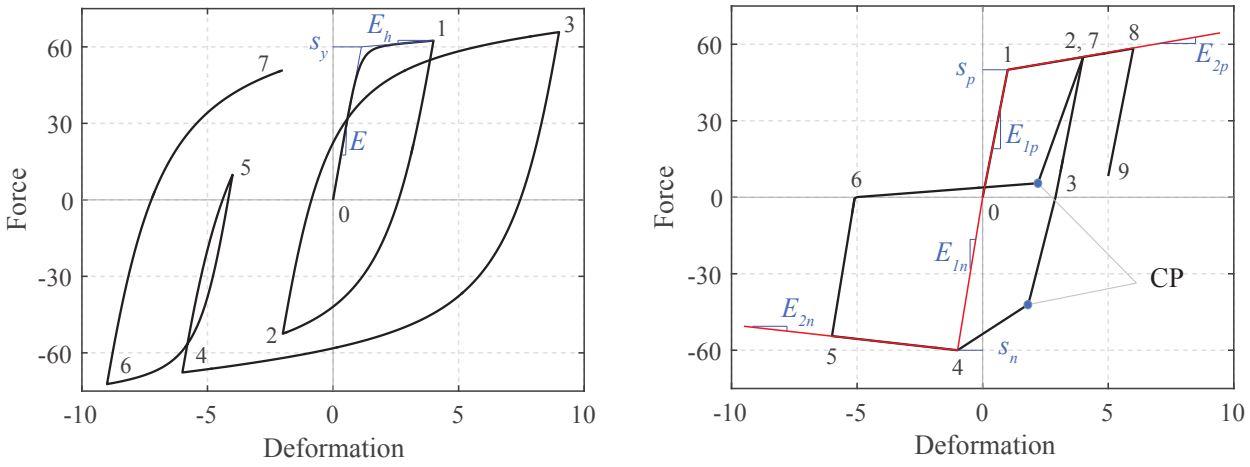

(a) GMP model

(b) Bilinear hysteretic model

Figure 2.2: Selected force-deformation relations in effective space

The second force-deformation relation in effective space has two bilinear curves with independent parameters for accommodating asymmetric behavior in tension and compression, as Figure 2.2(b) shows. Each bilinear curve depends on three parameters: the yield strength s_y, the elastic modulus E_1, and the post-yield modulus E_2. The subscript p or n refers to the bilinear curve under a positive or negative deformation, respectively. Unloading takes place with the modulus E_1 of the corresponding backbone curve, while reloading takes place from

the point of complete unloading to the maximum or minimum deformation for a positive or negative deformation increment, respectively. The reloading path is bilinear with the first branch connecting the point of complete unloading with an intermediate point p_x and p_y, and the second branch connecting the latter with the point of maximum or minimum previous deformation. Asymmetric reloading behavior is possible with different reloading parameters in tension (p_{xp} and p_{yp}) than in compression (p_{xn} and p_{yn}). Figure 2.2(b) illustrates an asymmetric reloading response with pinching behavior for reloading in the positive direction, and a Bauschinger effect for reloading in the negative direction. The intermediate point coordinates p_x and p_y are defined relative to the deformation and force range of the reloading path: $p_x = p_y$ results in a linear peak-oriented reloading path in Figure 2.3(a), $p_x < p_y$ describes a reloading behavior similar to the Bauschinger effect of metallic materials in Figure 2.3(b), and $p_x > p_y$ describes "pinching" behavior in Figure 2.3(c).

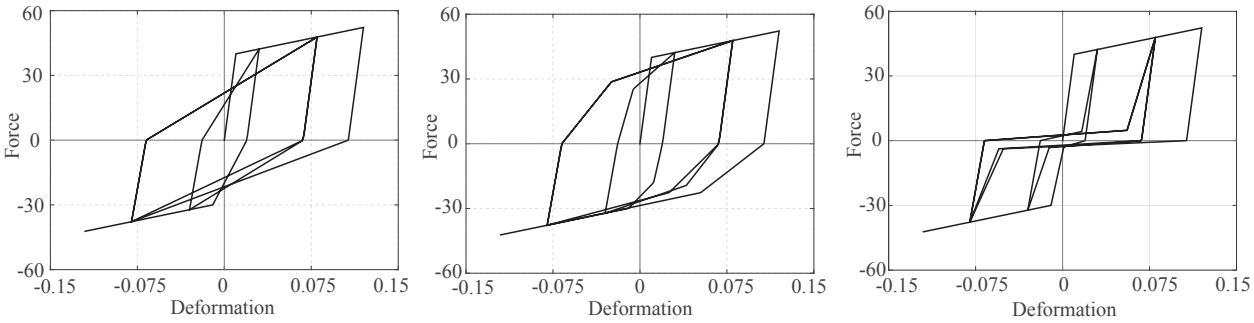

(a) $p_x = p_y = 1$ (b) $p_x = 0.3$, $p_y = 0.6$ (c) $p_x = 0.9$, $p_y = 0.1$

Figure 2.3: Effect of p_x and p_y on the reloading response of the hysteretic model

2.2.2 Damage loading function.

The damage loading function represents the criterion for damage growth. In the proposed model this criterion is defined in terms of the energy dissipation in the effective force space. Because structural components may exhibit different damage evolution under a positive force than under a negative force, it is important that the damage loading function distinguishes between the energy dissipation under positive force states from that under negative force states. To accomplish this the following definition separates the positive effective force $\bar{s}^+$ from the negative effective force $\bar{s}^-$:

$$\bar{s}^{\pm} = \frac{\bar{s} \pm |\bar{s}|}{2} \tag{2.1}$$

Consequently, $\bar{s}^+$ is equal to $\bar{s}$ for $\bar{s} \geq 0$ and equal to zero otherwise. In contrast, $\bar{s}^-$ is equal to $\bar{s}$ for $\bar{s} \leq 0$ and is equal to zero otherwise.

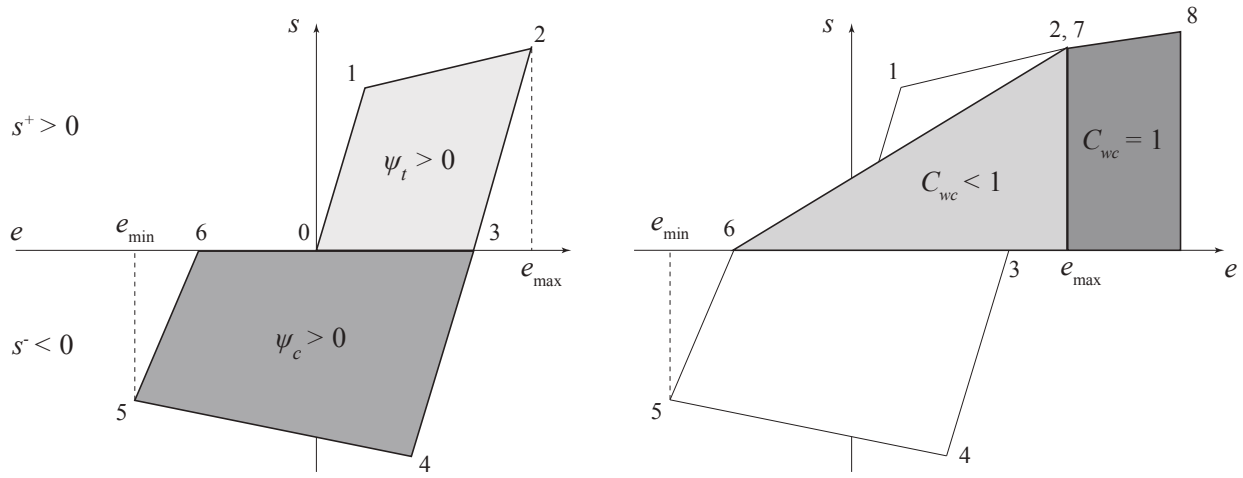

(a) Determination of ψ_t and ψ_c (b) Half cycle with partial and full energy dissipation

Figure 2.4: Illustration of ψ_t and ψ_c and of the effect of the parameter C_{wc}

The damage loading function is expressed in terms of two variables ψ_t and ψ_c in Figure 2.4 representing the energy dissipation under positive effective forces and negative effective forces, respectively. These are defined by the integral of the product of $\bar{s}^+$ or $\bar{s}^-$ with the deformation increment $(\dot{e})d\tau$ over the pseudo-time variable τ

$$\psi_t(t) = \int_{t_0}^{t} C_{wc}^{+}(e)\ \bar{s}^{+}(e)\ \dot{e}(\tau)\ d\tau \tag{2.2}$$

$$\psi_c(t) = \int_{t_0}^{t} C_{wc}^{-}(e)\ \bar{s}^{-}(e)\ \dot{e}(\tau)\ d\tau \tag{2.3}$$

$\dot{e}$ denotes the deformation derivative with respect to the pseudo-time τ, t_0 denotes the time at the start of loading, and t denotes the pseudo-time at the current state. Figure 2.4(b) shows that the constants $C_{wc}^{\pm}$ in the integrals of Equation (2.2) and Equation (2.3) serve as weights of the energy dissipation increment for differentiating the effect of deformations exceeding the previous extreme values from the effect of deformations within the extreme values. Denoting with $e_{\min}$ the minimum and $e_{\max}$ the maximum previous deformation the weights C_{wc} are defined by:

$$C_{wc}(e) = \begin{cases} 1 & \text{if } e < e_{\min} \quad \text{or} \quad e > e_{\max} \\ 0 \le C_{wc} \le 1 & \text{if } e_{\min} \le e \le e_{\max} \end{cases} \tag{2.4}$$

C_{wc} in Equation (2.2) and Equation (2.3) thus represents the effect of primary and follower half cycles in [49] and [63] on the energy dissipation with continuous updating of the energy

dissipation variables as opposed to the discrete updating at the end of each half cycle in many earlier models.

The separation of the energy dissipation into contributions under positive and negative effective forces in Equation (2.2) and Equation (2.3) offers the opportunity to account for the coupling effect that the energy dissipation in one loading direction has on the damage in the opposite loading direction, as exhibited by the hysteretic behavior of different types of structural components, e.g. concrete shear walls [77]. To include this coupling effect two energy dissipation variables ψ^+ and ψ^- are introduced as the linear combination of ψ_t and ψ_c in the following form:

$$\begin{pmatrix} \psi^+ \\ \psi^- \end{pmatrix} = \begin{bmatrix} 1 & C_{cd}^+ \\ C_{cd}^- & 1 \end{bmatrix} \begin{pmatrix} \psi_t \\ \psi_c \end{pmatrix} \tag{2.5}$$

In this definition $C_{cd}^{\pm}$ are damage coupling parameters with $C_{cd}^+ \geq 0$ weighing the contribution of the energy dissipation under negative forces on the energy variable ψ^+ and $C_{cd}^- \geq 0$ weighing the contribution of the energy dissipation under positive forces on the energy variable ψ^-.

To complete the definition of the damage loading function the energy threshold $\tilde{\psi}^{\pm}$ for damage growth needs to be defined. The maximum previous energy dissipation serves this purpose with the definition:

$$\tilde{\psi}^{\pm}(t) = \max \psi^{\pm}(\tau) \qquad t_0 \leq \tau < t \tag{2.6}$$

Consequently, the damage loading function is defined by:

$$g^{\pm}(t) = \psi^{\pm}(t) - \tilde{\psi}^{\pm}(t) \tag{2.7}$$

Damage growth occurs when $g^{\pm}(t) > 0$.

2.2.3 Damage evolution law

The third component of the hysteretic damage model is the damage evolution law that relates the energy dissipation variables $\psi^{\pm}(t)$ to the damage variable d. Noting that the damage variable d in CDM ranges from 0 at damage initiation to 1 at complete loss of strength, the damage evolution law requires the definition of a threshold energy $\psi_{d0}^{\pm}$ for damage initiation and a limit (ultimate) energy $\psi_{d1}^{\pm}$ at complete loss of strength. These energies are defined as multiples of the corresponding energy at yield initiation $\psi_y^{\pm}$ according to:

$$\psi_{d0}^{\pm} = C_{d0}^{\pm} \psi_y^{\pm} \tag{2.8}$$

$$\psi_{d1}^{\pm} = C_{d1}^{\pm} \psi_y^{\pm} \tag{2.9}$$

where $C_{d0}^{\pm}$ and $C_{d1}^{\pm}$ are model parameters. $C_{d0} = 0$ implies that the damage evolution starts with the virgin material, while $C_{d0} = 1$ implies that the damage initiation coincides with the

yield point of the effective force-deformation relation. The greater $C_{d0} > 1$ is, the more the damage initiation is delayed after yielding. The parameters $C_{d1}^{\pm}$ play the same role as the deformation ductility at the complete strength loss of the component.

With the introduction of the threshold and the limit energy the energy dissipation can be normalized according to:

$$\hat{\psi}^{\pm} = \frac{\psi^{\pm} - \psi_{d0}^{\pm}}{\psi_{d1}^{\pm} - \psi_{d0}^{\pm}} \tag{2.10}$$

with $\hat{\psi}^{\pm}$ denoting the normalized energy dissipation of the component.

Noting that the damage variable d ranges from 0 to 1 it is convenient to tap into the vast array of cumulative probability distribution functions (CDF) for the damage evolution law with the normalized energy $\hat{\psi}$ in Equation (2.10) taking the place of the random variable and the damage variable d the place of the cumulative probability.

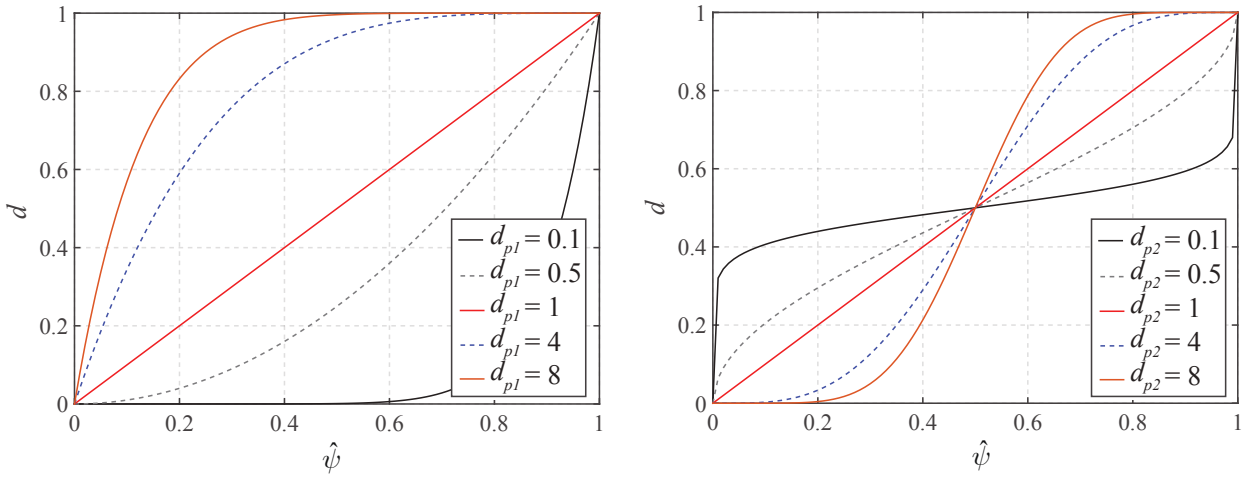

(a) Effect of d_{p1} for $d_{p2} = 1$ (b) Effect of d_{p2} for $d_{p1} = 1$

Figure 2.5: Effect of parameters $d_p^{\pm}$ on the damage evolution

Among possible CDFs the proposed model uses the beta CDF [101] for the damage evolution law, because it seems to match better the degradation of structural components and fits the analytical form of the model well. With it the dependence of the damage variable d on the normalized energy dissipation $\hat{\psi}$ becomes:

$$d^{\pm} = F_B(\hat{\psi}^{\pm}, \beta_1^{\pm}, \beta_2^{\pm}) \tag{2.11}$$

where F_B is the beta CDF with its parameters β_1 and β_2. The latter can be assigned different values for the damage evolution under $\hat{\psi}^{+}$ than under $\hat{\psi}^{-}$, as reflected by the superscripts.

For better identification of the effect of the parameters β_1 and β_2 on the damage evolution it is useful to introduce the following relations:

$$d_{p1} = \beta_2/\beta_1 \tag{2.12}$$
$$d_{p2} = \min(\beta_1, \beta_2) \tag{2.13}$$

The parameter d_{p1} thus represents the ratio of β_2 to β_1, while the parameter d_{p2} is equal to the smaller of β_1 and β_2. Figure 2.5 shows the benefit of this parameter change in the interpretation of the parameter effect on the damage evolution. Figure 2.5(a) shows the effect of d_{p1} on the damage evolution under constant $d_{p2} = 1$. The value $d_{p1} = 1$ corresponds to a uniform rate of damage accumulation with normalized energy dissipation $\hat{\psi}$, while a value $d_{p1} > 1$ biases the damage rate accumulation toward the early stages of energy dissipation, and a value of $d_{p1} < 1$ biases it toward the later stages. Figure 2.5(b) shows the effect of d_{p2} on the damage evolution under constant $d_{p1} = 1$. The value $d_{p2} = 1$ corresponds to a uniform rate of damage accumulation with normalized energy dissipation $\hat{\psi}$, while a value $d_{p2} > 1$ concentrates the damage accumulation in the middle range of energy dissipation and a value $d_{p2} < 1$ concentrates it in the early and late stages. It is evident from Figure 2.5 that the parameters d_{p1} and d_{p2} afford considerable flexibility in the description of the damage evolution.

Upon determination of the damage variables $d^{\pm}$ with the damage evolution law in Equation (2.11) the true force s results from the linear combination of the positive effective force $\bar{s}^+$ and the negative effective force $\bar{s}^-$ after multiplication with the respective damage variables

$$s = \left(1 - d^+\right) \bar{s}^+ + \left(1 - d^-\right) \bar{s}^- \tag{2.14}$$

The model formulation can be shown to be thermodynamically consistent. The state determination of the damage model evaluates the force s_n at step n given the deformation e_n and the history variables at step $n - 1$. Table 2.1 summarizes the algorithm.

2.3 Effect of Damage Parameters

Following the model description it is helpful to showcase the effect of the model parameters on the strength and stiffness deterioration of the hysteretic behavior. The following discussion also aims at facilitating the parameter selection by demonstrating the response sensitivity of the model to a range of parameter values. The discussion uses the backbone envelope in Figure 2.6 for the effective force-deformation relation. This choice is motivated by the recommendation of the FEMA study in [19] for the response description of different structural component types. The multi-linear envelope in Figure 2.6 consisting of the elastic range, the strength hardening range, two strength softening ranges, and the residual strength plateau can be adjusted to match the backbone envelope of different structural component types: to this end one or both strength softening ranges may be present while the strength hardening range and the residual strength plateau may be missing from the envelope [19].

1. State determination in effective space
  Evaluate $\bar{s}_n$ and internal variables
2. Energy variables
  Identify $C_{wc}^{\pm}$ in (2.4)
  Compute ψ_t and ψ_c in (2.2)-(2.3)
  Evaluate ψ^+ and ψ^- in (2.5)
3. Damage loading functions
  Identify $\tilde{\psi}^{\pm}$ in (2.6)
  Evaluate $g^{\pm}$ in (2.7)
  IF $g^* < 0$ with $* =$ '+', '-' THEN:
    No damage growth, go to Step 4a
  ELSE:
    Damage accumulates, go to Step 4b
4a. No damage loading: $d_n^* = d_{n-1}^*$
4b. Damage loading
  Evaluate $\hat{\psi}^*$ in (2.10)
  Update d_n^* in (2.11)
5. Update s_n in (2.14)

Table 2.1: State determination algorithm of hysteretic damage model

The following parameter study sets the residual strength plateau to zero, since this has little bearing on the parameter influence of the response.

The damage threshold coefficient C_{d0} in Equation (2.8) controls the damage initiation and affects the post-yield range prior to the onset of strength softening, as Figure 2.7(a) shows: a higher C_{d0} value delays the onset of damage and increases the range of the post-yield hardening range. The limit (ultimate) damage coefficient C_{d1} in Equation (2.9) controls the energy at complete strength loss thus affecting the ultimate deformation ductility and the strength softening behavior: a higher C_{d1} increases the ultimate deformation at complete loss of strength in Figure 2.7(b) thus reducing the rate of strength softening. The damage evolution parameters d_{p1} and d_{p2} in Equation (2.12)-Equation (2.13) affect the rate of damage accumulation. Figure 2.7(c)-(d) illustrate their effect on the response, as discussed in connection with Figure 2.5: d_{p1} controls the bias of damage growth between the early and late response stages, while d_{p2} controls the evolution of the rate of damage growth with energy dissipation.

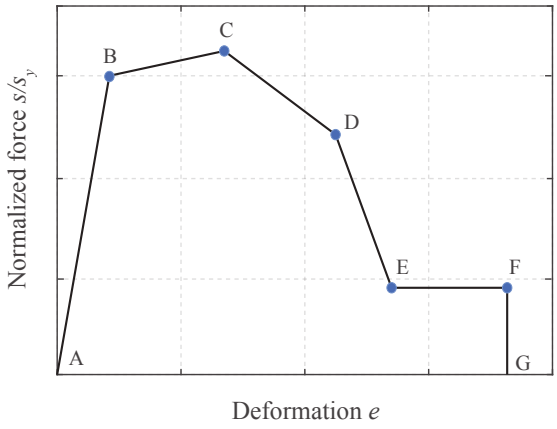

Figure 2.6: FEMA force-deformation envelope

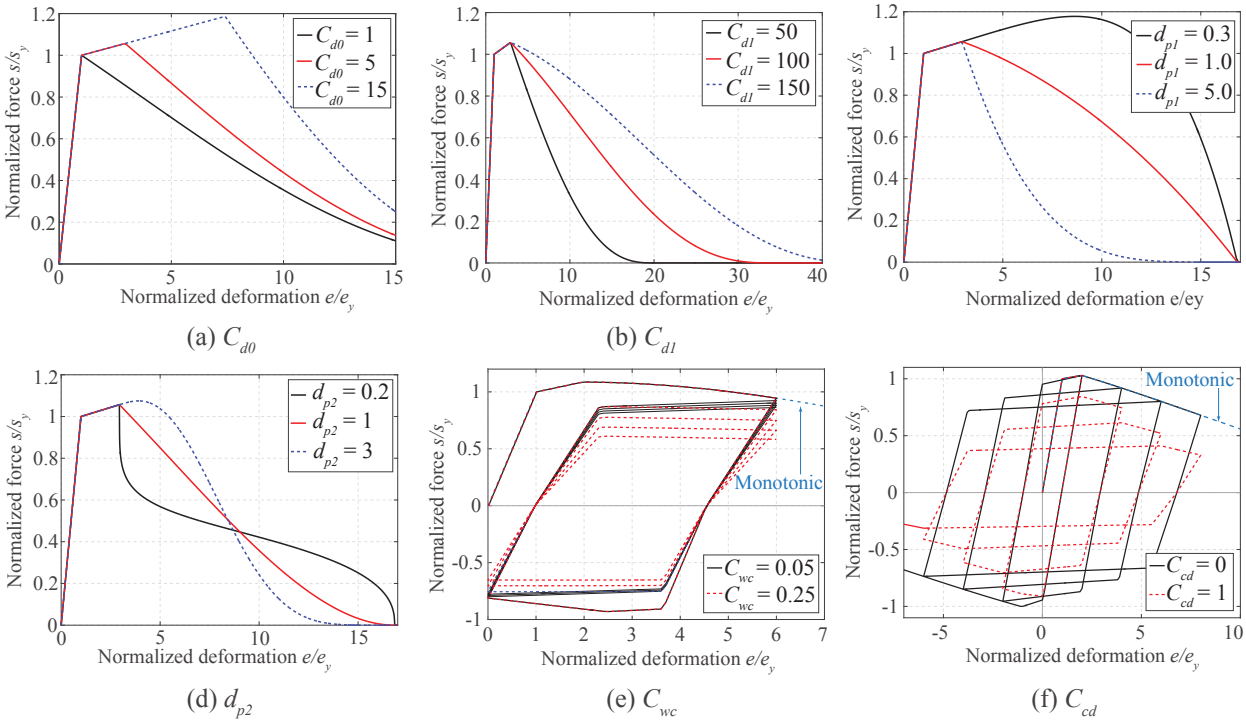

Figure 2.7: Effect of damage parameters on force-deformation relation

The cyclic degradation coefficient C_{wc} in Equation (2.4) controls the contribution of the energy dissipation under follower half cycles on the damage growth: while a value of $C_{wc} = 0$ neglects completely this contribution, a value of $C_{wc} = 1$ accounts for it fully and results in more severe strength and stiffness degradation under cyclic loading. Figure 2.7(e) shows the effect of two typical values of C_{wc} on the strength and stiffness deterioration of the hysteretic

response. Later correlation studies show that this range of values covers the hysteretic behavior of most specimens. Finally, the damage coupling coefficient C_{cd} in Equation (2.5) controls the effect of the energy dissipation under a positive effective force on the damage variable for the response under a negative effective force and vice versa. Figure 2.7(f) shows the behavior of the model for two limit values of C_{cd}: for $C_{cd} = 0$ the energy dissipation under a positive force has no effect on the strength and stiffness deterioration under a negative force and vice versa. For $C_{cd} = 1$ the energy dissipation under a positive force is accounted for fully in the determination of the damage variable for the response under a negative force and the same is true for the energy dissipation under a negative force for the response under a positive force.

2.4 Illustrative example

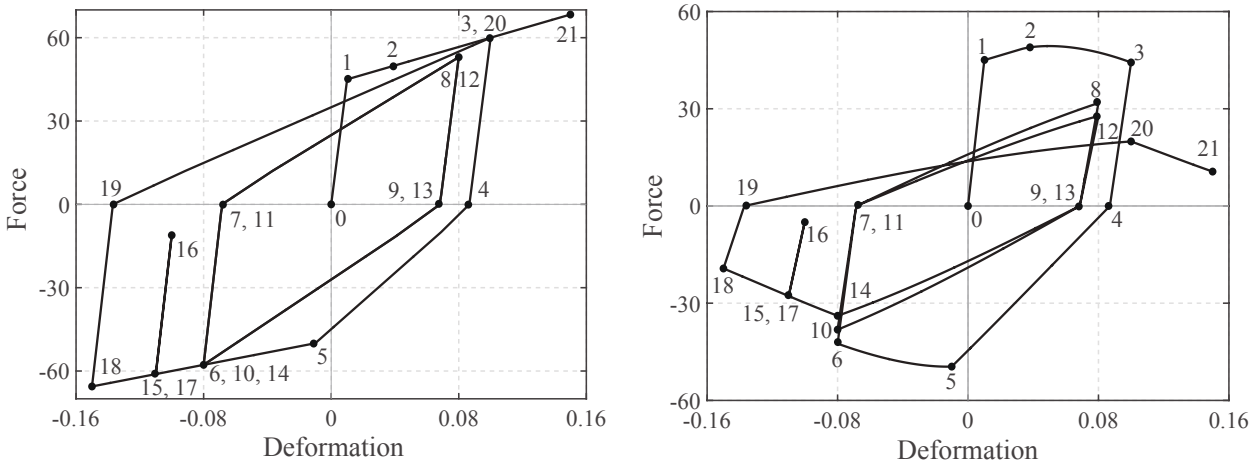

(a) Effective response without damage

(b) True response with damage

Figure 2.8: Sample cyclic response of proposed model

The following example illustrates the hysteretic behavior of the proposed model. The example uses the bilinear model of Figure 2.2(b) for the effective force-deformation relation with the following parameters: s_{yp} = 45, E_{1p} = 4,500, E_{2p} = 150, s_{yn} = -50, E_{1n} = 5,000, E_{2n} = 100. Under cyclic reloading, the selection of $p_x = p_y$ ensures a straight reloading path from the point of complete unloading to the largest previous deformation in the opposite direction. Figure 2.8(a) shows the force-deformation relation in the effective space without damage, while Figure 2.8(b) shows the evolution of strength and stiffness deterioration of the hysteretic force-deformation relation under the imposed cyclic deformation history. The parameters for the damage loading function are $C^{\pm}_{d0} = 5$, $C^{\pm}_{d1} = 100$, $C^{\pm}_{wc} = 0.2$, $C^{\pm}_{cd} = 0.25$, while the parameters for the damage evolution law are $[d^{\pm}_{p1}; d^{\pm}_{p2}] = [2; 1.5]$.

The onset of damage after yielding at load point (LP) 1 occurs at LP 2 because of the selection of C_{d0} greater than 1. The strength reduction between LP 2 and 3 is evident. The effect of the energy dissipation up to LP 4 is evident in the strength reduction between LP 4, 5 and 6 because of the value for the damage coupling parameter C_{cd}^{-} set at 0.25 for the case in hand.

The proposed hysteretic damage model accommodates both types of degradation in FEMA P440A [19]: the cyclic or between-cycle degradation, which describes the loss of strength and stiffness from one cycle to the next, and the in-cycle degradation, which describes the loss of strength and stiffness within a cycle. The former is evident in the strength and stiffness reduction between LP 6, 10 and 14, and between LP 8 and 12. The latter is evident in the continuous strength reduction between LP 2 and 3, and between LP 5 and 6. Moreover, it is evident in the model response when the deformation exceeds the maximum previous value in the same direction, as is the case between LP 14 and 18, and between LP 20 and 21.

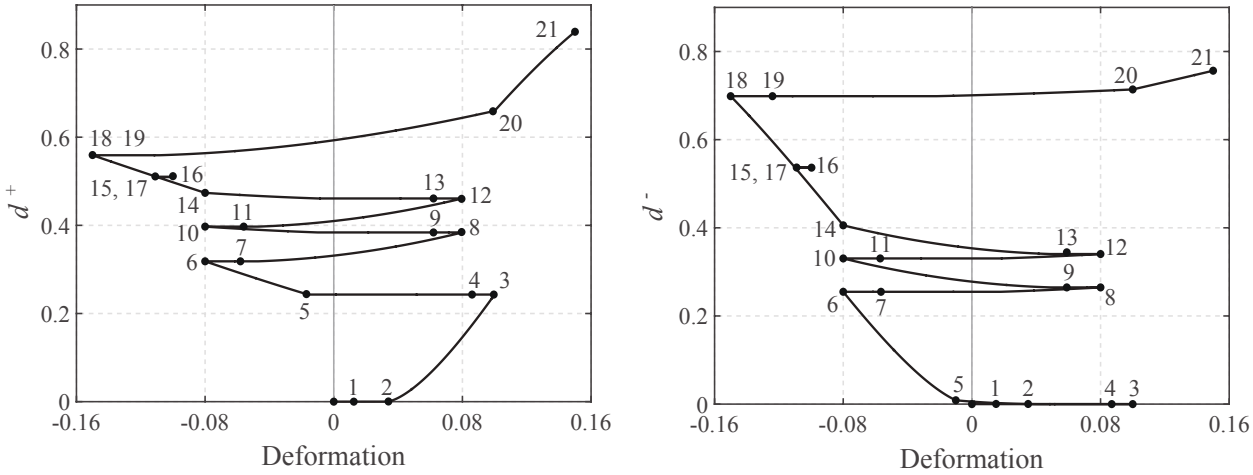

(a) Positive damage variable d^{+} (b) Negative damage variable d^{-}

Figure 2.9: Evolution of damage variables $d^{\pm}$ under cyclic loading

Figure 2.9 shows the evolution of the positive damage variable d^{+} in Figure 2.9(a) and of the negative damage variable d^{-} in Figure 2.9(b) for the load history in Figure 2.8. The rate of increase of the positive damage variable d^{+} is highest when the positive deformation exceeds the maximum previous value as is the case between LP 2 and 3, and between LP 20 and 21 in Figure 2.9(a). The same is true for the negative damage variable d^{-} between LP 5 and 6, and between LP 14 and 18 in Figure 2.9(b). The non-zero damage coupling parameter C_{cd} causes the increase of the positive damage variable d^{+} under negative deformations between LP 5 and 6, and between LP 14 and 18 in Figure 2.9(a) albeit at a slower rate because of the selection $C_{cd}^{+} = 0.25$. The same is true for the negative damage variable d^{-}

under positive deformations between LP 20 and 21 in Figure 2.9(b) for which the damage coupling parameter $C_{cd}^{-} = 0.25$ is responsible.

The positive damage variable d^{+} also increases but at a lower rate under positive deformations not exceeding the previous maximum value, as is the case between LP 7 and 8, and between LP 11 and 12 in Figure 2.9(a). The rate of this increase is controlled by the parameter $C_{wc}^{+} = 0.2$. Similarly, the negative damage variable d^{-} increases between LP 9 and 10, and between LP 13 and 14 in Figure 2.9(b), with the rate of increase controlled by the parameter $C_{wc}^{-} = 0.2$.

The proposed model describes the stiffness deterioration more consistently than models based on the pivot rule [72, 81], in which the point at complete unloading from a positive or negative force targets a predefined pivot point in the opposite load direction. Under a cyclic deformation history with decreasing magnitudes, the pivot rule leads to an increase in stiffness, whereas the proposed model describes a more realistic reduction of the unloading stiffness, as Figure 2.8 shows between LP 3-4 and LP 8-9. The proposed model also captures well the continuous reduction of the unloading stiffness, as is evident by the comparison of the unloading stiffness between LP 15 and 16 with that between LP 18 and 19 in Figure 2.8, in contrast to existing models with discrete updating which fail to characterize the gradual unloading stiffness reduction in large excursions with incomplete unloading and reloading. Figure 2.10(a) shows a sample hysteretic behavior of a reinforced concrete column subjected to a cyclic displacement pattern with decreasing amplitude [99]. The numerical solution using the proposed model shown in red captures well the evolution of the stiffness deterioration in the three unloading branches. It is confirmed in the higher damage values at the three unloading instants in Figure 2.10(b).

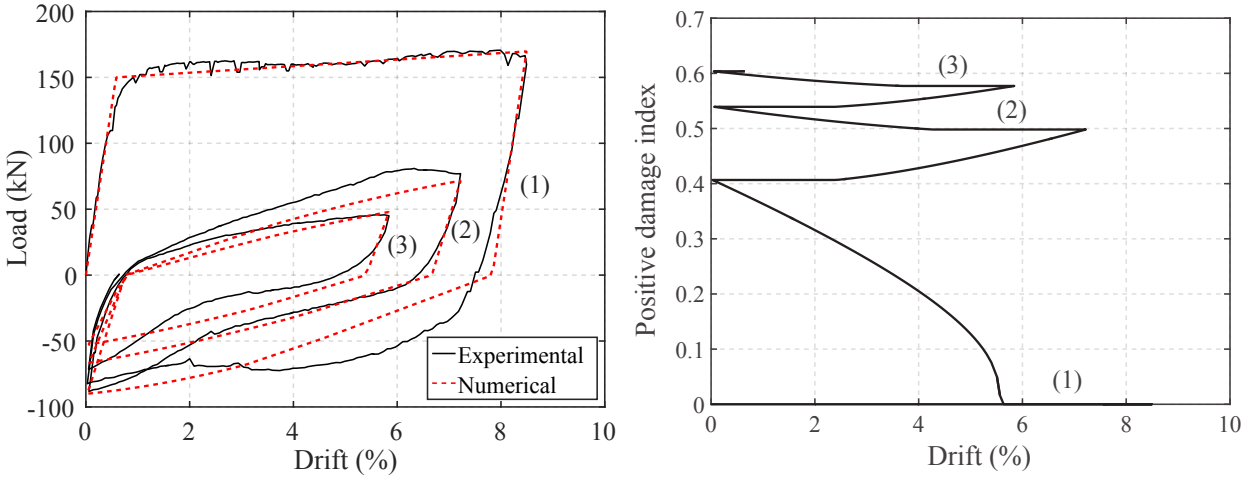

Force-deformation relation Positive damage evolution

Figure 2.10: Stiffness degradation under cyclic loading with decreasing magnitudes

2.5 Validation Studies

This section presents five case studies for validations of the proposed hysteretic damage model: the first presents simulations of reinforced concrete columns, the second simulates the cyclic response of steel beam-column subassemlies, the third examines the low-cycle fatigue behavior of steel cantilever beam under repeated loading, the fourth investigates the effect of load history on the degrading response of plywood shear walls, and the fifth is a comprehensive case study addressing the simulation of various structural systems classified by FEMA [19]. The objective of the validation studies is two-fold: (1) to showcase the ability of the model to represent accurately the degradation of various structural components, (2) to provide insight of typical parameter ranges for different types of structural systems.

2.5.1 Reinforced concrete columns

The first example studies the cyclic response and the failure mechanisms of four reinforced concrete columns. The two specimens in Figures 2.11(a)-(b) are flexure-critical (FC) and exhibit significant degradation in the plastic regions due to bending. Flexural failure mechanism occurs mostly in well-designed slender structural components with adequate shear reinforcement. In contrast, the two specimens in Figures 2.11(c)-(d) are flexure-shear-critical and shear-critical (SC), and fail in shear-related mechanisms. Shear-critical components fail because the shear strength is exceeded, mainly either in deep members or due to insufficient shear reinforcement.

Parameter	**Kanda et al**	**Kono et al**	**Ohue et al**	**Umehara et al**
s_y (kN)	70	1.2	100	200
E_1 (kN/mm)	14	0.25	33	80
E_2 (kN/mm)	1.3	0.025	6	30
p_x	0	0.5	0.8	0.8
p_y	0	0.9	0.2	0.1
C_{d0}	[1; 1]	[1; 1]	[1; 1]	[1; 1]
C_{d1}	[100; 100]	[100; 100]	[60; 60]	[60; 60]
C_{wc}	[0.05; 0.05]	[0.05; 0.05]	[0.25; 0.25]	[0.25; 0.25]
C_{cd}	[0.5; 0.5]	[0.5; 0.5]	[0.7; 0.7]	[0.6; 0.6]
d_p^+	[2; 1]	[3; 1]	[3; 1.5]	[3; 1.5]
d_p^-	[2; 1]	[3; 1]	[3; 1.5]	[3; 1.5]

Table 2.2: Parameters used in simulations of reinforced concrete columns

Table 2.2 summarizes the parameters used in the simulations. To represent different reloading behaviors, the bilinear hysteretic model in Figure 2.2(b) is used in the effective space. Since the response is quite symmetric under positive and negative deformations, the same parameters are used to describe the response under positive and negative deformations.

The different reloading behaviors are reflected in the reloading parameters p_x and p_y. For specimen STC2 in Figure 6(a), $p_x = p_y$ captures the typical peak-oriented reloading behavior commonly observed in reinforced concrete components. For specimen L1N60 in Figure 6(b), $p_x < p_y$ describes the Bauschinger effect due to a high reinforcement ratio. For specimen 4D13RS in Figure 6(c) and specimen CUW in Figure 6(d), $p_x > p_y$ captures the pronounced pinching behavior due to sliding, slip, and shear failure.

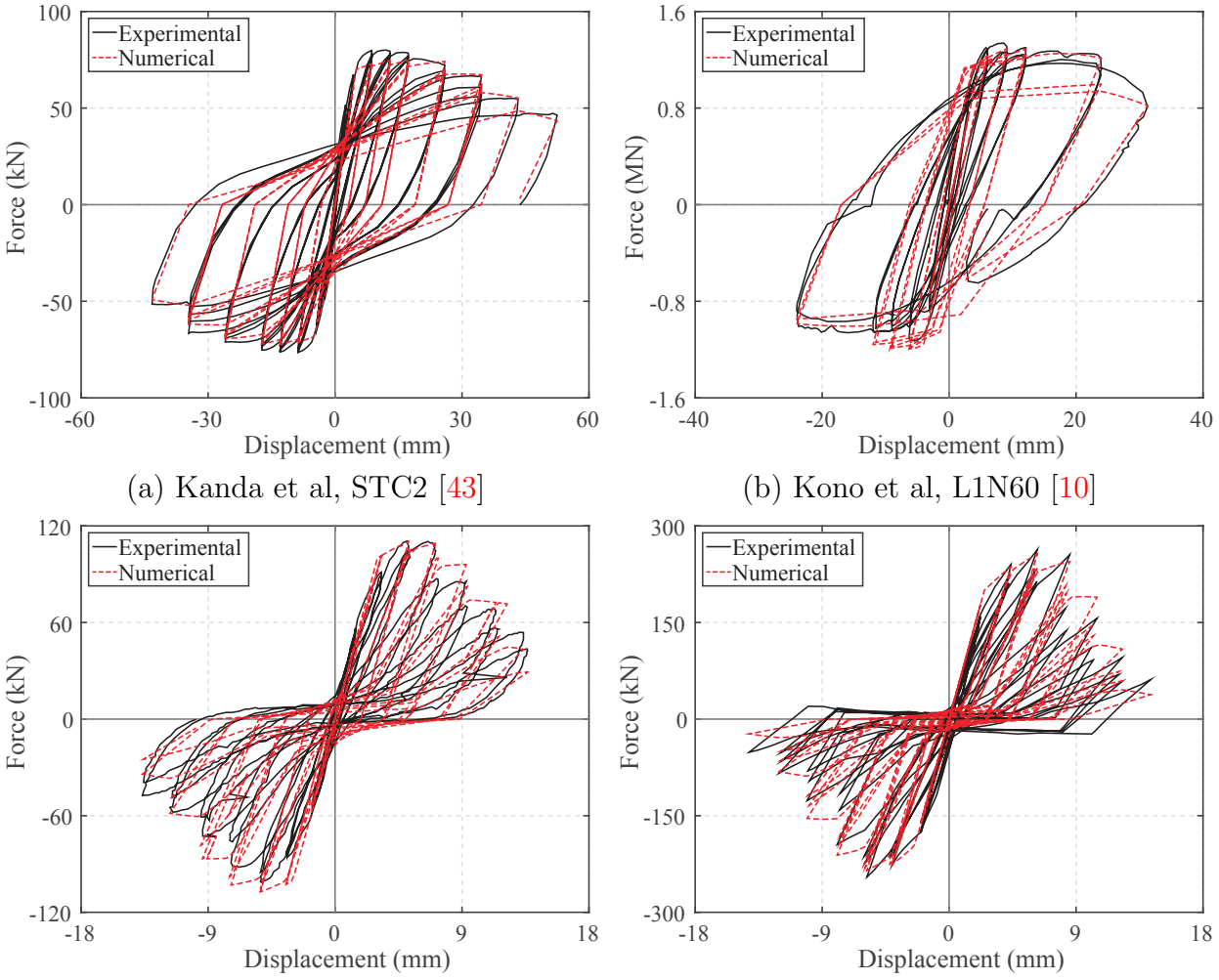

(a) Kanda et al, STC2 [43]

(b) Kono et al, L1N60 [10]

(c) Ohue, 4D13RS [69]

(d) Umehara, CUW [103]

Figure 2.11: Simulations of reinforced concrete columns

In all specimens, the threshold coefficient $C_{d0} = 1$ indicates the onset of degradation upon reinforcement yielding. The damage parameters distinguish well the degrading behaviors of FC and SC columns. The limit coefficient C_{d1} for the FC specimens ($C_{d1} = 100$) is higher than for the SC specimens ($C_{d1} = 60$) to indicate a higher ductility capacity of the FC columns. A relatively high cyclic degradation coefficient ($C_{wc} = 0.25$) and damage coupling

coefficient ($C_{cd} = 0.6$–0.7) seem to capture adequately the rapid strength deterioration under cyclic shear.

2.5.2 Steel beam-column joints

Figure 2.12 compares the experimental and the numerical load-displacement of four steel beam-column subassemblages. This example selects the GMP model in Figure 2.2(a) to describe the effective response.

The model captures well the smooth transition from the elastic to the plastic range and the Bauschinger effect in the reloading response. This is achieved with the reloading parameter r that varies within a relatively small range between 4–5. The threshold coefficients $C_{d0}^{\pm}$ are greater than 1 for all specimens so that strength degradation initiates after yielding. The relatively high displacement ductility of the steel specimens is reflected in the limit coefficients $C_{d1}^{\pm}$ in the range between 100–125. The damage evolution parameters $d_{p1}^{\pm}$ between 4–5 and $d_{p2}^{\pm} = 1$ capture well the degradation rate in the softening range. The cyclic coefficients C_{wc} and the damage coupling coefficients C_{cd} simulate accurately the strength and stiffness degradation due to cyclic loading. Similar damage parameters are specified for the positive and negative response due to symmetric degrading behavior. One exception is a higher d_{p1}^{+} than d_{p1}^{-} in specimen UCSD-3R to capture the more severe deterioration under positive forces.

Parameter	EERC-RN2	EERC-RN3	UCSD-1R	UCSD-3R
E (kip/in)	100	100	100	100
s_y (kip)	150	150	130	140
b	0.04	0.05	0.045	0.045
r	4	5	4	4
C_{d0}	[3; 3]	[2; 2]	[3; 3]	[3; 3]
C_{d1}	[125; 125]	[100; 100]	[100; 100]	[120; 120]
C_{wc}	[0.12; 0.12]	[0.1; 0.1]	[0.15; 0.15]	[0.15; 0.15]
C_{cd}	[0.5; 0.5]	[0.5; 0.5]	[0.5; 0.5]	[0.5; 0.5]
d_p^+	[4.2; 1]	[5; 1]	[4.5; 1]	[5; 1]
d_p^-	[4.2; 1]	[5; 1]	[4.5; 1]	[3; 1]

Table 2.3: Parameters used in simulations of steel beam-column joints

2.5.3 Low-cycle fatigue of steel components

To study the low-cycle fatigue behavior, the experimental campaign by Krawinkler [51] furnishes measurements of the hysteretic behavior for steel components. Three identical cantilever steel beams are selected for the response simulation: specimen B24 is subject to a monotonic deformation history, and specimens B25 and B28 to cyclic load protocols.

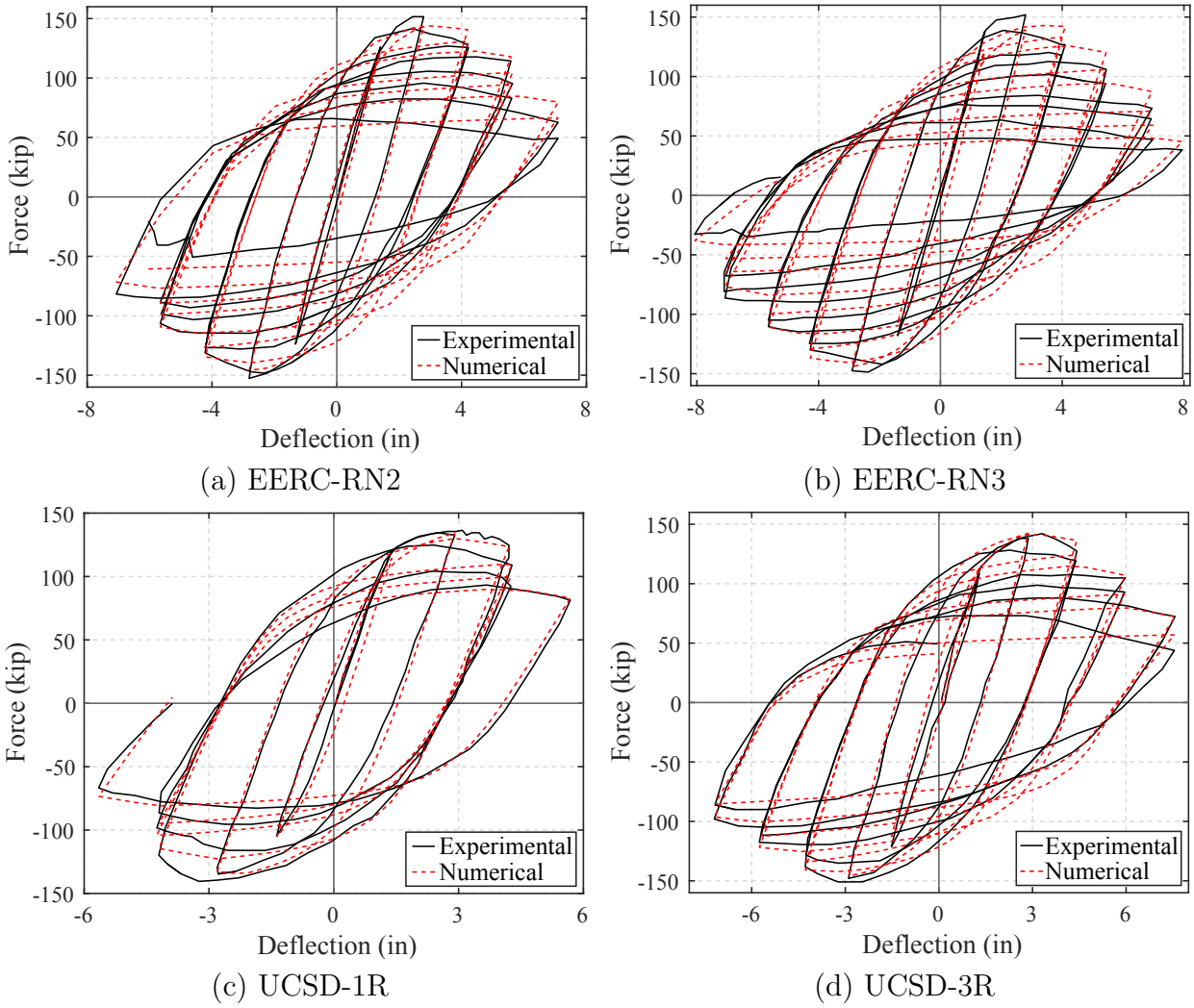

(a) EERC-RN2 (b) EERC-RN3

(c) UCSD-1R (d) UCSD-3R

Figure 2.12: Simulations of steel beam-column assemblages

The subsequent simulations use the GMP model in Figure 2.2(a) to describe the effective force-deformation relation. The same parameters are specified to reflect the symmetric geometry and properties of the specimens under positive and negative deformations. The following parameters are satisfactory for specimen B24 in Figure 2.13(a): $E = 28$, $s_y = 9.8$, $b = 0.04$, $r = 4$, $C_{d0} = 5$, $C_{d1} = 150$, $d_{p1} = 3$, $d_{p2} = 1.5$. The selection of C_{d0} greater than 1 is typical for steel components to indicate that the strength reduction initiates after yielding. The values of C_{d1}, d_{p1} and d_{p2} are also representative of steel components. The numerical solution matches rather well the post-yield response of the specimen. The evolution of the hysteretic energy in Figure 2.13(a2) confirms that the numerical solution agrees rather well with the experimental result.

Next, the cyclic test B25, which consists of several cycles at a constant displacement

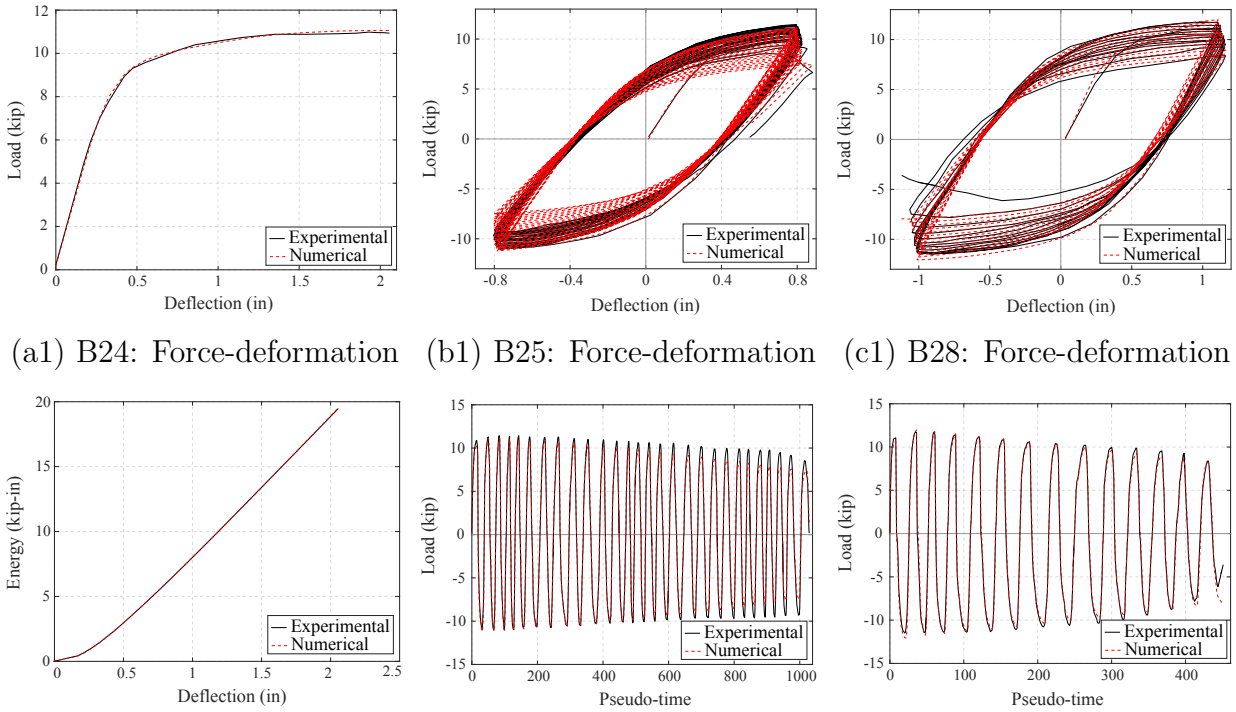

(a1) B24: Force-deformation (b1) B25: Force-deformation (c1) B28: Force-deformation

(a2) B24: Hysteretic energy (b2) B25: Force time history (c2) B28: Force time history

Figure 2.13: Simulation of steel cantilever beams under cyclic loading

amplitude, facilites the calibration of the cyclic degradation coefficient C_{wc} and the damage coupling coefficient C_{cd}. The numerical force-deformation relation with $C_{wc} = 0.14$ and $C_{cd} = 0.5$ in Figure 2.13(b) compares reasonably well with the experimental measurements. One limitation is the inadequate representation of the rapid strength degradation in the last half cycle. The parameters d_{p1} and d_{p2} of the damage evolution function could be modified to concentrate more damage at larger energy dissipation. The discrepancy also suggests that the selection of the limit coefficient $C_{d1} = 150$ may not be accurate enough. Instead a slightly lower value may represent better the rapid degradation and the lower ductility capacity. Nonetheless, the force time history in Figure 2.13(b2) confirms that the proposed damage model captures adequately the peak forces in the half cycles.

To validate the calibration, the same parameters are used to simulate the response of another identical specimen under a different cyclic deformation history. Figure 2.13(c) shows the force-deformation relation for specimen B28, which is subjected to a cyclic deformation history with larger amplitudes. The numerical solution agrees well with the experimental result albeit with the same limitations as previously discussed. Although the model underestimates the strength in compression, the numerical solution shows a consistent pattern of strength degradation in reasonable agreement with the experiment, as the force time history in Figure 2.13(c2) shows.

2.5.4 Effect of load histories on plywood shearwalls response

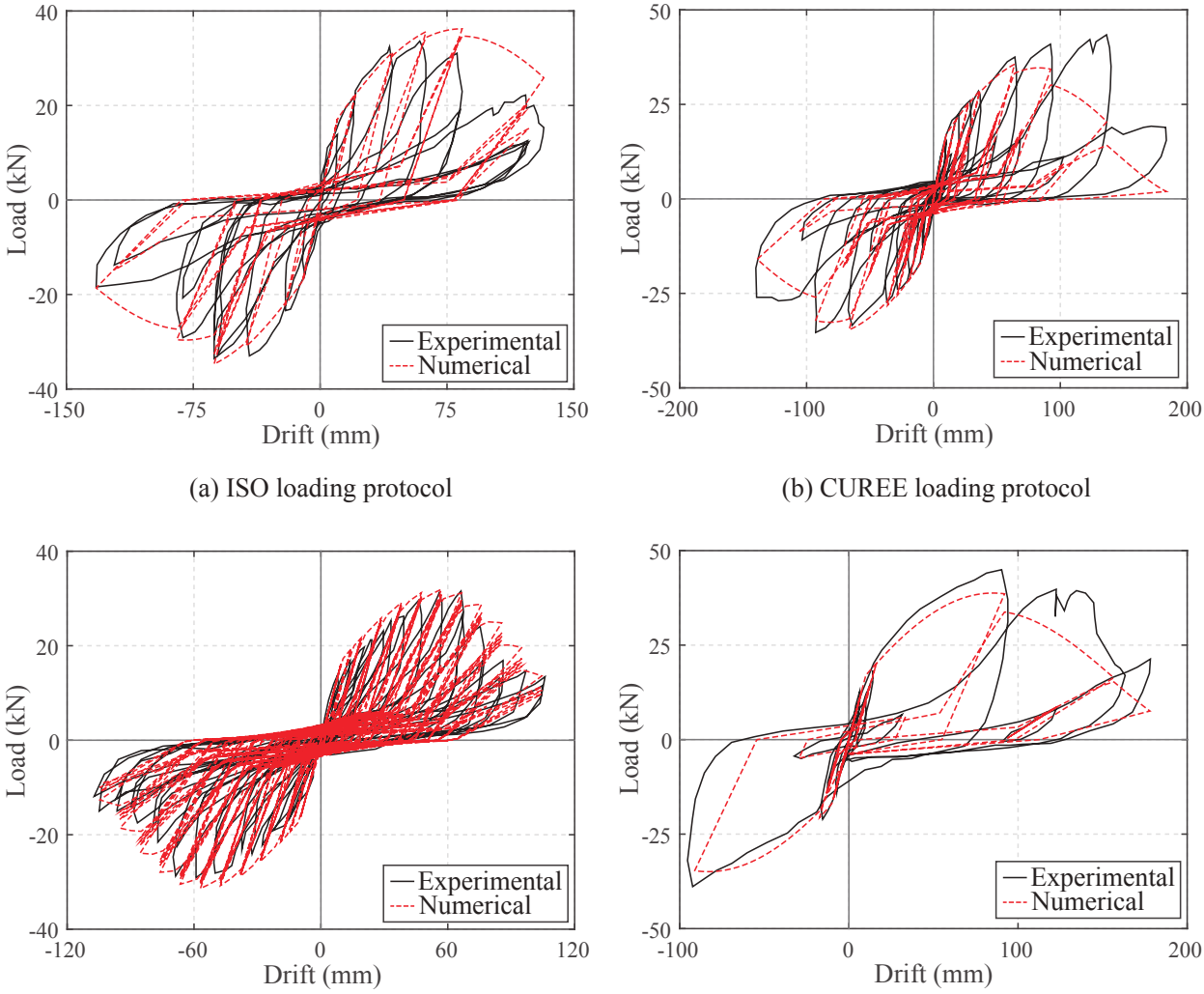

(a) ISO loading protocol

(b) CUREE loading protocol

(c) SPD loading protocol

(d) NF loading protocol

Figure 2.14: Numerical and experimental correlation for plywood shear walls

To study the model response under different load histories the experimental campaign by Gatto and Uang [29] furnishes measurements of the hysteretic behavior for four identical plywood shear walls under different deformation histories corresponding to the ISO, CUREE, SPD and NF loading protocol. For the first three protocols the loading consists of groups of displacement cycles of either constant or variable amplitude from one cycle to the next with gradually increasing average amplitude of the group as loading progresses. The NF loading protocol consists of several cycles with small but ever increasing displacement amplitude followed by very few large displacement cycles of increasing amplitude to simulate the effect

of near-fault ground motions [50].

Figure 2.14 shows the numerical results for the plywood shear walls under the four load histories. The proposed damage model uses the bilinear hysteretic model in Figure 2.2(b) to represent the force-deformation relation of the plywood shear wall in the effective space. The same parameters are used for the effective response under positive and negative deformations with the following properties: s_{yp} = 17 kN, E_{1p} = 1.7 kN/mm, E_{2p} = 0.6 kN/mm, s_{yn} = -17 kN, E_{1n} = 1.7 kN/mm, E_{2n} = 0.6 kN/mm. To account for the pronounced pinching of the hysteretic force-displacement relation during reloading the control point coordinates of the bilinear reloading branch are selected as $p_x = 0.9$, $p_y = 0.2$, very similar to the values for systems S1, S2 and S5 in Table 2.4. The same reloading parameters are used in both loading directions.

The parameters of the damage loading function are $C_{d0}^{\pm} = 1$, $C_{d1}^{\pm} = 200$, $C_{wc}^{\pm} = 0.15$, and $C_{cd}^{\pm} = 0.2$, with the parameters of the damage evolution law set as $[d_{p1}^{\pm}; d_{p2}^{\pm}] = [2.25; 1]$. These parameters are kept the same for the analysis of the plywood shear walls under the four load histories.

The comparison of the numerical results with the experimental measurements show satisfactory agreement for the evolution of the strength and stiffness deterioration of the plywood shear walls under the four load histories. The agreement is particularly good for the SPD load history Figure 2.14(c) and quite good for the NF load history in Figure 2.14(d). The ability of the model to capture the non-symmetric damage evolution between positive and negative deformations in Figure 2.14(d) is noteworthy since this type of loading proved challenging for earlier models. The underestimation of the actual deterioration in the early cycles under the ISO load protocol in Figure 2.14(a) and the overestimation of the deterioration under the CUREE load protocol in Figure 2.14(b) suggest that the energy dissipation of displacement cycles with large amplitude may have a stronger impact on the deterioration than the energy of displacement cycles with small amplitude which are quite numerous in the CUREE protocol for simulating the effect of far field ground motions. This leads to the conclusion that a value for the damage evolution law parameter $d_{p2}^{\pm}$ greater than 1 may be a more suitable choice than the selected value $d_{p2}^{\pm}$=1, which corresponds to the damage variable d being proportional to the normalized energy dissipation in Figure 2.5(b). As noted already, no effort is made in this study to optimize the selection of parameters for best fit, which is left for further study with parameter identification methods. The extensively calibrated hysteretic model by Ibarra et al. [39] shows similar discrepancies between the numerical and the experimental results for the early cycles of the ISO and CUREE load history underscoring the importance of further study for the calibration of the damage evolution law.

2.5.5 Degrading behavior of structural systems

To further showcase the ability of the proposed damage model to represent the hysteretic behavior of different structural component types, the comprehensive study of the effects of strength and stiffness degradation on the seismic response of structural systems in the framework of the FEMA P440A Recommendations is used as a reference [19]. The capacity

boundary curves of the FEMA P440A Recommendations inform the parameter selection for the damage loading function and for the damage evolution law of each structural component. The following structural components are used in the correlation studies: a typical gravity frame, subsequently referred to as system S1, a non-ductile moment frame (S2), a ductile moment frame (S3), a stiff non-ductile system (S4), a stiff and highly-pinched non-ductile system (S5), and a limited ductility moment frame (S7). These categories of hysteretic behavior follow the classification in the FEMA P440A Recommendations.

2.5.5.1 System S1 - Typical Gravity Frame

The capacity boundary for a typical gravity frame is characterized by a sudden strength drop of 45% of the yield strength of the component following yielding [19]. This capacity boundary is representative of the moment-rotation relation of a beam-to-column shear tab connection in Figure 2.15(b), as established by experiments such as those by Liu and Astaneh [58]. The observed strength degradation of these connections is caused by the closing of the gap between the beam and the column flange causing the bearing strength failure of the bolts in the shear tab and eventually leading to the shear connection failure [58]. The response under positive and negative deformation does not appear to be the same, but the FEMA P440A Recommendations do not discuss the matter.

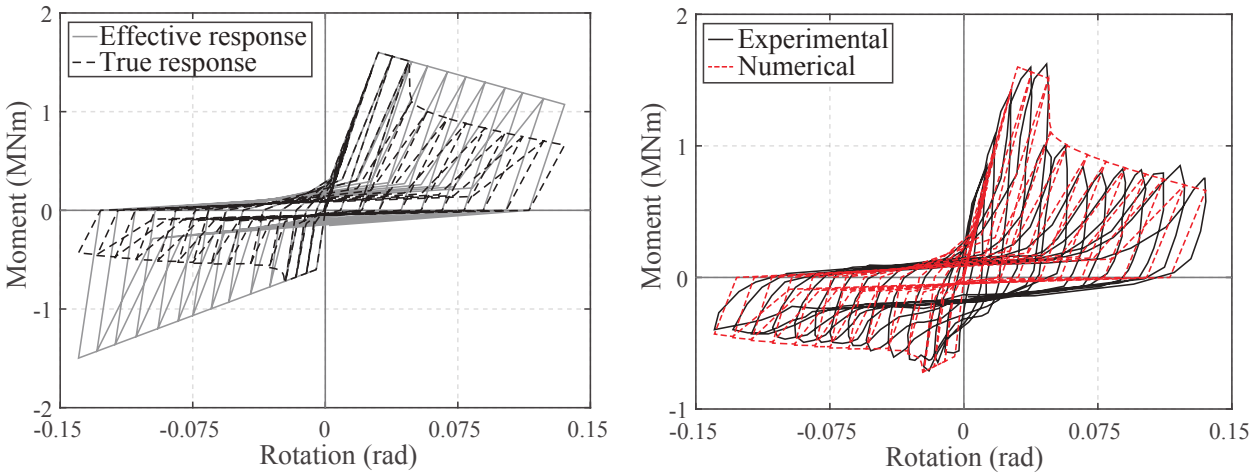

(a) Relation between effective and true response

(b) Numerical and experimental correlation

Figure 2.15: Simulation of beam-to-column shear tab connections (S1 system)

Figure 2.15(a) shows the bilinear hysteretic model in Figure 2.2(b) for the effective moment-rotation relation of the shear tab connections with the values reported in the column under the label S1 in Table 2.4. The values s_y, E_1 and E_2 under a positive rotation are different from the values under a negative rotation to do justice to the observed response in Figure 2.15(b). The same is true for the damage parameters C_{d0} and C_{d1} for the damage initiation and the damage limit, respectively. To account for the pronounced pinching of the

hysteretic moment-rotation relation during reloading, the relative control point coordinates of the bilinear reloading branch are selected as $p_x = 0.90$ and $p_y = 0.20$. Furthermore, the parameter d_{p2} of the damage evolution law is selected to account for the sudden strength loss and the subsequent reduced strength plateau of the connections. In accordance with Figure 2.5 the smaller the value of d_{p2} is relative to 1 the sharper the early drop, particularly if it is weighted with a value of d_{p1} larger than 1. Accordingly, $d_{p2}^{+} = 0.1$ and $d_{p2}^{-} = 0.3$ are selected along with $d_{p1}^{+} = 1$ and $d_{p2}^{-} = 2$. Figure 2.15(a) shows the resulting true response according to Equation (2.14) for the cyclic deformation history of the experimental results. The true response of the damage model compares quite favorably with the experimental measurements in Figure 2.15(b), particularly with regard to the strength degradation of the connection.

2.5.5.2 System S2 - Non-Ductile Moment Frame

The capacity boundary for a non-ductile moment frame is characterized by a very sharp strength drop to 15% of the yield strength of the component following yielding [19]. The strength plateau at this strength extends from a relative drift of 3% to the ultimate drift of 6%. This capacity boundary is representative of older steel and concrete structures [19], such as the steel moment-resisting frames with pre-Northridge welded beam-column connections, in which connection fracture leads to the sudden strength drop, and reinforced concrete frames with inadequate column and joint confinement as well as poor detailing of the reinforcement, in which the sudden strength drop is related to the shear failure of columns and joints. Figure 2.16(b) shows the measured moment-rotation relation of a pre-Northridge welded steel beam-to-column connection from the experiments by Stojadinovic and Goel [96]. The response under positive and negative moment is not the same, but the FEMA P440A Recommendations do not discuss the matter.

Figure 2.16(a) shows the bilinear hysteretic model in Figure 2.2(b) for the effective moment-rotation relation of the non-ductile welded steel beam-column connection with the values reported in the column under the label S2 in Table 2.4. The values s_y, E_1 and E_2 under a positive rotation are only slightly different from the values under a negative rotation to account for the observed response in Figure 2.16(b). The damage parameter C_{d0} is set to 1 for positive and negative deformations to reflect the fact that damage initiates at the onset of yielding. The significant difference in the resulting true response in Figure 2.16(a) and (b) arises from the large difference in the value of the damage limit parameter C_{d1} (Table 2.4): it is set to 10 under positive deformations and to 200 under negative deformations. The low value of C_{d1}^{+} represents very well the rapid strength loss of the fracturing connections in Figure 2.16(b). To account for the asymmetric reloading behavior, different control point coordinates are selected for the two bilinear reloading branches with $p_{xp} = 0.1$ and $p_{yp} = 0.4$ representing the evident Bauschinger effect under positive moments, and $p_{xn} = 0.95$ and $p_{yn} = 0.1$ describing the pronounced pinching under negative moments.

The parameter d_{p2} of the damage evolution law is selected again to account for the sudden strength loss of the connections under positive rotations. In accordance with Figure 2.5 the

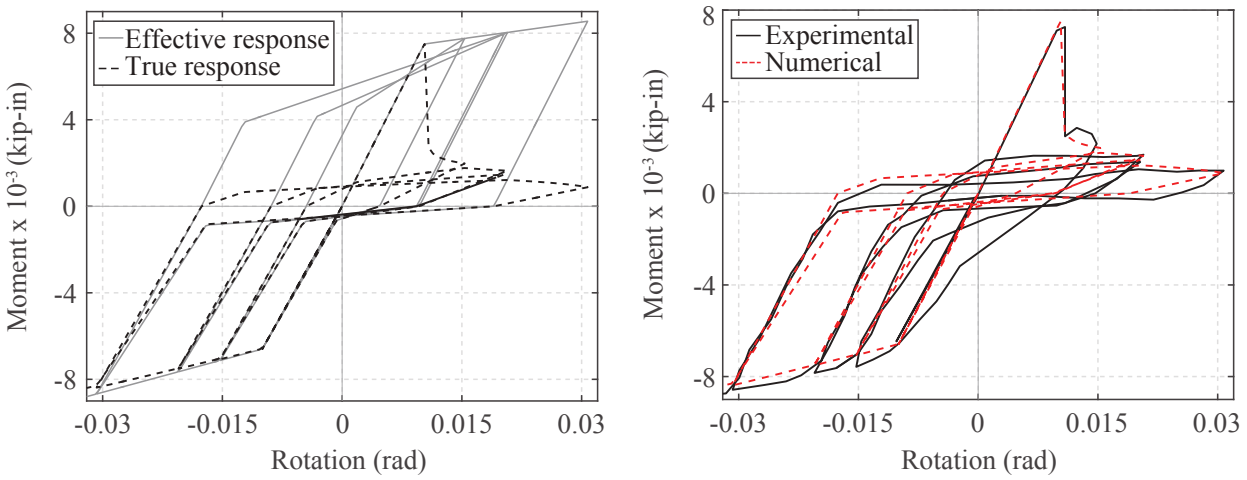

(a) Relation between effective and true response

(b) Numerical and experimental correlation

Figure 2.16: Simulation of pre-Northridge non-ductile welded steel beam-column connections (system S2)

smaller the value of d_{p2} is relative to 1 the sharper the early drop, particularly if it is weighted with a value of d_{p1} larger than 1. Accordingly, $d_{p2}^{+} = 0.05$ is selected along with $d_{p1}^{+} = 4$. In contrast, the parameters of the damage evolution law under negative deformations are left to the default values of 1 (Table 2.4). Figure 2.16(a) shows the resulting true response according to Equation (2.14) for the cyclic deformation history of the experimental results. The true response of the damage model is consistent with the experimental measurements for all cycles in Figure 2.16(b) with regard to the strength deterioration under positive and negative moments. The Bauschinger effect under reloading in the positive direction is consistent with the experimental observations for all cycles. In contrast, the pinching of the hysteretic moment-rotation relation during reloading in the negative direction is only captured well in the late cycles. To improve these results, the future extension of the bilinear hysteretic model should consider relating the coordinates of the reloading control point to the damage evolution.

2.5.5.3 System S3 - Ductile Moment Frame

The capacity boundary for a ductile moment frame consists of 4 linear segments: the linear elastic range is followed by the strength hardening segment with stiffness equal to 2% of the initial stiffness, which is then followed by a strength softening segment over the deformation range from 4% to 6%, and a residual strength plateau up to the ultimate deformation of 8%. This capacity boundary is representative of newer steel and concrete structures, such as the post-Northridge steel special moment-resisting frames with ductile beam-column connections and well detailed reinforced concrete moment resisting frames [19].

Figure 2.17(b) shows the measured moment-rotation relation of a post-Northridge welded

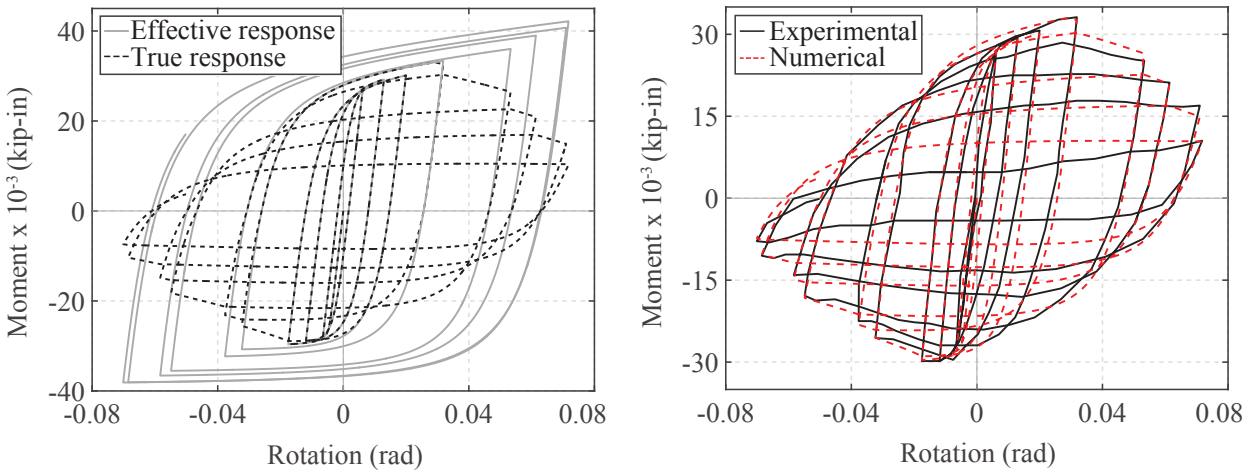

(a) Relation between effective and true response

(b) Numerical and experimental correlation

Figure 2.17: Simulation of post-Northridge ductile steel beam-column connections (system S3)

beam-column connection with reduced beam section from the experiments by Venti and Engelhardt [106]. Because all metallic components show a Bauschinger effect during reloading, the effective response is based on the GMP model in Figure 2.2(a). To accommodate the discrepancy in the hardening and reloading behavior under positive and negative moments, the parameter values for b, r, c_{R1}, c_{R2} for the positive branch are different from those for the negative branch. The relatively large $r^+ = 7$ and $r^- = 10$ in combination with $c^+_{R2} = 0.75$ and $c^-_{R2} = 1$ result in full hysteresis loops with large energy dissipation capacity. The parameters $c^+_{R1} = 0.82$ and $c^-_{R1} = 0.85$ make the transition from elastic to plastic behavior more gradual as the deformation amplitude increases. Figure 2.17(a) shows the cyclic behavior of the model in the effective space.

The model captures the asymmetric onset of strength deterioration in Figure 2.17(b) with a value for the damage threshold parameter under positive deformations $C^+_{d0} = 22$ that differs from that of the same parameter under negative deformations $C^-_{d0} = 11$. Both values indicate that strength reduction initiates after significant plastic deformation. The high values of $C^{\pm}_{d1} = 150$ represent very well the significant ductility of the steel component. The asymmetric strength degradation is captured by selecting two values for the damage parameter d_{p2}, with d^-_{p2} under negative moment less than 1 for describing an early strength reduction, while d^+_{p2} is equal to 1. Both d_{p1} values are set equal to 2 slightly biasing the strength reduction to smaller normalized energy dissipation values according to Figure 2.5. Figure 2.17(a) shows the resulting true response for the cyclic deformation history of the specimen. Except for the reloading response in the last cycle, the true response of the damage model compares very well with the experimental results in Figure 2.17(b) with regard to the reloading behavior and the strength and stiffness deterioration under the cyclic load history.

2.5.5.4 System S4 - Stiff, Non-Ductile System

The capacity boundary for a relatively stiff lateral force-resisting system is characterized by the significant and rapid strength loss to 30% of the yield strength at a deformation of 0.4% [19]. The strength loss is followed by an extensive strength plateau from a deformation of 2% to the ultimate deformation of 8%. This capacity boundary is representative of concentrically braced steel frames that experience a significant and rapid strength loss due to brace buckling at a small lateral drift [19].

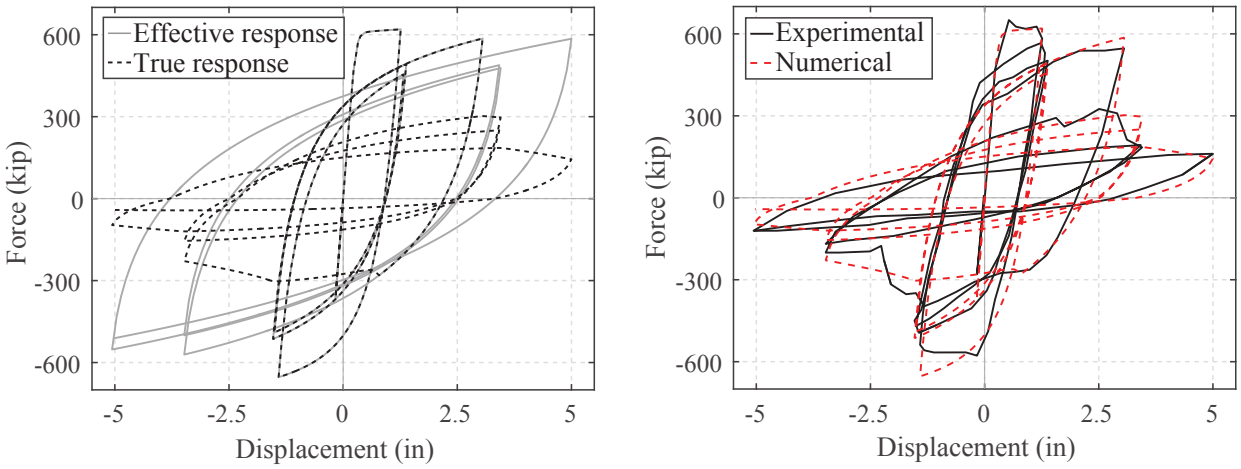

(a) Relation between effective and true response

(b) Numerical and experimental correlation

Figure 2.18: Simulation of stiff, non-ductile concentrically braced steel frame (system S4)

Figure 2.18 shows the force-displacement relation of a concentrically braced steel frame from the experiments by Uriz and Mahin [104]. To capture the Bauschinger effect during reloading, the GMP model in Figure 2.2(a) is used for the effective force-deformation relation. Similar to specimen S3, a large value for parameters $r^{\pm} = 10$ and $c^{\pm}_{R2} = 0.5$ describes a full hysteresis loop in the first cycle with a relatively sharp transition from the elastic to the plastic range. In contrast to the ductile response of specimen S3, a high value for the parameters $c^{\pm}_{R1} = 0.96$ is used to extend the gradual transition range during reloading and represents well the reloading stiffness deterioration after buckling initiation.

Slightly different values for the damage threshold coefficients, $C^{+}_{d0} = 35$ and $C^{-}_{d0} = 30$, are selected to simulate the asymmetric onset of strength deterioration under positive and negative deformation. Similar to the steel specimen S3, the values indicate that strength reduction initiates after significant plastic deformation. A damage parameter value d_{p2} less than 1 with $d^{+}_{p2} = 0.5$ and $d^{-}_{p2} = 0.3$ in combination with a $d^{\pm}_{p1}$ value greater than 1 captures very well the rapid strength deterioration after buckling initiation at the end of the second loading cycle. The severe cyclic degradation and the damage coupling under positive and negative deformations for the non-ductile system are reflected in relatively high values for C_{wc} and C_{cd}, with $C^{\pm}_{wc} = 0.27$ and $C^{\pm}_{cd} = 0.50$. Figure 2.18(b) shows that overall the resulting

true response compares rather well with the experimental measurements in regard to the evolution of the strength and stiffness degradation of the non-ductile concentric steel braced frame, even though the model slightly overestimates the measured strength in the first cycle under negative deformation.

2.5.5.5 System S5 - Stiff, Non-Ductile System with Pronounced Pinching

The capacity boundary for a relatively stiff, non-ductile system consists of 4 linear segments: the linear elastic range is followed by the strength hardening segment with high relative stiffness, which is then followed by two strength softening segments up to the ultimate deformation of 6% [19]. This capacity boundary is representative of non-ductile masonry walls and concrete frames with masonry infill with the elastic range corresponding to the pre-cracking response and the steep strength hardening segment to the post-cracking response until yielding [19]. Figure 2.19(b) shows the measured force-displacement relation of a masonry wall from the experiments by Shing [90].

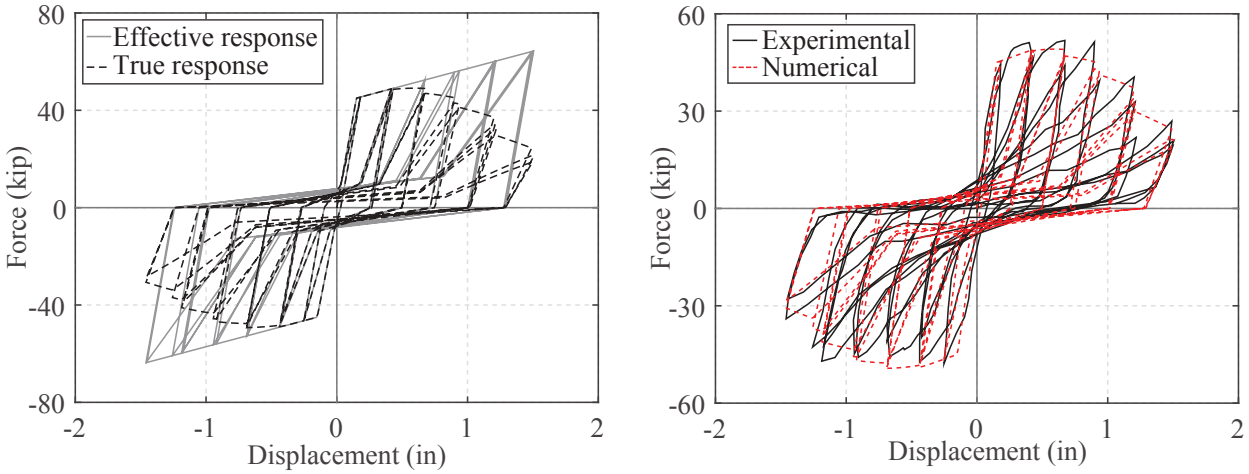

(a) Relation between effective and true response

(b) Numerical and experimental correlation

Figure 2.19: Simulation of stiff, non-ductile masonry wall with pronounced pinching (system S5)

Figure 2.19(a) shows the shows the bilinear hysteretic model in Figure 2.2(b) for the effective force-displacement relation of the masonry wall. Because the experimental response under positive and negative deformations is quite similar, the same parameters are used for the effective force-deformation relation under positive and negative deformations. The same is true for all damage parameters of the model except for d_{p1}. The column under label S5 in Table 2.4 lists the parameter values for the true response in Figure 2.19(a). The damage threshold coefficient $C_{d0}^{\pm}$ is set equal to 1 to indicate that the onset of strength reduction for the masonry wall coincides with the yielding of the reinforcement. The relatively low displacement ductility of the system is reflected in the limit damage parameter value $C_{d1}^{\pm}$

= 80. To account for the pronounced pinching of the hysteretic force-displacement relation during reloading the control point coordinates of the bilinear reloading branch are selected as $p_x = 0.80$ and $p_y = 0.20$. The selection of the value of 0.15 for the cyclic degradation coefficient $C_{wc}^{\pm}$ appears to capture well the effect of the energy dissipation during follower cycles of the deformation history. The true response of the damage model compares rather well with the experimental measurements in Figure 2.19(b) in regard to the evolution of the strength and stiffness deterioration of the masonry wall. The hysteretic behavior also shows reasonable agreement.

2.5.5.6 System S7 - Limited Ductility Moment Frame

The capacity boundary for a structural component of limited ductility consists of 4 linear segments: the linear elastic range is followed by the yield plateau with limited ductility, which is then followed at a deformation of 2% by a strength softening segment that terminates at 20% of the yield strength of the component. This is followed, in turn, by a short residual strength plateau up to the ultimate deformation of 6% [19]. This capacity boundary is representative of older lightly reinforced concrete columns and beam-column joints with inadequate confinement that are susceptible to shear failure [19]. Figure 2.20(b) shows the measured force-displacement relation of a lightly reinforced concrete column from the experiments by Sezen and Moehle [89].

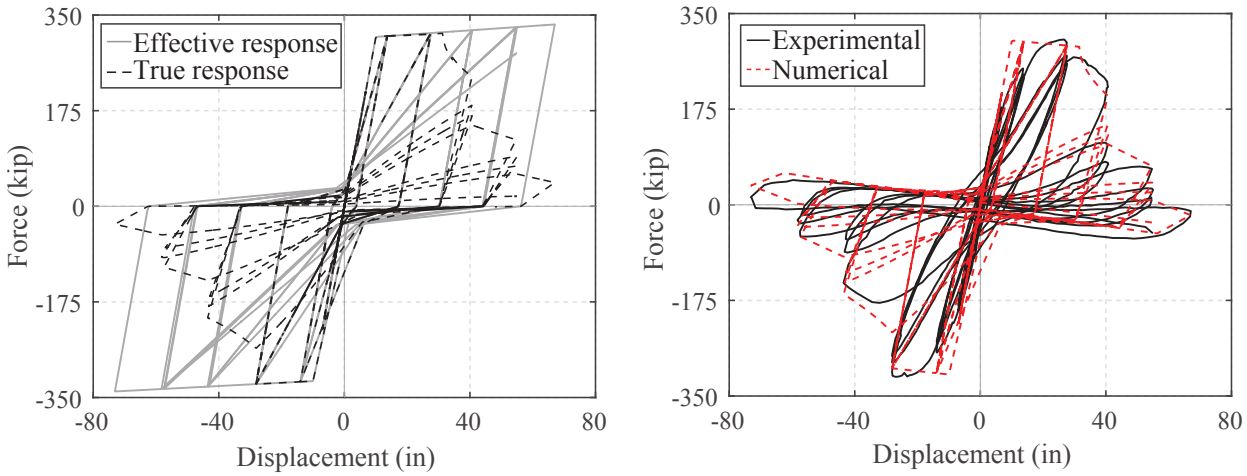

(a) Relation between effective and true response

(b) Numerical and experimental correlation

Figure 2.20: Simulation of lightly reinforced concrete column with limited-ductility (system S7)

Figure 2.20(a) shows the the shows the bilinear hysteretic model in Figure 2.2(b) for the effective force-displacement relation of the lightly reinforced concrete column. Because the experimental response under positive and negative deformations is practically the same, the same parameters are used for the effective force-deformation relation under positive and

negative deformations. The same is true for the damage parameters of the model, which are listed in the column under label S7 in Table 2.4. To account for the yield plateau of limited ductility, a small value of $E_{2p} = E_{2n} = 0.4$ is assigned to the strain hardening stiffness. For the same reason the damage threshold coefficient $C_{d0}^{\pm}$ is set equal to 10 to delay the onset of damage until an energy dissipation of 10 times the yield energy. The low displacement ductility of the system is reflected in the limit damage parameter value $C_{d1}^{\pm} = 40$. The selection of the value of 0.5 for the damage parameter $d_{p2}^{\pm}$ in combination with the value of 2.1 for the damage parameter $d_{p1}^{\pm}$ is meant to capture the rapid strength deterioration following the onset of damage. To account for the pronounced pinching of the hysteretic force-displacement relation during reloading the control point coordinates of the bilinear reloading branch are selected as $p_x = 0.50$ and $p_y = 0.10$ under positive and negative deformations. The selection of the value of 0.25 for the cyclic degradation coefficient $C_{wc}^{\pm}$ appears to capture well the effect of the energy dissipation during follower cycles of the deformation history. Equally important is the effect of the energy dissipation under positive moments and of the energy dissipation under negative moments on the strength reduction in the opposite direction, as reflected in the relatively high value of the coupling damage parameter $C_{cd}^{\pm} = 0.5$. While Figure 2.20(a) only includes the nonlinear material response of the specimen, the numerical response in Figure 2.20(b) superimposes the additional force contribution from the nonlinear geometry effect under the axial force of the column, which is noticeable as negative stiffness during the early reloading stage under large deformations. Figure 2.20(b) shows that the resulting true response compares quite favorably with the experimental measurements in regard to the evolution of the strength and stiffness degradation of the lightly reinforced concrete column. The hysteretic behavior also seems to be adequately captured.

2.5.5.7 Conclusions from the simulations of degrading behavior

The preceding simulations demonstrate the flexibility of the proposed damage model for the simulation of the hysteretic behavior of different structural component types. Table 2.4 summarizes the parameters for the simulations. The top 16 rows of the table contain the parameters of the force-deformation relation in effective space. The effective response with the GMP model in Figure 2.2(a) requires 14 parameters: the initial stiffness E, the yield strength s_y, the hardening ratios $b^{\pm}$, the reloading parameters $r^{\pm}$, $c_{R1}^{\pm}$, $c_{R2}^{\pm}$, and the isotropic hardening parameters a_1, a_2, a_3, a_4. The first two parameters are the same under positive and negative deformations. The default values $a_2 = a_4 = 0$ are assumed in all simulations to represent the onset of isotropic hardening behavior at the start of the deformation history.

The strength envelope for the bilinear hysteretic model in Figure 2.2(b) requires 6 material parameters, 3 for the envelope under positive deformations and 3 for the envelope under negative deformations. These are the yield strength s_y, the initial modulus E_1, and the post-yield modulus E_2. Furthermore, the bilinear hysteretic model requires four more parameters for the coordinates of the control point for the bilinear reloading branch in Figure 2.2(b), p_{xp} and p_{yp} in the positive reloading direction and p_{xn} and p_{yn} in the negative reloading direction. These can be used for the description of the Bauschinger effect in metallic structural

components or for the description of pinching in structural members with sliding, slip and shear deformations.

Parameter	**S1**	**S2**	**S3**	**S4**	**S5**	**S7**
E	-	-	6,000	2,167	-	-
s_y	-	-	28	580	-	-
$[b^+; b^-]$	-	-	[0.0125; 0]	[0.005; 0.005]	-	-
$[r^+; r^-]$	-	-	[7; 10]	[10; 10]	-	-
$[c^+_{R1}; c^-_{R1}]$	-	-	[0.82; 0.85]	[0.96; 0.96]	-	-
$[c^+_{R2}; c^-_{R2}]$	-	-	[0.75; 1]	[0.5; 0.5]	-	-
$[a_1; a_3]$	-	-	[0.025; 0.025]	[0.05; 0.05]	-	-
$[a_2; a_4]$	-	-	[0; 0]	[0; 0]	-	-
s_{yp}	1.6	7.5	-	-	45	310
E_{1p}	53.3	730	-	-	300	31
E_{2p}	-5.0	50	-	-	14.3	0.4
s_{yn}	-0.6	-6.6	-	-	-45	-310
E_{1n}	120	660	-	-	300	31
E_{2n}	6.7	100	-	-	14.3	0.4
$[p_{xp}; p_{yp}]$	[0.9; 0.2]	[0.1; 0.4]	-	-	[0.8; 0.2]	[0.5; 0.1]
$[p_{xn}; p_{yn}]$	[0.9; 0.2]	[0.95; 0.1]	-	-	[0.8; 0.2]	[0.5; 0.1]
C_{d0}	[3; 10]	[1; 1]	[22; 11]	[37; 31]	[5; 5]	[10; 10]
C_{d1}	[120; 200]	[10; 200]	[150; 150]	[110; 110]	[80; 80]	[40; 40]
C_{wc}	[0.05; 0.05]	[0.25; 0.25]	[0.14; 0.14]	[0.27; 0.27]	[0.15; 0.15]	[0.25; 0.25]
C_{cd}	[0.30; 0.30]	[0.50; 0.50]	[0.36; 0.36]	[0.50; 0.50]	[0.20; 0.20]	[0.50; 0.50]
$[d^+_{p1}; d^+_{p2}]$	[1.0; 0.1]	[4.5; 0.05]	[2.0; 1.0]	[1.5; 0.5]	[2.0; 1.5]	[2.1; 0.5]
$[d^-_{p1}; d^-_{p2}]$	[2.0; 0.3]	[1.0; 1.0]	[2.0; 0.75]	[3; 0.3]	[1.5; 1.5]	[2.1; 0.5]

Table 2.4: Parameters for the simulations of the degrading hysteretic behavior of structural components

Most parameters of the effective response correspond to mechanical properties of the structural components, such as the initial stiffness and the yield strength, and can, therefore, be readily established. The hardening or softening post-yield behavior can also be readily established for typical structural components. Observations about the reloading behavior of a structural component are used for the selection of the parameters p_x and p_y: the case $0 \leq p_y < p_x \leq 1$ represents pinching behavior, while the case $0 \leq p_x < p_y \leq 1$ represents reloading behavior mimicking the Bauschinger effect. The selection $p_x = p_y$ results in a linear reloading branch from the point of complete unloading to the maximum previous deformation under a force of opposite sign. While any $p_x = p_y \leq 1$ is equally suited for the purpose, the discussion makes reference to $p_x = p_y = 1$ for this case.

The remaining 12 parameters control the evolution of strength and stiffness deterioration

and have a clear physical meaning. Of these 4 are relatively easy to establish from the capacity boundary of a structural component: the threshold damage parameter $C_{d0}^{\pm}$ and the limit damage parameter $C_{d1}^{\pm}$. The determination of the remaining 8 parameters should ideally be based on formal parameter identification methods. Such a formal process is beyond the scope of this study. Moreover, the correlation studies of the numerical results with the experimental measurements show that very satisfactory agreement results with a relatively consistent set of values for these parameters across a wide spectrum of observed hysteretic behavior of structural components. This conclusion is supported by the small range of variation for the numerical values of C_{cd} and C_{wc} in Table 2.4. The same is also true for the values of d_p, particularly after consideration of Figure 2.5.

While the agreement between numerical simulations and experimental results in Figure 2.15-Figure 2.20(d) can certainly be improved, the description for the evolution of the strength and stiffness deterioration seems very satisfactory. The small variation of the parameters C_{cd}, C_{wc} in Table 2.4 and the direct relation of the parameters d_p to the damage evolution according to Figure 2.5 implies that a selection of values within the range of Table 2.4 is likely to result in a very satisfactory representation of the observed hysteretic behavior.

2.6 Damage Variables

2.6.1 Comparison with Park-Ang index

The purpose of the following discussion is two-fold: first to show that the damage variable d of the proposed model can be calibrated to give an assessment of the damaged state of a structural component that is consistent with the well known damage index by Park-Ang for standard cases of structural component characteristics and loading, and second to highlight the flexibility and some of the capabilities of the proposed formulation by pointing out specific cases where the damage variable deviates from the Park-Ang damage index. It is worth pointing out at the outset that alternative damage indices such as the one proposed by Mehanny and Deierlein [63], or, improvements of the Park-Ang index such as the proposal by Bozorgnia and Bertero could have been used for the comparison without changing the essence of the argument.

The Park-Ang (PA) damage index d_{PA} [73] is the linear combination of the maximum deformation e_m and the hysteretic energy dissipation E

$$d_{PA} = \frac{e_m}{e_u} + \frac{\beta}{s_y e_u} \int dE \tag{2.15}$$

where e_u is the deformation capacity under monotonic loading. This damage index has been extensively calibrated and is referenced often in seismic response studies. Because the original proposal does not distinguish between the effect of positive and negative deformations, the following discussion is limited to cases with symmetric response. Because the proposed

model accounts for the effect of two damage variables on the hysteretic response according to Equation (2.14), the following discussion is limited to load histories with the largest excursion of each cycle occurring under positive deformations, so that the Park-Ang index can be compared with the damage variable d^+.

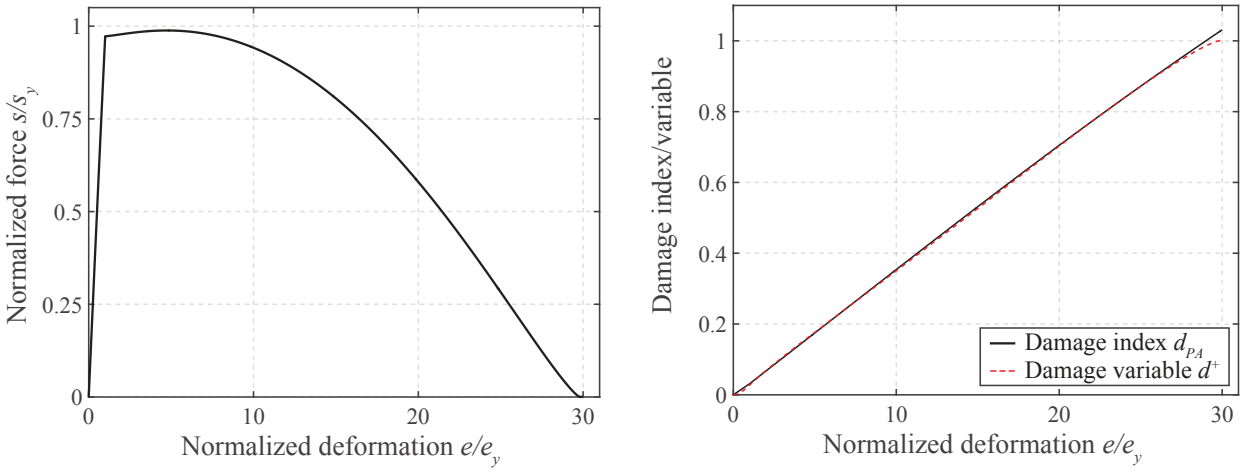

(a) Monotonic response (b) Comparison of damage evolution after calibration

Figure 2.21: Monotonic response and comparison of Park-Ang damage index with damage variable d^+

At the outset of the comparison the following parameters are selected for the proposed model: $E_{2p}/E_{1p} = 0.05$, $C_{d0} = 0$, $C_{d1} = 100$, $d_{p1} = 1.5$, $d_{p2} = 0.8$. While the first and third parameter are arbitrary, C_{d0} is set equal to zero to match the assumption of the Park-Ang index that damage initiates even under elastic deformation, which may not be realistic for many structural components [12]. The selection of the parameters d_{p1} and d_{p2} is so that the damage evolution law of the model is almost linear with increasing deformation to match the linear evolution of the Park-Ang damage index. This parameter selection results in the normalized force-deformation response in Figure 2.21(a) for the bilinear hysteretic model in Figure 2.2(b) for the effective force-deformation relation. The d_{PA} parameters in Equation (2.15), i.e. the ultimate deformation e_u and the energy dissipation parameter β, are then selected to match the damage evolution of the model in Figure 2.21(a): with the selection $e_u/e_y = 32$ where e_y is the yield deformation and $\beta = 0.15$, d_{PA} and d^+ are practically the same in Figure 2.21(b). The Park-Ang damage index d_{PA} varies linearly with the normalized deformation e/e_y. As already noted, the damage evolution law parameters d_{p1} and d_{p2} were specifically selected to match this linear variation as closely as possible. Figure 2.5, however, shows the considerable flexibility of the proposed model in the description of the damage evolution by variation of these parameters.

After calibrating the monotonic response of the proposed model to match the Park-Ang damage index, it is possible to select the parameters C_{wc} and C_{cd} of the model that affect the damage evolution under cyclic loading to give a good agreement with the Park-Ang

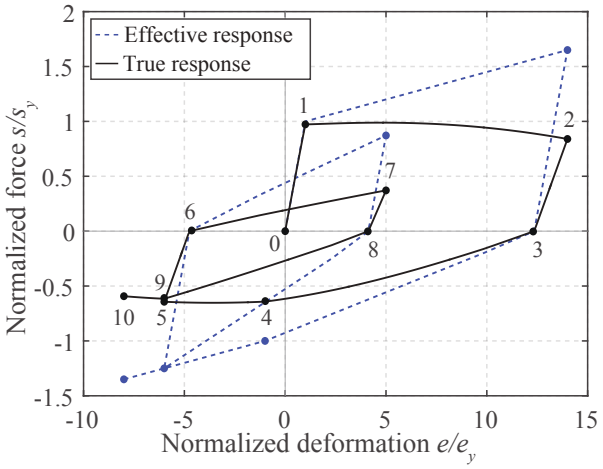

(a) Cyclic response for $C_{wc} = 0.15$ and $C_{cd} = 0.30$

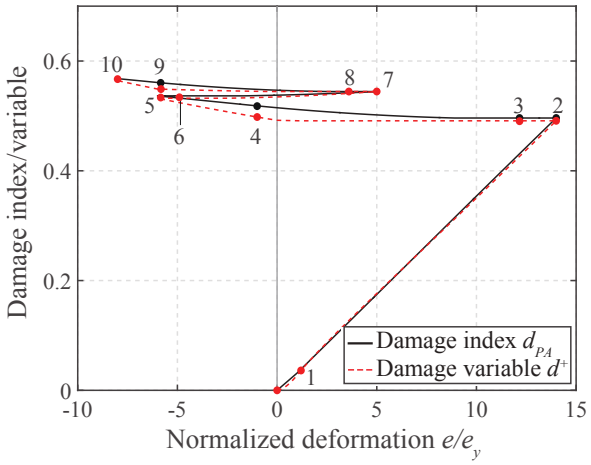

(b) Comparison of damage evolution after calibration

Figure 2.22: Cyclic response and comparison of damage index d_{PA} with damage variable d^+

damage index d_{PA}. Selecting the cyclic response in Figure 2.22(a) for the calibration, the selection $C_{wc} = 0.15$ and $C_{cd} = 0.30$ gives a very satisfactory agreement of d_{PA} and d^+ in Figure 2.22(b). The value C_{wc} is near the lower end of the range of values for this parameter in Table 2.4, while the value of C_{cd} is near the middle of the range of parameter values.

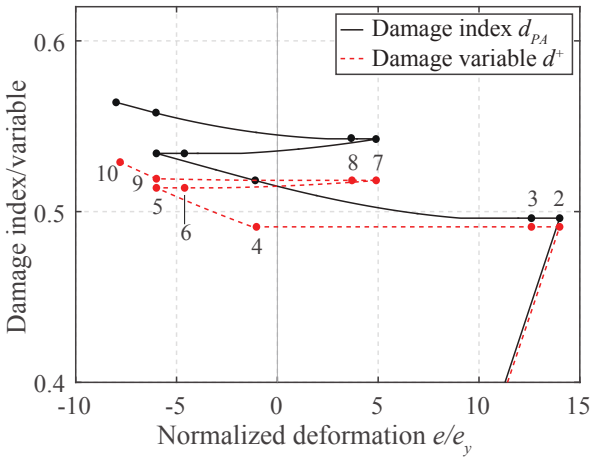

(a) $C_{wc} = 0.05$, $C_{cd} = 0.20$

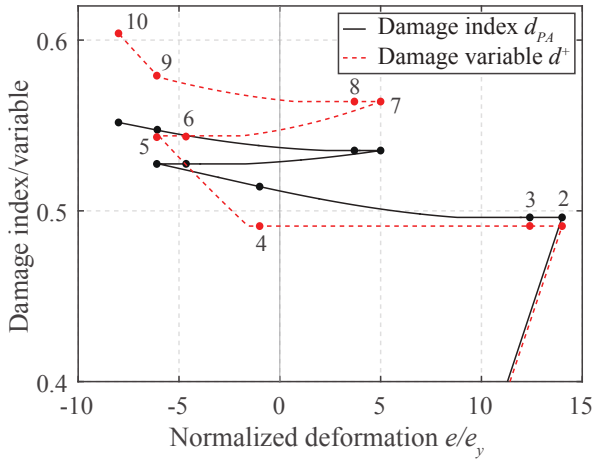

(b) $C_{wc} = 0.25$, $C_{cd} = 0.50$

Figure 2.23: Effect of parameters C_{wc} and C_{cd} on damage index d_{PA} and damage variable d^+

Clearly connected with the selection of parameters C_{wc} and C_{cd} is the concept of primary and follower half cycles by Krätzig [49] which is also adopted in the damage index proposal of Mehanny and Deierlein [64]. To illustrate the flexibility of the proposed model to account

for the effect of primary and follower half cycles, Figure 2.23 shows the discrepancy that arises between the damage variable d^+ and the Park-Ang damage index d_{PA} when selecting values for the parameters C_{wc} and C_{cd} at the low end of the range of values in Table 2.4 for Figure 2.23(a) and at the high end of the range of values in Table 2.4 for Figure 2.23(b). In the former case the Park-Ang index evolves faster than the damage variable of the proposed model, while the opposite is true in the latter case with more significant discrepancy. The slight difference of the Park-Ang index between Figure 2.23(a) and Figure 2.23(b) stems from the change in the energy dissipation of the cyclic response because of the change in the model parameter values from Figure 2.23(a) to Figure 2.23(b).

2.6.2 Damage states

The preceding section demonstrates the correlation of the damage variables to the Park-Ang damage index. This section goes one step further in order to demonstrate the calibration of the damage variables for several typical damage states of steel components. The simulations of two identical steel subassemblages from the experimental campaign by Yu et al. [111] are used for the purpose.

Figure 2.24 compares the experimental and the numerical response of the specimens under different cyclic load histories. The GMP model in Figure 2.2(a) is adopted for the effective response. The following parameters give consistent results with the experimental data: $E = 100$ kip/in, $s_y = 110$ kip, $b = 0.045$, $r = 5$, $C_{d0} = 3$, $C_{d1} = 130$, $C_{wc} = 0.15$, $C_{cd} = 0.4$, $[d_{p1}^+ , d_{p2}^+] = [d_{p1}^- , d_{p2}^-] = [3.6, 1.25]$. The same parameters are used for specimen LS1 and LS2 because of the same geometry.

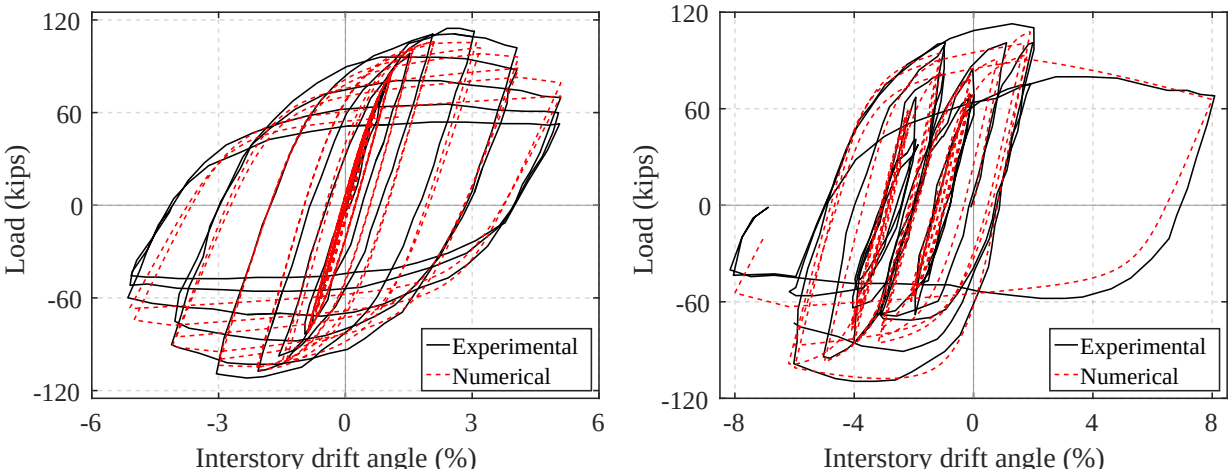

(a) LS1 (b) LS2

Figure 2.24: Response of steel beam-column subassemblages under cyclic load protocols

To illustrate the deterioration in the specimens, Figures 2.25(a)-(b) plot the evolution of the damage variables in the simulation of specimen LS2 and compare it with the Park-Ang damage index. Six load points (LP) are identified corresponding to important events observed during the experiment. Between LP 1 and LP 2 the specimen is subjected to a large negative displacement leading to pronounced yielding and the initiation of buckling. Between LP 2 and LP 3, the specimen undergoes small cycles without exceeding the previous minimum and maximum displacements and experiences pronounced buckling. Between LP 3 and LP 4 the specimen is subjected to a large positive displacement causing severe damage with a fatigue crack in the bottom flange at the reduced beam section (RBS). Between LP 4 and LP 5, the displacement reverses to the negative direction. The previous minimum displacement is exceeded at LP 5, and the specimen continues to load into the negative displacement range to LP 6, where large cracks develop through the flange thickness causing a fracture failure.

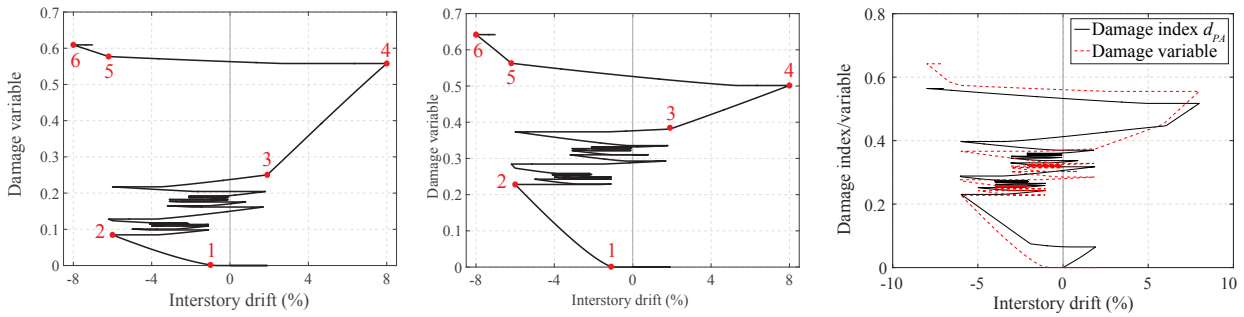

(a) Positive damage (b) Negative damage (c) Damage comparison

Figure 2.25: Comparison of damage evolution in specimen LS2

For a direct comparison with the Park-Ang damage index [73], Figure 2.25(c) plots a single damage variable d that represents both the positive and negative damage variables $d^{\pm}$. For simplicity, this damage variable is taken as the maximum of the positive and negative damage variables $d = \max(d^+, d^-)$. As expected from the comparison study in Section 2.6.1, the damage variable d and the Park-Ang damage index d_{PA} are consistent for this standard case. Table 2.5 correlates the observed events with the corresponding damage values.

The correlation gives rise to the following damage thresholds:

- **d = 0.0–0.2**: yielding of panel zone, beam flange and web
- **d = 0.2–0.4**: initiation of buckling leading to some strength deterioration
- **d = 0.4–0.6**: crack propagation and significant strength degradation
- **d = 0.6–1.0**: failure through fracture

Limit state	Damage variable	Park-Ang index	Damage level
Panel zone yielding	0.02	0.08	Light
Beam bottom flange yielding	0.2	0.2	Moderate
Notable buckling	0.3	0.3	Moderate
Fatigue crack in bottom flange RBS	0.55	0.51	Severe
Cracks through flange thickness and fracture	0.63	0.57	Severe

Table 2.5: Correlation of damage measures and limit states for specimen LS2

It is instructive to extend the calibration to a wider variety of specimens and load histories. This task is, however, beyond the scope of this work and left for future studies.

2.7 Damage Evolution Law for Brittle Failure

Often times fracture initiates and the structural components undergo a drastic reduction in strength and stiffness. The damage evolution function based on the CDF of the beta distribution accounts for such sudden strength deterioration through the selection of parameters C_{d0}, C_{d1}, d_{p1}, d_{p2}. With a small difference in the values for C_{d0} and C_{d1}, the limit energy ψ_{d1} is very close to the threshold ψ_{d0} and the damage evolution is rapid. Suitable values for d_{p1} and d_{p2} accelerate damage in certain deformation ranges, for example, $d_{p1} > 1$ and $d_{p2} < 1$ leads to rapid damage accumulation in early cycles. Both methods are reasonable for simulating brittle response but they have certain limitations. In the former, the damage initiation coincides with the onset of the brittle failure, which implies that the model is unable to describe the gradual damage prior to fracture. In the latter, since the damage evolution law is a smooth function, it is unable to distinguish the distinct behaviors in the damage accumulation pre- and post-fracture.

To address these issues, a composite damage evolution law is proposed. The composite function introduces two energy variables ψ_f and ψ_u that satisfy $\psi_{d0} \leq \psi_f < \psi_u \leq \psi_{d1}$. ψ_f is the energy at which fracture takes place and ψ_u is the ultimate energy at complete strength loss. The energy variables can be normalized to give the condition $0 \leq \hat{\psi}_f < \hat{\psi}_u \leq 1$. Different values can be specified for the variables under positive and negative moments at end i and end j, and for brevity, the superscript $\pm$ and the subscript i and j have been dropped. The damage evolution in the preceding sections is modified to account for the rapid strength degradation following fracture:

$$d = \begin{cases} F_B\left(\hat{\psi}, \beta_1, \beta_2\right), & 0 \leq \hat{\psi} \leq \hat{\psi}_f \\ F_B\left(\hat{\psi}_f, \beta_1, \beta_2\right) + \dfrac{1 - F_B\left(\hat{\psi}_f, \beta_1, \beta_2\right)}{\hat{\psi}_u - \hat{\psi}_f}\left(\hat{\psi} - \hat{\psi}_f\right), & \hat{\psi}_f < \hat{\psi} \leq \hat{\psi}_u \\ 1, & \hat{\psi}_u < \hat{\psi} \leq 1 \end{cases} \tag{2.16}$$

In Equation (2.16) the damage evolution consists of three segments. When the energy $\hat{\psi}$ is less than the fracture energy $\hat{\psi}_f$, the damage evolution follows the cumulative distribution function (CDF) of the beta distribution similar to the formulation without brittle damage. When the energy $\hat{\psi}$ exceeds the fracture threshold $\hat{\psi}_f$ but is less than the ultimate threshold $\hat{\psi}_u$, the damage variable increases linearly to 1 at $\hat{\psi} = \hat{\psi}_u$. At higher energy, the strength is completely lost and the damage variable remains equal to 1. Figure 2.26 shows the three segments of the damage evolution.

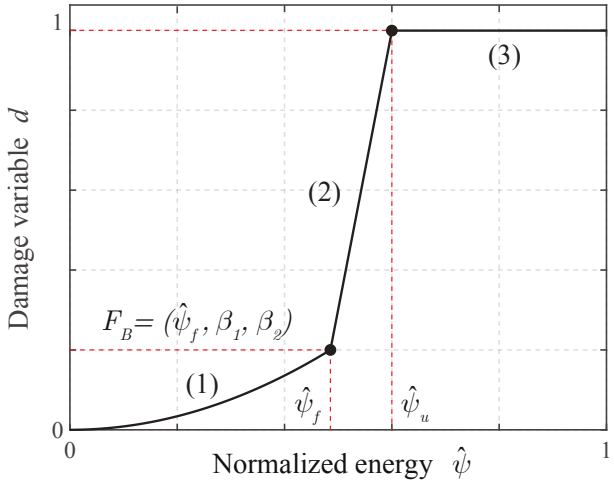

Figure 2.26: Damage evolution with brittle failure

To illustrate the proposed damage evolution law for brittle failure, the following presents simulations of steel cantilever beams under repeated cyclic loading from the experiments by Krawinkler [51]. Two specimens selected for the simulations are B13 and B18. Note that three other specimens from the same experimental campaign have been simulated in 2.5.3 to investigate the low-cycle fatigue phenomenon: B24, B25, and B28. The two groups B1 and B2 exhibit vastly different behaviors. While the specimens in group B2 experience gradual deterioration due to local buckling in beam flanges, the specimens in group B1 fail from crack propagation at weldments with relatively higher rate of deterioration [51].

The following damage parameters are used in the simulation of B13 and B18: $C_{d0} = 10$, $C_{d1} = 300$, $C_{wc} = 0.13$, $C_{cd} = 0.3$, $[d_{p1}, d_{p2}] = [3, 1.5]$, $\hat{\psi}_f = 0.078$, $\hat{\psi}_u = 0.1$. These parameters result in the damage evolution that is consistent with the distinct deterioration patterns in the B1 and B2 groups. For specimens in group B1, the slow crack propagation in the early cycles causes little deterioration for a larger number of cycles in the beginning, but as the crack approaches its critical size, the specimens show rapid strength reduction. On the other hand, for specimens in group B2, strength reduction due to local flange buckling initiates earlier but the deterioration rate is more gradual [51]. Such behaviors are captured by the threshold coefficient C_{d0} and the limit coefficient C_{d1}, which are higher in the simulation of specimens in group B1 than in group B2. The higher C_{d0} allows damage to initiate later while the higher C_{d1} results in more ductile response prior to the onset of fracture.

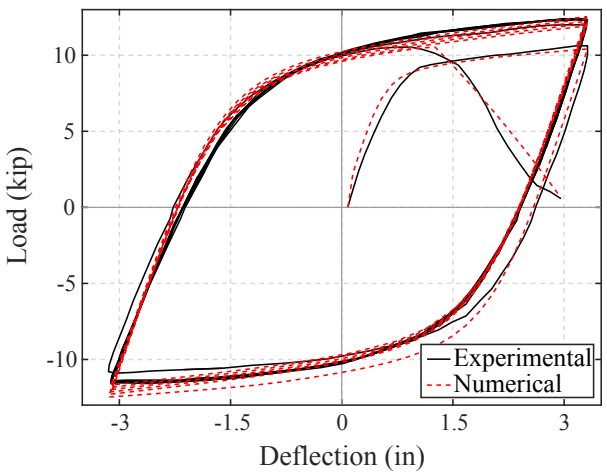

(a) B13: load-displacement

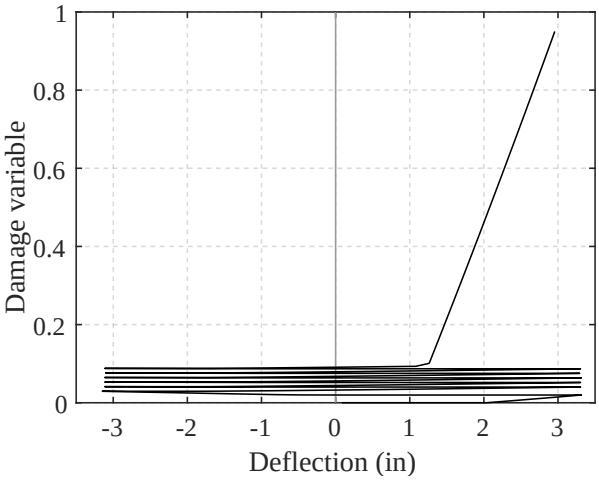

(b) B13: damage evolution

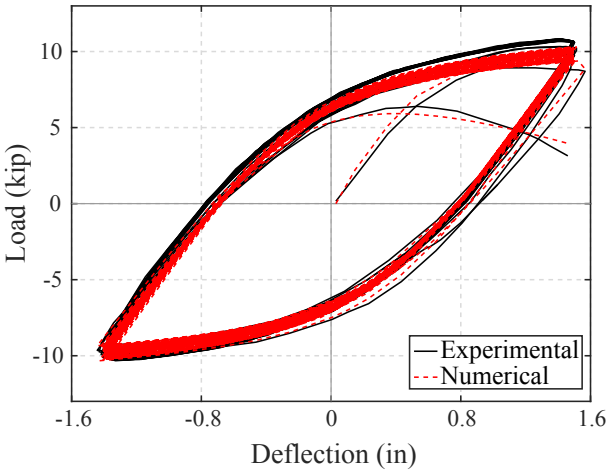

(c) B18: load-displacement

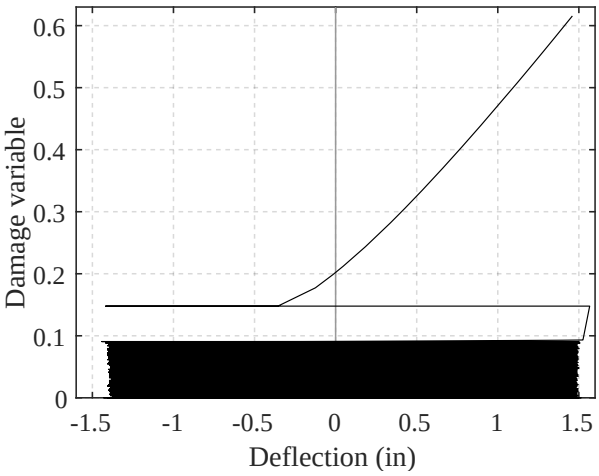

(d) B18: damage evolution

Figure 2.27: Simulations of steel beam with brittle failure

Figure 2.27 shows the load-displacement relation and the evolution of the positive damage variable d^+ for specimens B13 and B18. The model also simulates well the limited deterioration prior to the onset of fracture. The damage evolution function in Equation (2.16) with $\hat{\psi}_f = 0.078$ and $\hat{\psi}_u = 0.1$ captures accurately the sharp strength reduction in both specimens during the last half cycle. The distinct deterioration rates prior and post-fracture are evident in the damage evolution in Figure 2.27(b) and (d).

More extensive calibration is required to identify practical values for the parameters $\hat{\psi}_f$ and $\hat{\psi}_u$ and correlate them with physical properties of components. Nonetheless, the excellent results in the case study show that the model has significant promise in the hysteretic response simulation of structural members susceptible to brittle failure.

Chapter 3

Damage-Plasticity Beam Model

This chapter extends the 1d hysteretic damage model in Chapter 2 to formulate a new beam element based on damage-plasticity for the response simulation and damage assessment of steel structures under extreme load conditions. First, the series beam element based on resultant plasticity and the serial springs formulation is introduced to describe the nondegrading force-deformation relation in the effective space. The inelastic response is monitored at two locations offset from the element ends to account for the spread of inelasticity for hardening response and the size of the damage zones for softening response. The plastic hinge offsets accommodate the response coupling between the two element ends and represent more accurately the post-yield hardening behavior.

The damage formulation allows the beam element to describe the main characteristics of steel components, including the accumulation of plastic deformations, the cyclic strength hardening in early cycles, the low-cycle fatigue behavior, the distinct deterioration rates in primary and follower half cycles. The damage evolution function is extended to accommodate the sudden strength and stiffness deterioration from element brittle failure.

The chapter concludes with an extensive parameter calibration for more than 50 steel components under monotonic and cyclic load histories. A regression analysis is then used to establish guidelines for the damage parameter selection in relation to the geometry and the boundary conditions of the structural member. The validation studies indicate the dependence of the strength and stiffness deterioration on the section compactness and the element slenderness. The proposed model compares favorably in terms of computational efficiency with more sophisticated models with fiber discretization of the cross section while achieving excellent agreement in the response description for homogeneous metallic structural components. The implementation of the damage-plasticity elements with the return-mapping algorithm ensures excellent convergence characteristics for the state determination. Because of the computational efficiency and excellent accuracy, the proposed beam element holds great promise for the large scale seismic response simulation of structural systems with strength and stiffness deterioration and should prove very useful in the damage assessment and the collapse simulation of structures under extreme loading conditions.

3.1 Series Beam Element

3.1.1 Formulation

The series beam element model relates the basic element forces $\mathbf{q} = [q_a \ q_i \ q_j]^T$, where q_a is the axial force and q_i and q_j are the flexural forces at end i and end j, to the corresponding element deformations $\mathbf{v} = [v_a \ v_i \ v_j]^T$. The beam model assumes that the axial response is linear elastic and uncoupled from the flexural response. The model consists of a linear elastic beam element in series with nonlinear plastic hinges at the element ends. The plastic hinges are rigid-plastic and linear hardening that activate when the element end forces reach the plastic capacity M_p. Figure 3.1 sketches a series beam element of length L with axial stiffness EA, flexural stiffness EI, and two plastic hinges at the ends.

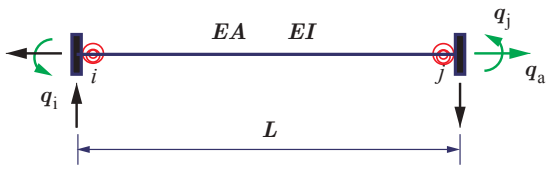

Figure 3.1: Series beam element

The element offers three main advantages over existing beam models based on concentrated plasticity in the literature. First, the element describes exactly the rigid-plastic behavior of the plastic hinges and do not suffer from the numerical issues that plague existing series models using a high elastic stiffness for the rigidity of the plastic hinge before yielding. Second, the formulation avoids additional nodes at the interface between the zero-length inelastic springs and the elastic element, and thus, permits a better-conditioned model with fewer degrees of freedom. Third, the element state determination adopts the robust return-mapping algorithm in classical plasticity to ensure excellent convergence properties.

The beam element is formulated based on resultant plasticity with an associative flow rule [92] and the concept of a serial spring model. The equilibrium and compatibility relations of the series beam model are illustrated in Figure 3.2, where $\mathbf{q}_e$-$\mathbf{v}_e$, $\mathbf{q}_p$-$\mathbf{v}_p$, $\mathbf{q}$-$\mathbf{v}$ represent the force-deformation relation of the linear elastic element, of the nonlinear hinges, and of the element, respectively.

The equilibrium relation equates the element force $\mathbf{q}$ to the force in the elastic component $\mathbf{q}_e$ and the plastic component $\mathbf{q}_p$:

$$\mathbf{q} = \mathbf{q}_e = \mathbf{q}_p \tag{3.1}$$

The kinematic relation assumes an additive decomposition of the element deformation $\mathbf{v}$ into the elastic deformation $\mathbf{v}_e$ and the plastic deformation $\mathbf{v}_p$, which is analogous to the strain decomposition in material models in classical plasticity [92].

$$\mathbf{v} = \mathbf{v}_e + \mathbf{v}_p \tag{3.2}$$

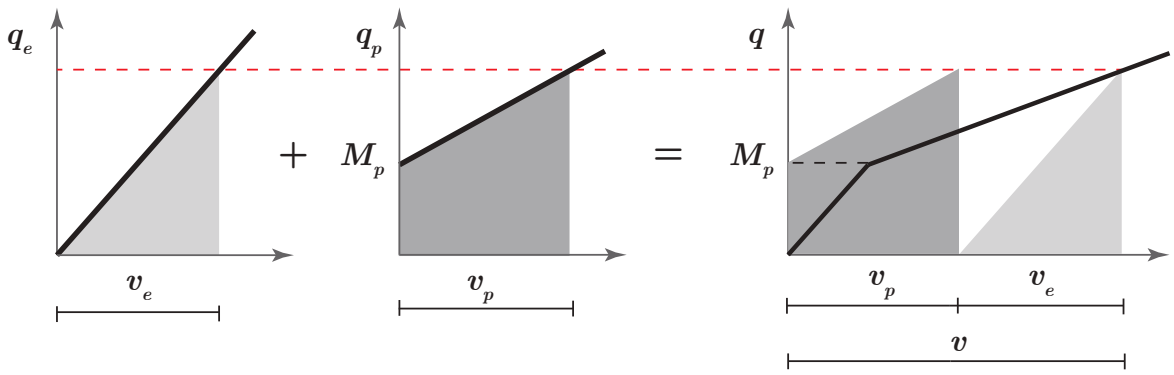

Figure 3.2: Equilibrium and compatibility relations of series beam model

The constitutive law of the elastic component relates the force $\mathbf{q}$ to the elastic deformation $\mathbf{v}_e$ through the elastic stiffness $\mathbf{k}_e$:

$$\mathbf{q} = \mathbf{k}_e \mathbf{v}_e = \mathbf{k}_e \left(\mathbf{v} - \mathbf{v}_p\right) \tag{3.3}$$

The following discusses the three main aspects of the element formulation: the yield function, the flow rules, and the hardening rules.

Yield function

Two yield functions f_i and f_j describe the admissible force state of the response at end i and end j, respectively. f_i and f_j are functions of three history variables: the element forces $\mathbf{q}$, the back-forces $\mathbf{q}_b = [q_{b,a}\ q_{b,i}\ q_{b,j}]^T$ describing the kinematic hardening behavior, and the internal variables $\boldsymbol{\alpha} = [\alpha_i\ \alpha_j]^T$ governing the isotropic hardening behavior. With $\mathbf{M}_p = [M_{p,i}\ M_{p,j}]^T$ denoting the plastic flexural capacities and $H_{i,i}$ and $H_{i,j}$ denoting the isotropic hardening modulus of the response at end i and j, the yield functions f_i and f_j are given by:

$$f_i\left(\mathbf{q}, \mathbf{q}_b, \boldsymbol{\alpha}\right) = \left|q_i - q_{b,i}\right| - \left(M_{p,i} + H_{i,i}\alpha_i\right) \tag{3.4}$$

$$f_j\left(\mathbf{q}, \mathbf{q}_b, \boldsymbol{\alpha}\right) = \left|q_j - q_{b,j}\right| - \left(M_{p,j} + H_{i,j}\alpha_j\right) \tag{3.5}$$

While the model accommodates unequal plastic capacities at the two ends, the same capacity $M_{p,i} = M_{p,j} = M_p$ is used in this study, which is a reasonable assumption for steel components. Figure 3.3 plots the two initial yield surfaces defined by the yield functions f_i and f_j in the $(q_i,\ q_j)$ force space and the four unit normals $\mathbf{n}_i^{\pm}$ and $\mathbf{n}_j^{\pm}$. The yield envelope consists of four lines $q_i = \pm M_p$ and $q_j = \pm M_p$.

The normal $\mathbf{n}$ to the yield envelope is given by:

$$\mathbf{n} = \left[\mathbf{n}_i\ \mathbf{n}_j\right] = \begin{bmatrix} \dfrac{\partial f_i}{\partial \mathbf{q}} & \dfrac{\partial f_j}{\partial \mathbf{q}} \end{bmatrix} = \begin{bmatrix} 0 & 0 \\ \operatorname{sign}\left(q_i - q_{b,i}\right) & 0 \\ 0 & \operatorname{sign}\left(q_j - q_{b,j}\right) \end{bmatrix} \tag{3.6}$$

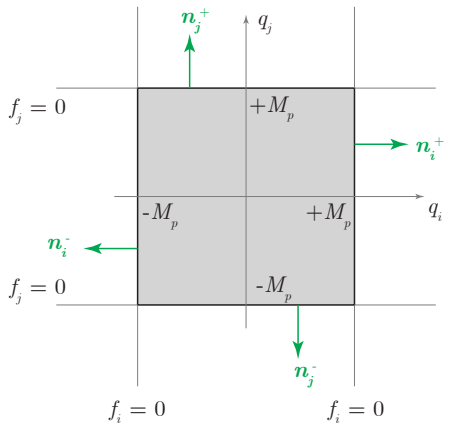

Figure 3.3: Yield envelope of series element

The yield functions in Equations (3.4)–(3.5) can be written more compactly as follows:

$$\mathbf{f}\left(\mathbf{q}, \mathbf{q}_b, \boldsymbol{\alpha}\right) = \mathbf{n}^T\left(\mathbf{q} - \mathbf{q}_b\right) - \left(\mathbf{M}_p + \mathbf{H}_i\boldsymbol{\alpha}\right) \tag{3.7}$$

where $\mathbf{H}_i$ is a diagonal 2×2 isotropic hardening matrix with the isotropic hardening moduli $H_{i,i}$ and $H_{i,j}$ on the diagonal. It is noteworthy that the yield envelope given by f_i and f_j in Equations (3.4)–(3.5) is nonsmooth with four singular points on the boundary of the elastic domain.

Flow rules

The associative flow rule describes the evolution of the plastic deformation $\mathbf{v}_p$. To account for the singularity at the corners, the Koiter's rule [47] states that the plastic deformation rate $\dot{\mathbf{v}}_p$, or equivalently, the plastic deformation increment $\Delta\mathbf{v}_p$, is a linear combination of the normals $\mathbf{n}_i$ and $\mathbf{n}_j$:

$$\dot{\mathbf{v}}_p = \beta_i\mathbf{n}_i + \beta_j\mathbf{n}_j = \mathbf{n}\boldsymbol{\beta} \tag{3.8}$$

where $\boldsymbol{\beta} = [\beta_i \;\; \beta_j]^T$ is a vector of the consistency parameters.

Figure 3.4 illustrates three scenarios of the plastic deformation increment. In Figure 3.4(a), only the yield surface defined by f_i is 'active', that is, $\beta_i > 0$ and $\beta_j = 0$ and the plastic deformation increment is colinear to the normal $\mathbf{n}_i$. In Figure 3.4(b), only the yield surface defined by f_j is 'active', that is, $\beta_j > 0$ and $\beta_i = 0$ and the plastic deformation increment is colinear to the normal $\mathbf{n}_j$. In Figure 3.4(c), both yield surfaces are 'active' and the plastic deformation increment depends on both $\mathbf{n}_i$ and $\mathbf{n}_j$.

Hardening rules

The rate of the internal variable $\boldsymbol{\alpha}$ and the back-force $\mathbf{q}_b$ are given as functions of the

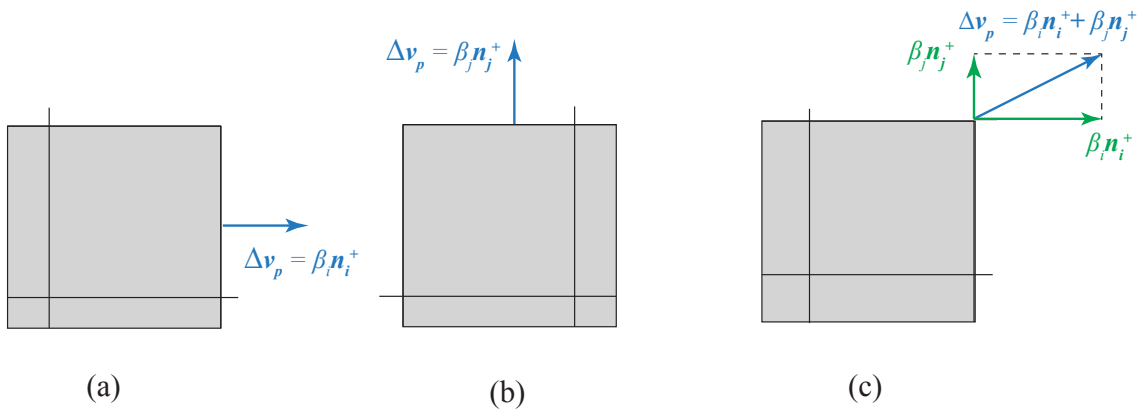

Figure 3.4: Scenarios of plastic deformation increments: (a) only f_i active, (b) only f_j active, (c) both f_i and f_j active

consistency parameters $\boldsymbol{\beta}$:

$$\dot{\boldsymbol{\alpha}} = \boldsymbol{\beta} \tag{3.9}$$

$$\dot{\mathbf{q}}_b = \mathbf{H}_k \mathbf{n} \boldsymbol{\beta} \tag{3.10}$$

where $\mathbf{H}_k$ is a 3×3 diagonal matrix with '0' and the kinematic hardening moduli $H_{k,i}$ and $H_{k,j}$ on the diagonal.

The consistency parameter $\boldsymbol{\beta}$ and the yield function $\mathbf{f}$ satisfy the unilateral constraints known as the Kuhn-Tucker condition:

$$\boldsymbol{\beta} \geq \mathbf{0} \quad \text{and} \quad \mathbf{f} \leq \mathbf{0} \quad \text{and} \quad \beta_m f_m = 0, \;\; m = i, j \tag{3.11}$$

The consistency condition asserts additional loading/unloading conditions for the yield surfaces:

$$\beta_m \dot{f}_m = 0, \quad m = i, j \tag{3.12}$$

Given the deformation rate $\dot{\boldsymbol{v}}$, the consistency parameter $\boldsymbol{\beta}$ can be evaluated as follows:

$$\boldsymbol{\beta} = \left[\mathbf{n}^T \left(\mathbf{k}_e + \mathbf{H}_k\right) \mathbf{n} + \mathbf{H}_i\right]^{-1} \mathbf{n}^T \mathbf{k}_e \dot{\mathbf{v}} \tag{3.13}$$

The expresion of the tangent stiffness upon plastic loading is:

$$\mathbf{k}_t = \mathbf{k}_e - \mathbf{k}_e \mathbf{n} \left[\mathbf{n}^T \left(\mathbf{k}_e + \mathbf{H}_k\right) \mathbf{n} + \mathbf{H}_i\right]^{-1} \mathbf{n}^T \mathbf{k}_e \tag{3.14}$$

The derivation of the consistency parameters and the tangent stiffness can be found in Appendix B.

3.1.2 Plastic hinge offset

The series beam element in Section 3.1 is generalized by placing the two nonlinear springs at distances $\chi_i = c_i/L$ and $\chi_j = c_j/L$ from the ends. Figure 3.5 sketches the series beam element of length L, axial stiffness EA and flexural stiffness EI composed of a linear elastic beam element in series with two offset rigid-plastic plastic hinges in the interior of the element. While the model permits different offset ratios χ_i and χ_j at the two ends, for simplicity a symmetric placement of the plastic hinges $\chi_i = \chi_j = \chi$ is used in the remaining of the dissertation.

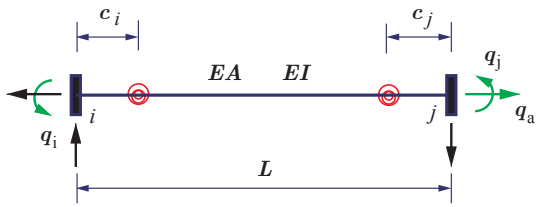

Figure 3.5: Series beam element with plastic hinge offset

The governing relations in Equations (3.1)–(3.3) still apply. It is noteworthy that the plastic force $\mathbf{q}_p$ and plastic deformation $\mathbf{v}_p$ are associated with the response at the element ends, and the plastic response is activated when the moment reaches the plastic capacity M_p at the hinge location. In the absence of element loading, the moment distribution is linear along the beam span, and the hinge moments M_i and M_j can be linearly interpolated from the element flexural forces q_i and q_j, as Figure 3.6 shows.

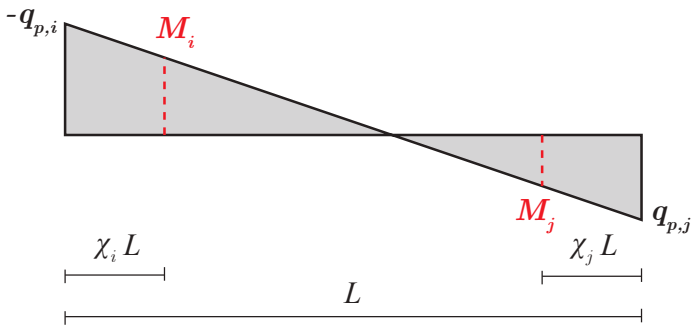

Figure 3.6: Moment interpolation between the hinge locations and the element ends

The moment interpolation matrix $\mathbf{b_p}$ is defined based on the plastic hinge offset χ:

$$\mathbf{b}_p = \begin{bmatrix} 1 & 0 & 0 \\ 0 & \chi & \chi \\ 0 & \chi & 1-\chi \end{bmatrix} \tag{3.15}$$

The force and deformation of the plastic hinges $\mathbf{q}_h$–$\mathbf{v}_h$ can be related to the plastic force and deformation $\mathbf{q}_p$–$\mathbf{v}_p$ through the force interpolation matrix $\mathbf{b_p}$:

$$\mathbf{q}_h = \mathbf{b}_p \mathbf{q}_p \tag{3.16}$$

$$\mathbf{v}_p = \mathbf{b}_p^T \mathbf{v}_h \tag{3.17}$$

where $\mathbf{q}_h = [N,\ M_i,\ M_j]^T$ denotes the axial force and the bending moments at the plastic hinge locations and $\mathbf{v}_h = [\theta_a,\ \theta_i,\ \theta_j]^T$ are the corresponding hinge axial deformations and rotations. Due to the assumption of linear elastic axial response, the axial deformation in the plastic hinges θ_a is zero.

The yield functions in Equation (3.7) become:

$$\mathbf{f} = \mathbf{n}^T(\mathbf{b}_p\mathbf{q} - \mathbf{q}_b) - (\mathbf{M}_p + \mathbf{H}_i\boldsymbol{\alpha}) \tag{3.18}$$

where the normal $\mathbf{n}$ can be evaluated as:

$$\mathbf{n} = \begin{bmatrix} 0 & 0 \\ \text{sign}\left[(\chi-1)q_i + \chi q_j - q_{b,i}\right] & 0 \\ 0 & \text{sign}\left[-\chi q_i + (1-\chi)q_j - q_{b,j}\right] \end{bmatrix} \tag{3.19}$$

It is evident in Equation (3.19) that the plastic hinge offsets couple the forces at the two element ends.

The same hardening rules in Equations (3.9)–(3.10) are adopted for the evolution of the back-force $\mathbf{q}_b$, and the internal variable $\boldsymbol{\alpha}$. The plastic deformation rate $\dot{\mathbf{v}}_p$ is then given by the interpolation matrix $\mathbf{b}_p$, the normal to the yield surface $\mathbf{n}$, and the consistency parameter $\boldsymbol{\beta}$:

$$\dot{\mathbf{v}}_p = \mathbf{b}_p^T \mathbf{n} \boldsymbol{\beta} \tag{3.20}$$

The consistency parameter $\boldsymbol{\beta}$ have the following expression:

$$\boldsymbol{\beta} = \left[\mathbf{n}^T\left(\mathbf{b}_p\mathbf{k}_e\mathbf{b}_p^T + \mathbf{H}_k\right)\mathbf{n} + \mathbf{H}_i\right]^{-1}\mathbf{n}\mathbf{k}_e\dot{\mathbf{v}} \tag{3.21}$$

and the tangent stiffness $\mathbf{k}_t$ is given by:

$$\mathbf{k}_t = \mathbf{k}_e - \mathbf{k}_e\mathbf{b}_p^T\mathbf{n}\left[\mathbf{n}^T\left(\mathbf{b}_p\mathbf{k}_e\mathbf{b}_p^T + \mathbf{H}_k\right)\mathbf{n} + \mathbf{H}_i\right]^{-1}\mathbf{n}^T\mathbf{b}_p\mathbf{k}_e \tag{3.22}$$

The series beam model in Section 3.1.1 is a special case with $\chi = 0$. It is possible to extend the formulation with more than two plastic hinges to accommodate various inelastic phenomenon, such as shear and bond-slip; however, it is left for future studies.

3.1.3 State determination: Return-mapping algorithm

Given the deformation $\mathbf{v}_n$ at the current step n and the previous history variables, the state determination of the element model evaluates the end force $\mathbf{q}_n$, the internal hardening

variable $\mathbf{q}_{b,n}$ and $\boldsymbol{\alpha}_n$, the plastic deformation $\mathbf{v}_{p,n}$, and the tangent stiffness $\mathbf{k}_t$. The element state determination is based on the return-mapping algorithm in classical multisurface plasticity.

The algorithm starts with an elastic predictor assuming that the deformation increment is entirely elastic, and evaluates the trial force $\mathbf{q}^{tr}$, the trial back-force $\mathbf{q}_b^{tr}$, and the trial internal variable $\boldsymbol{\alpha}^{tr}$:

$$\mathbf{q}^{tr} = \mathbf{k}_e \left(\mathbf{v}_n - \mathbf{v}_{p,n-1}\right) \tag{3.23}$$

$$\mathbf{q}_b^{tr} = \mathbf{q}_{b,n-1} \tag{3.24}$$

$$\boldsymbol{\alpha}^{tr} = \boldsymbol{\alpha}_{n-1} \tag{3.25}$$

The trial normal to the yield surface $\mathbf{n}^{tr}$ can be expressed as:

$$\mathbf{n}^{tr} = \begin{bmatrix} 0 & 0 \\ \text{sign}\left[(\chi-1)q_i^{tr} + \chi q_j^{tr} - q_{b,i}^{tr}\right] & 0 \\ 0 & \text{sign}\left[-\chi q_i^{tr} + (1-\chi)q_j^{tr} - q_{b,j}\right] \end{bmatrix} \tag{3.26}$$

The trial yield function $\mathbf{f}^{tr}$ is evaluated from the trial force and state variables:

$$\mathbf{f}^{tr} = \left(\mathbf{n}^{tr}\right)^T \left(\mathbf{b}_p \mathbf{q}^{tr} - \mathbf{q}_b^{tr}\right) - \left(\mathbf{M}_p + \mathbf{H}_i \boldsymbol{\alpha}^{tr}\right) \tag{3.27}$$

If *both* yield functions are positive, $f_i^{tr} > 0$ and $f_j^{tr} > 0$, the trial force state is admissible and the element response is elastic. The trial elastic state is accepted and the end force $\mathbf{q}_n$ equals to the trial value $\mathbf{q}^{tr}$:

$$\mathbf{q}_n = \mathbf{q}^{tr} \tag{3.28}$$

Similarly, the state variables are equal to the corresponding trial values:

$$\mathbf{q}_{b,n} = \mathbf{q}_b^{tr} \tag{3.29}$$

$$\boldsymbol{\alpha}_n = \boldsymbol{\alpha}^{tr} \tag{3.30}$$

$$\mathbf{v}_{p,n} = \mathbf{v}_{p,n-1} \tag{3.31}$$

and the tangent stiffness $\mathbf{k}_t$ is equal to the elastic stiffness $\mathbf{k}_e$:

$$\mathbf{k}_t = \mathbf{k}_e \tag{3.32}$$

If at least one yield condition is violated, $f_i^{tr} \geq 0$ and/or $f_j^{tr} \geq 0$, plastic correction is required to adjust the force back to the admissible domain. A yield surface m is considered 'active' if the consistency parameter $\beta_m > 0$ and the corresponding yield function $f_m = 0$ after the correction with $m = i, j$. The selection of active surfaces satisfies two constraints of the Kuhn-Tucker conditions after the plastic correction: (1) the consistency parameter $\boldsymbol{\beta}$ is positive, (2) the yield function $\mathbf{f}$ defined by the corrected variables $\mathbf{q}_n$, $\mathbf{q}_{b,n}$, and $\boldsymbol{\alpha}_n$ are non-positive, that is, the point (q_i, q_j) does not fall outside the admissible domain in the force space upon correction. The identification of the active yield surfaces involves two steps:

(1) Both yield surfaces are assumed active, the trial consistency parameter $\boldsymbol{\beta}^{tr}$ is evaluated:

$$\boldsymbol{\beta}^{tr} = \left[\mathbf{n}^T \left(\mathbf{b}_p \mathbf{k}_e \mathbf{b}_p^T + \mathbf{H}_k\right) \mathbf{n} + \mathbf{H}_i\right]^{-1} \mathbf{f}^{tr} \tag{3.33}$$

(2) Enforcing the Kuhn-Tucker conditions, the active surfaces can be shown to correspond to the positive trial consistency parameters $\boldsymbol{\beta}^{tr}$.

$$m \in \mathbf{J}_{act} = \{i, j \mid \beta_m^{tr} > 0\} \tag{3.34}$$

where $\mathbf{J}_{act}$ denotes the indices of the active yield surfaces.

To account only for the active constraints, the normal $\mathbf{n}^{tr}$ is revised to include only the active yield surfaces. For example, if both yield surfaces are active, $\mathbf{n}^{tr} = \left[\mathbf{n}_i^{tr} \ \mathbf{n}_j^{tr}\right]$. If only the yield surface at end i is active, $\mathbf{n}^{tr} = \mathbf{n}_i^{tr}$.

$$\mathbf{n}^{tr} = \left[\mathbf{n}_m^{tr}\right], \qquad m \in \mathbf{J}_{act} \tag{3.35}$$

Similarly, the trial yield function $\mathbf{f}^{tr}$ and the isotropic hardening modulus $\mathbf{H}_i$ are revised to reflect the active yield surfaces. For example, if only the yield surface at end i is active, $\mathbf{f}^{tr} = f_i^{tr}$ and $\mathbf{H}_i = H_{i,i}$.

$$\mathbf{f}^{tr} = \left[\mathbf{f}_m^{tr}\right], \qquad m \in \mathbf{J}_{act} \tag{3.36}$$

$$\mathbf{H}_i = \mathbf{H}_i \left(\mathbf{J}_{act}, \mathbf{J}_{act}\right) \tag{3.37}$$

With the modifications in Equation (3.35)–(3.37) to include only the active surface(s), the consistency parameters $\boldsymbol{\beta}$ can then be evaluated as follows:

$$\boldsymbol{\beta} = \left[\mathbf{n}^T \left(\mathbf{b}_p \mathbf{k}_e \mathbf{b}_p^T + \mathbf{H}_k\right) \mathbf{n} + \mathbf{H}_i\right]^{-1} \mathbf{f}^{tr} \tag{3.38}$$

The plastic deformations $\mathbf{v}_p$, the internal variables $\boldsymbol{\alpha}$ and the back-forces $\mathbf{q}_b$ are then updated:

$$\mathbf{v}_{p,n} = \mathbf{v}_{p,n-1} + \mathbf{b}_p^T \mathbf{n} \boldsymbol{\beta} \tag{3.39}$$

$$\mathbf{q}_{b,n} = \mathbf{q}_{b,n-1} + \mathbf{H}_k \mathbf{n} \boldsymbol{\beta} \tag{3.40}$$

$$\boldsymbol{\alpha}_n = \boldsymbol{\alpha}_{n-1} + \boldsymbol{\beta} \tag{3.41}$$

The force $\mathbf{q}_n$ is updated from the trial value $\mathbf{q}^{tr}$ as follows:

$$\mathbf{q}_n = \mathbf{q}^{tr} - \mathbf{k}_e \mathbf{b}_p^T \mathbf{n} \boldsymbol{\beta} \tag{3.42}$$

Finally the tangent stiffness $\mathbf{k}_t$ is given in Equation (3.22). Table 3.1 summarizes the state determination algorithm of the general series beam model with offsets.

Figure 3.7 is a graphical illustration of the returning-mapping scheme for an element response under the assumption of an elasto-plastic behavior and no plastic hinge offset for simplicity. The shaded region is the elastic domain with $f_i < 0$ and $f_j < 0$. Plastic correction is required when the trial force $\mathbf{q}^{tr}$ falls outside this region. Note that the force correction is $\Delta\mathbf{q} = \mathbf{q}^{tr} - \mathbf{q} = \mathbf{k}_e \mathbf{n} \boldsymbol{\beta} = \beta_i \mathbf{k}_e \mathbf{n}_i + \beta_j \mathbf{k}_e \mathbf{n}_j$, which is a linear combination of $\mathbf{k}_e \mathbf{n}_i$ and $\mathbf{k}_e \mathbf{n}_j$. The area outside the elastic domain can be divided into three regions A, B, C separated by these vectors, as shown in Figure 3.7(a).

Given: end deformations $\mathbf{v}_n$ and history variables at step $n-1$
Required: state variables at step n

1. Elastic predictor:
  Evaluate $\mathbf{q}^{tr}$, $\mathbf{q}_b^{tr}$, $\boldsymbol{\alpha}^{tr}$ in (3.23)–(3.25)
  Evaluate $\mathbf{n}^{tr}$ in (3.26)
2. Check of plastic process:
  Evaluate $\mathbf{f}^{tr}$ in (3.27)
  IF $f_i^{tr} < 0$ and $f_j^{tr} < 0$ THEN:
    Elastic update, go to Step 3
  ELSE:
    Plastic correction, go to Step 4
  ENDIF
3. Elastic update:
  Update $\mathbf{q}_{b,n}$, $\boldsymbol{\alpha}_n$, $\mathbf{v}_{p,n}$ in (3.29)–(3.31)
  Update $\mathbf{q}_n$, $\mathbf{k}_t$ in (3.28) and (3.32)
  EXIT
4. Identification of active yield surfaces in two steps
  Assume both surfaces are active and evaluate trial $\boldsymbol{\beta}^{tr}$ in (3.33)
  Identify active surfaces $\mathbf{J}_{act}$ that correspond to positive $\boldsymbol{\beta}^{tr}$
5. Consistency parameters $\boldsymbol{\beta}$:
  Update $\mathbf{n}^{tr}$, $\mathbf{f}^{tr}$, $\mathbf{H}_i$ in (3.35)–(3.37)
  Compute $\boldsymbol{\beta}$ in (3.38)
6. State variables update:
  Update $\mathbf{v}_{p,n}$ in (3.39)
  Update $\mathbf{q}_{b,n}$, $\boldsymbol{\alpha}_n$ in (3.40)–(3.41)
7. Element end forces and tangent stiffness:
  Update $\mathbf{q}_n$ in (3.42)
  Evaluate $\mathbf{k}_t$ in (3.22)

Table 3.1: State determination algorithm of series beam model with plastic hinge offset

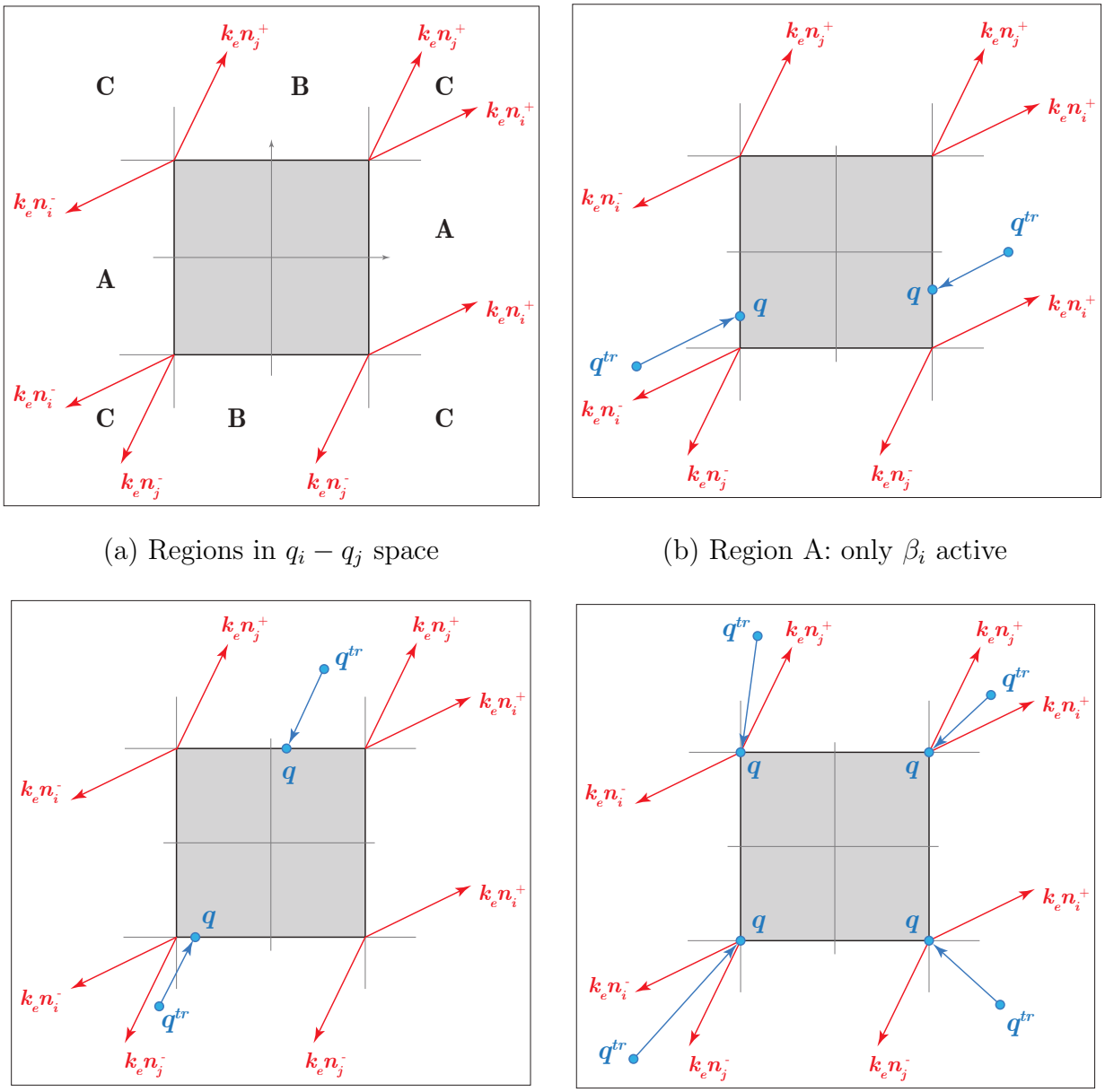

(a) Regions in $q_i - q_j$ space

(b) Region A: only β_i active

(c) Region B: only β_j active

(d) Region C: both β_i and β_j active

Figure 3.7: Return-mapping algorithm for series element

(i) **Region A**: This region corresponds to a positive trial yield function at end i, $f_i^{tr} > 0$, and is defined by the area outside the yield envelope between vectors $\mathbf{k}_e\mathbf{n}_i^+$ for $q_i > 0$ and between vectors $\mathbf{k}_e\mathbf{n}_i^-$ for $q_i < 0$. If the trial force $\mathbf{q}^{tr}$ falls in this region, only the yield surface at end i is active, i.e. the consistency parameter $\beta_i > 0$ and $\beta_j = 0$. The normal $\mathbf{n}^{tr} = \mathbf{n}_i^{tr}$ in Equation (3.35) and the plastic deformation increment $\Delta\mathbf{v}_p$ is parallel to the normal $\mathbf{n}_i$ of the yield surface $f_i = 0$. The force correction $\Delta\mathbf{q}$ is parallel to $\mathbf{k}_e\mathbf{n}_i$. The corrected force $\mathbf{q}$ gives $f_i = 0$ and $f_j < 0$. The plastic correction scheme is shown in Figure 3.7(b).

(ii) **Region B**: This region corresponds to a positive trial yield function at end j, $f_j^{tr} > 0$, and is defined by the area outside the yield envelope between vectors $\mathbf{k}_e\mathbf{n}_j^+$ for $q_j > 0$ and between vectors $\mathbf{k}_e\mathbf{n}_j^-$ for $q_j < 0$. If the trial force $\mathbf{q}^{tr}$ falls in this region, only the yield surface at end j is active, i.e. the consistency parameter $\beta_j > 0$ and $\beta_i = 0$. The normal $\mathbf{n}^{tr} = \mathbf{n}_j^{tr}$ in Equation (3.35) and the plastic deformation increment $\Delta\mathbf{v}_p$ is parallel to the normal $\mathbf{n}_j$ of the yield surface $f_j = 0$. The force correction $\Delta\mathbf{q}$ is parallel to $\mathbf{k}_e\mathbf{n}_j$. The corrected force $\mathbf{q}$ gives $f_i < 0$ and $f_j = 0$. The plastic correction scheme is shown in Figure 3.7(c).

(iii) **Region C**: This region is defined by the area outside the yield envelope and between the vectors $\mathbf{k}_e\mathbf{n}_i^\pm$ and $\mathbf{k}_e\mathbf{n}_i^\pm$ in the same quadrant of the force space. If the trial force $\mathbf{q}^{tr}$ falls in this region, both yield surfaces are active, i.e. the consistency parameters $\beta_i > 0$ and $\beta_j > 0$. The normal $\mathbf{n}^{tr} = \left[\mathbf{n}_i^{tr}\ \mathbf{n}_j^{tr}\right]^T$ in Equation (3.35). The plastic deformation increment $\Delta\mathbf{v}_p$ is a linear combination of the normals $\mathbf{n}_i$ and $\mathbf{n}_j$. The correction process adjusts the force $\mathbf{q}$ to the 'corner' of the admissible domain and gives $f_i = 0$ and $f_j = 0$. The plastic correction scheme is shown in Figure 3.7(d).

(iv) Along the common edges between two regions, A & C and B & C, the correction scheme is similar to the scheme in regions A and B, respectively. The only difference is that upon the correction process, the force $\mathbf{q}$ targets the singular point of the yield envelope and gives $f_i = f_j = 0$.

The force correction processes in Figures 3.7(b)–(d) results from the two-step scheme in the previous discussion. An example is shown in Figure 3.8. In the first step, both surfaces are assumed active and the trial force $\mathbf{q}^{tr}$ is projected to the nearest corner in the quadrant in Figure 3.8(a). The trial consistency parameters $\boldsymbol{\beta}^{tr}$ can be interpreted as the projection of the force increment $\Delta\mathbf{q}$ to vectors $\mathbf{k}_e\mathbf{n}_i$ and $\mathbf{k}_e\mathbf{n}_j$. In the second step, since $\beta_j^{tr} < 0$, only the yield surface i is active and the force correction is adjusted accordingly as shown in Figure 3.8(b).

It is important to point out that the signs of the trial yield functions $\mathbf{f}^{tr}$ are not sufficient to identify the active surfaces. For example, if only one trial yield function is positive, $f_i^{tr} > 0$ and $f_j^{tr} < 0$, it is not guaranteed that only the surface i is active, $\beta_i > 0$ and $\beta_j = 0$. The force correction affects both q_i and q_j due to the coupling terms in the elastic stiffness $\mathbf{k}_e$, and could activate the surface j after the correction, $f_j > 0$, and thus violates the Kuhn-Tucker

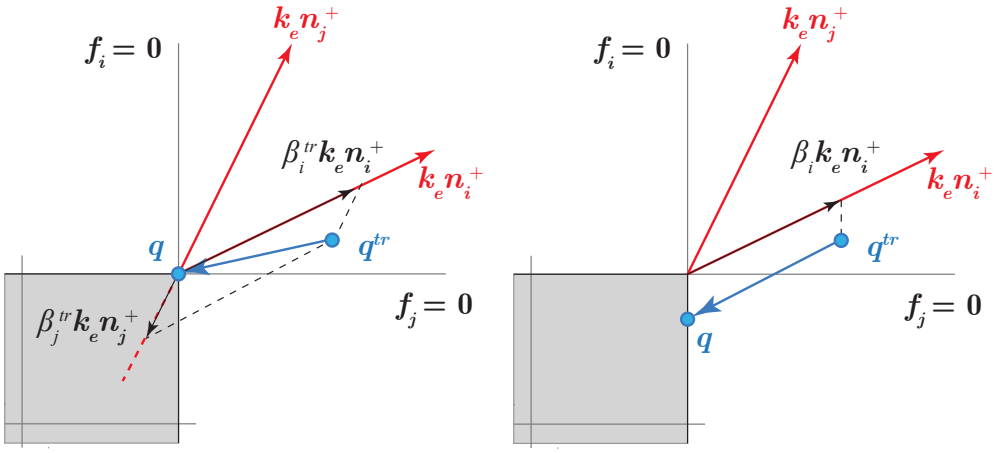

(a) Step 1: Evaluate β^{tr} (b) Step 2: Update active surfaces

Figure 3.8: Two-step identification of active surfaces

condition. Figure 3.9 illustrates two scenarios in which determining the active surfaces based solely on the signs of the trial yield functions is erroneous.

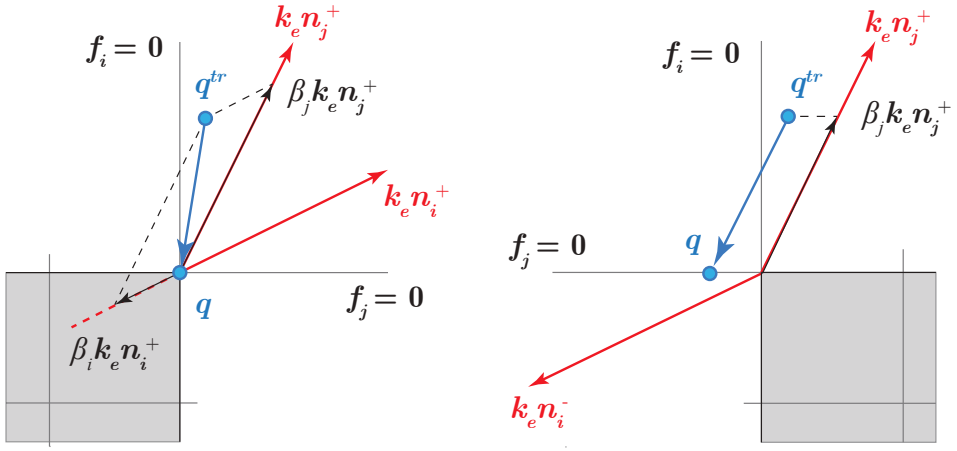

(a) $\beta_i < 0$ (b) $f_i > 0$

Figure 3.9: Violation of Kuhn-Tucker condition due to incorrect active β's

In the first scenario in Figure 3.9(a), the trial force $\mathbf{q}^{tr}$ gives a positive value for both trial yield functions $f_i^{tr} > 0$ and $f_j^{tr} > 0$. If both surfaces are assumed active, the correction brings the force $\mathbf{q}^{tr}$ to the corner to satisfy $f_i = f_j = 0$. However, this projection of the force increment $\Delta\mathbf{q}$ onto vectors $\mathbf{k}_e\mathbf{n}_i$ and $\mathbf{k}_e\mathbf{n}_j$ indicates that $\beta_i < 0$, and thus violates the

Kuhn-Tucker condition that requires positive consistent parameters $\boldsymbol{\beta}$. In this scenario, the trial force $\mathbf{q}^{tr}$ lies in region B in Figure 3.7(a), which shall only activate surface j even though $f_i^{tr} > 0$.

In the second scenario in Figure 3.9(b), the trial force $\mathbf{q}^{tr}$ gives $f_i^{tr} < 0$ and $f_j^{tr} > 0$. If the active surfaces are based on signs of the trial yield functions, only surface j is active and the force correction is parallel to $\mathbf{k}_e\mathbf{n}_j$. However, the correction gives $f_i > 0$ and brings the force $\mathbf{q}^{tr}$ outside the admissible domain. This violates the Kuhn-Tucker condition that requires the yield functions to remain nonpositive, $\mathbf{f} \leq \mathbf{0}$. In this scenario, the trial force $\mathbf{q}^{tr}$ lies in region C in Figure 3.7(a), which shall activate both surfaces i and j even though $f_i^{tr} < 0$.

3.1.4 Model parameters

The series beam element requires 7 parameters: the Young modulus E, the cross-sectional area A, the moment of inertia I, the flexural plastic capacity M_p, the kinematic hardening ratio H_{kr}, the isotropic hardening ratio H_{ir}, and the offset parameter χ. Since the first 4 parameters are readily available from the material properties and the member geometry, this section addresses the last 3 parameters.

3.1.4.1 Hardening parameters H_{kr} and H_{ir}

The kinematic hardening ratio H_{kr} and the isotropic hardening ratio H_{ir} are directly related to the kinematic hardening modulus H_k and the isotropic hardening modulus H_i in terms of the flexural stiffness under antisymmetric bending $6EI/L$:

$$H_k = H_{kr}\frac{6EI}{L} \tag{3.43}$$

$$H_i = H_{ir}\frac{6EI}{L} \tag{3.44}$$

Figure 3.10 illustrates the evolution of the yield surface with linear isotropic and kinematic hardening from f_{n-1} to f_n. The end forces evolve from an elastic state $\mathbf{q}_{n-1}$ to a plastic state $\mathbf{q}_n$. Kinematic hardening translates the yield surface while isotropic hardening expands or contracts the yield surface in the force space.

Figures 3.10(a1)-(a2) illustrate the evolution of the yield envelope in the case of kinematic hardening with $H_{kr} > 0$. In Figure 3.10(a1) only the yield surface j is active, $\beta_j > 0$, and the yield envelope translates parallel to the normal $\mathbf{n}_j$. The force $\mathbf{q}_n$ gives $f_{n,i} < 0$ and $f_{n,j} = 0$. In Figure 3.10(a2) both yield surfaces i and j are active, $\beta_i > 0$ and $\beta_j > 0$, and the translation of the yield envelope is a linear combination of both $\mathbf{n}_i$ and $\mathbf{n}_j$. The force $\mathbf{q}_n$ targets the corner of the new yield surfaces, implying that $f_{n,i} = 0$ and $f_{n,j} = 0$.

Figures 3.10(b1)-(b2) illustrate the evolution of the yield envelope in the case of isotropic hardening with $H_{ir} > 0$. In Figure 3.10(b1) only the yield surface i is active, $\beta_i > 0$, and the yield envelope expands in the direction parallel to the normal $\mathbf{n}_i$. The force $\mathbf{q}_n$ gives

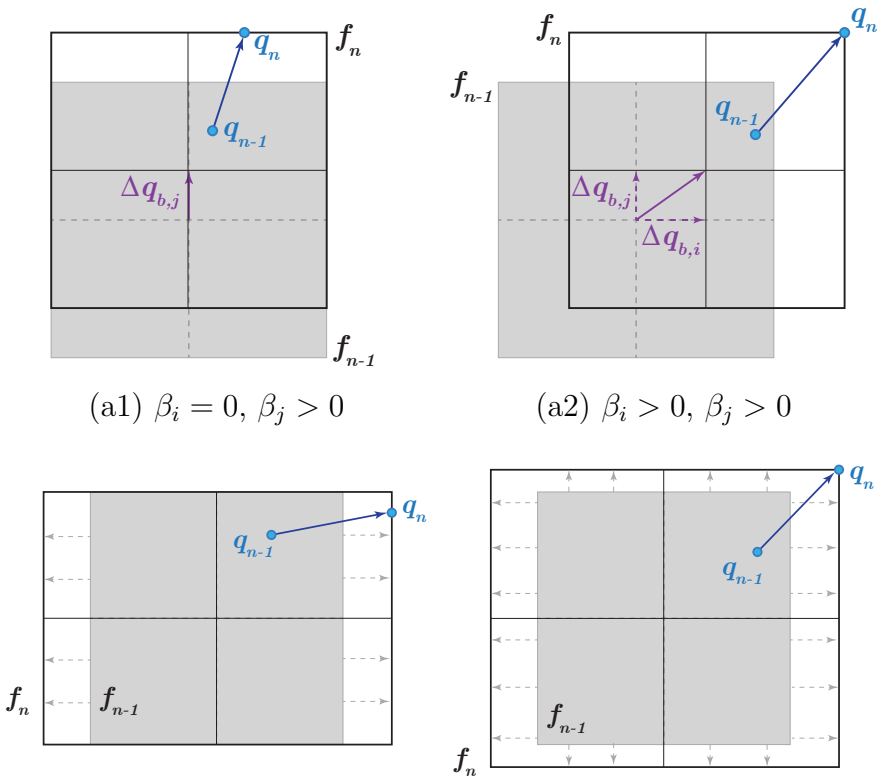

Figure 3.10: Evolution of yield surfaces: (a) kinematic hardening with $H_{kr} > 0$, and (b) isotropic hardening with $H_{ir} > 0$

$f_{n,i} = 0$ and $f_{n,j} < 0$. In Figure 3.10(b2) only the yield surface j is active, $\beta_j > 0$, and the yield envelope expands in the direction that is a linear combination of both $\mathbf{n}_i$ and $\mathbf{n}_j$. The force $\mathbf{q}_n$ targets the corner of the new yield surface, implying $f_{n,i} = 0$ and $f_{n,j} = 0$.

Figures 3.11(a)-(b) compare the cyclic response for different values of the hardening ratios H_{kr} and H_{ir}. Figures 3.11(c)-(d) show the cyclic response with combined hardening: $H_{kr} = 0.005$ and $H_{ir} = 0.005$ in Figure 3.11(c) leads to strength hardening with increasing inelastic deformations, whereas $H_{kr} = 0.005$ and H_{ir} = -0.005 in Figure 3.11(d) gives a gradual strength degradation with increasing inelastic deformations. The horizontal slope in the reloading segments results from the fact that H_{kr} = -H_{ir}. Different colors are used in Figures 3.11(c)-(d) to distinguish the response in each cycle.

With different signs and relative values of H_{kr} and H_{ir}, the model can accommodate cyclic hardening as well as strength degradation. Although a gradual strength deterioration is possible with $H_{ir} < 0$, the range of degrading behaviors the model can describe is limited and the model does not accommodate stiffness deterioration. These limitations will be addressed in the later section by introducing damage to the element response.

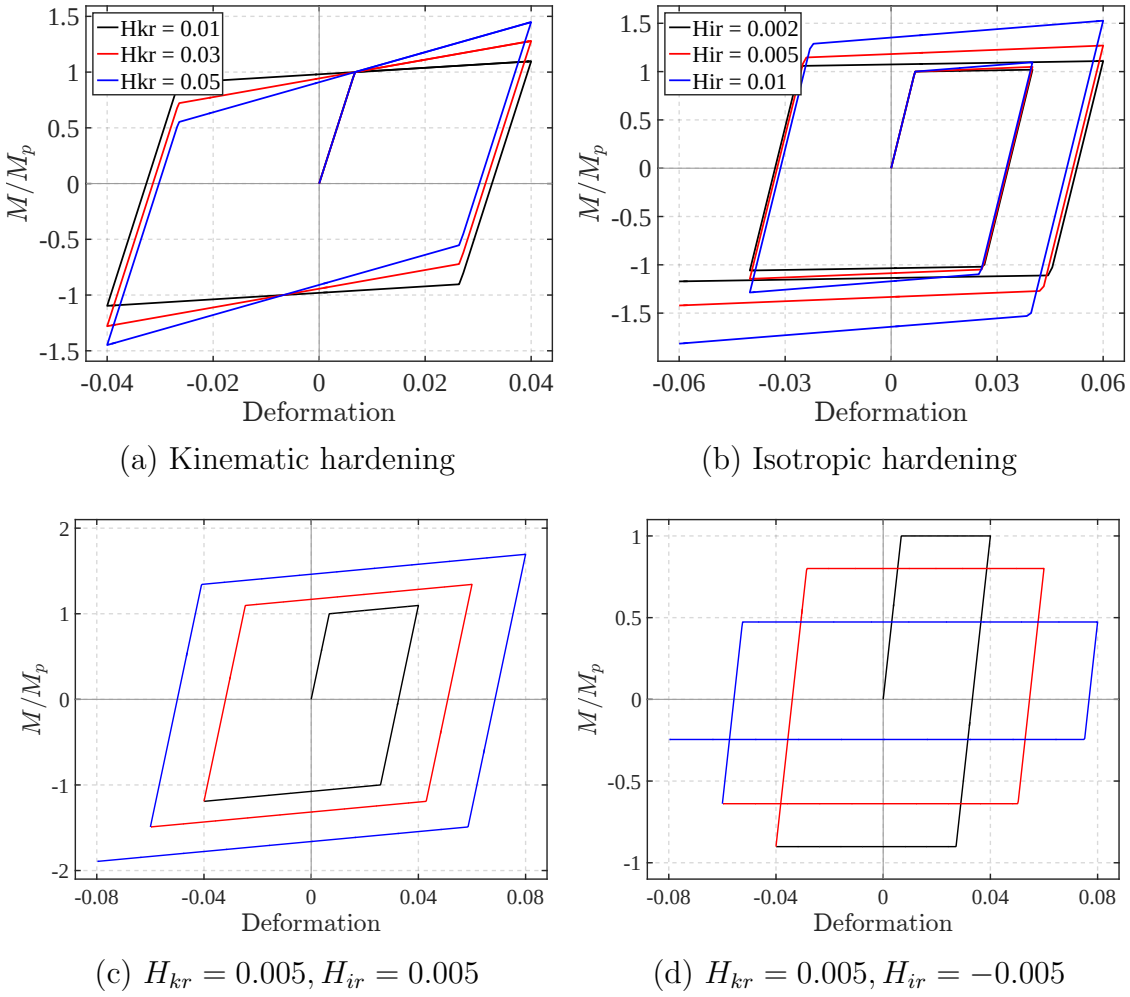

(a) Kinematic hardening

(b) Isotropic hardening

(c) $H_{kr} = 0.005, H_{ir} = 0.005$

(d) $H_{kr} = 0.005, H_{ir} = -0.005$

Figure 3.11: Sample cyclic response with linear kinematic and isotropic hardening

3.1.4.2 Offset parameter

The offset parameter χ represents the location of the plastic hinges from the element ends and ranges from $\chi = 0$ for the hinges at the element ends to $\chi = 0.5$ for the hinges at the element midspan. Figure 3.12 compares the flexural force-deformation relation at the base of a cantilever beam subjected to a monotonically increasing transverse load at the free end for different offset parameter $\chi = 0, 0.05, 0.1$. For the linear moment distribution in this case study, the offset parameter χ increases the yield moment at the base. This strength increase results from the extrapolation of moment from the hinge locations to the element ends, with a larger offset leading to a higher moment amplification.

The ability of the plastic hinge offsets to describe the coupling of the inelastic zones at the element ends is demonstrated in the following section.

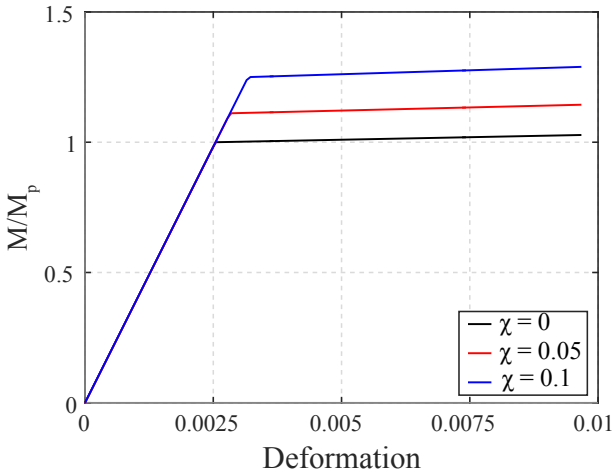

Figure 3.12: Effect of offset on flexural response of a cantilever beam

3.2 Examples of Series Beam Element

3.2.1 Pushover analysis of portal frame

This example compares the series beam element to a more sophisticated element based on distributed plasticity in a simple structure under a standard load pattern. The steel portal frame in Figure 3.13 is used for illustration. The columns are subjected to an axial compression of $P_v = 160$ kips, which is 10% of the column axial plastic capacity N_p to represent the effect of gravity loading on the portal frame. The frame is subjected to a monotonically increasing lateral displacement at the girder level.

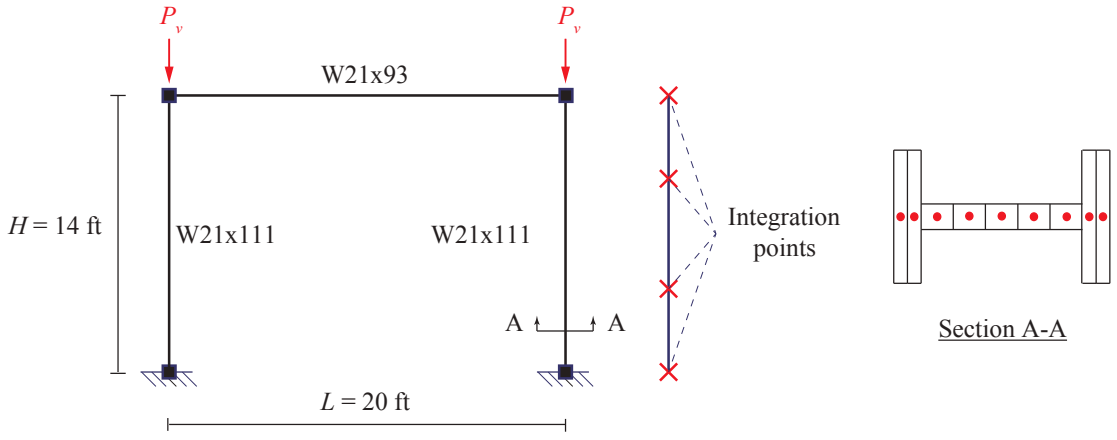

Figure 3.13: Structural model of portal frame

The column and beam elements assume an elastic-perfectly-plastic (EPP) behavior. The

corotational formulation is used to account for the nonlinear geometry. Each column is modeled with a force-based distributed beam-column element with 4 integration points along the length and 9 fibers in each cross section: 2 in each flange and 5 in the web. The idealized model of the column and its discritization scheme is shown in Figure 3.13. The distributed plasticity model is used to capture the axial-flexure interaction in the columns.

For comparison, two different models are used to simulate the girder: (1) Model M1 using a force-based beam-column element with the same discretization scheme as the columns, and (2) Model M2 using the series beam element. In this example, no plastic hinge offset is specified in the girder, $\chi = 0$.

Figure 3.14 compares the global and the local response in the two models. The base shear-lateral drift relation in Figure 3.14(a) is practically identical. Both models can capture the linear elastic segment at small drifts, followed by the gradual yielding and transition to plastic behavior, and the linear softening range. The negative stiffness in Figure 3.14(a) indicates the effect of the column axial force under the large lateral displacement.

The girder response in the two models are shown in Figure 3.14(b). While the elastic response is identical, the plastic behavior shows slight discrepancies between the models. Model M1 gives a smooth transition from the elastic to the plastic range due to the gradual yielding of the fibers. In contrast, model M2 exhibits an abrupt yielding when the girder moment reaches the plastic capacity M_p. The yield moment in model M1 is slightly smaller than in model M2 due to a small axial force in the girder that reduces the flexural yield strength. The series beam element in model M2 neglects the axial-flexure interaction, and thus, does not capture this strength reduction. However, the discrepancy is negligible (within 2%).

The response of the left column is shown in Figures 3.14(c)–(d). It is noteworthy that even though the two models use the same column element, the column response show slight discrepancies due to the differences in the girder response. The girder in model M2 yields at a higher moment, which leads to a higher transverse shear and imposes a higher axial force demand on the columns. Consequently, the columns in model M2 yield at a smaller moment.

One advantage of the concentrated plasticity over the distributed plasticity approach is the improvement in the numerical efficiency because model M1 requires state determination and storage of all fiber response whereas model M2 only monitors the response at the element ends. The running time of model M2 is 2 times faster than model M1 in this simple example.

3.2.2 General bending of simply-supported beam

The objectives of this example are two-fold: (1) to illustrate the calibration of the hardening parameters, and (2) to showcase the ability of the plastic hinge offsets to couple the inelastic response at the element ends and describe accurately the hardening response. For the purposes, the study uses a simply-supported beam with a bilinear moment-curvature relation that is subjected to proportional rotations at two ends. The 10-ft beam, shown in Figure 3.15, is made of a W30x173 steel profile with $f_y = 50$ ksi yield strength. The imposed

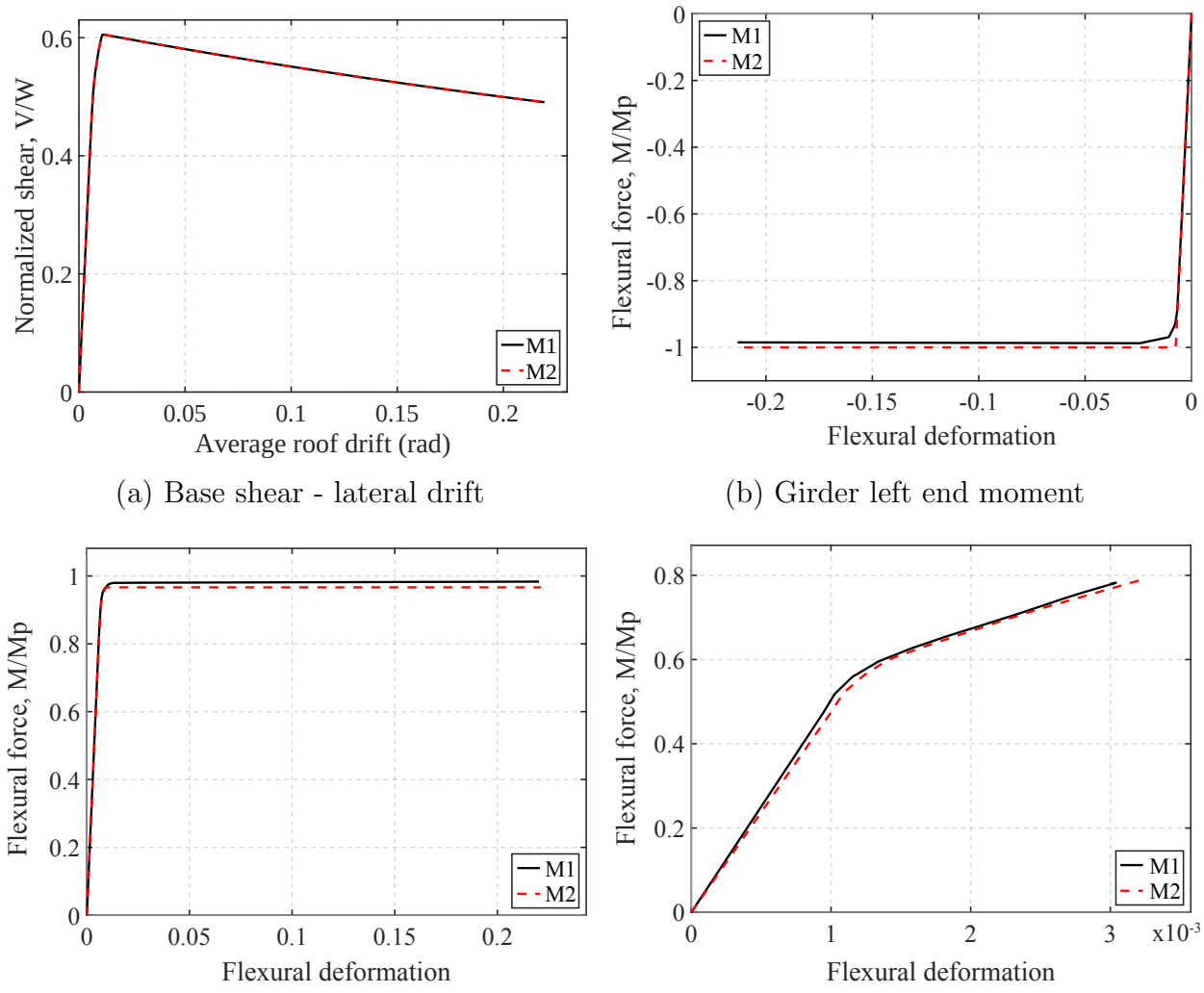

(a) Base shear - lateral drift

(b) Girder left end moment

(c) Left column base moment

(d) Left column top moment

Figure 3.14: Pushover response of portal frame with EPP element behavior

rotation ratio is $\rho = v_j/v_i$, where v_i and v_j are the element deformations at the left and right end of the beam, respectively. The following evaluates the moment distribution under different rotation ratio ρ ranging from -1 to 1. $\rho = -1$ represents a uniform moment and curvature distribution while $\rho = 1$ corresponds to antisymmetric bending.

For comparison, three different alternatives are used to model the beam:

(1) *Model DP*: represents the distributed plasticity formulation. This model uses one Euler-Bernoulli force-based distributed plasticity beam-column element with 3 integration points along its length. Each cross section is discretized into 9 fibers: 2 in each flange and 5 in the web. The number of elements and integration points have

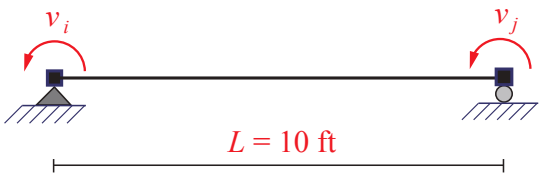

Figure 3.15: Simply-supported beam with proportional end rotations

been calibrated to give sufficient accuracy in the numerical response. The fiber stress-strain constitutive relation adopts the bilinear plasticity model with linear kinematic hardening $H_k = 1.5\%E$ and no isotropic hardening $H_i = 0$.

(2) *Model CP1*: represents the concentrated plasticity formulation without plastic hinge offsets. A kinematic hardening ratio $H_{kr} = 2.5\%$ is used to describe the post-yield hardening behavior. No plastic hinge offset is specified, $\chi = 0$.

(3) *Model CP2*: represents the concentrated plasticity formulation with plastic hinge offsets. This model is similar to model CP1 except the kinematic hardening ratio $H_{kr} = 1\%$ and the offset $\chi = 0.065$.

Figure 3.16(a) illustrates the calibration of the hardening parameter H_{kr} in model CP1. To account for the gradual yielding and a slightly higher yield strength than the nominal value M_p in model DP, the hardening parameter in model CP1 is calibrated to match the moment at a target rotation value v_{target} under antisymmetric bending with equal end deformations $\rho = 1$. In this example, $v_{target} = 0.03$ is used, which results in the hardening parameter $H_{kr} = 2.5\%$.

Another common approach, shown in Figure 3.16(b), is to introduce a constant 'fictitious plastic moment' M_p^* higher than the nominal value M_p. The stiffness transition initiates when the moment reaches the 'fictitious' yield strength M_p^* to accommodate the higher strength during the gradual yielding. However, this approach does not capture the coupling of the response at the element ends that changes the fictitious moment M_p^* under different rotation ratios ρ. This limitation can be addressed with the plastic hinge offsets, as will be shown in the following discussion.

Figure 3.17 compares model DP and models CP1 and CP2 in the monotonic moment-rotation at both two element ends under three rotation ratios $\rho = 0.5$, $\rho = -0.5$, and $\rho = -1$. Each curve is denoted by the model name followed by the element end, for instance, 'DP-i' represents the moment-rotation relation at end i in model DP. Model CP1 captures rather well the response under antisymmetric bending with $\rho = 0.5$ in Figure 3.17(a). However, it is evident in Figures 3.17(b)-(c) that $H_{kr} = 2.5\%$ gives excessive hardening under symmetric bending with $\rho = -0.5$ and $\rho = -1$. Model CP1 underestimates the moment at rotations smaller than the target value while it overestimates the moment beyond the target rotation.

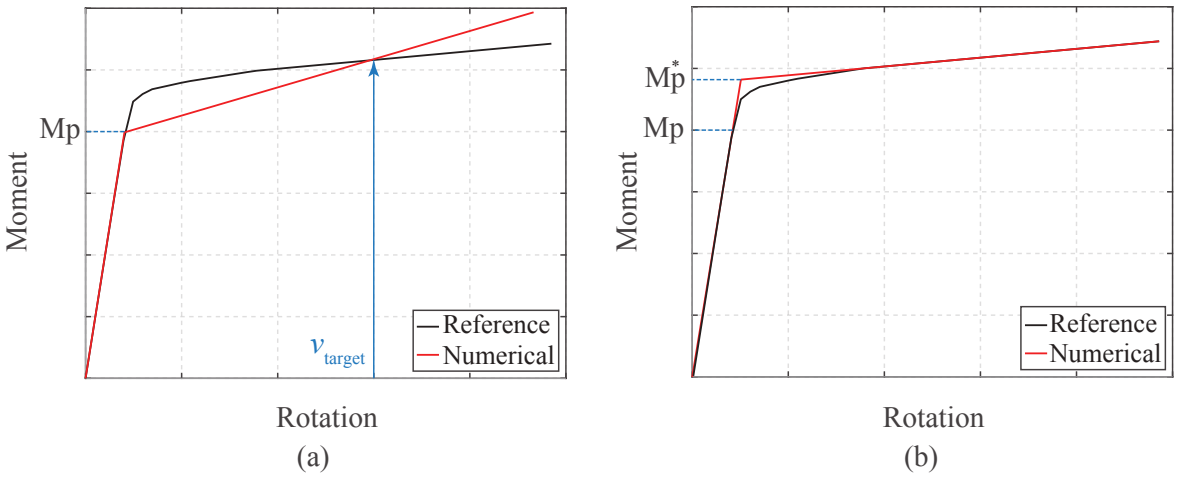

Figure 3.16: Calibration of post-yield hardening parameter: (a) with target deformation v_{target}, (b) with fictitious moment M_p^*

The moment-rotation relation in model CP2 under different rotation ratios is shown in Figures 3.17(d)-(f). The plastic hinge offsets couple the response at the element ends and capture better the variation in the yield strength under different rotation ratios. The response under antisymmetric bending is almost identical to model DP while the response under symmetric bending shows a better agreement than model CP1.

Calibration of the hardening parameter in model CP2 with plastic hinge offsets is performed in two steps: (1) calibrate the hardening ratio H_{kr} to match the post-yield response given by the DP model under $\rho = 1$, and (2) identify the fictitious yield moment M_p^*, then evaluate the offset parameter $\chi = 1/2 - M_p/2M_p^*$. The offsets offer more flexibility in the parameter calibration. While model CP1 has the kinematic hardening ratio H_{kr} as the only degree of freedom to calibrate the hardening response, model CP2 has two, which are the kinematic hardening ratio H_{kr} and the offset parameter χ. The additional parameter allows model CP2 to avoid the rather arbitrary target rotation in model CP1.

Next the beam ends are subjected to a proportional cyclic rotation history with a fixed rotation ratio $\rho = v_i/v_j$. The rotation at end j follows a cyclic pattern with the following peak rotation values: 0.01, −0.01, 0.02, −0.02, 0.04, −0.04. Figure 3.18 compare model DP with model CP1 and CP2, respectively, in the moment-rotation at both ends for 3 cases $\rho = 1, 0.5, -0.5$. Same parameters in the monotonic cases are used in the simulations. It is evident that the plastic hinge offsets capture very well the coupling of the response at the two ends and describe more consistently the post-yield hardening behavior. It is also noteworthy that the both CP models are significantly more efficient than model DP with a factor of 5–10 times reduction in the computation time.

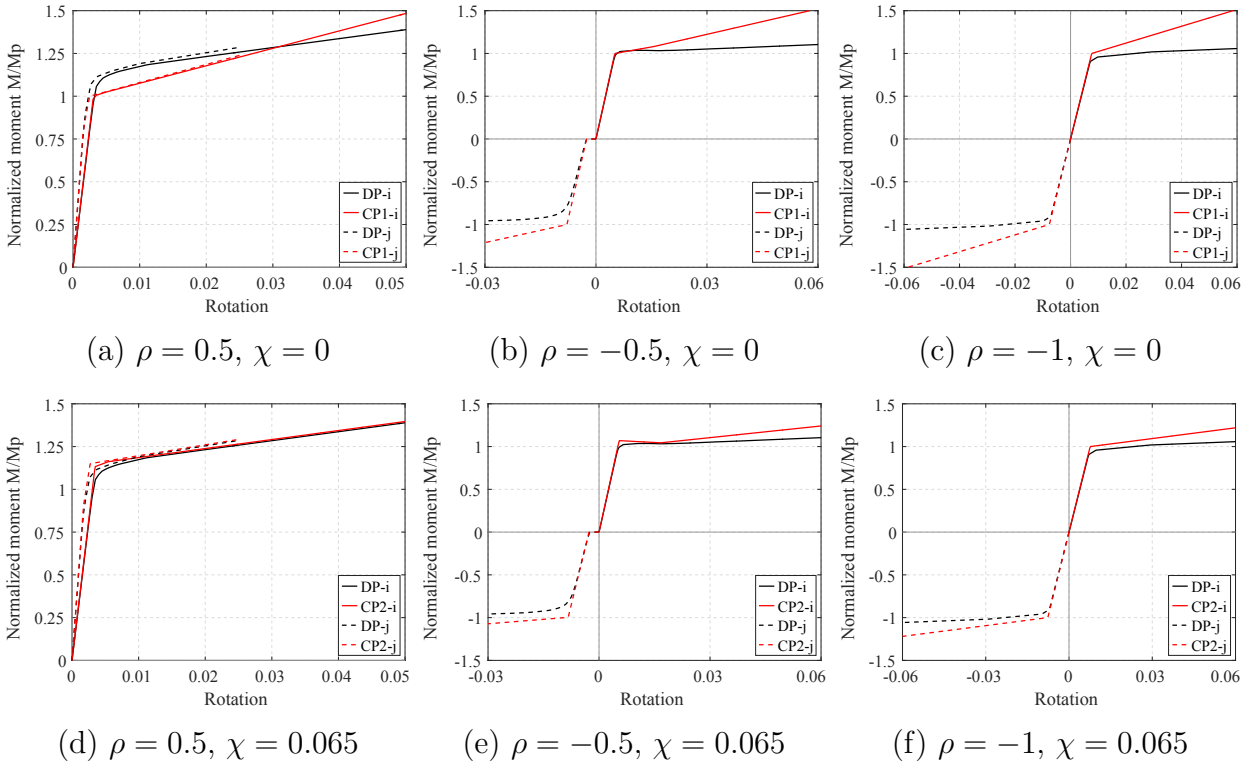

(a) $\rho = 0.5$, $\chi = 0$ (b) $\rho = -0.5$, $\chi = 0$ (c) $\rho = -1$, $\chi = 0$

(d) $\rho = 0.5$, $\chi = 0.065$ (e) $\rho = -0.5$, $\chi = 0.065$ (f) $\rho = -1$, $\chi = 0.065$

Figure 3.17: Moment-rotation relation of simply-supported beam under monotonic loading

3.2.3 Reduced beam section (RBS) connections

In earthquake-resistant design of steel structures, reduced beam sections (RBS) intentionally move the plastic hinges away from the beam ends. Properties of the RBS depend on two main parameters: (1) location of the RBS from the beam ends, and (2) design of the RBS such as the radius cut. The latter reduces the strength at the RBS relative to the nominal section strength along the beam span.

In practice, a beam with RBS is usually modeled by 3 elastic beams in series with 2 nonlinear springs at the RBS locations as shown in Figure 3.19(a). This modeling approach, so-called model A, requires 6 nodes for the assembly, 4 of which locate at the interface between the elastic beams and the plastic hinges, and as a result, generate additional global dofs. The moment-rotation relation of the plastic hinges is specified by the user. Ideally, the hinges are rigid-plastic, but in practice, they are often approximated as semi rigid-plastic with a very large initial stiffness. This proposition is known to give rise to numerical problems, including excessive damping forces and violation of equilibrium at degrees of freedom (dofs) with no inertial forces [15].

An improved modeling approach, so-called model B, shown in Figure 3.19(b), is a serial assembly of 2 exterior linear elastic beam elements and 1 interior inelastic beam element

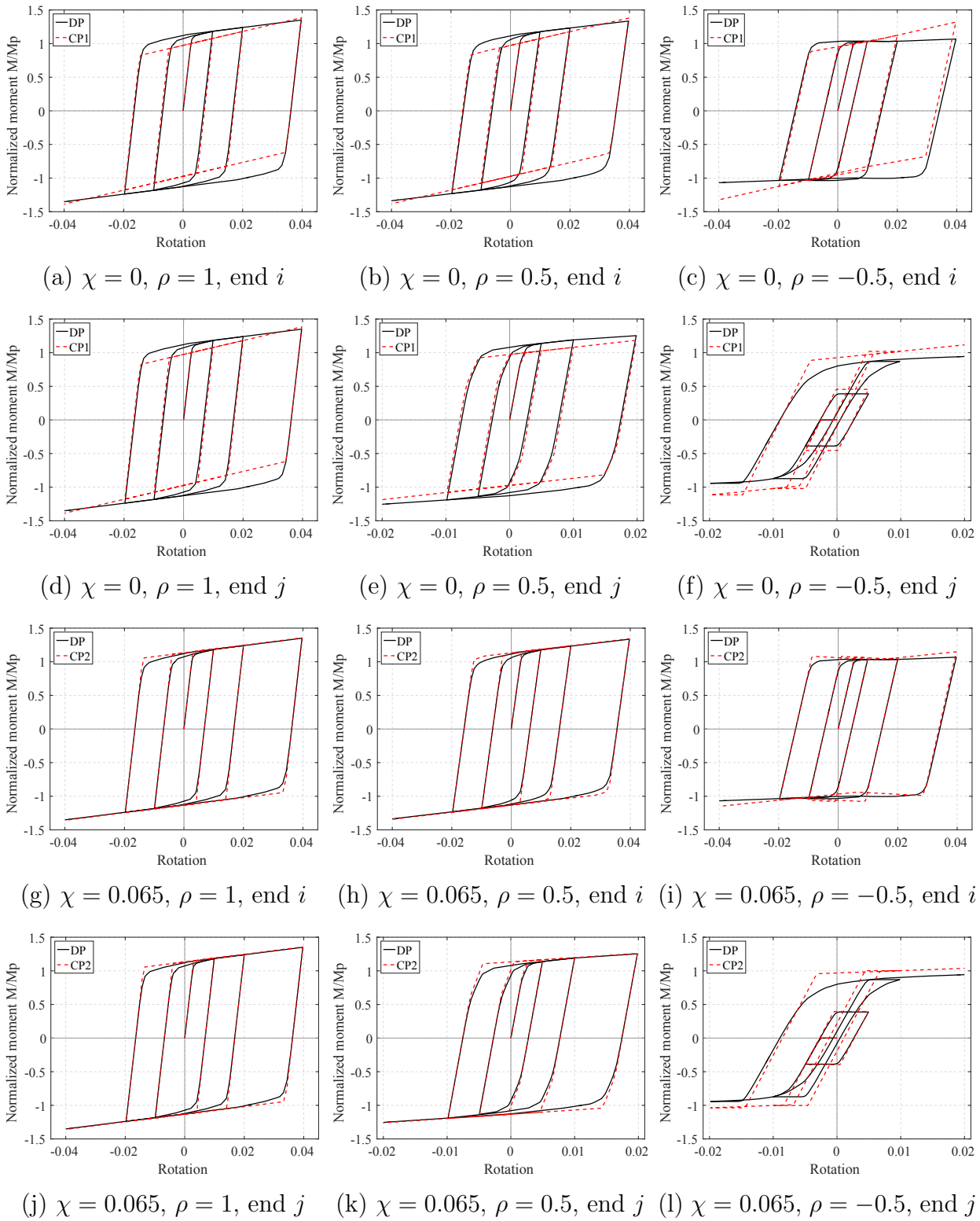

(a) $\chi = 0$, $\rho = 1$, end i (b) $\chi = 0$, $\rho = 0.5$, end i (c) $\chi = 0$, $\rho = -0.5$, end i

(d) $\chi = 0$, $\rho = 1$, end j (e) $\chi = 0$, $\rho = 0.5$, end j (f) $\chi = 0$, $\rho = -0.5$, end j

(g) $\chi = 0.065$, $\rho = 1$, end i (h) $\chi = 0.065$, $\rho = 0.5$, end i (i) $\chi = 0.065$, $\rho = -0.5$, end i

(j) $\chi = 0.065$, $\rho = 1$, end j (k) $\chi = 0.065$, $\rho = 0.5$, end j (l) $\chi = 0.065$, $\rho = -0.5$, end j

Figure 3.18: Moment-rotation relation of simply-supported beam under cyclic loading

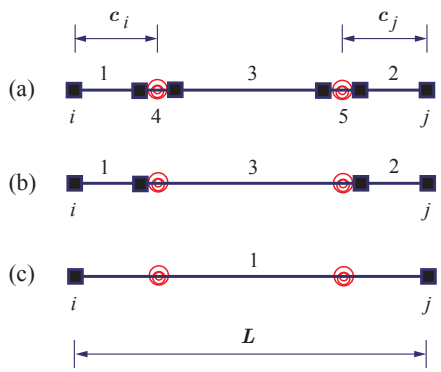

Figure 3.19: Modeling approaches for reduced-beam sections: (a) 3 linear-elastic beams with 2 zero-length springs, (b) 2 linear-elastic beams with 1 series beam without offset, (c) 1 series beam with offset

with plastic hinges at the ends. The state determination of the plastic hinges are performed implicitly in the inelastic element. This method requires 4 nodes, 2 of which locate in the beam interior between the elastic elements and the inelastic element. In the subsequent discussion, the series beam element with the plastic hinges at the element ends is selected to represent the inelastic element in model B. The exact representation of the rigid-plastic behavior in model B avoids the numerical problems in model A.

A more direct approach, so-called model C, is proposed here to use 1 beam element with plastic hinge offsets, as shown in Figure 3.19(c). As opposed to model A and B, model C does not require additional nodes and dofs at the interface between the plastic hinges and the elastic beam. The RBS design is reflected in two parameters in model C: the offset parameter χ and the strength modification factor λ. The offset χ indicates the RBS location at distance $c = \chi L$ from the element ends. The strength modification factor λ gives the moment capacity at the RBS relative to the nominal strength M_p with $0 < \lambda \leq 1$.

The simply-support beam under general bending in Section 3.2.2 is revisited but with reduced sections in the beam interior. Figure 3.20 compares the moment-rotation relation at the beam ends and at the hinge locations for three load scenarios using model B and model C. All parameters in the two models are the same except for the hardening ratio H_{kr}. To describe the same post-yield hardening stiffness H_k in Equation (3.43), the kinematic hardening ratios in model B, $H_{kr}^{(B)}$, and in model C, $H_{kr}^{(C)}$, are proportional to the flexural stiffness:

$$\frac{H_{kr}^{(B)}}{H_{kr}^{(C)}} = \frac{EI/L^{(B)}}{EI/L^{(C)}} = \frac{1}{1-2\chi} \tag{3.45}$$

This modification accounts for the different flexural stiffness EI/L in the two models due to the element length: while the element in model C has length L, the interior beam in model B has length $(1-2\chi)L$. The adjustment in Equation (3.45) ensures the same hardening response in the two models regardless of the RBS location. It is evident that

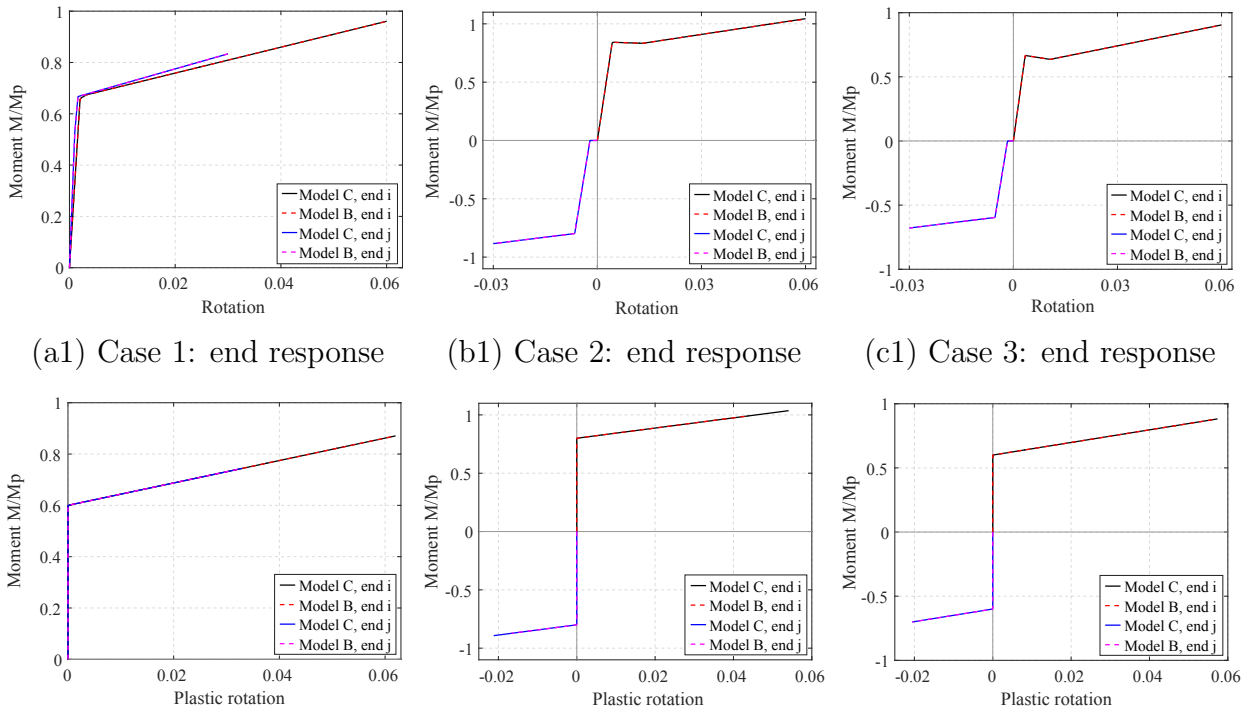

(a1) Case 1: end response (b1) Case 2: end response (c1) Case 3: end response

(a2) Case 1: hinge response (b2) Case 2: hinge response (c2) Case 3: hinge response

Figure 3.20: Moment-rotation of beam with RBS: (a) $\rho = 0.5$, $\chi = 0.05$, $\lambda = 0.6$, (b) $\rho = -0.5$, $\chi = 0.05$, $\lambda = 0.8$, (c) $\rho = -0.5$, $\chi = 0.1$, $\lambda = 0.6$

the two models give identical response. The rigid-plastic response at the plastic hinges are accurately represented by proposed beam model.

The following subsections present two case studies: a portal frame and a three-story frame. The structure in both examples have RBS in the beam interior. The objective is to showcase the effect of the hinge offset location and the strength reduction at the RBS on the structural response.

3.2.3.1 Example 1: Portal frame

The first example illustrates the effect of the plastic hinge offsets and the strength reduction on the sequence of yielding at a beam-column joint and its effect on the local and global response. For the purpose, a portal frame with height $H = 14$ ft and bay width $L = 20$ ft is used. The columns and girders are made of W21x111 and W24x104 wide flange section, respectively. The columns are subjected to an axial compression of $P_v = 160$ kips, which is 10% of the column axial plastic capacity N_p to represent the effect of gravity loading on the portal frame. Three RBS designs are considered: (i) $\lambda = 0.8, \chi = 0.1$, (ii) $\lambda = 0.7, \chi = 0.1$, (iii) $\lambda = 0.8, \chi = 0.05$, and compared to the reference design without RBS: $\lambda = 1, \chi = 0$. In

this example, the columns and girders are simulated by the proposed beam-column model. The element response is elasto-plastic. Figure 3.21 plots the base shear against the lateral drift, the left column response at the base and the top, and the girder response at the left end in a pushover analysis.

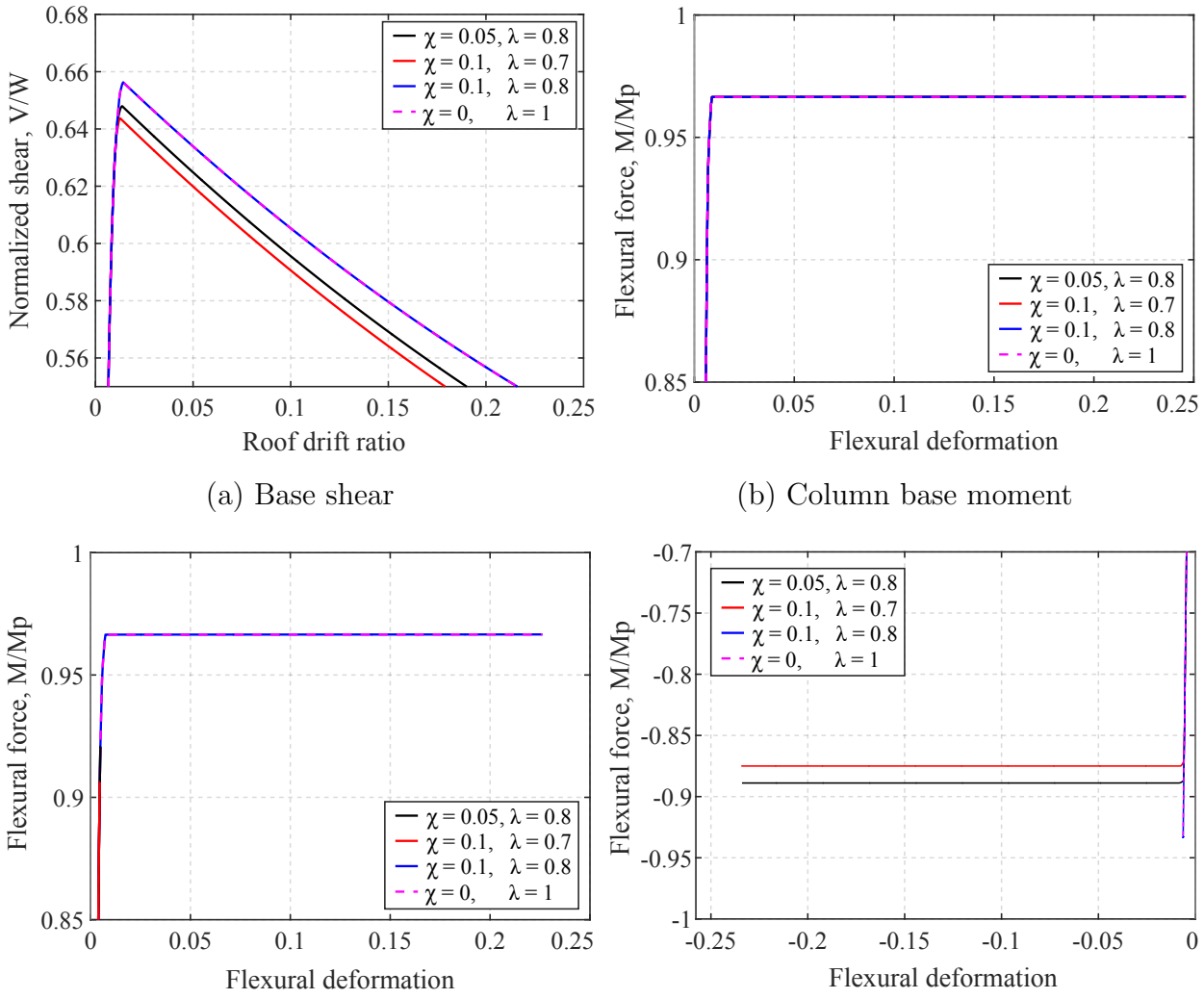

(a) Base shear

(b) Column base moment

(c) Column top moment

(d) Girder left moment

Figure 3.21: Effect of hinge offset on portal frame response: static response

Without the RBS, yielding occurs at the base and the top of the columns while the girder remains elastic. This results from the smaller capacity $M_{p,g}$ in the girder relative to the capacity $M_{p,c}$ in the column that is reduced due to the axial forces. Column yielding is typically undesirable and avoided in earthquake-resistant design. Figure 3.21 suggests that while the column base yields in all four cases, the response at the top and in the girder vary

with the RBS parameters. The response with $\chi = 0.1$, $\lambda = 0.8$, shown in blue in Figure 3.21, is identical to the reference response without RBS, that is, the columns yield while the girder is elastic. In the alternative RBS designs with $\chi = 0.1$, $\lambda = 0.7$ (in red), and with $\chi = 0.05$, $\lambda = 0.8$ (in black), the girder induces plastic rotations while the column tops remain elastic. The parameters are selected ensure the amplified moment at the girder end is below the capacity of the columns. These designs efficiently divert the inelastic behavior away from the beam-column interface. For the same RBS location, a lower RBS capacity reduces the moment at the beam ends, and in turns, the moment at the top of the columns and the lateral base shear. Moreover, for the same RBS capacity, a smaller displacement of the RBS from the column face lowers the amplified end moments, which in turns reduces the moment at the column tops and the lateral base shear. Therefore, the two cases $\chi = 0.1$, $\lambda = 0.7$ and $\chi = 0.05$, $\lambda = 0.8$ give a smaller base shear than the case $\chi = 0.1$, $\lambda = 0.8$.

3.2.3.2 Example 2: Collapse mechanism of 3-story frame

This example demonstrates the RBS connection as an effective design alternative to prevent a weak story mechanism and examines the effect of different RBS designs on the collapse mechanisms. A 3-story 1-bay frame with a fundamental period of 1.12 sec in Figure 3.22 is used for illustration. The frame is modeled with distributed plasticity elements for the columns and concentrated plasticity elements for the girders. Each column is represented by one forced-based element with four integration points along the column height to account for the axial-flexure interaction. Each section in the column is discretized into 9 layers, 2 in each flange and 5 in the web. Each girder is modeled by one series beam element. This example assumes an elastic-perfectly plastic behavior in the element response and neglects the effect of floor slabs on the member strength and stiffness as well as the shear deformations in the panel zones.

Columns and girders are of wide flange sections: W21x73 in the 1st and 2nd floor girders, W21x57 in the girder at the roof level, W24x84 in the 1st and 2nd story columns, and W24x76 in the 3rd story columns. Pushover analysis with a lateral load distribution proportional to the fundamental mode shape is performed to assess the structural performance. The structure forms a 1-story collapse mechanism at large roof drifts, as shown in Figure 3.23(a), with significant plastic deformations at the base of the 1st-story columns, in the 1st-floor girders, and especially, at the top end of the 1st-story columns.

The weak-story mechanism is highly undesirable and shall be avoided in design. To enhance the structural performance at collapse, several design alternatives are proposed. One approach is to modify the column design to utilize larger sections. Two such alternatives are considered for comparison: model MC1 uses W24x94 sections for the 1st story columns, while model MC2 uses W24x94 sections for both the 1st and the 2nd story columns. In both models, other members are the same as in the original design, which shall be referred as the reference model MR hereafter. The key design parameters of the models are summarized in Table 3.2. With larger column sections, the collapse behavior is improved, that is, model MC1 initiates a 2-story mechanism and model MC2 forms a full mechanism involving all

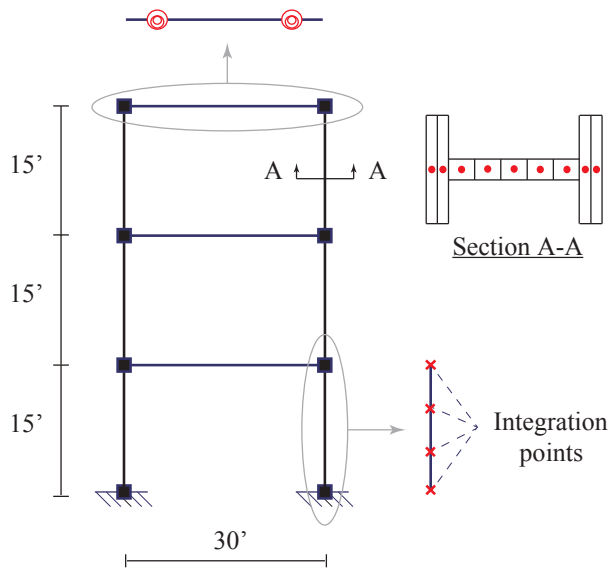

Figure 3.22: Structural model of 3-story moment frame

three stories. Figure 3.23 plots the 3-fold magnified deformed shape of models MR, MC1, MC2, respectively, at the instant of 20% reduction in the maximum base shear. Increasing the column capacity reduces the adverse effect of column hinging by accumulating more plastic deformations in the girders instead of the columns.

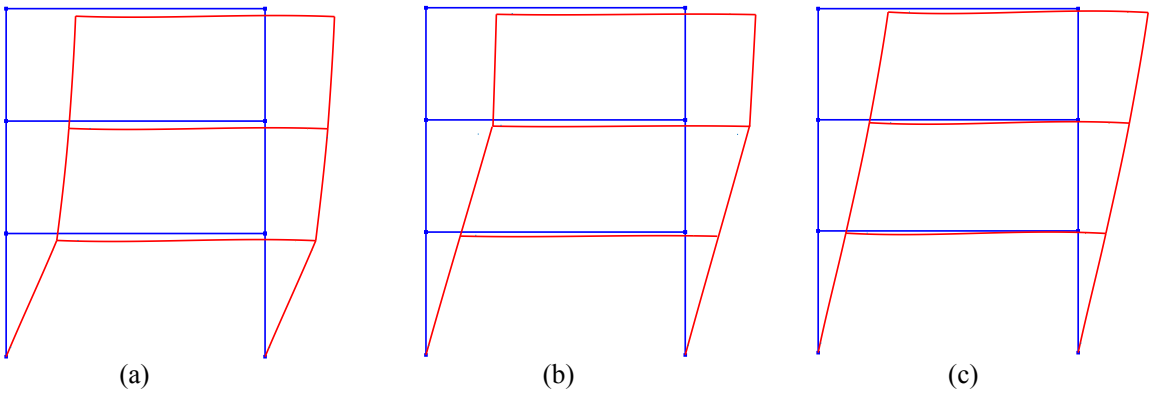

Figure 3.23: Collapse mechanisms of 3-story 1-bay moment frame: (a) 1-story, (b) 2-story, (c) full 3-story

Figure 3.24 compares the pushover response of the three models. As expected, models MC1 and MC2 show higher base shear than model MR due to the increased column strength. The collapse mechanism is reflected in the slope of the softening segment in the plot of base shear versus roof drift in Figure 3.24(a). Under the same gravity load, the geometric

stiffness contribution is the highest in the 1-story mechanism and the smallest in the full 3-story mechanism; therefore, at collapse model MR shows the steepest softening segment while model MC2 has the flattest softening slope. As expected, the softening slope in model MC1 and MC2 is approximately 2 and 3 times the slope in model MR, respectively. The different collapse mechanisms are also evident in the interstory drift distribution at 0.04 roof drift ratio in Figure 3.24(b).

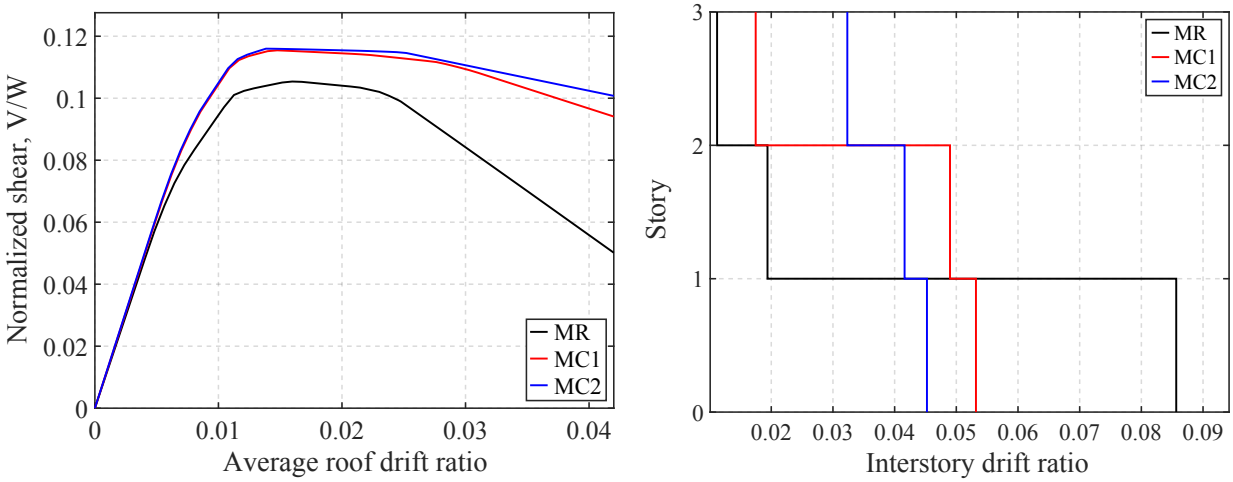

(a) Normalized base shear (b) Drift distribution

Figure 3.24: Response comparison of design alternatives

The design refinement reflects the widely-used 'strong column - weak beam' concept, which requires the capacity of the columns to exceed the girders at a beam-column joint to avoid excessive column hinging. The criteria enforces the ratio SCWB to be greater than unity:

$$SCWB = \frac{\sum M^*_{pc}}{\sum M^*_{pb}} \geq 1 \tag{3.46}$$

where $\sum M^*_{pc}$ is the sum of the projections of the nominal flexural strength of the columns above and below the joint to the beam centerline with a reduction for the axial force in the columns. $\sum M^*_{pb}$ is the sum of the projections of the expected flexural strength of the beams at the plastic hinge locations to the column centerline. Similar to the AISC recommendations, the nominal beam yield strength is amplified by $R_y = 1.5$ factor, which is the ratio of the expected yield stress to the specified minimum yield stress. In this case study, the SCWB ratio at a beam-column joint on the 1st story in models MR, MC1, MC2 are 1.30, 1.39, 1.47, respectively. The result suggests that the criteria SCWB >1 is not sufficient to prohibit the undesirable weak story collapse mechanisms.

Another approach to enhance the design of steel structures is to utilize reduced beam sections (RBS) in girders. Three alternative designs are considered with varying RBS location

χ and strength λ relative to the nominal strength of the original section. Model MO1 has $\chi = 0.08$ and $\lambda = 0.75$ while model MO2 has higher RBS strength capacity $\lambda = 0.8$ and model MO3 specifies a farther offset $\chi = 0.095$ from the beam-column interface. The key design parameters of the models are summarized in Table 3.2.

Figure 3.25 compares the pushover response of the three alternative designs with RBS and the reference model MR. All three models with RBS give smaller peak base shear than the reference model because of the strength reduction in the girders due to the RBS. The softening behavior suggests that models MR, MO2, and MO3 have the same collapse mechanism whereas model MO1 shows a different behavior. This observation is reinforced in the interstory drift distribution at 0.04 roof drift ratio. While models MR, MO2, and MO3 form a 1-story mechanism as evident in the excessive drift in the 1st-story relative to the upper levels, model MO3 indicates a full 3-story mechanism with a relatively regular drift distribution across the building height.

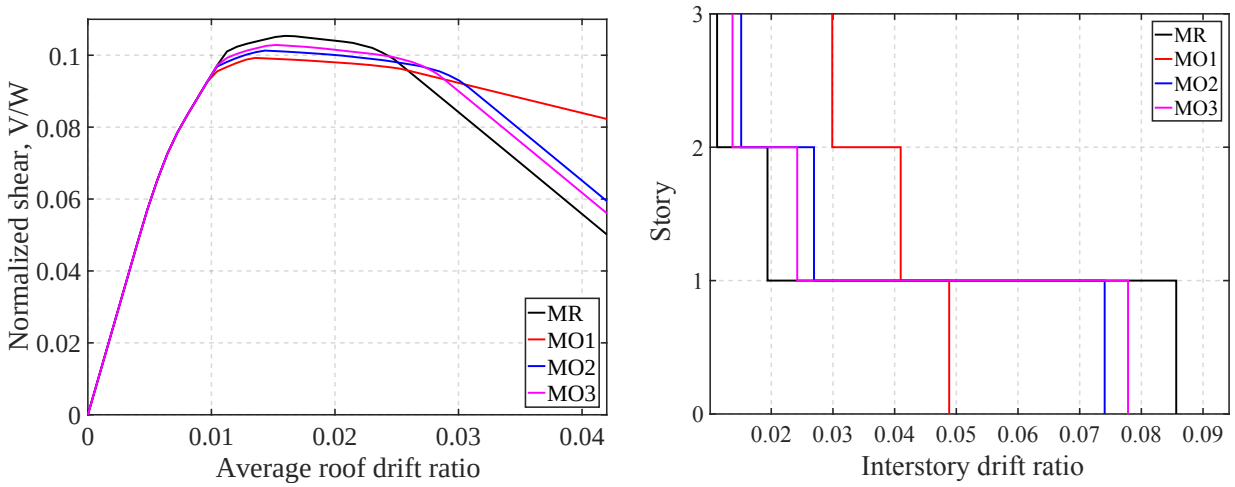

(a) Normalized base shear

(b) Drift distribution

Figure 3.25: Response comparison of RBS designs

Figure 3.26 plots the force-deformation response at the beam-column joint on the 1st story to illustrate the force redistribution in the two distinct collapse mechanisms. In models MR, MO2, MO3, the 1st-story column exhibits significant plastic deformations at the top end while the 1st-floor girder accumulates less. The two members show distinct behavior as the 1-story mechanism is triggered, in which the column continues to load inelastically whereas the girder unloads elastically. Less column plastic deformations are induced in models MO2 and MO3 than in model MR due to the smaller girder end moment, which attracts relatively more plastic deformations in the girder and less in the columns. On the other hand, in model MO1, the 1st story column remains elastic while significant plastic deformations are induced in the 1st floor girders. Plastic hinges only form in the girders and at the base of the 1st story columns, which gives rise to the full 3-story mechanism.

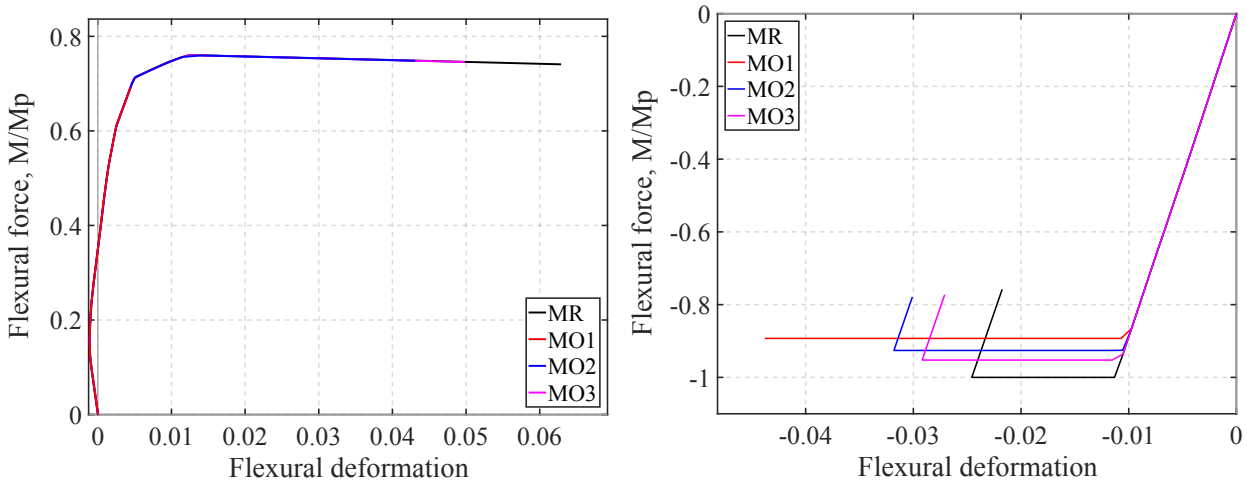

(a) 1st story column top

(b) 1st floor girder

Figure 3.26: Member response at the beam-column joint in the 1st story

The case study suggests that the RBS has a significant effect on the collapse behavior of steel moment frames. In this example, the RBS design in model MO1 is effective to avoid the undesirable weak story mechanism, while model MO2 and MO3 are not. The latter two not only fail to safeguard against the undesirable story mechanism but also weaken the structure due to the reduced strength at the RBS. The results lead to an important implication in frame design, that is, the RBS must be properly designed to avoid the large extrapolated moment from the RBS to the girder end that is still unable to prevent the excessive column plastic deformations.

Model	**1st story column**	**2nd story column**	**3rd story column**	λ_{RBS}	χ_{RBS}	**SCWB**	**Mechanism**
MR	W24x84	W24x84	W24x76	1	0	1.30	1-story
MC1	W24x94	W24x84	W24x76	1	0	1.39	2-story
MC2	W24x94	W24x94	W24x76	1	0	1.47	full
MO1	W24x84	W24x84	W24x76	0.75	0.08	1.30	full
MO2	W24x84	W24x84	W24x76	0.80	0.08	1.30	1-story
MO3	W24x84	W24x84	W24x76	0.75	0.095	1.30	1-story

Table 3.2: Design alternatives of 3-story frame

3.3 Damage-Plasticity Beam Element

This section adopts the 1d damage hysteretic model in Chapter 2 to the series beam element in the preceding sections to describe the strength and stiffness deterioration in the element behavior. The moment and rotation in the plastic hinges, $M_i - \theta_i$ at end i and $M_j - \theta_j$ at end j, are the work-conjugate variables that govern the damage accumulation, which are analogous to the force s and the deformation e in the 1d formulation.

Figure 3.27 illustrates the equilibrium and the compatibility conditions for the element response in the effective space and the true space. The effective response is represented by the black line and the true response is shown in red. In both configurations, under the same force q, the element end deformation v is the sum of the elastic deformation v_e and the plastic deformation v_p, in which the latter is defined as the permanent deformation upon complete elastic unloading. The damage variable d reduces the forces in both the elastic and the plastic components to enforce equilibrium $q = q_e = q_p$ at the element ends. While the elastic component unloads at a reduced stiffness than the initial elastic stiffness, the plastic component unloads vertically due to the rigid-plastic behavior.

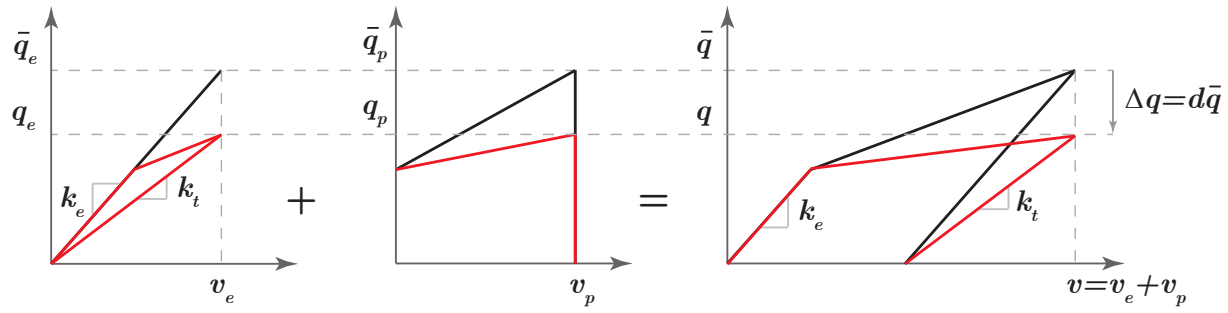

Figure 3.27: Equilibrium and compatibility relations of plastic-damage beam model

The following subsections describe the three parts of the element formulation in detail: (1) an undamaged response in the effective space, (2) a damage loading function, and (3) a damage evolution law; and highlight the key differences from the 1d damage model.

3.3.1 Effective response

The effective response describes the relation between the effective end forces $\bar{\mathbf{q}}$ to the end deformations $\mathbf{v}$. While any force-deformation relation $\bar{\mathbf{q}}$–$\mathbf{v}$ of a beam element can be used, this study adopts the series beam element with plastic hinge offsets in Section 3.1 to describe the constitutive relation in the effective space. The overscore symbol represents the variables in the effective space, for instance, the effective moments at the hinge locations are $\bar{\mathbf{M}} = \left[\bar{M}_i \;\; \bar{M}_j\right]^T$.

3.3.2 Damage loading function

The damage loading function describes the relation between the variables in the effective space with the energy dissipation that controls the damage evolution. In the proposed element model, the bending moment at the plastic hinges, $\bar{M}_i$ and $\bar{M}_j$, and the plastic hinge rotations, θ_i and θ_j, are the work-conjugate variables that govern the damage accumulation analogous to the force $\bar{s}$ and the deformation e in the 1d damage model. To accommodate the asymmetrical response under positive and negative moments, the model isolates the positive effective moments $\bar{\mathbf{M}}^+$ and the negative effective moments $\bar{\mathbf{M}}^-$:

$$\bar{\mathbf{M}}^{\pm} = \frac{\bar{\mathbf{M}} \pm |\bar{\mathbf{M}}|}{2} \tag{3.47}$$

where $|\bar{\mathbf{M}}| = \left[|\bar{M}_i| \;\; |\bar{M}_j|\right]^T$ represents the magnitude of the effective hinge moments, $\bar{\mathbf{M}}^+ = \left[\bar{M}_i^+ \;\; \bar{M}_j^+\right]^T$ and $\bar{\mathbf{M}}^- = \left[\bar{M}_i^- \;\; \bar{M}_j^-\right]^T$ are the positive and the negative components of the effective hinge moments, respectively. The positive effective moment at hinge i, $\bar{M}_i^+$, is equal to $\bar{M}_i$ for $\bar{M}_i > 0$ and zero otherwise. Similarly, the negative effective moment at hinge i, $\bar{M}_i^-$, is equal to $\bar{M}_i$ for $\bar{M}_i < 0$ and zero otherwise.

The damage loading function is expressed in terms of two variables $\boldsymbol{\psi}^+$ and $\boldsymbol{\psi}^-$ representing the energy dissipation under positive effective moments and negative effective moments, respectively.

$$\boldsymbol{\psi}^+ = \begin{pmatrix} \psi_i^+ \\ \psi_j^+ \end{pmatrix} \qquad \boldsymbol{\psi}^- = \begin{pmatrix} \psi_i^- \\ \psi_j^- \end{pmatrix} \tag{3.48}$$

The energy variables are defined by the integral of the product of $\bar{\mathbf{M}}^+$ or $\bar{\mathbf{M}}^-$ with the rotation increment $d\boldsymbol{\theta}$. Equations (3.49)–(3.50) give the expressions of the positive energy ψ_i^+ and ψ_j^+, and the negative energy ψ_i^- and ψ_j^-, where the subscript m represents end i and j. Similar to the 1d damage formulation, the energy variables $\boldsymbol{\psi}$ depend on the cyclic degradation parameters $C_{wc,m}^{\pm}$ and the damage coupling coefficients $C_{cd,m}^{\pm}$:

$$\psi_m^+ = \int C_{wc,m}^+ \bar{M}_m^+ d\theta_m + C_{cd,m}^+ \int C_{wc,m}^- \bar{M}_m^- d\theta_m \tag{3.49}$$

$$\psi_m^- = \int C_{wc,m}^- \bar{M}_m^- d\theta_m + C_{cd,m}^- \int C_{wc,m}^+ \bar{M}_m^+ d\theta_m \tag{3.50}$$

The coefficient C_{wc} serves as a weight of the energy dissipation increment for differentiating the effect of the rotations exceeding the previous extreme values from the effect of the rotations within the extreme values. Denoting with $\theta_{m,\min}$ the minimum and $\theta_{m,\max}$ the maximum previous hinge rotation, the weight $C_{wc,m}$ is defined as:

$$C_{wc,m} = \begin{cases} 1 & \text{if } \theta_m < \theta_{m,\min} \;\text{ or }\; \theta_m > \theta_{m,\max} \\ 0 \le C_{wc,m} \le 1 & \text{if } \theta_{m,\min} \le \theta_m \le \theta_{m,\max} \end{cases} \tag{3.51}$$

In Equations (3.49)–(3.50), $C^{\pm}_{cd,m}$ are the damage coupling parameters with $C^{+}_{cd,m} \geq 0$ weighing the contribution of the energy dissipation under negative moments on the energy variable ψ^{+}_{m}, and $C^{-}_{cd,m} \geq 0$ weighing the contribution of the energy dissipation under positive moments on the energy variable ψ^{-}_{m}.

It is noteworthy that in the element formulation, the energy variables $\boldsymbol{\psi}^{\pm}$ in Equations (3.49)–(3.50) depend on the plastic hinge rotation $\boldsymbol{\theta}$, and in turns, the plastic deformation $\mathbf{v}_p$. This is different than the 1d damage formulation in which the energy dissipation ψ is depend on the total deformation e.

The model defines the energy thresholds $\tilde{\psi}^{\pm}_{m}$:

$$\tilde{\psi}^{\pm}_{m}(t) = \max \psi^{\pm}(\tau) \qquad t_0 \leq \tau < t \tag{3.52}$$

where τ is a pseudo-time variable and t is the current pseudo-time.

Four damage loading functions g^{+}_{i}, g^{-}_{i}, g^{+}_{j}, g^{-}_{j} compare the energy variables $\psi^{\pm}$ in Equations (3.49)–(3.50) with the corresponding thresholds $\tilde{\psi}^{\pm}_{m}$ in Equation (3.52). Damage grows when the energy exceeds the threshold value.

$$g^{\pm}_{m} = \psi^{\pm}_{m} - \tilde{\psi}^{\pm}_{m}, \qquad m = i, j \tag{3.53}$$

3.3.3 Damage evolution law

The element model computes four damage variables for the positive and negative response at the two plastic hinges:

$$\mathbf{d} = \begin{bmatrix} \mathbf{d}^{+} & \mathbf{d}^{-} \end{bmatrix} = \begin{bmatrix} d^{+}_{i} & d^{-}_{i} \\ d^{+}_{j} & d^{-}_{j} \end{bmatrix} \tag{3.54}$$

The damage evolution law relates the damage variables $\mathbf{d}$ to the energy dissipation variables $\boldsymbol{\psi}^{\pm}$ in Equations (3.49)–(3.50). The evolution law requires a definition of the energy thresholds $\bar{\psi}^{\pm}_{d0}$ corresponding to an undamaged state and the energy limits $\bar{\psi}^{\pm}_{d1}$ corresponding to a complete loss of strength. These energies are expressed as multiples of the yield energy $\boldsymbol{\psi}_y$ of a cantilever beam:

$$\psi_{y,m} = \frac{M^2_{p,m} L}{6EI} \tag{3.55}$$

where M_p is the plastic flexural capacity, EI is the element flexural stiffness, and L is the element length.

With C_{d0} and C_{d1} denoting the damage threshold coefficient and the damage limit coefficient, the energy thresholds $\bar{\psi}^{\pm}_{d0}$ and the energy limits $\bar{\psi}^{\pm}_{d1}$ are given as:

$$\psi^{\pm}_{d0,m} = C^{\pm}_{d0,m} \psi_{y,m} \tag{3.56}$$

$$\psi^{\pm}_{d1,m} = C^{\pm}_{d1,m} \psi_{y,m} \tag{3.57}$$

It is convenient to normalize the energy variables $\boldsymbol{\psi}^{\pm}$ in terms of the energy thresholds and energy limits:

$$\hat{\psi}^{\pm}_{m} = \frac{\psi^{\pm}_{m} - \psi^{\pm}_{d0,m}}{\psi^{\pm}_{d1,m} - \psi^{\pm}_{d0,m}} \tag{3.58}$$

The cumulative distribution function (CDF) of the beta distribution is used to evaluate the element damage variables $\mathbf{d}$:

$$d_m^{\pm} = F_B\left(\hat{\psi}_m^{\pm}, \beta_{1,m}^{\pm}, \beta_{2,m}^{\pm}\right) \tag{3.59}$$

where F_B denotes the CDF of the beta distribution and β_1 and β_2 are the parameters of the CDF. Similar to the 1d damage formulation, to better identify the effect of the parameters on the damage evolution, the damage evolution law introduces two damage evolution parameters d_{p1} and d_{p2} defined as the ratio and the smaller of the two original parameters β_1 and β_2.

The true moments $\mathbf{M}$ result from linear combinations of the positive and negative effective moments, $\bar{\mathbf{M}}^+$ and $\bar{\mathbf{M}}^-$ after multiplication with the respective damage variables:

$$M_m = \left(1 - d_m^+\right)\bar{M}_m^+ + \left(1 - d_m^+\right)\bar{M}_m^- \qquad m = i, j \tag{3.60}$$

The true flexural end forces $\mathbf{q}_f = [q_i, q_j]$ are extrapolated from the moments at the hinge locations to the element ends:

$$\mathbf{q}_f = \mathbf{b}_{pf}^{-1}\mathbf{M} \tag{3.61}$$

where $\mathbf{b}_{pf}$ denotes a subset of the moment interpolation matrix $\mathbf{b}_p$ without the axial terms. Note that the damage-plasticity beam formulation assumes that the axial response is linear elastic and uncoupled from the flexural response. Consequently, the axial force q_a in the true space is equal to the effective axial force:

$$q_a = \bar{q}_a = \frac{EA}{L}v_a \tag{3.62}$$

Finally, the tangent stiffness $\mathbf{k}_t$ is the derivative of the true end forces $\mathbf{q}_n$ with respect to the end deformations $\mathbf{v}_n$. Table 3.3 summarizes the state determination of the damage-plasticity beam model.

3.4 Examples of Damage-Plasticity Beam Element

3.4.1 Simply-supported beam

This example extends the case study of the simply-supported beam under general bending in Section 3.2.2 by introducing damage to the element behavior. The objectives are two-fold: (1) to showcase the ability of plastic hinge offsets to describe the coupling of plasticity and damage in the element response, and (2) to compare the proposed damage-plasticity beam element to a distributed plasticity element with a degrading stress-strain relation in the material response. The example compares the moment-rotation relation using the following three models to simulate the beam: (1) Model CP1: a damage-plasticity beam element without plastic hinge offset $\chi = 0$, (2) Model CP2: a damage-plasticity beam element with plastic hinge offset, and (3) Model DP: a distributed plasticity element with force-based formulation.

Given: end deformations $\mathbf{v}_n$ and history variables at step $n-1$
Required: state variables at step n

1. State determination in effective space:
Procedure for the series beam model in Table 3.1
Outputs: $\bar{\mathbf{q}}_n$, $\mathbf{v}_{p,n}$, $\boldsymbol{\alpha}_n$, $\mathbf{q}_{b,n}$, $\bar{\mathbf{M}}$, $\boldsymbol{\theta}$
2. Decomposition of $\bar{\mathbf{M}}_n$ into $\bar{\mathbf{M}}_n^+$ and $\bar{\mathbf{M}}_n^-$ in (3.47)
3. Energy variables $\psi_{i,n}^{\pm}$ and $\psi_{j,n}^{\pm}$ (3.49)–(3.50)
4. Damage loading functions:
Evaluate the energy threshold $\tilde{\psi}_{i,n}^{\pm}$ and $\tilde{\psi}_{j,n}^{\pm}$ in (3.52)
Evaluate damage loading functions $g_i^{\pm}$ and $g_j^{\pm}$ in (3.53)
5. Check of damage for each of the four damage loading functions:
IF $g \leq 0$, THEN
Damage unloading, go to 6a
ELSE
Damage loading, go to 6b
6a. Damage unloading:
Update $d_{i,n}^{\pm} = d_{i,n-1}^{\pm}$ and $d_{j,n}^{\pm} = d_{j,n-1}^{\pm}$
Go to 7
6b. Damage loading:
Compute normalized energy $\hat{\psi}_i^{\pm}$ and $\hat{\psi}_j^{\pm}$ in (3.58)
Evaluate $d_{i,n}^{\pm}$ and $d_{j,n}^{\pm}$ in (3.59)
Go to 7
7. End forces and tangent stiffness:
Update the hinge moments $\mathbf{M}_n$ from $\mathbf{M}_n^{\pm}$ and $\mathbf{d}_n^{\pm}$ in (3.60)
Update the end forces $\mathbf{q}_n$ in (3.61)–(3.62)
Evaluate the tangent stiffness $\mathbf{k}_t$

Table 3.3: State determination algorithm of damage-plasticity beam model

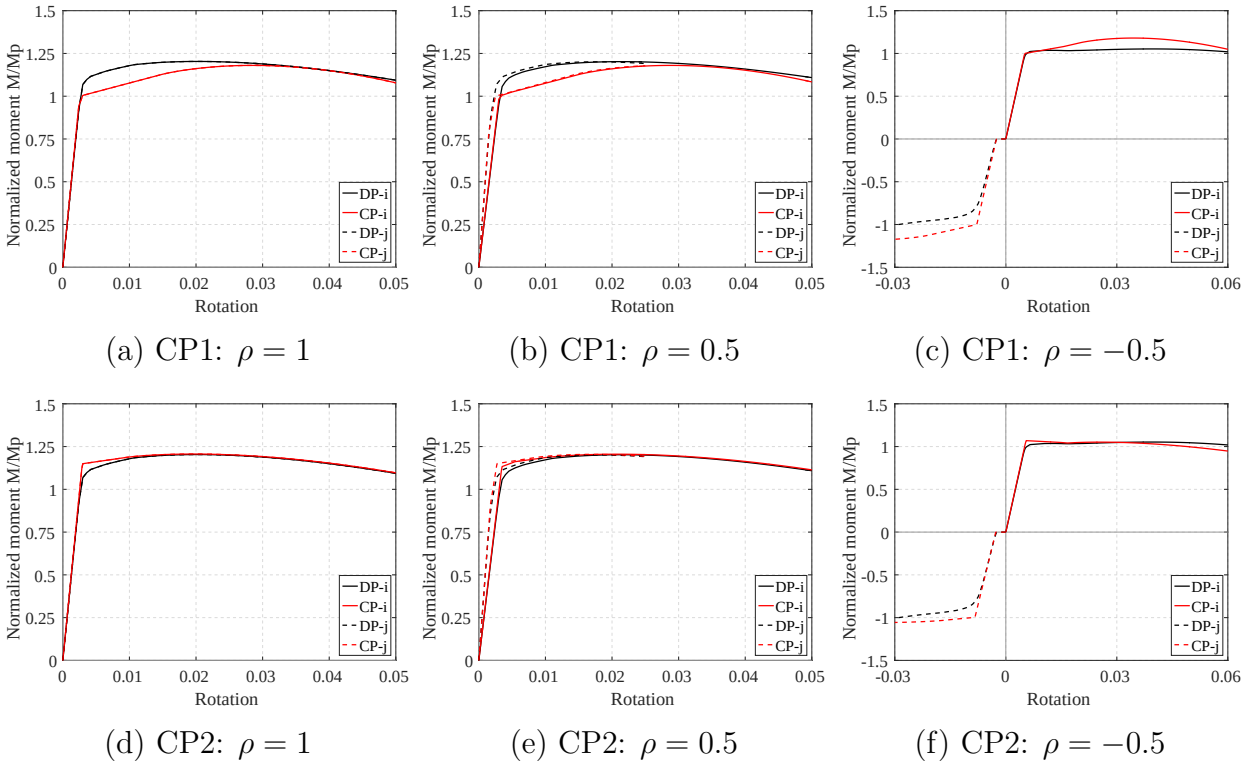

(a) CP1: $\rho = 1$ (b) CP1: $\rho = 0.5$ (c) CP1: $\rho = -0.5$

(d) CP2: $\rho = 1$ (e) CP2: $\rho = 0.5$ (f) CP2: $\rho = -0.5$

Figure 3.28: Degrading moment-rotation relation of simply-supported beam under monotonic loading

Model DP uses a bilinear plasticity model with linear hardening for the effective response and the following damage parameters to describe the deterioration: $C_{d0} = 10$, $C_{d1} = [500; 300]$, $[d_{p1}, d_{p2}] = [2.5, 1.5]$, $C_{wc} = 0.12$, $C_{cd} = 0.3$. The limit coefficients $C_{d1}^{-} < C_{d1}^{+}$ captures the lower ductility of under compressive stresses to account for the more severe strength deterioration due to buckling. In model CP1, the damage is described by the following parameters: $C_{d0} = 5$, $C_{d1} = 120$, $[d_{p1}, d_{p2}] = [2.5, 1.5]$, $C_{wc} = 0.12$, $C_{cd} = 0.3$. In reference to Figure 3.16, the hardening parameters in model CP1 are calibrated for the target rotation $v_{target} = 0.03$ under $\rho = 1$. In model CP2, a plastic hinge offset $\chi = 0.065$ is specified at both element ends. The following damage parameters describe the strength and stiffness degradation: $C_{d0} = 5$, $C_{d1} = 160$, $[d_{p1}, d_{p2}] = [2.5, 1.5]$, $C_{wc} = 0.12$, $C_{cd} = 0.3$.

Figure 3.28 shows the degrading moment-rotation under monotonic rotation histories. Both models CP1 and CP2 describe with sufficient accuracy the strength softening under various bending ratios. In model CP1, the agreement in the response with model DP is better under antisymmetric bending. However, as expected, model CP1 underestimates the strength at rotations smaller than the target v_{target} under antisymmetric bending. The plastic hinge offsets in model CP2 couple the response at the two ends and allow the model to capture more accurately the variation in the yield strength and the strength deterioration.

Not only does the softening range is closely captured, the response prior to softening is described more consistently. The improvement in the response simulation under symmetric bending $\rho = -0.5$ is significant with the plastic hinge offsets.

To conclude the comparison study, the following compares the degrading moment-rotation with and without the plastic hinge offsets under cyclic loading. It is evident in Figure 3.29 that the plastic hinge offsets and the damage parameters capture well the response under both antisymmetric bending and symmetric bending scenarios.

3.4.2 Portal frame

The objectives of this example are two-fold: (1) to evaluate the local and the global response of a simple structure with and without strength deterioration in the girder, and (2) to investigate the effect of cyclic degradation on the force-deformation relation and the damage evolution in the element response. This example examines the dynamic response of a steel portal frame with height $H = 14$ ft and bay width $L = 20$ ft in Figure 3.13 under the LA30 ground motion. Following the 'strong column-weak beam' concept, damage is assumed to accumulate in the girder while the columns have an elasto-plastic behavior. To account for the axial-flexure interaction, each column is modeled with a force-based distributed beam-column element with 4 integration points along the length and 9 fibers in each cross section: 2 in each flange and 5 in the web. The girder is modeled with the proposed damage-plasticity beam element. To investigate the effect of element damage and cyclic degradation, three models with different girder response are examined:

- *Model M0*: The girder response is elasto-plastic without strength deterioration.
- *Model M1*: The damage parameters are $C_{d0} = 0$, $C_{d1} = 120$, $[d_{p1}, d_{p2}] = [2.5, 1.5]$, $C_{wc} = 0.1$, $C_{cd} = 0.3$. The threshold coefficient $C_{d0} = 0$ implies damage initiation at the onset of yielding. The cyclic degradation coefficient C_{wc} and the coupling coefficient C_{cd} indicate a relatively mild level of strength and stiffness deterioration due to cyclic loading.
- *Model M2*: Same as model M1, but the parameters that govern the cyclic degradation are higher: $C_{wc} = 0.3$ and $C_{cd} = 0.6$ to describe more severe deterioration in the girder response.

It is evident in Figure 3.30 that the element damage has a significant impact on the dynamic behavior of the portal frame. The time history of the lateral displacement in Figure 3.30(a) shows higher displacement amplification with more severe strength and stiffness deterioration in the girder. While model M0 and M1 result in residual displacements in the negative direction, model M2 induces residual displacements in the opposite direction.

Figures 3.30(b)-(d) highlight the effect of cyclic degradation on the local response in the girder. Figure 3.30(b) plots the moment-rotation relation in model M0 and model M1 to

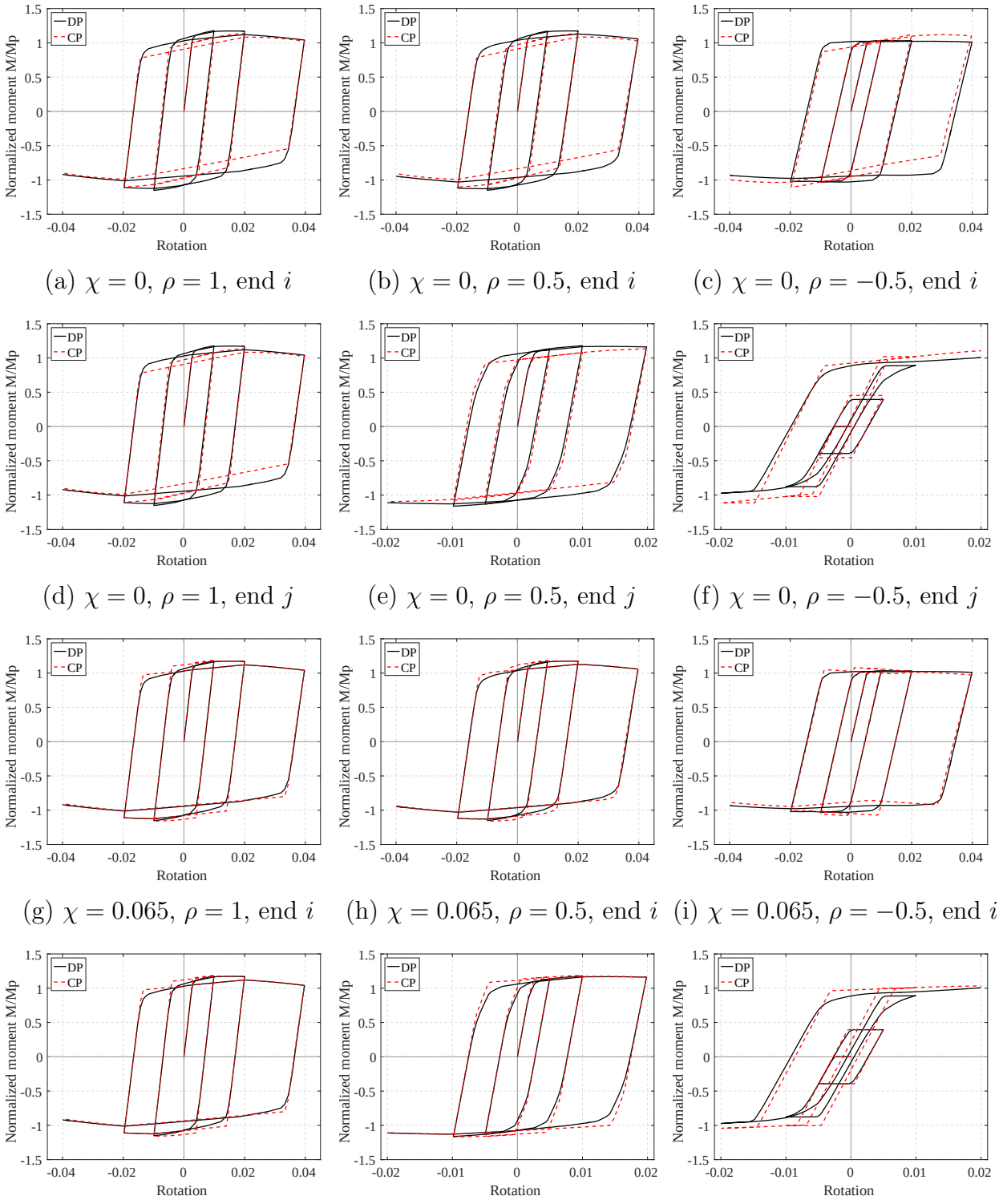

(a) $\chi = 0$, $\rho = 1$, end i (b) $\chi = 0$, $\rho = 0.5$, end i (c) $\chi = 0$, $\rho = -0.5$, end i

(d) $\chi = 0$, $\rho = 1$, end j (e) $\chi = 0$, $\rho = 0.5$, end j (f) $\chi = 0$, $\rho = -0.5$, end j

(g) $\chi = 0.065$, $\rho = 1$, end i (h) $\chi = 0.065$, $\rho = 0.5$, end i (i) $\chi = 0.065$, $\rho = -0.5$, end i

(j) $\chi = 0.065$, $\rho = 1$, end j (k) $\chi = 0.065$, $\rho = 0.5$, end j (l) $\chi = 0.065$, $\rho = -0.5$, end j

Figure 3.29: Degrading moment-rotation relation of simply-supported beam under cyclic loading

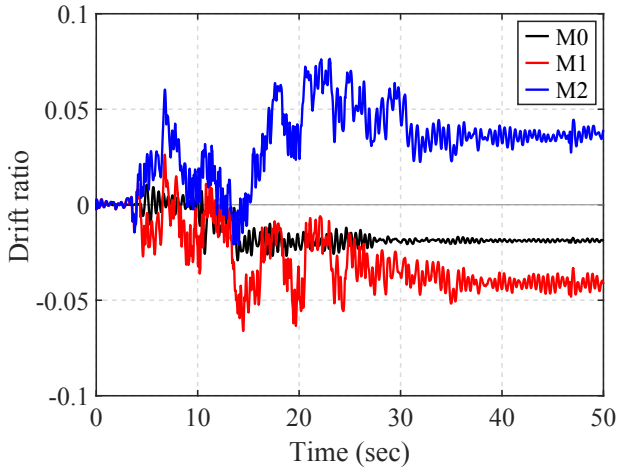

(a) Lateral displacement time history

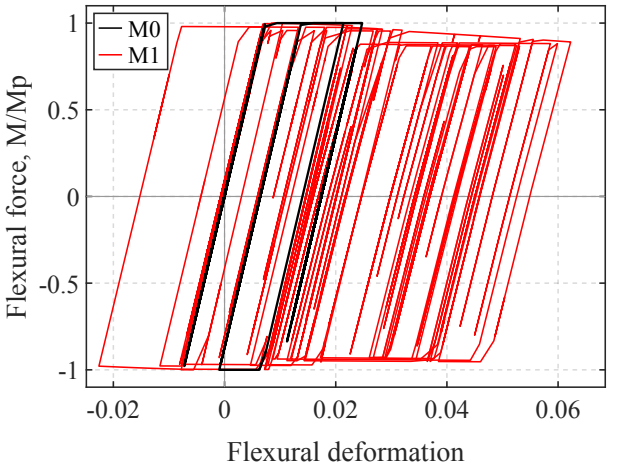

(b) Girder response with and without damage

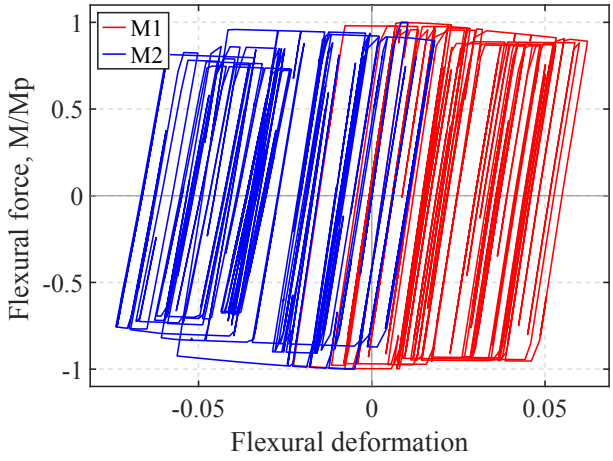

(c) Girder response with cyclic degradation

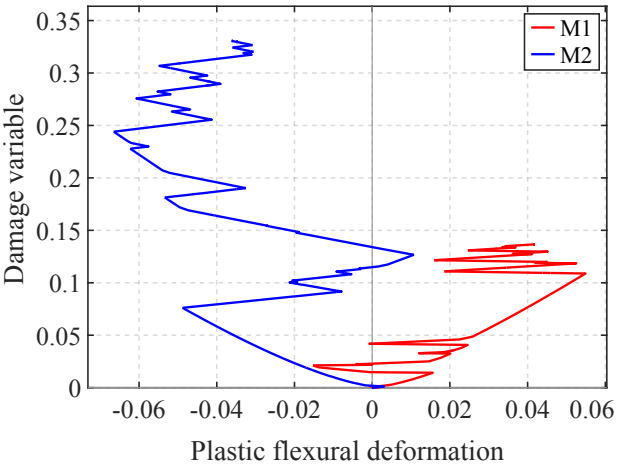

(d) Girder damage evolution

Figure 3.30: Dynamic response of portal frame

study the effect of element damage. Model M1 shows a wider range of rotation in the hysteresis loops, which leads to more excessive lateral drift in the negative direction. Figure 3.30(c) compares the moment-rotation relation in model M1 and model M2 to examine the effect of cyclic degradation. As expected from the lateral displacement time history, the rotations in the two cases depart to opposite directions. Higher values of C_{wc} and C_{cd} lead to a more pronounced strength reduction especially in the follower cycles, which are numerous in this ground motion. Figure 3.30(d) compares the evolution of a damage variable at the girder left end in model M1 and model M2, which is taken as the higher of the two variables d_i^+ and d_i^-. In model M2, the higher values of the damage parameters result in 35% strength

loss in contrast to 15% in model M1.

Figures 3.31–3.32 isolate several load cycles in model M1 and model M2 to correlate the strength reduction in the force-deformation relation to the evolution of the damage variable. Note that the damage variable in Figures 3.31–3.32 are plotted against the *total* rotation instead of the *plastic* rotation in Figure 3.30(d).

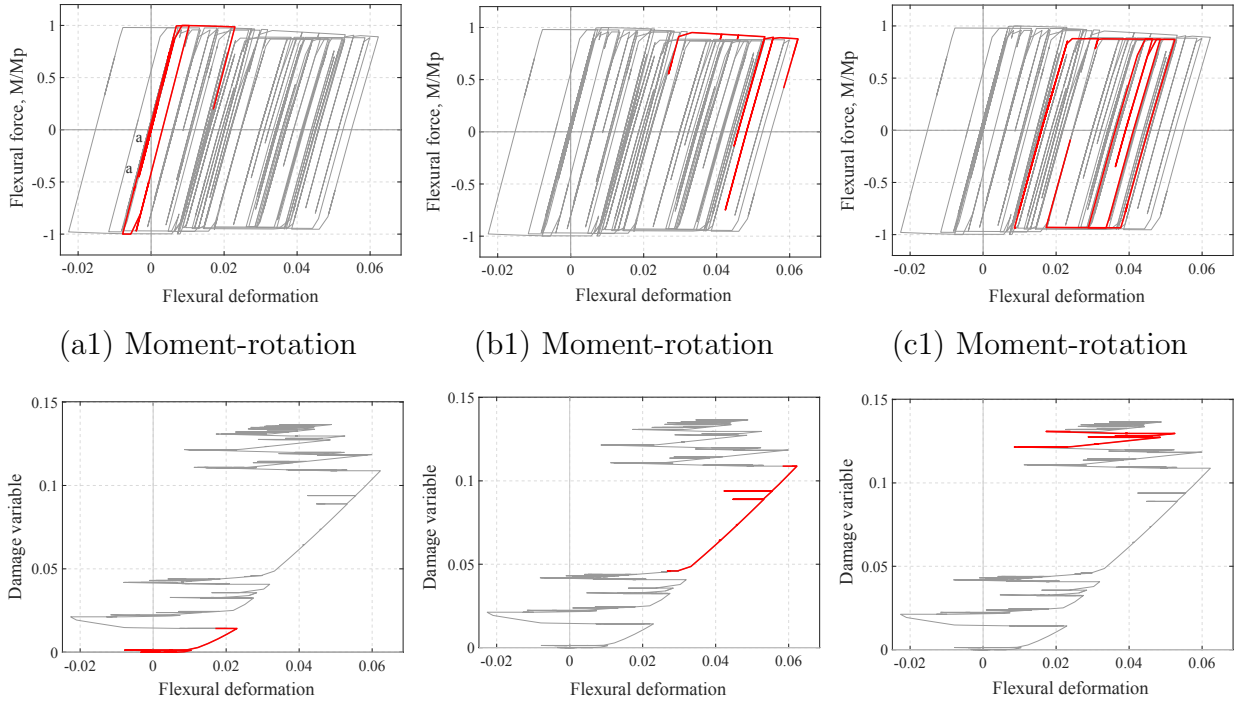

(a1) Moment-rotation (b1) Moment-rotation (c1) Moment-rotation

(a2) Damage evolution (b2) Damage evolution (c2) Damage evolution

Figure 3.31: Girder moment-rotation and damage evolution in model M1

Figure 3.31 presents the response in model M1. Figure 3.31(a) shows the response from the beginning of the load history up to the load cycle with the largest rotation increment in the positive direction. The girder first undergoes several cycles while remaning elastic then yields and initiates damage. The large rotation increment in the primary cycle exceeds the previous maximum rotation and results in a rapid increase in the damage variable. Figure 3.31(b) highlights the primary cycle with the largest rotation increment. Since the previous maximum rotation of approximately 0.032 is exceeded, the damage evolution is relatively rapid. During this period, the girder unloads and reloads several times without yielding and accumulating damage under negative rotation, which is reflected in the horizontal segments in the damage evolution plot. Figure 3.31(c) illustrates the follower cycles near the end of the load history. With $C_{wc} = 0.1$, only a portion of the energy dissipation increment contributes to the damage growth, and consequently, the damage accumulation is relatively gradual.

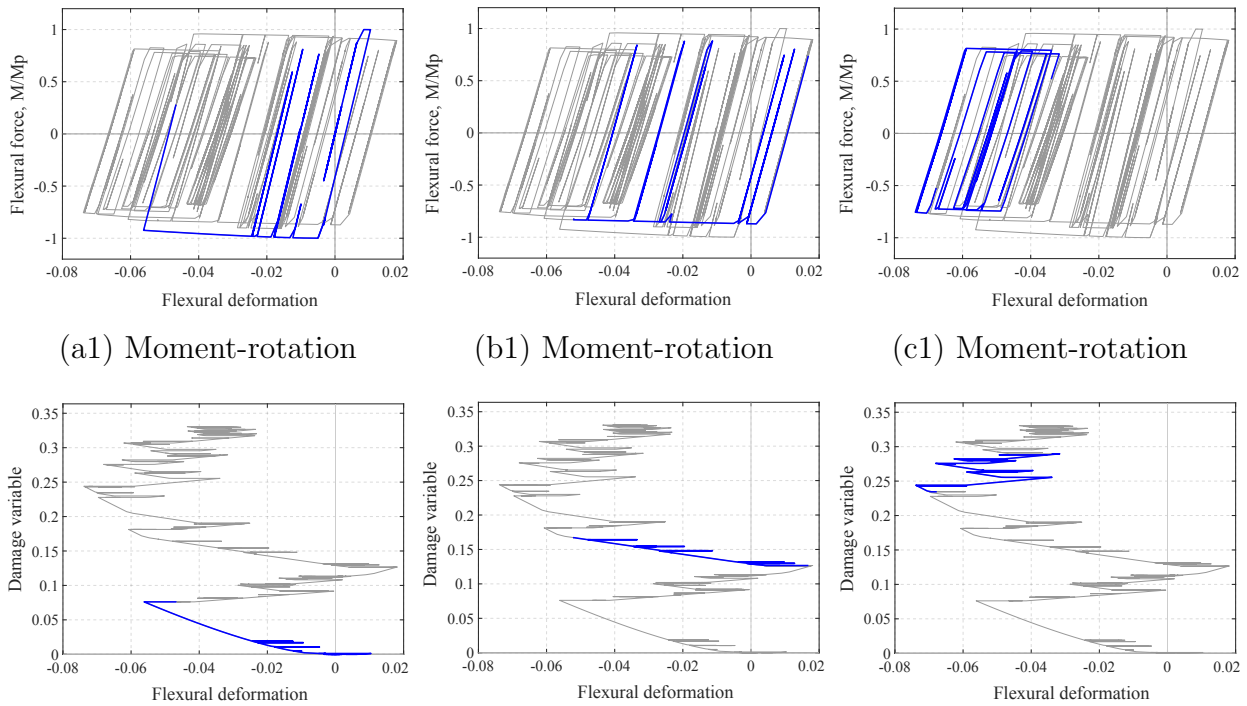

(a1) Moment-rotation (b1) Moment-rotation (c1) Moment-rotation

(a2) Damage evolution (b2) Damage evolution (c2) Damage evolution

Figure 3.32: Girder moment-rotation and damage evolution in model M2

Figure 3.32 presents the moment-rotation and the damage evolution in model M2. Figure 3.32(a) shows the response from the beginning of the load history to the load cycle with the largest rotation increment in the negative direction. The large rotation increment in the primary cycle results in a rapid damage growth. In contrast to model M1 with mild cyclic degradation, the element damage accumulates relatively earlier and induces a significant displacement increment in the opposite direction. Figure 3.32(b) highlights the follower half cycles in which the previous maximum rotation magnitude is not exceeded. The girder is reloading in the negative rotation direction with a few instances of unloading and reloading *without* accumulating further damage. The deterioration rate is quite rapid in these follower cycles because of the high cyclic degradation parameter C_{wc}. Figure 3.32(c) illustrates the follower half cycles near the end of the load history. In contrast to the load cycles in Figure 3.32(b), damage accumulates from the rotation reversals in both loading directions.

In summary, based on the comparison of the global and the local response, it is important to account for the strength and stiffness deterioration in the element behavior. The cyclic degradation proves to have a significant impact on the dynamic behavior of structures, especially in this case study with a ground motion record with numerous cycles. Moreover, the damage-plasticity model captures well the distinct deterioration rates in primary and follower half cycles.

3.5 Validation Studies

A database with more than 50 experiments of steel wide-flange components is assembled for the validation of the proposed damage-plasticity beam model. The geometry of specimens in the database satisfies the following conditions:

$$5 \leq b_f/2t_f \leq 8 \qquad 30 \leq h/t_w \leq 55 \qquad 35 \leq L_b/r_y \leq 120 \tag{3.63}$$

where b_f is the flange width, t_f is the flange thickness, h is the fillet-to-fillet web depth, t_w is the web thickness, L_b is the unbraced length, and r_y is the radius of gyration about the weak axis of the cross section.

A calibration study is performed to showcase the capabilities of the model to capture the measured degrading response as well as to correlate the model's damage parameters with physical properties of specimens, such as the geometry and material properties. Based on the response comparison, a multivariate regression analysis is performed to derive empirical functions for the damage parameters. These functions establish a set of guidelines for the parameter selection.

The section first illustrates the simulation of a sample steel specimen from the database. Then, a multivariate regression analysis is presented to derive the empirical formulae for the parameters. The study concludes with a parameter sensitivity analysis to identify the extent to which each parameter affects the numerical solutions.

3.5.1 Simulation of steel components

The experimental campaign by Yu et al. [111] provides measurements of the hysteretic behavior of two identical steel beam-to-column subassemblages under different deformation histories, referred to as experiment LS1 and LS3. The load protocol of specimen LS1 is a standard symmetrical cyclic history consisting of groups of displacement cycles with constant amplitudes from one cycle to the next with gradually increasing average amplitude of the group as loading progresses. The deformation history of specimen LS3 consists of several small cycles with variable and gradually increasing amplitudes followed by a few large displacement pulses. The LS1 deformation history represents the effect of far-field ground motions while the LS3 protocol simulates the effect of near-fault ground motions on the hysteretic behavior of steel components.

Figure 3.33 shows the numerical results for the steel assembly under the two load histories. The series beam model in Section 3.1 describes the force-deformation relation in the effective space with the kinematic hardening ratio $H_{kr} = 0.015$ and isotropic hardening ratio $H_{ir} = 0.002$. Although the plastic hinge offset could capture better the yield strength in the early cycles, no hinge offset is specified, $\chi = 0$, for simplicity. In this simulation the CDF of the beta distribution in Section 3.3.3 is used. The damage parameters are $C_{d0} = 5$, $C_{d1} = 130$, $d_{p1} = 3$, $d_{p2} = 1.5$, $C_{wc} = 0.14$, $C_{cd} = 0.4$. Same parameters are specified for the positive and negative response to account for the symmetrical degrading behavior of the steel specimen.

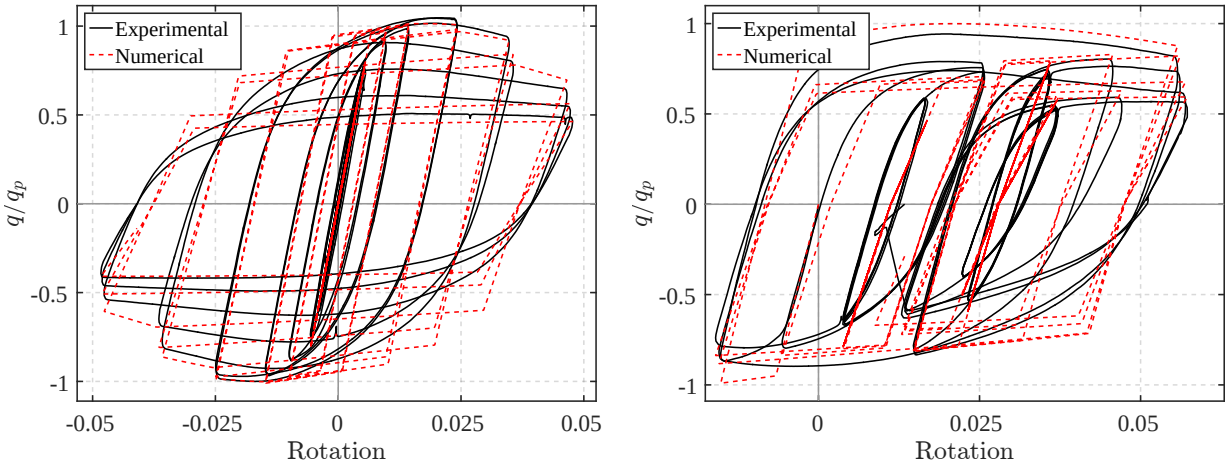

(a) Specimen LS1 (b) Specimen LS3

Figure 3.33: Moment-rotation relation of steel specimens LS1 and LS3 [111]

The damage threshold coefficient $C_{d0} > 0$ indicates damage initiation after significant plastic deformations in the steel specimens. The numerical solution simulates well the cyclic hardening behavior in the early cycles following yielding of the specimen. The limit coefficient $C_{d1} = 130$ appears to capture sufficiently the ductility capacity of the specimen in both load cases. The damage evolution parameter $d_{p1} > 1$ in combination with $d_{p2} > 1$ describe consistently the deterioration rate in both specimens. These values for d_{p1} and d_{p2} appear to be typical for steel specimens with ductile respone and high energy dissipation capacity. The cyclic coefficient C_{wc} and the couplding coefficient C_{cd} are able to capture the strength and stiffness degradation due to repeated load reversals.

One limitation in the response comparison is the inadequate representation of the Bauschinger effect in the reloading behavior. A possible solution is to use a different element model in the effective space to account for the gradual smooth transition from the elastic to plastic behavior, such as to adopt the generalized plasticity [7, 48]; however, this is not pursued further here. Nonetheless, the model simulates consistently the gradual strength and stiffness degradation of the specimen under both loading scenarios and the agreement with the experimental results is acceptable.

3.5.2 Regression analysis for parameter identification

The simulations of the specimens in the database indicate an evident correlation between the model's damage parameters and the section compactness and the specimen slendernes. These properties are reflected in: (1) the flange width-to-thickness ratio $b_f/2t_f$, (2) the web depth-to-thickness ratio h/t_w, and (3) the slenderness ratio L_b/r_y. Figure 3.34 illustrates the variation in the limit coefficient C_{d1} with the section compactness $b_f/2t_f$ and h/t_w and the

slenderness ratio L_b/r_y. The ductility capacity governed by the limit coefficient C_{d1} shows the strongest correlation with the slenderness of the components.

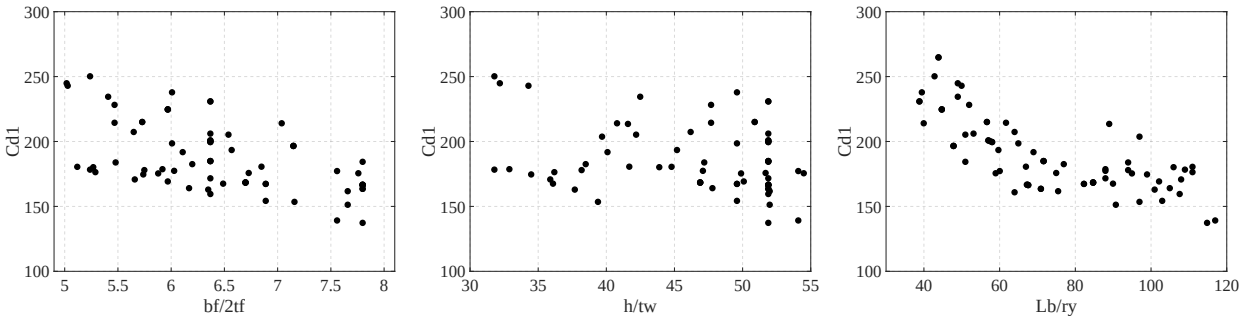

(a) C_{d1} vs. $b_f/2t_f$ (b) C_{d1} vs. h/t_w (c) C_{d1} vs. L_b/r_y

Figure 3.34: Variation in the limit coefficient C_{d1} with the section compactness and member slender

The value of a damage parameter can be evaluated empirically using the folowing expression, where X represents the parameter C_{d0}, C_{d1}, d_{p1}, d_{p2}, C_{wc}, C_{cd}.

$$X = \alpha_0 . \left(\frac{b_f}{2t_f}\right)^{\alpha_1} . \left(\frac{h}{t_w}\right)^{\alpha_2} . \left(\frac{L_b}{r_y}\right)^{\alpha_3} \tag{3.64}$$

The objective is to identify the coefficients α_0, α_1, α_2, α_3 to best fit the value of parameter X obtained from the simulations. Taking the natural logarithm of both sides, Equation (3.64) can be rewritten in a standard form of a linear multivariate regression problem:

$$\ln X = \ln \alpha_0 + \alpha_1 \ln\left(\frac{b_f}{2t_f}\right) + \alpha_2 \left(\frac{h}{t_w}\right) + \alpha_3 \left(\frac{L_b}{r_y}\right) \tag{3.65}$$

Table 3.4 lists the coefficients of the multivariate linear regression for the damage parameters.

Parameter	$\boldsymbol{\alpha_0}$	$\boldsymbol{\alpha_1}$	$\boldsymbol{\alpha_2}$	$\boldsymbol{\alpha_3}$
C_{d0}	37.44	0.2439	-0.3799	-0.0149
C_{d1}	2640	-0.6246	0.0122	-0.3631
C_{wc}	0.0166	0.0104	0.0723	0.4190
C_{cd}	0.0818	-0.1156	0.1328	0.3044
d_{p1}	2.092	0.0114	0.1321	-0.0485
d_{p2}	1.306	-0.0518	-0.0770	0.1148

Table 3.4: Regression coefficients for parameter calibration

3.5.3 Parameter sensitivity

For each damage parameter X, define the error ρ_X as the relative difference between the predicted value X_p using Equation (3.64) and the 'exact' value X_e from the simulation:

$$\rho_X = \frac{(X_p - X_e)}{X_e} \tag{3.66}$$

then the minimum value $\rho_{X,min}$ and the maximum $\rho_{X,max}$ give the boundary for the error in the prediction of parameter X.

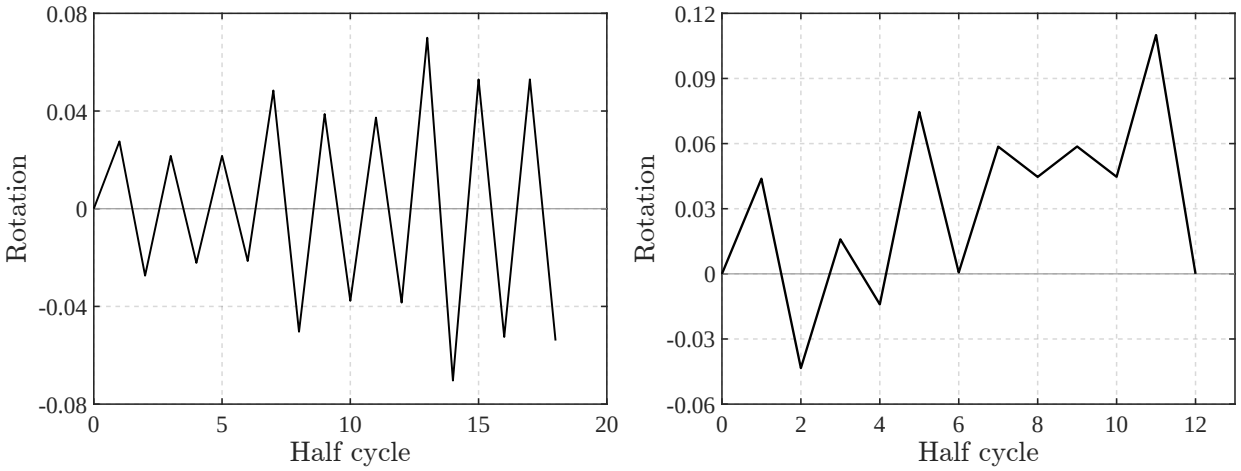

(a) CUREE (b) NF

Figure 3.35: Cyclic load protocols for cantilever beam

To evaluate the sensitivity of the numerical solution to the damage parameters, the proposed damage-plasticity beam model simulates the force-deformation relation of a steel W30x99 cantilever beam subjected to two different cyclic load patterns: the CUREE protocol and the NF protocol [50]. The CUREE protocol consists of groups of displacement cycles with gradually increasing average amplitude as the loading progresses. The NF protocol consists of several cycles of small but ever increasing displacement amplitude followed by very few large displacement pulses of increasing amplitude. The former simulates the effect of far-field ground motions and the latter represents the effect of near-fault ground motions.

In each load scenario, the numerical solution that uses the regression expression in Equation (3.64) for the parameter identification is selected as the reference response. For each parameter, while the remaining parameters are fixed, the numerical solution is reevaluated at $X_{\min} = (1 + \rho_{X,min})X_r$ and $X_{\max} = (1 + \rho_{X,max})X_r$, where X_r is the parameter value in the reference solution. These account for the uncertainty in the parameter estimation and provide an upper bound and a lower bound for the numerical response. Figure 3.36 shows the

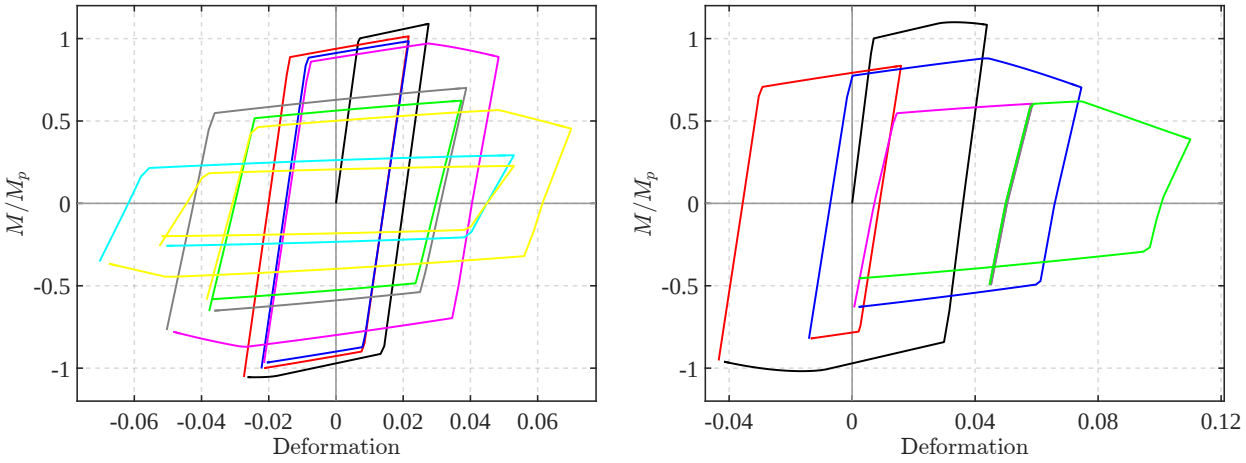

(a) CUREE (b) NF

Figure 3.36: Reference cyclic response under different loading histories

reference force-deformation relation in the two load scenarios and Figures 3.37–3.38 present the numerical solutions evaluated at different parameter values.

The change in the damage variable $d = \max(d^+, d^-)$ at the end of the load history is selected to quantify the effect of the parameters on the numerical solutions. Note that while other measures can be used for the comparison, this study makes use of the damage variable d because: (i) the damage variable is closely related to the energy dissipation, which is a common damage measure in performance-based design, (ii) the damage variable is readily available from the model state determination. The error ϵ_{min} is defined as the relative difference in the damage variable d at $X_{\min}$ and the error ϵ_{max} corresponds to $X_{\max}$.

$$\epsilon_{\min} = \frac{d_{\min} - d_r}{d_r} \qquad \epsilon_{\max} = \frac{d_{\max} - d_r}{d_r} \tag{3.67}$$

where $d_{\min}$ and $d_{\max}$ correspond to the damage variable d in the solution at $X_{\min}$ and $X_{\max}$, respectively, and d_r represents the damage variable d in the reference case. A positive ϵ overestimates the damage variable d and predicts more severe strength and stiffness deterioration in the response. A smaller magnitude of ϵ indicates that the response is less sensitive to the variation in the parameter value.

Table 3.5 summarizes the relative errors in the two load patterns. In each load scenario, the response sensitivity to the parameters is ranked based on the range of error $\Delta\epsilon = |\epsilon_{\max} - \epsilon_{\min}|$. The response is most sensitive to the parameter of rank '1' and least sensitive to the parameter of rank '6'.

In both load scenarios, the numerical solution is most sensitive to the limit coefficient C_{d1}. It is noteworthy that the excessive error in the damage variable of almost +25% in the NF load pattern corresponds to a $\rho_{\min} = +30\%$ overestimation in the value of C_{d1}. However,

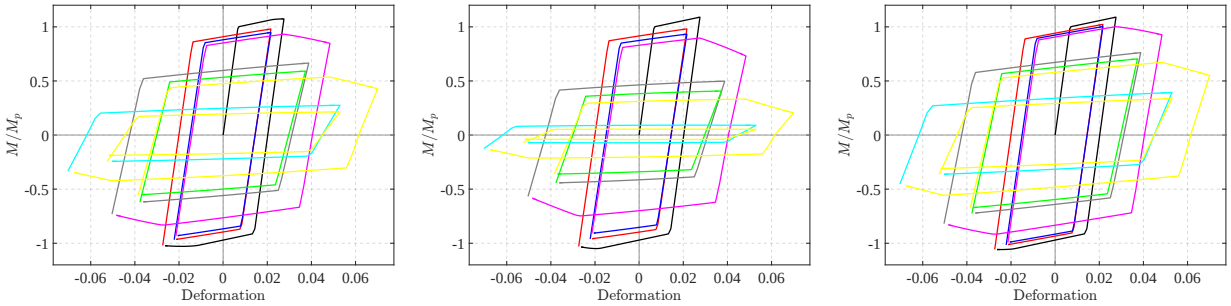

(a1) $0.7C_{d0}$ (b1) $0.7C_{d1}$ (c1) $0.7C_{wc}$

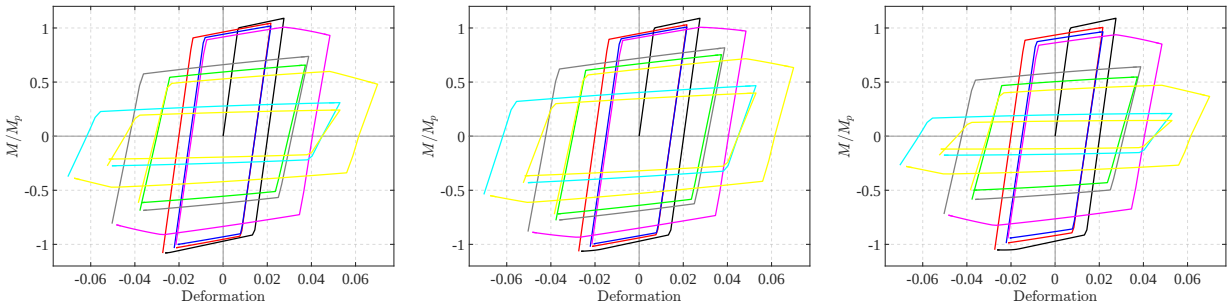

(a2) $1.3C_{d0}$ (b2) $1.3C_{d1}$ (c2) $1.3C_{wc}$

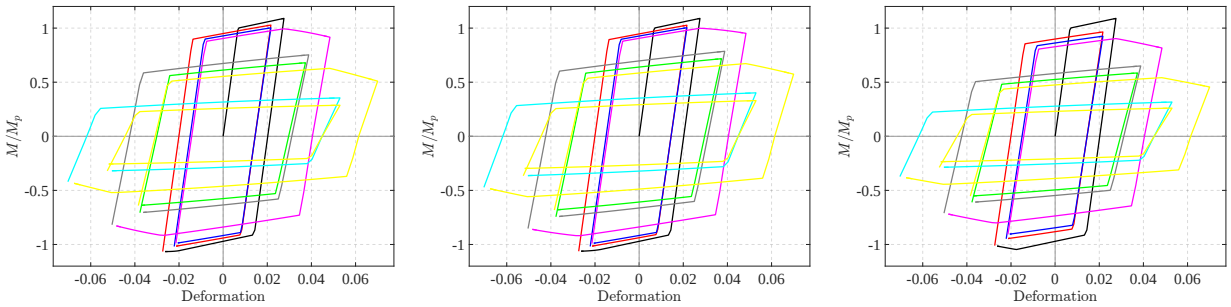

(d1) $0.7C_{cd}$ (e1) $0.8d_{p1}$ (f1) $0.7d_{p2}$

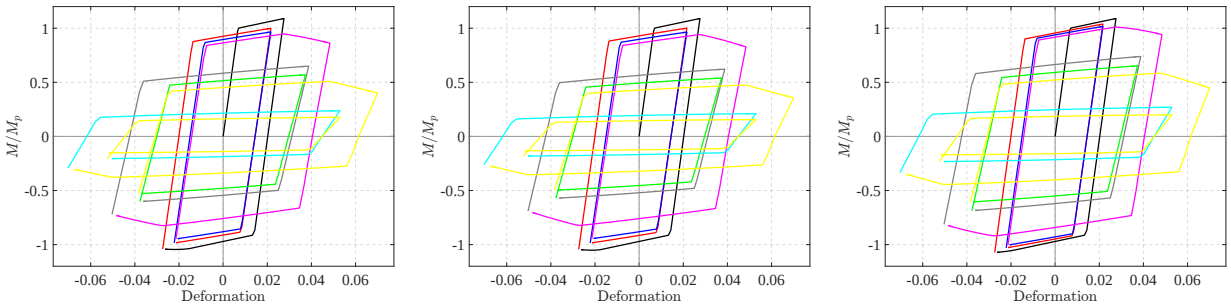

(d2) $1.3C_{cd}$ (e2) $1.2d_{p1}$ (f2) $1.3d_{p2}$

Figure 3.37: Sensitivity analysis: CUREE loading

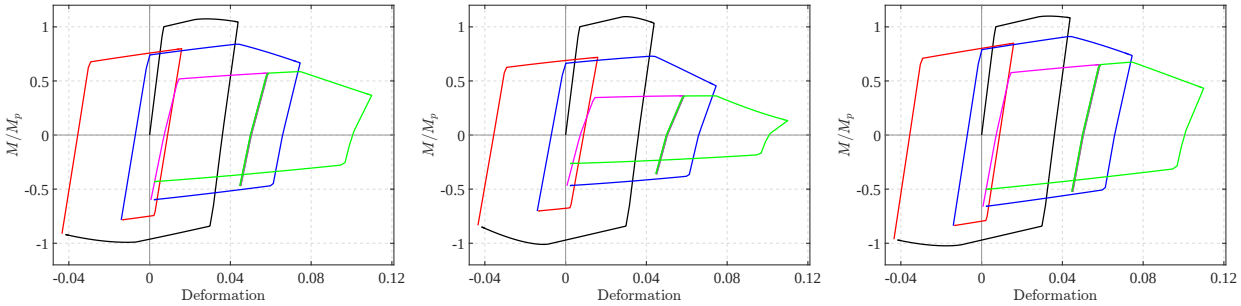

(a1) $0.7C_{d0}$ (b1) $0.7C_{d1}$ (c1) $0.7C_{wc}$

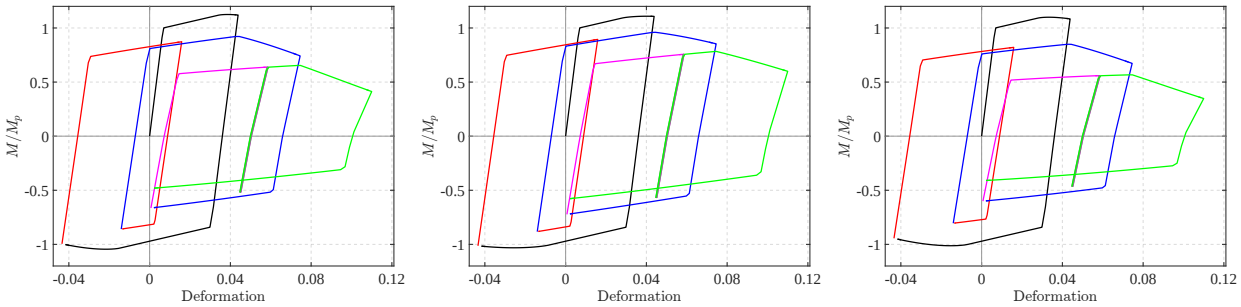

(a2) $1.3C_{d0}$ (b2) $1.3C_{d1}$ (c2) $1.3C_{wc}$

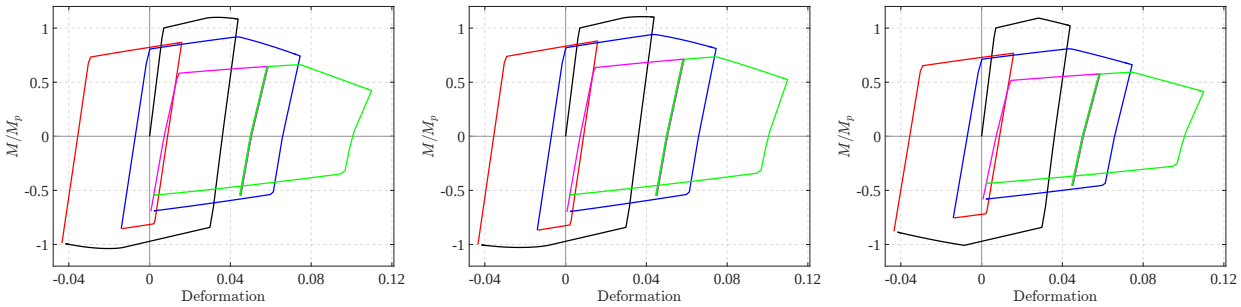

(d1) $0.7C_{cd}$ (e1) $0.8d_{p1}$ (f1) $0.7d_{p2}$

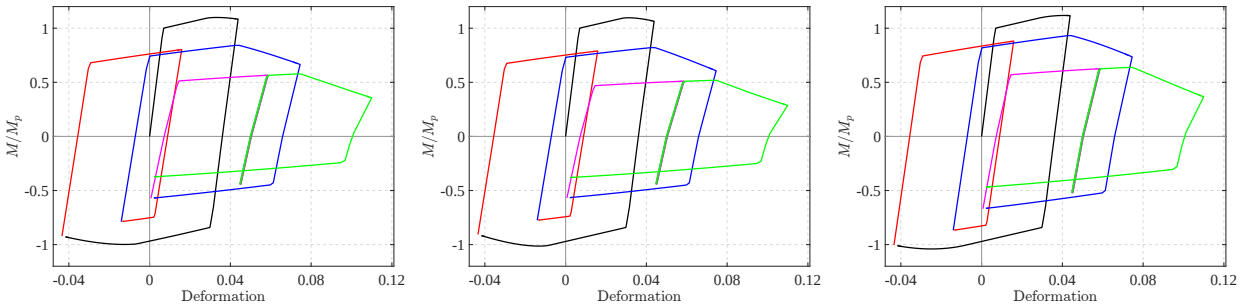

(d2) $1.3C_{cd}$ (e2) $1.2d_{p1}$ (f2) $1.3d_{p2}$

Figure 3.38: Sensitivity analysis: NF loading

Parameter	CUREE			NF		
	ϵ_{min}	ϵ_{max}	Ranking	ϵ_{min}	ϵ_{max}	Ranking
C_{d0}	+1.15%	-1.25%	6	+1.95%	-2.08%	6
C_{d1}	+15.48%	-16.77%	1	+23.14%	-19.57%	1
C_{wc}	-11.11%	+8.01%	2	-4.54%	+4.17%	3
C_{cd}	-5.72%	+4.77%	4	-3.64%	+3.40%	4
d_{p1}	-9.79%	+6.67%	3	-12.38%	+9.28%	2
d_{p2}	-3.58%	+2.94%	5	-2.51%	+2.35%	5

Table 3.5: Sensitivity ranking of damage parameters

only 4 among more than 50 specimens yield an error ρ between $\pm 20\%$ and $\pm 30\%$ while the others are within $\pm 20\%$ and give the maximum error ϵ of approximately 15%. This still indicates that the model is most sensitive to C_{d1} but the error in the prediction is far more reasonable.

The ranking of the damage evolution parameter d_{p1} and the cyclic degradation parameter C_{wc} are switched in the two load patterns. The error $\Delta\epsilon$ for parameter d_{p1} is relatively high in both load cases whereas the error $\Delta\epsilon$ for parameter C_{wc} is more significant in the CUREE protocol than in the NF protocol. Effect of the displacement history on the cyclic degradation is evident in the ranking of the cyclic degradation parameter C_{wc}. Cyclic degradation is significant in the CUREE protocol due to the numerous cycles with complete load reversals in contrast to the NF protocal with a displacement history that biases to one direction and consists of many incomplete cycles with little damage accumulation.

The model is least sensitive to the damage threshold coefficient C_{d0} and followed by the second damage evolution parameter d_{p2}. The effect of the damage threshold C_{d0} is mainly in the early cycles up to the onset of strength softening and less pronounced in the subsequent cycles. The negligible variation in the damage variable suggests that it is sufficient to specify constant values for C_{d0} and d_{p2} so as to reduce the number of parameters to be calibrated.

3.6 Damage Evolution with Brittle Failure

3.6.1 Formulation

To account for the sudden strength and stiffness deterioration in the event of brittle failure, the damage evolution law in Section 2.7 is adopted. The damage evolution function is shown in Figure 2.26. The damage evolution law introduces two energy variables: $\psi_f^{\pm}$ and $\psi_u^{\pm}$ that satisfy the constraint $\psi_{d0} \leq \psi_f^{\pm} < \psi_u^{\pm} \leq \psi_{d1}$. $\psi_f^{\pm}$ is the energy at which fracture takes place and $\psi_u^{\pm}$ is the ultimate energy at complete strength loss. The energy variables can be normalized to give the condition $0 \leq \hat{\psi}_f < \hat{\psi}_u \leq 1$. Different values can be specified for the variables under positive and negative moments at end i and end j, and for brevity the

superscript $\pm$ and the subscript i and j are dropped. The damage variables $d^{\pm}$ are evaluated from a composite function in Equation (2.16).

3.6.2 Validation studies

The section presents four simulations of steel cantilever beam specimens that exhibit brittle damage at large inelastic deformations. The damage-plasticity beam element with the damage evolution that accommodates the brittle damage is used in all simulations. Table 3.6 lists the damage parameters in each case, including the threshold coefficient C_{d0}, the limit coefficient C_{d1}, the evolution parameters d_{p1} and d_{p2}, the cyclic degradation coefficient C_{wc}, the damage coupling coefficient C_{cd}, the normalized fracture energy $\hat{\psi}_f$, and the normalized ultimate energy $\hat{\psi}_u$.

Parameter	**Popov, EERC-3**	**Uang, DC3**	**Ricles, 1E**	**Engelhardt, 3B**
C_{d0}	8	7	5	7
C_{d1}	110	200	140	170
C_{wc}	0.10	0.15	0.15	0.13
C_{cd}	0.40	0.40	0.50	0.40
d_{p1}	3	3	3	3
d_{p2}	1.5	1.5	1.5	1.5
$\hat{\psi}_f$	0.15	0.11	0.28	0.27
$\hat{\psi}_u$	0.20	0.12	0.33	0.30

Table 3.6: Parameters for the simulations of steel beams with brittle damage

Figure 3.39(a) shows the measured moment-rotation of the specimen EERC-3 from the experimental campaign by Popov [74]. The specimen is made of a W18x50 steel cantilever beam with a pre-Northridge connection. Figure 3.39(b) shows the measured moment-rotation of the steel specimen DC3 from the experiments by Uang [31] of a W27x194 beam section. Figure 3.39(c) shows the response of the specimen 1E from the experimental campaign by Ricles [84] with a W36x150 beam section. Figure 3.39(d) shows the response of the specimen 3B from the experiments by Engelhardt [25] with a W36x150 beam section and weld connection.

The proposed model simulates quite accurately the strength degradation pre- and post-fracture in the specimens. The first two specimen show negligible damage prior to the onset of fracture whereas the latter two specimens show a gradual strength and stiffness degradation before the onset of severe strength deterioration in the last cycle. The relatively low fracture energy parameter $\hat{\psi}_f$ in the first two specimen captures the drastic strength reduction at a lower normalized energy level with limited previous accumulated damage.

The specimens represent two distinct types of failure mechanisms observed in steel components under cyclic loading [51]. The first mechanism is related to crack propagation at

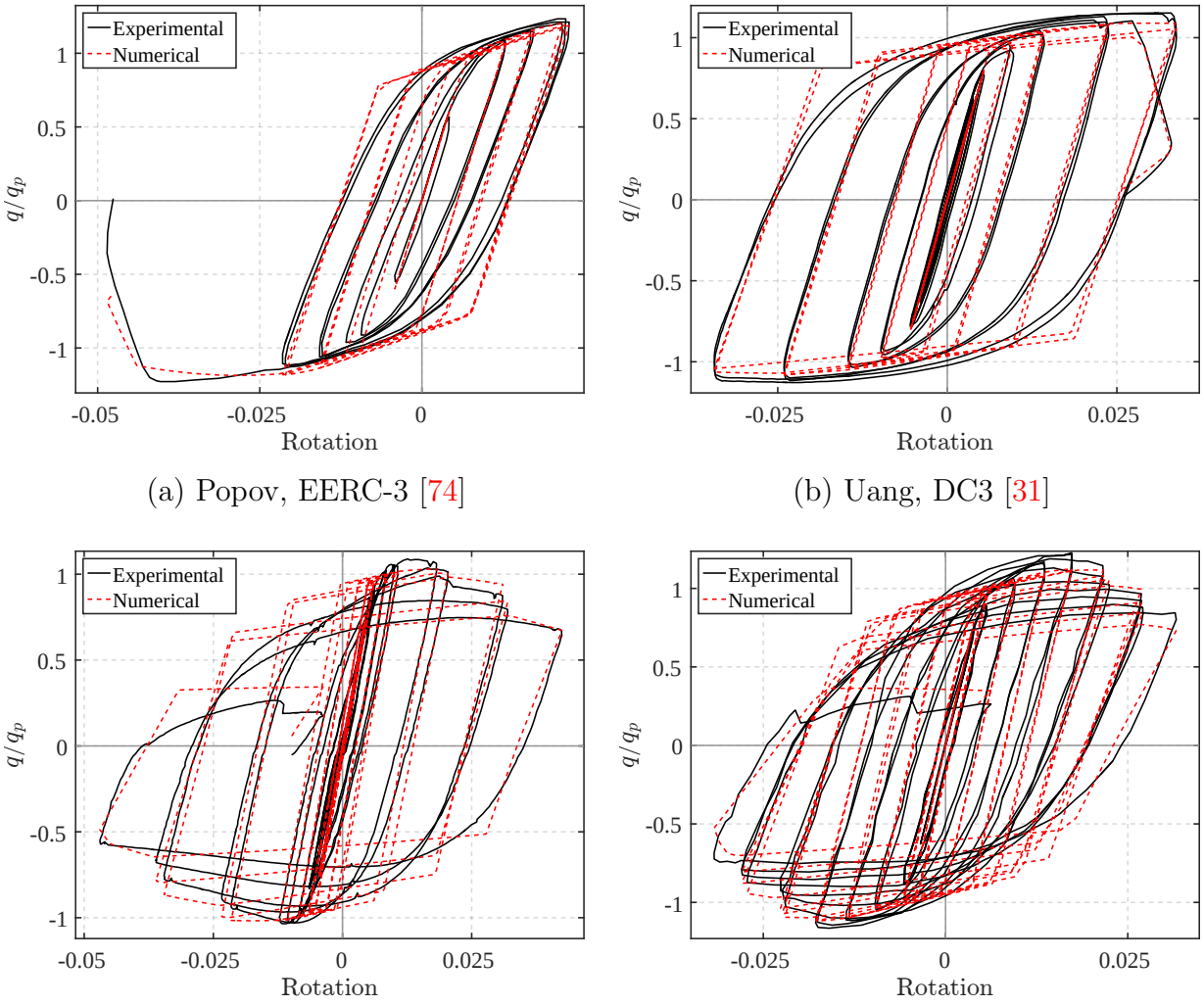

(a) Popov, EERC-3 [74]

(b) Uang, DC3 [31]

(c) Ricles, 1E [84]

(d) Engelhardt, 3B [25]

Figure 3.39: Moment-rotation relation of steel specimens with brittle failure

weldments, in which little deterioration is induced for a number of cycles in the beginning, then as the crack approaches its critical size, the specimens show rapid strength reduction. The second mechanism typically involves local buckling and leads to more gradual deterioration prior to the brittle failure. As evident in the response simulation of the two specimens in Figure 3.39, the composite evolution function accommodates well both types of degrading behavior.

Chapter 4

Damage-Plasticity Column Element

This chapter extends the 1d hysteretic damage model in Chapter 2 to formulate a new column element based on damage-plasticity for the response simulation and damage assessment of steel structures under extreme load conditions, especially when the axial forces are significant. First, the NMYS column element based on resultant plasticity and the serial springs formulation is introduced to describe the nondegrading force-deformation relation in the effective space. The model accounts for the axial-flexure interaction in a yield envelope with consistent associative flow rules and linear hardening laws. Similar to the beam formulation in Chapter 3, plastic hinge offsets are introduced to approximate the spread of inelasticity and enhance the simulation of the post-yield hardening response. The implementation of the damage-plasticity element with the return-mapping algorithm ensures excellent convergence characteristics for the state determination.

With the plastic axial energy dissipation accounted for in the damage loading function, the damage-plasticity column model captures the effect of a variable axial force on the strength and stiffness deterioration in flexure, the severe deterioration under high axial compression, the nonsymmetric response under variable axial forces, and the excessive plastic axial and flexural deformations near column failure. The damage-plasticity model compares favorably in terms of computational efficiency with more sophisticated models with fiber discretization of the cross section while achieving excellent agreement in the response description for homogeneous metallic structural components. The excellent accuracy is also confirmed by the agreement with experimental results from column specimens under the combined effect of axial and bending in various load scenarios. Because of the computational efficiency and excellent accuracy, the proposed column element holds great promise for the large scale seismic response simulation of structural systems with strength and stiffness deterioration and should prove very useful in the damage assessment and the collapse simulation of structures under extreme loading conditions.

4.1 NMYS Column Element

4.1.1 Force-deformation relation

The NMYS column model relates the basic element forces $\mathbf{q} = [q_a \;\; q_i \;\; q_j]^T$, where q_a is the axial force and q_i and q_j are the flexural forces at end i and end j, to the corresponding element deformations $\mathbf{v} = [v_a \;\; v_i \;\; v_j]^T$. The model describes the element basic force-deformation relation using a yield surface to account for the axial-flexure N-M interaction, thus gives rise to the name NMYS model. The NMYS column model consists of a linear elastic element in series with two rigid-plastic and linear hardening springs at the ends. The rigid-plastic springs are activated when the bending moment reaches a yield strength that varies with the axial force according to an N-M interaction diagram. Figure 4.1 sketches an NMYS column element of length L with axial stiffness EA and flexural stiffness EI and two nonlinear hinges at the ends.

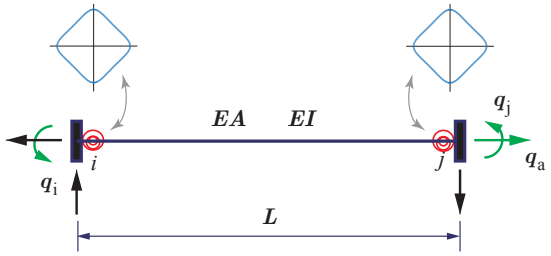

Figure 4.1: NMYS column element

The element model adopts the series formulation with an elastic and a plastic component. The force-deformation relation of the former is denoted by $\mathbf{q}_e$–$\mathbf{v}_e$, and the latter is given by the $\mathbf{q}_p$–$\mathbf{v}_p$. The force-deformation relation is governed by equilibrium, compatibility, and constitutive laws:

$$\text{Equilbrium :} \qquad \mathbf{q} = \mathbf{q}_e = \mathbf{q}_p \tag{4.1}$$

$$\text{Compatibility :} \qquad \mathbf{v} = \mathbf{v}_e + \mathbf{v}_p \tag{4.2}$$

$$\text{Constitutive law :} \qquad \mathbf{q} = \mathbf{k}_e \mathbf{v}_e = \mathbf{k}_e \left(\mathbf{v} - \mathbf{v}_p\right) \tag{4.3}$$

where $\mathbf{k}$ represents a stiffness matrix and the subscripts e and p indicate the variables of the elastic and the plastic components, respectively.

The following discusses the three main aspects of the element formulation: the yield function, the flow rules, and the hardening rules.

Yield function

Two yield functions f_i and f_j describe the admissibility of the element response at end i and end j, respectively. The yield envelope is defined by nonlinear functions of the axial

basic force q_a and the flexural basic forces q_i and q_j:

$$f_i = \left|\frac{q_a - q_{b,a}}{N_p}\right|^{c_1} + \left|\frac{q_i - q_{b,i}}{M_p}\right|^{c_2} + c_3 \left|\frac{q_a - q_{b,a}}{N_p}\right|^{c_4} \left|\frac{q_i - q_{b,i}}{M_p}\right|^{c_5} - (1 + H_{ip,i}\alpha_i) \tag{4.4}$$

$$f_j = \left|\frac{q_a - q_{b,a}}{N_p}\right|^{c_1} + \left|\frac{q_j - q_{b,j}}{M_p}\right|^{c_2} + c_3 \left|\frac{q_a - q_{b,a}}{N_p}\right|^{c_4} \left|\frac{q_j - q_{b,j}}{M_p}\right|^{c_5} - (1 + H_{ip,j}\alpha_j) \tag{4.5}$$

With the subscripts i and j dropped for brevity, q_b are the back-forces that govern the kinematic hardening behavior, N_p and M_p are the axial and flexural plastic capacities, H_{ip} is an isotropic hardening parameter, α is an internal variable that governs the isotropic hardening behavior, and c_1, c_2, c_3, c_4, c_5 are coefficients of the yield envelope. While it is possible to specify different coefficients c_1 to c_5 to distinguish the response at the two ends, this study limits to symmetrical yielding behavior and assumes the same coefficients at both ends.

In the case of elastic-perfectly-plastic response, the hardening parameters and variables are irrelevant: $q_{b,a} = 0$ and $q_{b,i} = q_{b,j} = 0$, $H_{ip,i} = H_{ip,j} = 0$, $\alpha_i = \alpha_j = 0$. In a purely axial force state, yielding initiates when the axial force reaches the plastic axial capacity, $q_a = \pm N_p, q_{i/j} = 0$. In a purely flexural force state, yielding initiates when the bending moment reaches the plastic flexural capacity, $q_a = 0$, $q_{i/j} = \pm M_p$. Figure 4.2(a) plots the yield envelope defined by two surfaces $f_i = 0, f_j = 0$ in the force space N-M_i-M_j. The red surface corresponds to $f_i = 0$ and the blue surface corresponds to $f_j = 0$. The admissible state is defined by the region inside both envelopes. Figure 4.2(b) shows a projection of the same envelope on the N-M_i plane. This is a 2d representation of the yield surface $f_i = 0$. The yield envelope in Figure 4.2 is given by the following parameters: $c_1 = 2$, $c_2 = 2$, $c_3 = 3.5$, $c_4 = 2.5, c_5 = 1.5$.

Flow rules

The associative flow rule describes the evolution of the plastic deformation $\mathbf{v}_p$ in terms of the normals $\mathbf{n}_i$ and $\mathbf{n}_j$ to the yield envelopes. The normals $\mathbf{n}_i$ and $\mathbf{n}_j$ are derivatives of the yield functions f_i and f_j with respect to the end force $\mathbf{q}$, respectively. To account for the singularities at the interface between the two yield surfaces, the Koiter's rule expresses the plastic deformation increment, or equivalently, the plastic deformation rate $\dot{\mathbf{v}}_p$ as a linear combination of the normals $\mathbf{n}_i$ and $\mathbf{n}_j$ [47].

$$\dot{\mathbf{v}}_p = \beta_i \mathbf{n}_i + \beta_j \mathbf{n}_j = \mathbf{n}\boldsymbol{\beta} \tag{4.6}$$

where $\boldsymbol{\beta} = [\beta_i \quad \beta_j]^T$ are the plastic consistency parameters. Since the axial and the flexural terms in Equations (4.4)–(4.5) are coupled, except for the pure bending force state, in general the element accummulates plastic axial deformations as yielding progresses. Consequently, the column model describes an elastic-plastic axial response as opposed to the linear elastic behavior in the beam model.

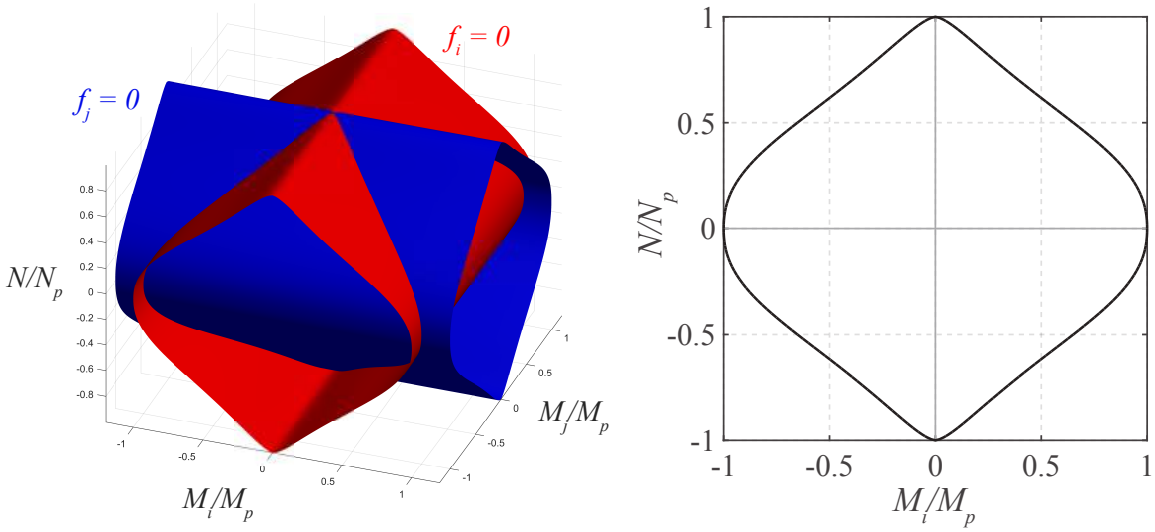

(a) $f_i = f_j = 0$ in N-M_i-M_j space (b) $f_i = 0$ in N-M_i plane

Figure 4.2: Yield surfaces

The *consistency condition* imposes plastic loading and unloading constraints on the two yield surfaces during plastic flow $\mathbf{f} = \mathbf{0}$:

$$\beta_m \dot{f}_m = 0, \quad m = i, j \tag{4.7}$$

Plastic unloading corresponds to zero consistency parameters $\beta_i = \beta_j = 0$ and negative increments of the yield function values $\dot{f}_i < 0$ and $\dot{f}_j < 0$. Plastic loading occurs when the consistency parameters are positive, $\beta_i > 0$ and/or $\beta_j > 0$, while the yield functions remain constant $\dot{f}_i = 0$ and/or $\dot{f}_j = 0$. During plastic loading, a yield surface is 'active' if the corresponding consistency parameter is positive $\beta > 0$, and otherwise, 'inactive' if the consistency parameter is zero $\beta = 0$. Identification of active yield surfaces of the column model is an iterative process and will be discussed in subsequent sections. If only the yield envelope at end i is active, $\beta_i \geq 0$, $\beta_j = 0$, and the plastic deformation increment is colinear with the normal to the surface i: $\dot{\mathbf{v}}_p = \beta_i \mathbf{n}_i$. If both envelopes are active, $\beta_i > 0$ and $\beta_j > 0$, and the plastic deformation increment is a linear combination of both normals: $\dot{\mathbf{v}}_p = \beta_i \mathbf{n}_i + \beta_j \mathbf{n}_j$.

Hardening rules

The evolution of the internal variable $\boldsymbol{\alpha}$ and the back-force $\mathbf{q}_b$ are described as functions of the consistency parameters $\boldsymbol{\beta}$:

$$\dot{\boldsymbol{\alpha}} = \boldsymbol{\beta} \tag{4.8}$$

$$\dot{\mathbf{q}}_b = \mathbf{H}_k \mathbf{n} \boldsymbol{\beta} \tag{4.9}$$

where $\mathbf{H}_k$ is a 3×3 kinematic hardening matrix with the hardening moduli of the axial and flexural response on the diagonal.

Finally, the *Kuhn-Tucker conditions* enforce unilateral constraints on the consistency parameter $\boldsymbol{\beta}$ and the yield functions $\mathbf{f} = [f_i \;\; f_j]^T$.

$$\boldsymbol{\beta} \geq \mathbf{0} \quad \text{and} \quad \mathbf{f} \leq \mathbf{0} \quad \text{and} \quad \beta_m f_m = 0, \;\; m = i, j \tag{4.10}$$

Remarks on model formulation:

The NMYS column model and the series beam model share many common features in the formulation. Both elements are classified as concentrated plasticity and are based on the series formulation with an elastic component in connection with two rigid-plastic and linear hardening springs. Both models adopt the associative flow rules and the Koiter's rule to account for multi-surface plasticity. The hardening rules of the two models are identical. The column element inherits similar positive features as the series beam element in Chapter 3: exact representation of the rigid-plastic hinge behavior, implicit state determination of the plastic hinge to avoid additional nodes and global degrees of freedom (dofs) at the interface between the elastic component and the plastic hinges, robust and efficient return-mapping algorithm.

The main difference between the models, which is also a major advantage of the proposed column model over several other commonly used concentrated plasticity column models in practice, is the ability to describe an inelastic axial response and to account for the effect of the axial force on the flexural yield strength. The beam model neglects the axial-flexure interaction and assumes a linear elastic axial response, whereas the NMYS column model accounts for the coupling and captures the axial plastic deformation and the elastic-linear hardening axial behavior. These assumptions are justified by a negligible axial force in beam members and a relatively large axial force in column members.

The yield functions of the beam model in Equations (3.4)–(3.5) have unit of bending moments, whereas the yield functions of the column model in Equations (4.4)–(4.5) are dimensionless because the element basic forces are normalized by the respective plastic capacities. The yield envelope of the beam model is defined by linear functions of the flexural forces q_i and q_j, whereas the yield envelope of the column model is given by nonlinear functions of both the axial force q_a and the flexural forces q_i and q_j. Consequently, the state determination of the column model is iterative.

It is noteworthy that the yield envelope of the beam model is a special case of Equations (4.4)–(4.5). With the coefficient c_1 assumes a very large value and $c_2 = 1$, $c_3 = 0$, the yield function in Equations (4.4)–(4.5) becomes:

$$f_m = \left| \frac{q_m - q_{b,m}}{M_p} \right| - (1 + H_{ip,m}\alpha_m) \qquad m = i, j \tag{4.11}$$

Multiplying Equation (4.11) by M_p and denoting $H_{i,m} = M_p H_{ip,m}$, the yield function becomes:

$$f_m^* = |q_m - q_{b,m}| - (M_p + H_{i,m}\alpha_m) \qquad m = i, j \tag{4.12}$$

which is the same as the yield function of the beam model in Equations (3.4)–(3.5)

Another discrepancy between the models is the definition of the isotropic hardening parameter, which will be addressed in Section 4.1.4.

4.1.2 Plastic hinge offset

The formulation in Section 4.1.1 places the rigid-plastic springs at the element ends. Similar to the series beam model, this section introduces the plastic hinge offset to concentrate the inelastic behavior at a distance away from the column ends. The objectives of the plastic hinge offset are two-fold: (1) to account for the spread of plasticity from the column ends into the interior region, and (2) to simulate more accurately the column post-yield hardening response.

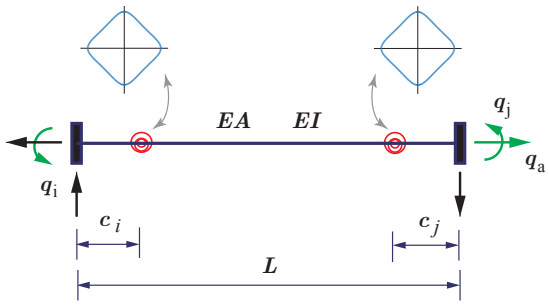

Figure 4.3: NMYS column element with plastic hinge offset

Assume the nonlinear springs are offset by the same distance $c_i = c_j$ from the element ends, the model defines the offset parameter $\chi = c_i/L = c_j/L$ where L is the element length. The force interpolation matrix $\mathbf{b}_p$ is introduced to evaluate the response at the spring locations:

$$\mathbf{b}_p = \begin{bmatrix} 1 & 0 & 0 \\ 0 & \chi - 1 & \chi \\ 0 & -\chi & 1 - \chi \end{bmatrix} \tag{4.13}$$

The normal and flexural forces in the plastic hinge $\mathbf{q}_h = [N \ M_i \ M_j]^T$, and the corresponding hinge normal and flexural deformations $\mathbf{v}_h = [\theta_a \ \theta_i \ \theta_j]^T$ are expressed in terms of the plastic forces $\mathbf{q}_p$ and plastic deformations $\mathbf{v}_p$:

$$\mathbf{q}_h = \mathbf{b}_p \mathbf{q}_p \tag{4.14}$$

$$\mathbf{v}_p = \mathbf{b}_p^T \mathbf{v}_h \tag{4.15}$$

With the plastic hinge offsets, the yield functions are defined for the spring force $\mathbf{q}_h$ instead of the element end force $\mathbf{q}$ in Equations (4.4)–(4.5). For consistency, the back-forces

N_b, $M_{b,i}$, $M_{b,j}$ follow the sign convention of internal axial force and bending moment. The yield functions are given as follows:

$$f_i = \left|\frac{N_i - N_b}{N_p}\right|^{c_1} + \left|\frac{M_i - M_{b,i}}{M_p}\right|^{c_2} + c_3 \left|\frac{N_i - N_b}{N_p}\right|^{c_4} \left|\frac{M_i - M_{b,i}}{M_p}\right|^{c_5} - (1 + H_{ip,i}\alpha_i) \tag{4.16}$$

$$f_j = \left|\frac{N_j - N_b}{N_p}\right|^{c_1} + \left|\frac{M_j - M_{b,j}}{M_p}\right|^{c_2} + c_3 \left|\frac{N_j - N_b}{N_p}\right|^{c_4} \left|\frac{M_i - M_{b,j}}{M_p}\right|^{c_5} - (1 + H_{ip,j}\alpha_j) \tag{4.17}$$

The original formulation in 4.1.1 with two plastic hinges at the element ends is a special case with $\chi = 0$. The next subsection presents the state determination of the NMYS column element model.

4.1.3 Return mapping algorithm

The state determination of the NMYS column model uses an iterative return-mapping algorithm to determine the element end force $\mathbf{q}_n$ and other variables at step n from the end deformation $\mathbf{v}_n$ and the history variables. First, an elastic predictor assumes no plastic deformation increment and gives a trial force $\mathbf{q}^{tr}$:

$$\mathbf{q}^{tr} = \mathbf{k}_e \left(\mathbf{v}_n - \mathbf{v}_{p,n-1}\right) \tag{4.18}$$

The trial axial force N^{tr} and bending moments M_i^{tr} and M_j^{tr} at the spring locations are computed from the trial force $\mathbf{q}^{tr}$ according to Equation (4.14). The trial internal variable $\boldsymbol{\alpha}^{tr}$ and the back-force $\mathbf{q}_b^{tr}$ assume the values from the previous step $n-1$:

$$\boldsymbol{\alpha}^{tr} = \boldsymbol{\alpha}_{n-1} \tag{4.19}$$

$$\mathbf{q}_b^{tr} = \mathbf{q}_{b,n-1} \tag{4.20}$$

The trial variables $\mathbf{q}^{tr}$, $\boldsymbol{\alpha}^{tr}$, $\mathbf{q}_b^{tr}$ are used to evaluate the trial yield functions $\mathbf{f}^{tr}$ in Equations (4.16)–(4.17). If both trial yield functions return a negative value, $f_i^{tr} < 0$ and $f_j^{tr} < 0$, the elastic assumption is valid and the trial variables are accepted.

$$\mathbf{q}_n = \mathbf{q}^{tr} \tag{4.21}$$

$$\boldsymbol{\alpha}_n = \boldsymbol{\alpha}^{tr} \tag{4.22}$$

$$\mathbf{q}_{b,n} = \mathbf{q}_b^{tr} \tag{4.23}$$

$$\mathbf{v}_{p,n} = \mathbf{v}_{p,n-1} \tag{4.24}$$

Otherwise, if at least one trial yield function returns a nonnegative value, $f_i^{tr} \geq 0$ and/or $f_j^{tr} \geq 0$, plastic correction is required. The correction uses the closest point projection algorithm and evaluates the variables at step n by applying the Newton-Ralphson scheme iteratively to reduce the residuals of the variable increments and enforce the Kuhn-Tucker conditions [92].

With the superscripts denoting the iteration number, the following residuals are defined: $\mathbf{R}_{vp}$ for the plastic deformation $\mathbf{v}_p$, $\mathbf{R}_f$ for the yield function $\mathbf{f}$, $\mathbf{R}_\alpha$ for the internal variable $\boldsymbol{\alpha}$, and $\mathbf{R}_b$ for the back-force $\mathbf{q}_b$.

$$\mathbf{R}_{vp}^{(k)} = -\mathbf{v}_{p,n}^{(k)} + \mathbf{v}_{p,n-1} + \mathbf{b}_p^T \mathbf{n}^{(k)} \boldsymbol{\beta}^{(k)} \tag{4.25}$$

$$\mathbf{R}_f^{(k)} = \mathbf{f}\left(\mathbf{q}_n^{(k)}, \boldsymbol{\alpha}_n^{(k)}, \mathbf{q}_{b,n}^{(k)}\right) \tag{4.26}$$

$$\mathbf{R}_\alpha^{(k)} = -\boldsymbol{\alpha}_n^{(k)} + \boldsymbol{\alpha}_{n-1} + \boldsymbol{\beta}^{(k)} \tag{4.27}$$

$$\mathbf{R}_b^{(k)} = -\mathbf{q}_{b,n}^{(k)} + \mathbf{q}_{b,n-1} + \mathbf{H}_k \mathbf{n}^{(k)} \boldsymbol{\beta}^{(k)} \tag{4.28}$$

The residual vector $\mathbf{R}$ is defined as:

$$\mathbf{R} = \begin{bmatrix} \mathbf{R}_{vp} & \mathbf{R}_f & \mathbf{R}_\alpha & \mathbf{R}_b \end{bmatrix}^T \tag{4.29}$$

At each iteration the goal is to reduce the residuals to zero:

$$\mathbf{R}^{(k)} = \mathbf{0} \tag{4.30}$$

The iterations solve for the state variable $\mathbf{x}$ that represents the consistency parameter $\boldsymbol{\beta}$, the end force $\mathbf{q}$, the internal variable $\boldsymbol{\alpha}$, and the back-force $\mathbf{q}_b$.

$$\mathbf{x} = \begin{bmatrix} \boldsymbol{\beta} & \mathbf{q} & \boldsymbol{\alpha} & \mathbf{q}_b \end{bmatrix}^T \tag{4.31}$$

The dimension of vectors $\mathbf{R}$ and $\mathbf{x}$ vary with the number of active yield surfaces. While the dimension of $\mathbf{R}_{vp}$ and $\mathbf{R}_b$ are 3×1, the residuals $\mathbf{R}_\alpha$ and $\mathbf{R}_f$ are 1×1 if only one surface is active and 2×1 if both are active. Similarly for the variable vector $\mathbf{x}$, the dimension of the element end force $\mathbf{q}$ and the back-force $\mathbf{q}_b$ are 3×1 while the consistency parameter $\boldsymbol{\beta}$ and the internal variable $\boldsymbol{\alpha}$ are 1×1 or 2×1.

A yield surface f_m is considered 'active' if the respective consistency parameter $\beta_m > 0$. The iterative procedure starts with an initial set of trial active constraints defined by $\mathbf{J}_{act}^{(0)}$.

$$\mathbf{J}_{act}^{(0)} = \{m \in i, j \mid f_m^{tr} \geq 0\} \tag{4.32}$$

The subsequent iterations modify this initial set and iteratively enforce the Kuhn-Tucker conditions. At each iteration, the set of active yield surfaces $\mathbf{J}_{act}$ is updated as follows:

(i) Let $\mathbf{J}_{act}^{(k-1)}$ denote the set of active yield surfaces at iteration $k-1$. If there exists indices m not in $\mathbf{J}_{act}^{(k-1)}$ such that the yield functions violate the admissibility, $f_m^{(k-1)} > 0$, include m in $\mathbf{J}_{act}^{(k-1)}$ and repeat the iteration.

(ii) The increment of the consistency parameters $\Delta\beta_m^{(k-1)}$, $m \in \mathbf{J}_{act}^{(k-1)}$ is computed by solving the linearized residual equations (4.30).

(iii) Update $\beta_m^{(k)} = \beta_m^{(k-1)} + \Delta\beta_m^{(k-1)}$ for $m \in \mathbf{J}_{act}^{(k-1)}$. If $\beta_m^{(k)} < 0$ for some $m \in \mathbf{J}_{act}^{(k-1)}$, remove these constraints from the active set $\mathbf{J}_{act}^{(k-1)}$ and restart the iteration with the new active constraints. Otherwise, set $\mathbf{J}_{act}^{(k)} = \mathbf{J}_{act}^{(k-1)}$ and proceed to the next iteration.

The Newton-Raphson iterations start with the intial consistency parameters $\boldsymbol{\beta}^{(0)} = \mathbf{0}$ and the initial state variables equal to the trial values.

$$\mathbf{q}^{(0)} = \mathbf{q}^{tr} \tag{4.33}$$

$$\boldsymbol{\alpha}^{(0)} = \boldsymbol{\alpha}^{tr} \tag{4.34}$$

$$\mathbf{q}_b^{(0)} = \mathbf{q}_b^{tr} \tag{4.35}$$

At iteration k, the Newton-Raphson scheme requires the Jacobian matrix $\mathbf{J}^{(k-1)}$, defined as the derivative of the residual $\mathbf{R}$ with respect to the variable $\mathbf{x}$ evaluated at $\mathbf{x}^{(k-1)}$.

$$\mathbf{J}^{(k-1)} = \frac{\partial \mathbf{R}}{\partial \mathbf{x}} = \begin{bmatrix} \dfrac{\partial \mathbf{R}_{vp}}{\partial \boldsymbol{\beta}} & \dfrac{\partial \mathbf{R}_{vp}}{\partial \mathbf{q}} & \dfrac{\partial \mathbf{R}_{vp}}{\partial \boldsymbol{\alpha}} & \dfrac{\partial \mathbf{R}_{vp}}{\partial \mathbf{q}_b} \\ \dfrac{\partial \mathbf{R}_{f}}{\partial \boldsymbol{\beta}} & \dfrac{\partial \mathbf{R}_{f}}{\partial \mathbf{q}} & \dfrac{\partial \mathbf{R}_{f}}{\partial \boldsymbol{\alpha}} & \dfrac{\partial \mathbf{R}_{f}}{\partial \mathbf{q}_b} \\ \dfrac{\partial \mathbf{R}_{\alpha}}{\partial \boldsymbol{\beta}} & \dfrac{\partial \mathbf{R}_{\alpha}}{\partial \mathbf{q}} & \dfrac{\partial \mathbf{R}_{\alpha}}{\partial \boldsymbol{\alpha}} & \dfrac{\partial \mathbf{R}_{\alpha}}{\partial \mathbf{q}_b} \\ \dfrac{\partial \mathbf{R}_{b}}{\partial \boldsymbol{\beta}} & \dfrac{\partial \mathbf{R}_{b}}{\partial \mathbf{q}} & \dfrac{\partial \mathbf{R}_{b}}{\partial \boldsymbol{\alpha}} & \dfrac{\partial \mathbf{R}_{b}}{\partial \mathbf{q}_b} \end{bmatrix} \text{ at } \mathbf{x} = \mathbf{x}^{(k-1)} \tag{4.36}$$

Equation (4.30) is linearized to solve for the increment of the state variable $\Delta\mathbf{x}^{(k-1)}$

$$0 \approx \mathbf{R}^{(k)} = \mathbf{R}^{(k-1)} + \frac{\partial \mathbf{R}}{\partial \mathbf{x}} \Delta\mathbf{x}^{(k-1)} \tag{4.37}$$

$$\Delta\mathbf{x}^{(k-1)} = -\mathbf{J}^{(k-1)} \backslash \mathbf{R}^{(k-1)} \tag{4.38}$$

The model variable at iteration k, $\mathbf{x}^{(k)}$, is updated from the history value $\mathbf{x}^{(k-1)}$ and the increment $\Delta\mathbf{x}^{(k-1)}$.

$$\mathbf{x}^{(k)} = \mathbf{x}^{(k-1)} + \Delta\mathbf{x}^{(k-1)} \tag{4.39}$$

With the new variable $\mathbf{x}^{(k)}$, the yield function $\mathbf{f}^{(k)}$ is evaluated. The iterations repeat with the updated active surfaces based on the consistency parameter $\boldsymbol{\beta}^{(k)}$. The plastic correction algorithm terminates when the residual norms are less than the specified tolerance values, $\|\mathbf{R}_w^{(k-1)}\| < tol_w$, where $w \in \{vp,\ f,\ \alpha,\ b\}$. Separate residual norms are checked against different tolerances for unit consistency and to avoid nonconvergence due to significant discrepancies between the residual norms when evaluating $\|\mathbf{R}\|$.

It is noteworthy that the element end force $\mathbf{q}_n$ can also be updated from the trial force $\mathbf{q}^{tr}$ as follows:

$$\mathbf{q}_n = \mathbf{q}^{tr} - \mathbf{k}_e \Delta\mathbf{v}_p = \mathbf{q}^{tr} - \mathbf{k}_e \mathbf{b}_p^T \mathbf{n} \boldsymbol{\beta} \tag{4.40}$$

In view of Equation (4.40), the consistency parameters $\boldsymbol{\beta}$ can be regarded as the contravariant components of the force correction $\Delta\mathbf{q} = \mathbf{q}^{tr} - \mathbf{q}_n$ along the vectors $\mathbf{k}_e \mathbf{b}_p^T \mathbf{n}_i$ and $\mathbf{k}_e \mathbf{b}_p^T \mathbf{n}_j$. Figure 4.4 gives a graphical illustration of the return mapping algorithm for a simple

case with an elasto-plastic element behavior and no plastic hinge offset. Figure 4.4(a) plots a cross-section of the yield surfaces $f_i = 0$ and $f_j = 0$ in the plane defined by vectors $\mathbf{k}_e\mathbf{b}_p^T\mathbf{n}_i$ and $\mathbf{k}_e\mathbf{b}_p^T\mathbf{n}_j$ evaluated at an intersection point. The region defined by $f_i > 0$ and $f_j > 0$ can be divided into 3 subregions Γ_i, Γ_j, Γ_{ij}. The condition $\beta_1 > 0$ and $\beta_2 > 0$ corresponds to subregion Γ_{ij}. In an iteration, if the trial force falls into this subregion, both surfaces are active. Conversely, region Γ_i gives $\beta_i > 0$ but $\beta_j < 0$, and region Γ_j gives $\beta_j > 0$ but $\beta_i < 0$. If the trial force falls into Γ_i or Γ_j, only one constraint is active although both yield functions are positive. The return-mapping procedure in subregions Γ_{ij} and Γ_j is shown in Figures 4.4(b)-(c), respectively. This illustration demonstrates that the sign of the yield function $\mathbf{f}$ is insufficient to determine the set of active surfaces.

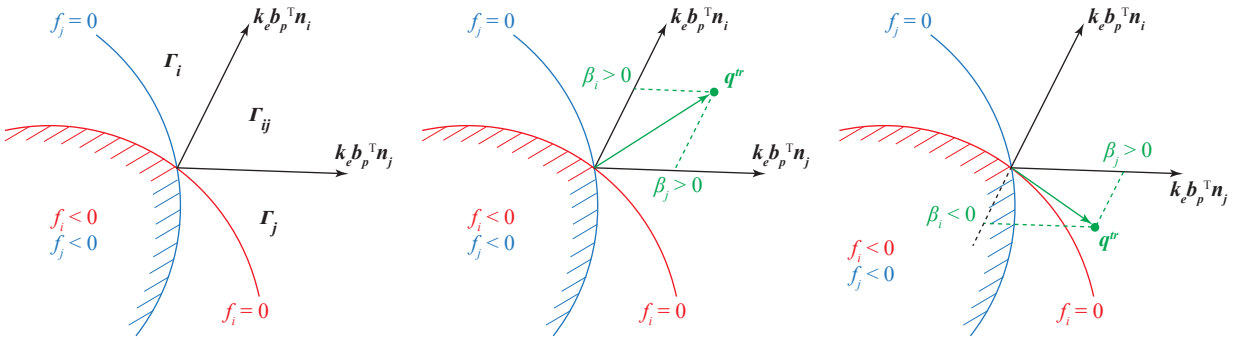

(a) Definition of Γ_i, Γ_j, Γ_{ij} (b) Γ_{ij}: $\beta_i > 0$ and $\beta_j > 0$ (c) Γ_j: $\beta_i < 0$ and $\beta_j > 0$

Figure 4.4: Geometric illustration of return-mapping algorithm at corner point

The state determination of the NMYS column model is summarized in Tables 4.1–4.2: the elastic predictor in Table 4.1 and the iterative plastic correction in Table 4.2. The algorithmic tangent $\mathbf{k}_t$ is the derivative of the end force $\mathbf{q}_n$ with respect to the end deformation $\mathbf{v}_n$. A derivation of the tangent is presented in Appendix B.

4.1.4 Model parameters

Parameters of the NMYS model can be classified into three main categories:

(1) *Parameters of the geometry and material properties*: the Young modulus E, the cross-sectional area A, the moment of inertia I, the axial and flexural plastic capacities N_p and M_p. These 5 parameters depend solely on the specimen geometry and material properties and do not require calibration;

(2) *Parameters of the yield envelope*: coefficients c_1, c_2, c_3, c_4, c_5 of the yield functions, presented in Section 4.1.4.1.

1. Elastic predictor:

Evaluate $\mathbf{q}^{tr}$, $\mathbf{q}_b^{tr}$, $\boldsymbol{\alpha}^{tr}$

Evaluate trial spring forces N^{tr}, M_i^{tr}, M_j^{tr}

2. Check of plastic process:

Evaluate $\mathbf{f}^{tr}$ in Equations (4.16)–(4.17)

IF $f_i^{tr} < 0$ and $f_j^{tr} < 0$ THEN:

Update $\mathbf{q}_{b,n}$, $\boldsymbol{\alpha}_n$, $\mathbf{v}_{p,n}$

Update $\mathbf{q}_n$, $\mathbf{k}_t$

EXIT

ELSE Initialization for plastic correction:

Initialize $\mathbf{J}_{act}^{(0)} = \{m \in i, j \mid f_m^{tr} > 0\}$

Initialize $\mathbf{q}_n^{(0)}$, $\boldsymbol{\alpha}_n^{(0)}$, $\mathbf{q}_{b,n}^{(0)}$, $\mathbf{f}^{(0)}$, $\mathbf{v}_{p,n}^{(0)}$

Initialize $\boldsymbol{\beta}^{(0)} = \mathbf{0}$

Set $k = 1$ and go to Table 4.2

ENDIF

Table 4.1: Elastic predictor algorithm

(3) *Hardening parameters*: the kinematic hardening ratio H_{kr} and the isotropic hardening parameter H_{ip}, presented in Section 4.1.4.2.

4.1.4.1 Yield surface parameters

Figure 4.5 illustrates the effect of 5 parameters c_1, c_2, c_3, c_4, c_5 on the yield envelope, which shows the projection of the 3d N-M_i-M_j surface onto N-M_i and/or N-M_j planes. The response with $c_1 = 2$, $c_2 = 2$, $c_3 = 4$, $c_4 = 2$, $c_5 = 2$ is used as a reference in all five plots. In each plot, one coefficient varies from 1 to 20 while the others remain equal to the respective reference values. Due to symmetry, it is sufficient to show the envelope in only one quadrant.

Increasing c_1, c_2, c_4, c_5 makes the yield envelope more convex, whereas increasing c_3 makes the envelope more concave. As c_3 varies, changes to the yield envelope is symmetrical about the reference axis $N/N_p = M/M_p$, whereas c_1 and c_2, c_4 and c_5 give asymmetrical changes to the yield envelope. The yield envelope is relatively less sensitive to c_1 and c_2 than c_3, c_4, c_5. Therefore, it is recommended to calibrate the latter three coefficients first.

1. Check of yield functions:

Evaluate the spring forces $N_n^{(k-1)}$, $M_{i,n}^{(k-1)}$, $M_{j,n}^{(k-1)}$ from $\mathbf{q}_n^{(k-1)}$

Evaluate yield function $f_m^{(k-1)}$, for $m = i, j$

IF $\exists m \notin \mathbf{J}_{act}^{(k-1)}$: $\quad f_m^{(k-1)} > 0$ THEN:

For all m, reset $\mathbf{J}_{act}^{(k-1)} = \mathbf{J}_{act}^{(k-1)} \cup \{m\}$ and repeat **1**

ELSE:

Go to **2**

ENDIF

2. Evaluation of residuals:

Evaluate $\mathbf{R}^{(k-1)} = [\mathbf{R}_{vp} \quad \mathbf{R}_f \quad \mathbf{R}_\alpha \quad \mathbf{R}_b]^T$

IF $\|\mathbf{R}_w^{(k-1)}\| < tol_w, \quad w \in \{vp,\ f,\ \alpha,\ b\}$, THEN:

Update $\mathbf{q}_n$, $\boldsymbol{\alpha}_n$, $\mathbf{q}_{b,n}$ and go to **7**

ELSE:

Go to **3**

ENDIF

3. Evaluation of force and internal variable increments:

Evaluate the Jacobian $\mathbf{J}^{(k-1)}$

Evaluate the increments $\Delta\mathbf{x}^{(k-1)} = [\Delta\boldsymbol{\beta} \quad \Delta\mathbf{q} \quad \Delta\boldsymbol{\alpha} \quad \Delta\mathbf{q}_b]^T$

4. Check of active constraints:

Update $\boldsymbol{\beta}^{(k)} = \boldsymbol{\beta}^{(k-1)} + \Delta\boldsymbol{\beta}^{(k-1)}$

IF $\boldsymbol{\beta}_m^{(k)} < 0$, $m \in \mathbf{J}_{act}^{(k-1)}$, THEN:

Reset $\mathbf{J}_{act}^{(k-1)} = \{m \in \mathbf{J}_{act}^{(k-1)} \mid \beta_m^{(k)} > 0\}$

Go to **2**

ELSE:

Go to **5**

5. Update of forces and internal variables:

Update $\mathbf{x}^{(k)}$ to obtain $\boldsymbol{\beta}_{n,m}^{(k)}$, $\mathbf{q}_n^{(k)}$, $\boldsymbol{\alpha}_{n,m}^{(k)}$, $\mathbf{q}_{b,n}^{(k)}$, $\quad m \in \mathbf{J}_{act}^{(k-1)}$

Set $\mathbf{J}_{act}^{(k)} = \mathbf{J}_{act}^{(k-1)}$

6. Set $k - 1 \leftarrow k$ and go to **1**

7. Evaluate the tangent stiffness $\mathbf{k}_t$

Table 4.2: Plastic correction algorithm: closest point projection

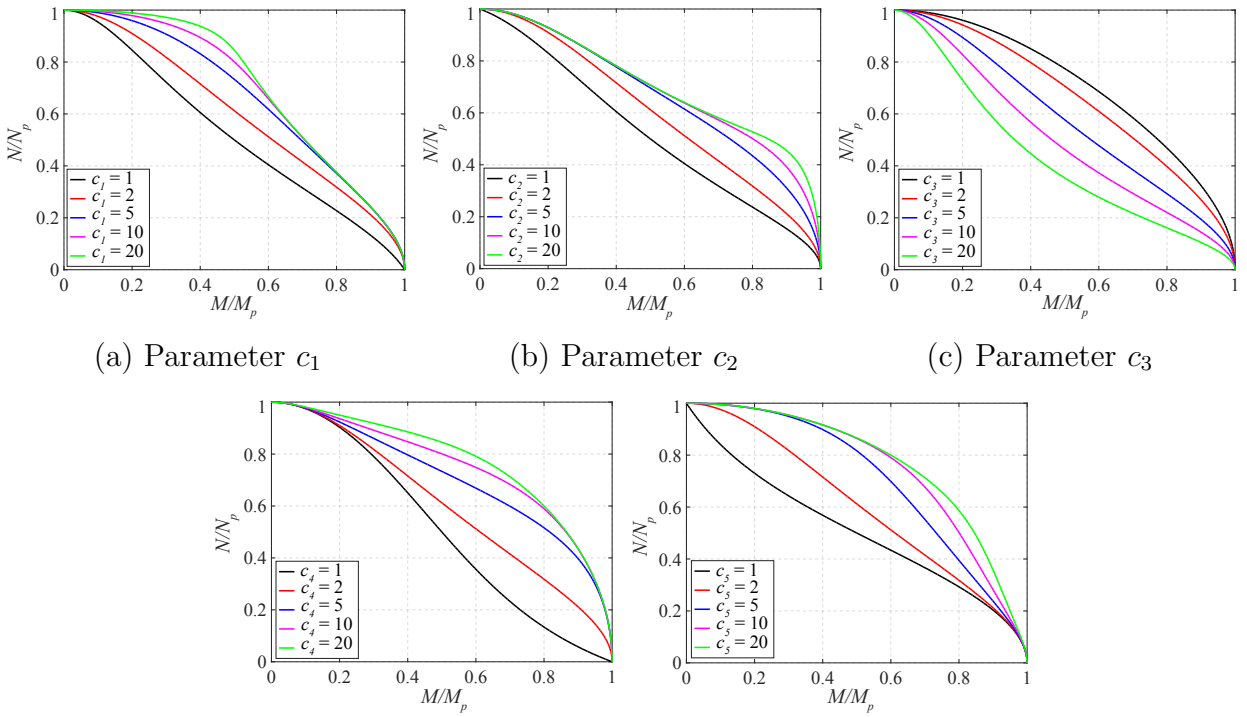

(a) Parameter c_1 (b) Parameter c_2 (c) Parameter c_3

(d) Parameter c_4 (e) Parameter c_5

Figure 4.5: Effect of yield surface parameters

4.1.4.2 Hardening parameters

The hardening behavior of the NMYS column element is governed by 2 parameters: the kinematic hardening ratio H_{kr} and the isotropic hardening parameter H_{ip}. The dimensionless ratio H_{kr} describes the kinematic hardening behavior and translates the yield envelope as plastic deformations accumulate. The hardening ratio H_{kr} relates to the hardening modulus H_k of the plastic hinge moment-rotation relation through the flexural stiffness $6EI/L$ under antisymmetric bending with equal end deformations:

$$H_k = \frac{6EI}{L} H_{kr} \tag{4.41}$$

The isotropic hardening parameter H_{ip} describes the istropic hardening behavior and expands or contracts the yield envelope as plastic deformations accumulate. It is noteworthy that the isotropic hardening parameter H_{ip} in Equations (4.4)–(4.5) is not equivalent to the isotropic hardening ratio H_{ir} in the series beam formulation in Chapter 3. Table 4.3 compares the units of relevant variables in the beam and the column models. The variables are in unit of force, deformation, or a combination thereof, or dimensionless ('1' in Table 4.3). In the series beam model, the isotropic hardening ratio H_{ir} is dimensionless, whereas in

the NMYS column model, the isotropic hardening parameter H_{ip} has dimension [force^{-1} $\times$ deformation^{-1}] .

Variable(s)	Beam model	Column model
f_i, f_j	force	1
n_i, n_j	1	force^{-1}
$\mathbf{v}_p$	deformation	deformation
β_i, β_j	deformation	force $\times$ deformation
α_i, α_j	deformation	force $\times$ deformation
H_{ir} or H_{ip}	1	force^{-1} $\times$ deformation^{-1}

Table 4.3: Unit comparison of beam and column models

Figure 4.6 illustrates the effect of the hardening behavior on the yield envelope. The kinematic hardening in Figure 4.6(a) translates the envelope while preserving the initial shape. The isotropic hardening with $H_{ip} > 0$ in Figure 4.6(b) expands the yield envelope. It is noteworthy that the shape of the yield envelope changes during the expansion or contraction.

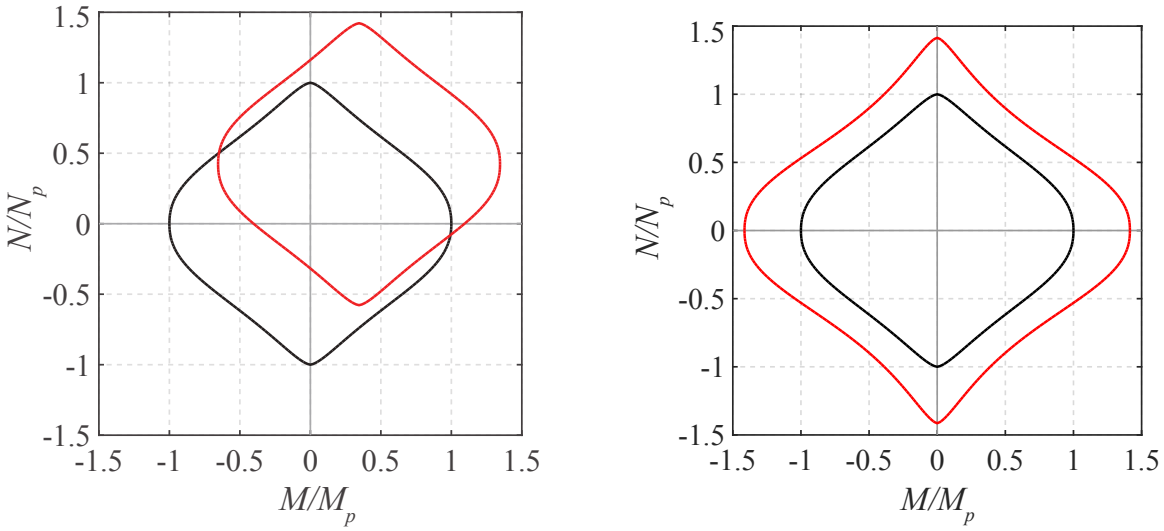

(a) Kinematic hardening (b) Isotropic hardening

Figure 4.6: Effect of hardening parameters on yield envelope

4.1.5 Example 1: Cantilever column

The first example examines the response of a cantilever column under a combined effect of axial forces and bending moments. The column, shown in Figure 4.7, is 10 ft in length and

has a W24x162 steel profile with a yield strength $f_y = 50$ ksi. For comparison, two element models are used to simulate the column response: a concentrated plasticity model (CP) and a distributed plasticity model (DP) . The objectives of this example are three-fold: (1) to calibrate the yield surface parameters c_1 to c_5 of the NMYS model, (2) to highlight the effect of the axial-flexure interaction on the yielding behavior, and (3) to validate the accuracy and efficiency of the NMYS model in comparison to the more sophisticated distributed plasticity approach.

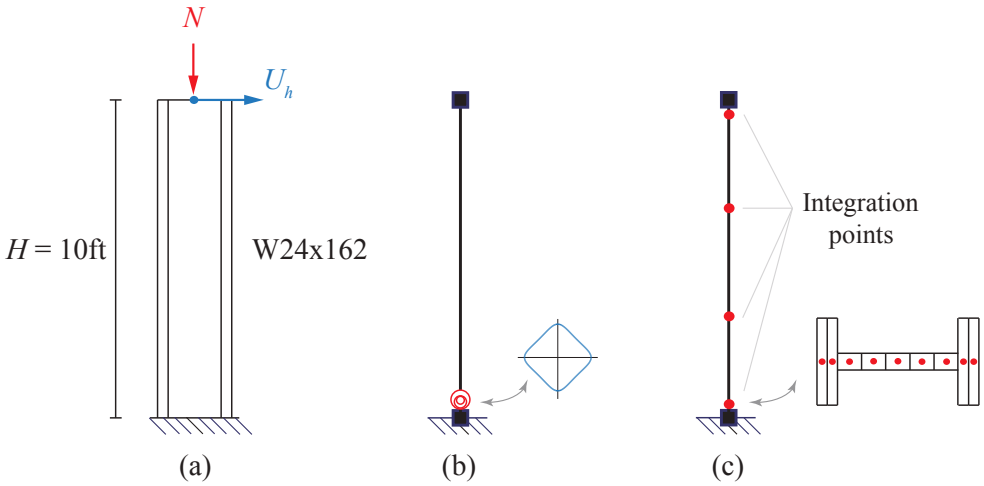

Figure 4.7: Cantilever column: (a) structure and loading, (b) concentrated plasticity (CP) model, (c) distributed plasticity (DP) model

In model DP, one force-based distributed plasticity element is used with 4 integration points along the column height. Each section is discretized into 9 fibers: 2 in each flange and 5 in the web. The Gauss-Lobatto integration rule is used along the element length and the mid-point rule in each cross section. The material constitutive relation assumes a bilinear elastic-plastic response [92]. In model CP, one NMYS element is used to simulate the column. The parameters E, A, I, N_p, and M_p are specified based on the geometry and material properties.

The following presents two case studies with different assumptions of the column behavior.

4.1.5.1 Elastic-perfectly-plastic element behavior

In the first case study, the column assumes an elastic-perfectly-plastic (EPP) behavior. In both models, same flexural deformations are increased monotonically under constant axial compressions, whose values range from 20% to 80% the plastic axial capacity, $N/N_p = -0.2$, -0.4, -0.6, -0.8. The yield surface coefficients c_1 to c_5 in the NMYS model are calibrated against the yield envelope given by model DP. Two response variables are compared in the models: the plastic axial deformation and the flexural yield strength.

The following coefficients are found to describe well the yield envelope: $c_1 = 2$, $c_2 = 2$, $c_3 = 2.95$, $c_4 = 2$, $c_5 = 1.33$. Without hardening, the yield function in Equations (4.4)–(4.5) becomes:

$$f_m = \left(\frac{N_m}{N_p}\right)^2 + \left(\frac{M_m}{M_p}\right)^2 + 2.95\left(\frac{N_m}{N_p}\right)^2\left(\frac{M_m}{M_p}\right)^{1.33} - 1 \tag{4.42}$$

where $m = i, j$ indicates the element end.

Figure 4.8(a) compares the normalized axial force N/N_p against the axial deformation v_a and Figure 4.8(b) plots the normalized bending moment M_i/M_p at end i against the corresponding flexural deformation v_i. The response comparison gives rise to two observations. First, the axial shortening given by the two models agree rather well, especially under the moderate axial load levels $N/N_p = -0.4$ and $N/N_p = -0.6$. Model CP underestimates the axial deformation under the small axial load level $N/N_p = -0.2$ and the high axial load level $N/N_p = -0.8$; however, the discrepancies are within 15% the response in model DP, which are acceptable considering the small deformation values. The satisfactory agreement suggests that the associative flow rule and the Koiter's rule are reasonable to describe the evolution of plastic deformations in steel components.

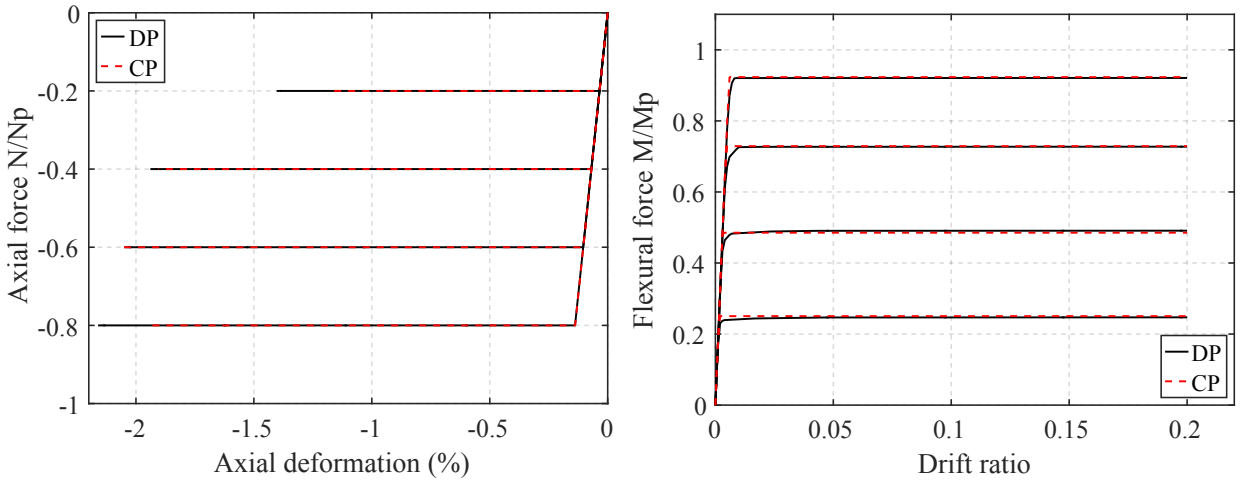

(a) Axial force-deformation (b) Flexural force-deformation

Figure 4.8: Monotonic response of cantilever column with EPP behavior

Second, the yield surface coefficients capture very well the axial-flexure interaction. Figure 4.8(b) proves that the variation in the yield moment is consistent between the two models. The response deviates slightly at the transtion from the elastic to the plastic range: while model DP describes a gradual yielding with a smooth curve, model CP shows sudden yielding with an abrupt stiffness transition. However, the discrepancies are minor and the two models are identical in the elastic and the post-yield response.

Next, the column is subjected to a number of load histories to further validate the accuracy of the NMYS element model. Figures 4.9–4.10 compare the column response in 6

load scenarios. For each load case (LC), three comparisons are shown: the load path on the axial-flexure interaction diagram N-M, the axial response $q_a/N_p - v_a/L$, and the flexural response at the base (end i) $q_i/M_p - v_i$.

(1) **LC1**: shown in Figure 4.9(a). The column is subjected to a constant axial compression $N/N_p = -0.4$ and a cyclic lateral displacement at the free end that consists of symmetric cycles about the undeformed configuration with increasing amplitudes from one cycle to the next. This cyclic displacement pattern is representative of far-field ground motions, and thus shall be referred to as the FF pattern in subsequent discussions. Except for the stiffness transition at yield initiation, the two models give essentially identical response.

(2) **LC2**: shown in Figure 4.9(b). The column is subjected to the FF pattern and a variable axial load history $N/N_p = -0.2 \mp 0.4$. First, an axial compression $N/N_p = -0.2$ is imposed to represent the effect of gravity loading. Then the axial load varies from $N/N_p = -0.6$ to $N/N_p = +0.2$ to represent the variation due to overturning effect. The axial compression is "in-phase" with the lateral displacement, that is, the column is compressed more with higher lateral displacement in the positive direction. The evolution of the axial deformation agrees well in early cycles and slightly deviates with increasing inelastic deformations. However, the discrepancies are relatively minor and model CP captures well the overall behavior. Model CP is able to simulate the asymmetrical flexural response under positive and negative moments due to the variable axial force. The satisfactory match in the load path confirms the model accuracy.

(3) **LC3**: shown in Figure 4.9(c). The column is subjected to a constant axial compression $N/N_p = -0.2$ and a cyclic lateral displacement history that consists of several large pulses and load reversals biased to one direction. This pattern is representative of near-field ground motions, and thus shall be referred to as the NF pattern in subsequent discussions. As expected from the observation in Figure 4.8(a), model CP underestimates the axial deformation under small axial compression $N/N_p = -0.2$. However, model CP captures well the flexural response and the overall axial deformation evolution.

(4) **LC4**: shown in Figure 4.9(d). The column is subjected to the NF pattern and a variable axial load history $N/N_p = -0.2 \mp 0.4$ same as LC2. Similar observations hold, including the consistency in the axial and the flexural response and slight discrepancies in the axial deformation. Same as LC2, model CP captures well the effect of the axial force variation on the column yielding.

(5) **LC5**: shown in Figure 4.9(e). The column is subjected to the FF pattern and a variable axial force history that ranges from $N/N_p = -0.6$ to $N/N_p = +0.2$. First, a reference constant axial compression $N/N_p = -0.2$ is imposed, then the axial force oscillates about this value with increasing amplitude as loading progresses. As opposed to LC2

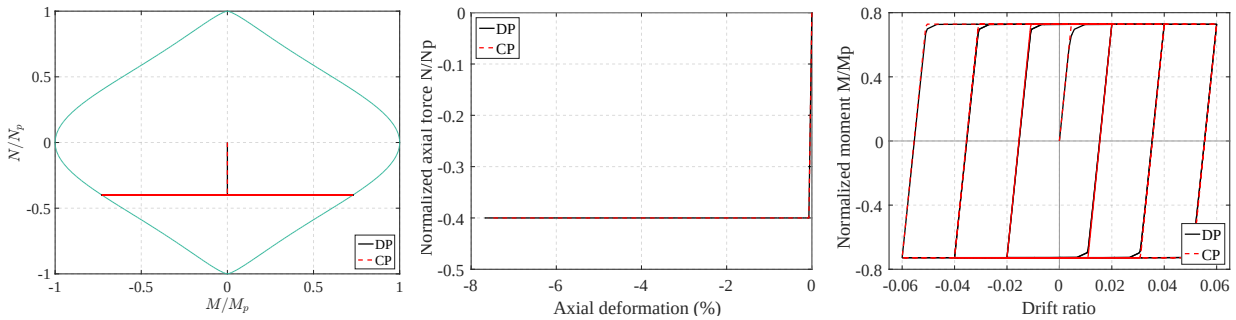

(a1) LC1: N-M (a2) LC1: axial response (a3) LC1: flexural response

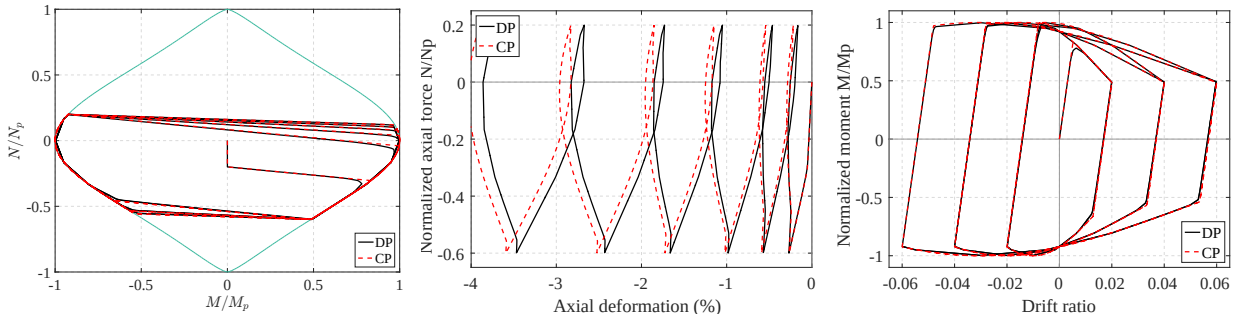

(b1) LC2: N-M (b2) LC2: axial response (b3) LC2: flexural response

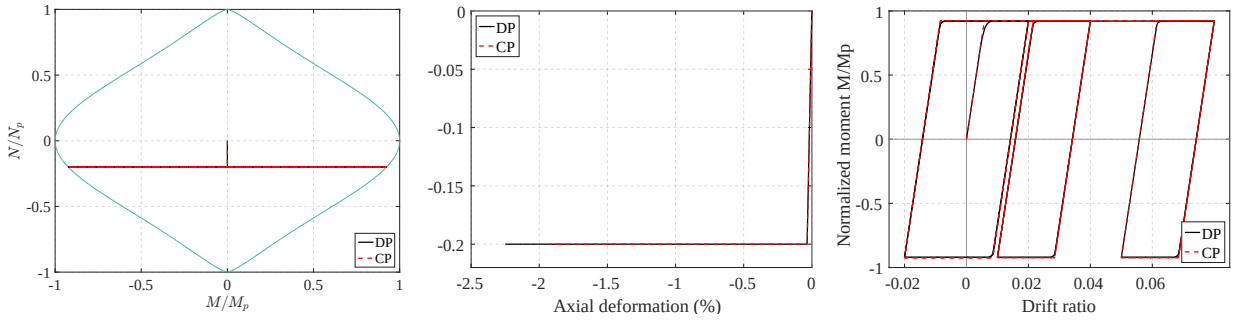

(c1) LC3: N-M (c2) LC3: axial response (c3) LC3: flexural response

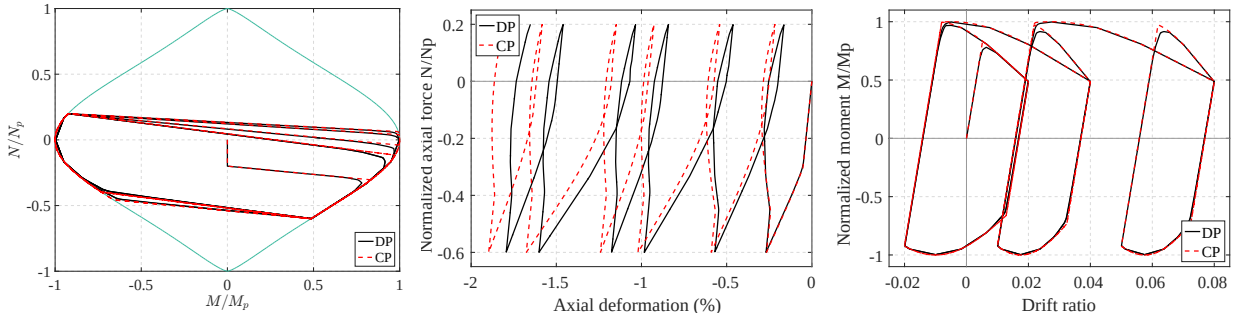

(d1) LC4: N-M (d2) LC4: axial response (d3) LC4: flexural response

Figure 4.9: Cyclic response of cantilever column with EPP response

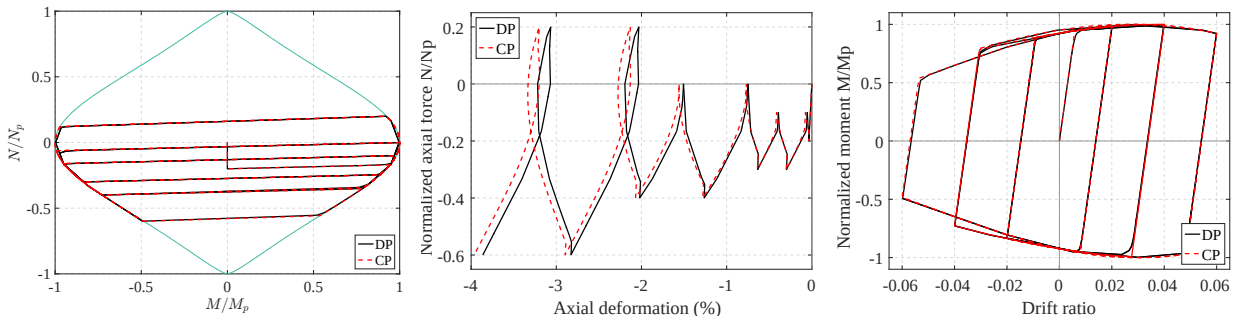

(e1) LC5: N-M (e2) LC5: axial response (e3) LC5: flexural response

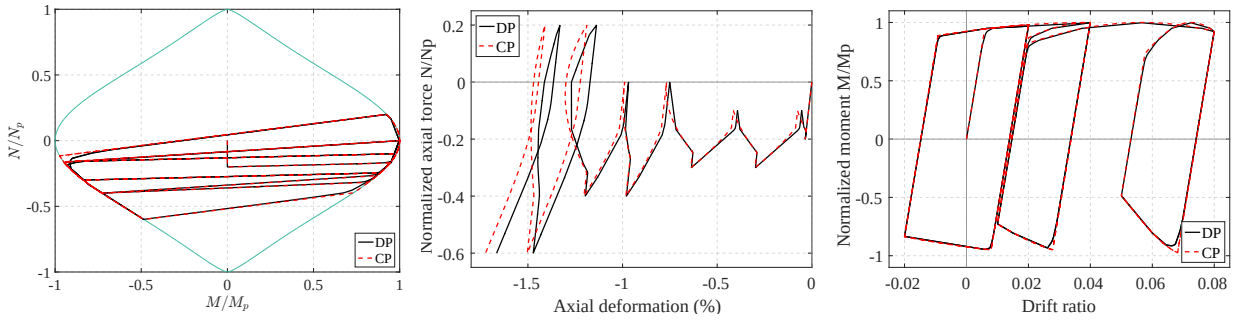

(f1) LC6: N-M (f2) LC6: axial response (f3) LC6: flexural response

Figure 4.10: Cyclic response of cantilever column with EPP response (continued)

and LC4, the axial compression is "out-of-phase" with the lateral displacement, that is, as the lateral displacement increases in the positive direction, the axial compression decreases and switches to tension in later cycles. Consequently, compared to LC2 and LC4, the flexural force-deformation relation exhibits a different trend in which the response under negative moments softens with increasing negative deformations.

(6) **LC6**: shown in Figure 4.9(f). The column is subjected to the NF pattern and the variable axial force history in LC5. The agreement in the two models is excellent..

Similar to the comparison between the DP and the CP beam models in Chapter 3, the NMYS column model outperforms the DP model in numerical efficiency with a factor of 2–3 times reduction in the computation time. Convergence in the NMYS model is quadratic and is achieved within 3–4 iterations per load step for a tolerance of 1e−16.

It is noteworthy that the simulations neglect the geometric nonlinearity and assume linear geometry. This is hypothetical because for such excessive lateral displacement values in these load cases, the effect of axial force is significant and nonlinear geometry must be accounted for to accurately represent the column behavior. However, for illustration purposes, the assumption of linear geometry is reasonable to focus only on the material nonlinearity. Moreover, since the two models are subjected to the same axial force histories

and show negligible discrepancies in the response, the above conclusions are expected to hold under nonlinear geometry.

4.1.5.2 Hardening element behavior

The second case study evaluates the NMYS element in the presence of hardening behavior to demonstrate the effect of the plastic hinge offsets χ. The same column in Figure 4.7 is subjected to a constant axial compression and a cyclic lateral displacement at the free end. Six levels of axial force are considered: $N/N_p = 0,\ -0.1,\ -0.2,\ -0.4,\ -0.6,\ -0.8$. The effect of the axial force at large displacement values is accounted for by the corotational formulation and is reflected in the post-yield stiffness reduction with increasing axial force levels.

Model DP assumes no isotropic hardening $H_i = 0$ and a kinematic hardening $H_k = 2\%E$. The normalized base moment M_i/M_p are plotted against the horizontal drift ratio for two cases of plastic hinge offsets: no offset $\chi = 0$ in Figure 4.11 and with offsets $\chi = 0.2$ in Figure 4.12. In model CP, the isotropic hardening parameter $H_{ip} = 0$, while the kinematic hardening ratio $H_{kr} = 0.0175$ for $\chi = 0$ and $H_{kr} = 0.0075$ for $\chi = 0.2$. Similar to the calibration in the series beam model in Chapter 3, without offsets, the kinematic hardening ratio H_{kr} is calibrated to match the moment at a target drift ratio, which is 0.1 in this case study. With offsets, the hardening ratio H_{kr} is selected to match the post-yield stiffness observed in model DP.

The response without plastic hinge offsets in Figure 4.11 shows that model CP captures well the reduction in the yield moment as the axial force increases. Similar to model DP, the NMYS element exhibits a behavior analogous to isotropic hardening, that is, the moment increases as the column cycles between same deformation values and accumulates plastic deformations. This phenomenon is evident during early cycles after the first yield initiation and more pronounced under higher axial compression. Overall, model CP without plastic hinge offsets offers a reasonable approximation of the 'exact' response given by model DP. The comparison, however, also identifies some limitations. Although the moment at the target rotation is captured well in all cases of axial force, model CP underestimates the moment at smaller rotations than the target value. Moreover, the excessive post-yield hardening exacerbates the discrepancies, especially under higher axial force levels.

Figure 4.12 proves that the plastic hinge offsets enhance model CP's response tremendously. Although model CP does not capture exactly the moment at every load reversal particularly under high axial compression $N/N_p = -0.6$ and $N/N_p = -0.8$, the agreement between model CP and DP is significantly improved. The column response under low to moderate axial compression, i.e. less than 50% the plastic axial capacity, which is typical in low- to mid-rise moment frames, is represented very well by the proposed NMYS element with offsets. Model CP captures satisfactorily the post-yield hardening even at high axial compression $N/N_p = -0.8$. However, some discrepancies remain, such as the insufficient representation of the Bauschinger effect in the reloading response and the strength increase due to cyclic loading under high axial force. The first limitation results from the assumption

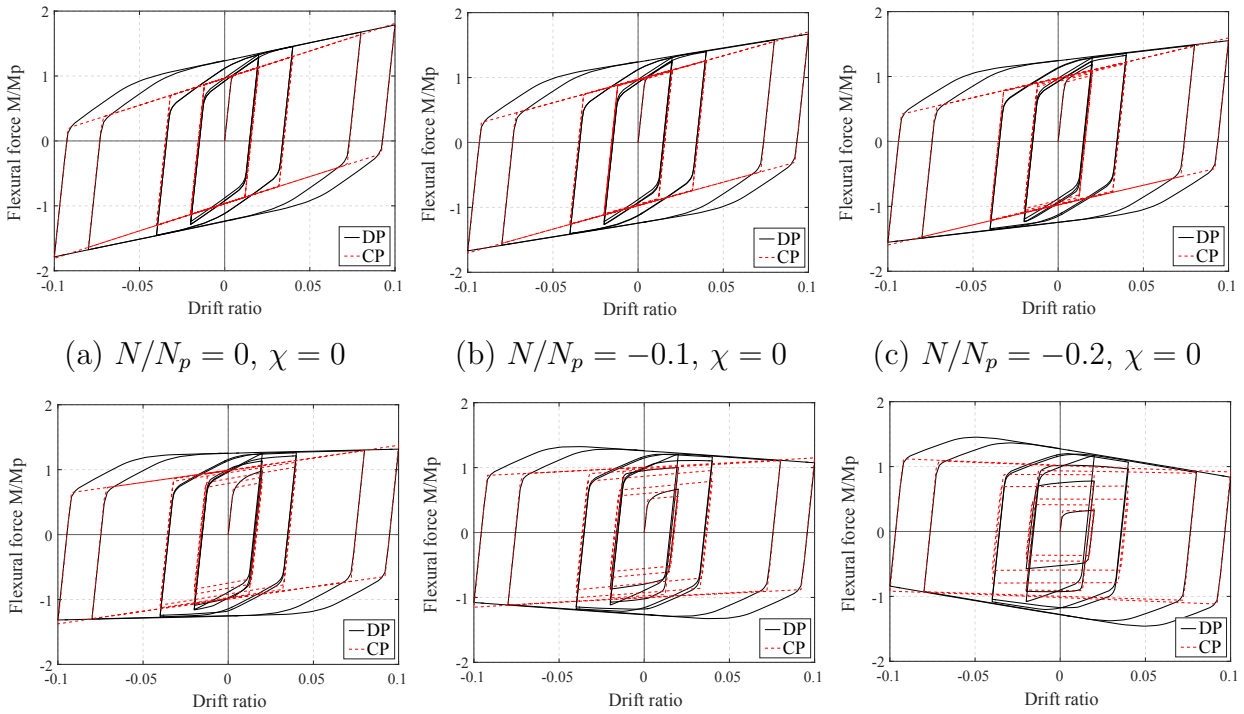

(a) $N/N_p = 0$, $\chi = 0$ (b) $N/N_p = -0.1$, $\chi = 0$ (c) $N/N_p = -0.2$, $\chi = 0$

(d) $N/N_p = -0.4$, $\chi = 0$ (e) $N/N_p = -0.6$, $\chi = 0$ (f) $N/N_p = -0.8$, $\chi = 0$

Figure 4.11: Cyclic response of cantilever column with hardening behavior, $\chi = 0$

of linear hardening, which could be addressed by introducing a nonlinear hardening rule to accommodate the gradual yielding, such as with generalized plasticity [7]. The second limitation suggests that a nonassociative flow rule may be explored to improve the description of the yield envelope evolution.

4.1.6 Example 2: Four-story three-bay frame

The second example evaluates the response of the NMYS column model and its interaction with other elements in a structural model. The study selects the four-story three-bay steel special moment frame (SMF) in Figure 4.13, which is adapted from the PG-2RSA performance group in the NIST study of FEMA P695 Methodology [68]. The columns and girders are wide-flange sections whose sizes are shown in Figure 4.13. The fundamental period obtained from an eigenvalue analysis of the structure is 1.62 sec. This is rather high for a four-story frame, but is adopted here to be consistent with the NIST report [68].

In this study, the girders and columns assume an elastic-perfectly-plastic (EPP) behavior. The effect of gravity loading is accounted for with constant axial compression on the columns. Two models are used to simulate the dynamic response of the SMF:

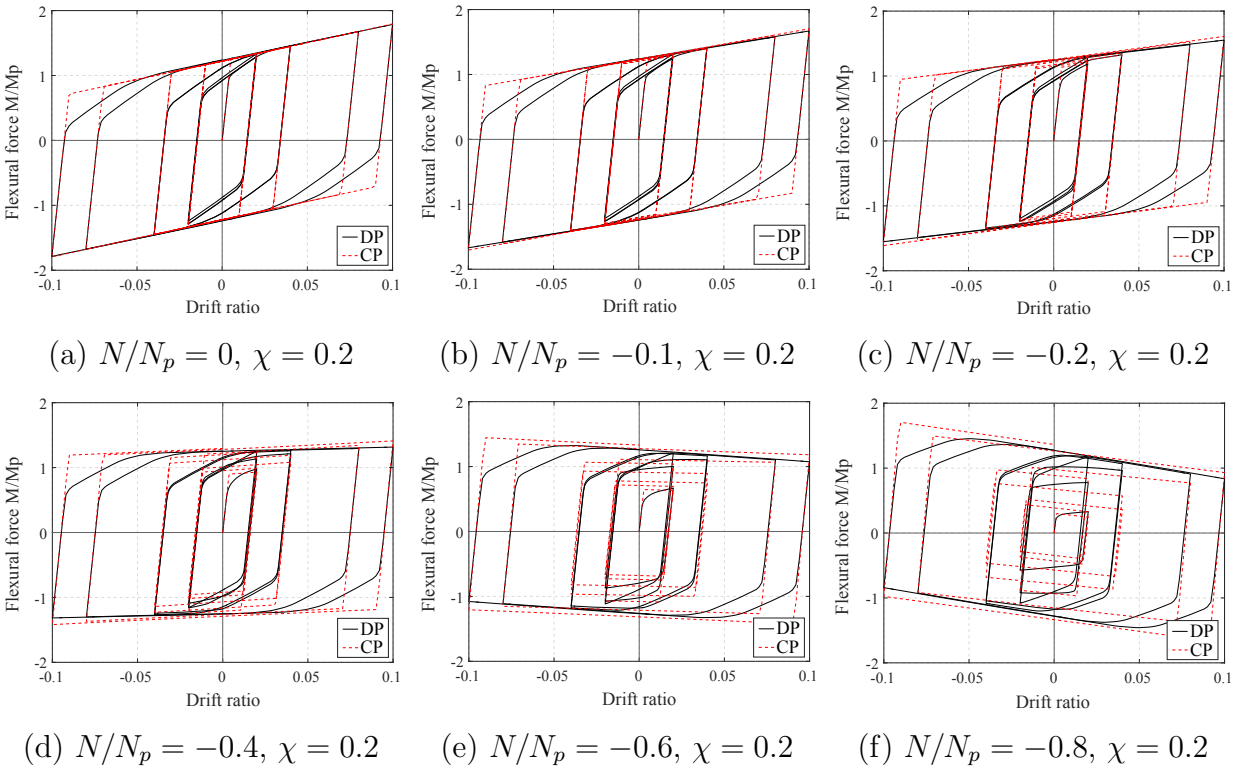

(a) $N/N_p = 0$, $\chi = 0.2$ (b) $N/N_p = -0.1$, $\chi = 0.2$ (c) $N/N_p = -0.2$, $\chi = 0.2$

(d) $N/N_p = -0.4$, $\chi = 0.2$ (e) $N/N_p = -0.6$, $\chi = 0.2$ (f) $N/N_p = -0.8$, $\chi = 0.2$

Figure 4.12: Cyclic response of cantilever column with hardening behavior, , $\chi = 0.2$

(1) **Model DP**: Each girder and column is represented by a force-based distributed plasticity beam-column element with 4 integration points along the element length. Each cross section is discretized into 12 layers: 3 in each flange and 6 in the web. The bilinear elastic-plastic material model is adopted with hardening parameters $H_k = H_i = 0$ to represent the fiber stress-strain relation.

(2) **Model CP**: Each girder is represented by a series beam element with $H_{kr} = H_{ir} = 0$. Each column is represented by a NMYS column element with $H_{kr} = 0$, $H_{ip} = 0$. No plastic hinge offset is specified in the members, $\chi = 0$, which gives sufficient accuracy for a cantilever column with EPP element behavior, as the example in Section 4.1.5 shows.

Both models assume rigid beam-column connections and neglect the effect of floor slabs and shear deformations in panel zones at the beam-column interface. Rayleigh damping is used with the damping matrix proportional to the mass matrix and the tangent stiffness matrix. The damping coefficients are obtained from the first and the third mode of vibration with a damping ratio of 2.5%. The corotational formulation is used to account for the nonlinear geometry effect.

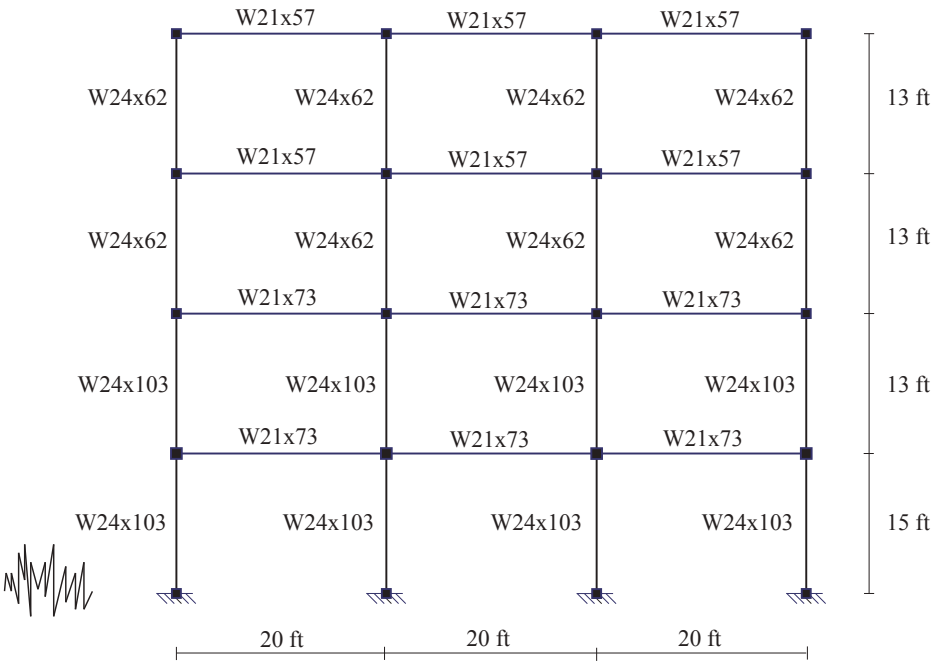

Figure 4.13: Four-story three-bay moment-resisting frame

The frame is subjected to the LA30 record. Figure 4.14 shows the global response of the SMF: the average 1st story drift in Figure 4.14(a) and the average roof drift in Figure 4.14(b). The models give identical response up to the major pulse at approximately 12 sec leading to a considerable drift increment. The response following the pulse deviates slightly; however, the discrepancies are negligible. Model CP captures well the main characteristics of the response, for instance, the residual drift is biased to the negative direction near the end of the load history.

Figures 4.14(c)-(d) show the distribution of the story drift ratios (DR) and the floor accelerations at the instant of respective maximum value attained. Both models give a similar story drift distribution and indicate the maximum DR of roughly 5.2% in the 3rd story. The floor acceleration distribution shows discrepancies in the bottom two floors: while model DP suggests a higher acceleration in the 2nd floor, model CP predicts a higher value in the 1st story. However, this does not significantly affect the accuracy because the difference is quite small and model CP captures well the maximum acceleration on the 3rd floor, which is more relevant in damage assessment of the SMF. The excessive 3rd story drift and floor acceleration relative to the others suggests a potential weak story mechanism that involves the 3rd story members and induces high plastic deformations at these locations.

Next, the local element response is examined. This study adopts the following naming convention for a member: '$X1$-$X2$-$X3$-$X4$', where the first three terms identify the member and the last term specifies the element end. $X1$ represents the member type: 'C' for a

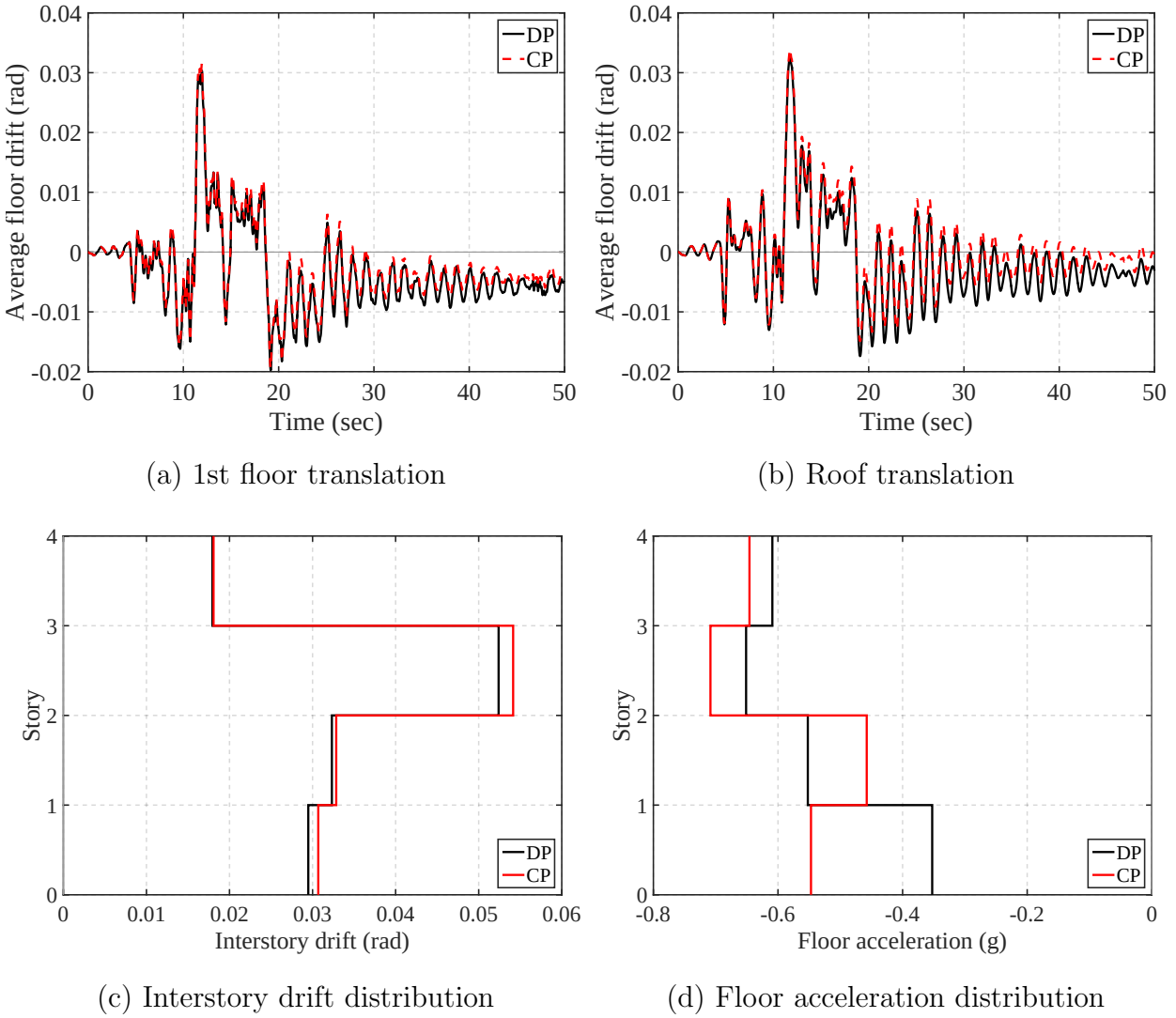

(a) 1st floor translation

(b) Roof translation

(c) Interstory drift distribution

(d) Floor acceleration distribution

Figure 4.14: Global dynamic response of four-story three-bay steel moment frame

column and 'G' for a girder. $X2$ represents the member location in the vertical direction, which equals the number of floor or story from the ground. $X3$ represents the member location in the lateral direction, which is the column line or the bay number from left to right. $X4$ indicates the element end: 'T' for the top and 'B' for the bottom end of a column, 'L' for the left and 'R' for the right end of a girder. For instance, C-1-3-B refers to the base of the first-story column that is the third from left, and G-2-1-R refers to the right end of the leftmost girder on the second-floor.

Figure 4.15 presents the response of several representative columns and girders, including the N-M load path as well as the axial and the flexural response.

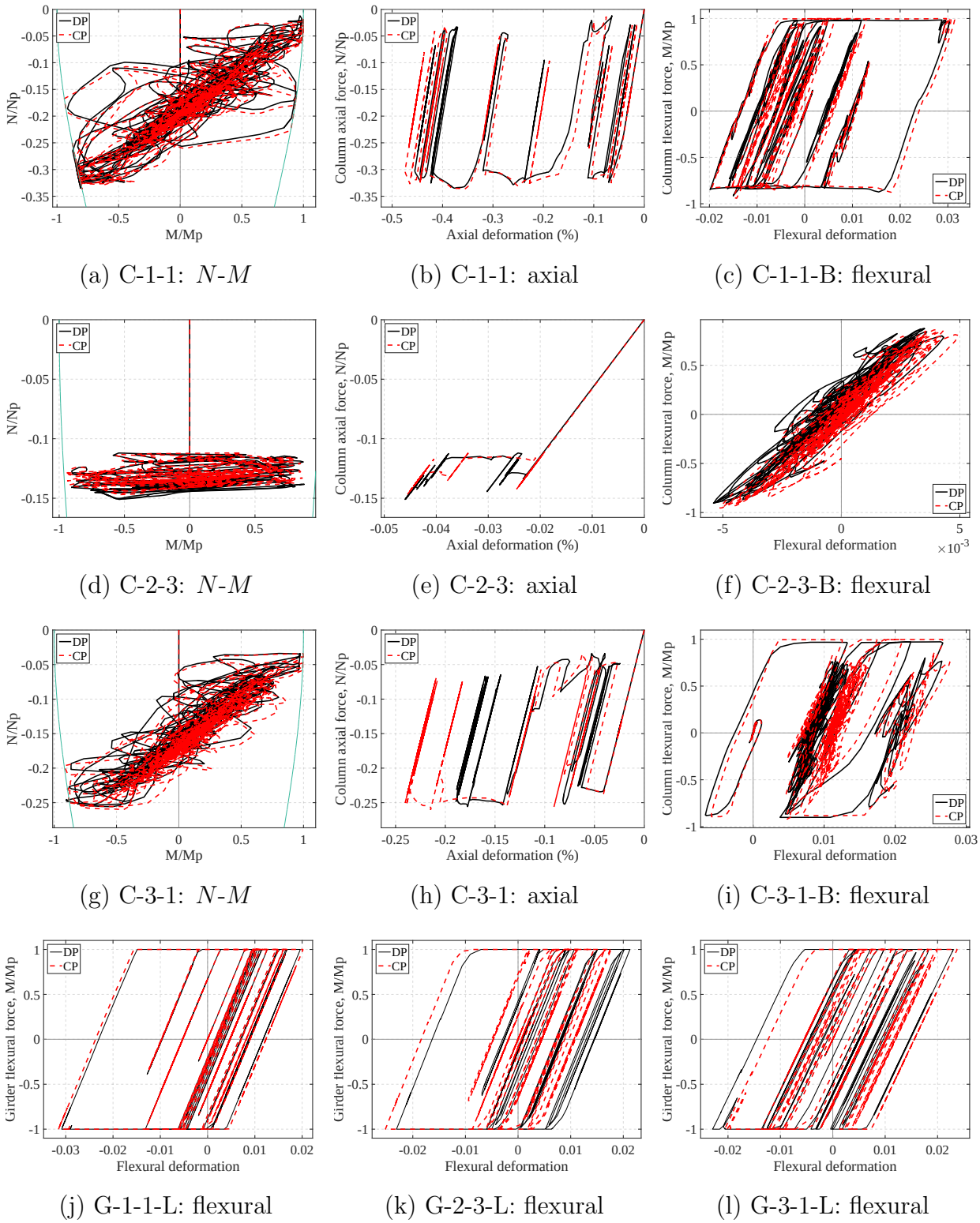

(a) C-1-1: N-M (b) C-1-1: axial (c) C-1-1-B: flexural

(d) C-2-3: N-M (e) C-2-3: axial (f) C-2-3-B: flexural

(g) C-3-1: N-M (h) C-3-1: axial (i) C-3-1-B: flexural

(j) G-1-1-L: flexural (k) G-2-3-L: flexural (l) G-3-1-L: flexural

Figure 4.15: Local dynamic response of four-story three-bay steel moment frame

(i) **C-1-1**: The agreement between the models in Figures 4.15(a)-(c) is excellent. Model CP is able to capture the variable axial compression of up to 35% the plastic axial capacity. The model describes well the asymmetric yield strength under positive and negative moments. The load cycles under negative moments correspond to higher axial compression, and in turns, smaller flexural yield strength according to the N-M interaction diagram.

(ii) **C-2-3**: Model CP accurately predicts the column elastic state throughout the load history, which is evident in the load path inside the initial yield envelope. Both models give consistent axial response with a compression of up to 15% the plastic axial capacity.

(iii) **C-3-1**: Despite the overestimation in the axial shortening of 0.05% the element length, model CP gives an excellent estimate of the axial force level and the flexural force-deformation relation. The model is able to capture the smaller flexural yield strength due to higher axial compression under negative moments. The axial compression in C-3-1 is higher than C-2-3 because the overturning effect exerts additional compression on the left columns as the structure leans permanently to the left direction relative to the ground.

(iv) **G-1-1, G-2-3, G-3-1**: Model CP describes accurately the flexural force-deformation relations and the spread of yielding up to the higher floors. In this case, the yield strength is practically equal to the nominal strength M_p, which supports the assumption to neglect the axial-flexure interaction in the series beam model.

4.2 Damage-Plasticity Column Element

4.2.1 Formulation

The damage-plasticity column element adopts the damage mechanics concepts to describe the continuous strength and stiffness degradation in the column response. The framework for the formulation is similar to the beam element in Section 3.3 and consists of three main components: a constitutive relation in effective space, a damage loading function, and a damage evolution law. The following discussion highlights the key aspects of each component.

4.2.1.1 Effective response

A major difference between the damage-plasticity formulation of the beam and the column models is the force-deformation relation in the effective space. While the beam model neglects the axial-flexure interaction due to small axial force in girder members, the column model accounts for this coupling effect. Although any force-deformation relation with N-M interaction could be used, this study adopts the NMYS column model in Section 4.1 to describe the effective response.

4.2.1.2 Damage loading function

The damage loading function describes the relation between the variables in the effective space and the energy dissipation that controls the damage evolution. In the proposed element model, the effective force and deformation in the plastic hinges $\bar{N}-\theta_a$, $\bar{M}_i-\theta_i$, $\bar{M}_j-\theta_j$ are the work-conjugate variables that govern the damage accumulation, which are analogous to the effective force $\bar{s}$ and the deformation e in the 1d damage model in Chapter 2. To accomodate asymmetrical response under positive and negative forces, the model isolates the positive and the negative components of the effective forces $\bar{\mathbf{q}}_h$ in the plastic hinge:

$$\bar{\mathbf{q}}_h^{\pm}=\begin{pmatrix}\bar{N}^{\pm}\\ \bar{M}_i^{\pm}\\ \bar{M}_j^{\pm}\end{pmatrix}=\frac{1}{2}\begin{pmatrix}\bar{N}\\ \bar{M}_i\\ \bar{M}_j\end{pmatrix}\ \pm\ \frac{1}{2}\begin{pmatrix}|\bar{N}|\\ |\bar{M}_i|\\ |\bar{M}_j|\end{pmatrix} \tag{4.43}$$

where $|\bar{\mathbf{q}}_h|=\begin{bmatrix}|\bar{N}| & |\bar{M}_i| & |\bar{M}_j|\end{bmatrix}^T$ represents the magnitude of the effective hinge forces, $\bar{\mathbf{q}}_h^{+}=\begin{bmatrix}\bar{N}^{+} & \bar{M}_i^{+} & \bar{M}_j^{+}\end{bmatrix}^T$ and $\bar{\mathbf{q}}_h^{-}=\begin{bmatrix}\bar{N}^{-} & \bar{M}_i^{-} & \bar{M}_j^{-}\end{bmatrix}^T$ are the positive and the negative components of the effective hinge forces, respectively.

The model assumes damage accumulation is governed by the energy dissipation. It is instructive to distinguish the energy dissipation due to the axial and flexural response. To this end, the axial energy variables $\psi_a^{\pm}$ and the flexural energy variables $\psi_f^{\pm}$ are defined as integrals of the product of the effective hinge force with the corresponding deformation increment and scaled by two coefficients C_{wc} and C_{cd}:

$$\psi_{a,m}^{\pm}=C_{i,m}^{\pm}\int C_{wc,m}^{\pm}\bar{N}^{-}d\theta_a \tag{4.44}$$

$$\psi_{f,m}^{\pm}=\int C_{wc,m}^{\pm}\bar{M}_m^{\pm}d\theta_m+C_{cd,m}^{\pm}\int C_{wc,m}^{\mp}\bar{M}_m^{\mp}d\theta_m \tag{4.45}$$

where $m=i,j$. Similar to the 1d damage formulation in Chapter 2, $C_{wc,i}^{\pm}$ and $C_{wc,j}^{\pm}$ are the cyclic degradation coefficients that determine the weight of the energy increment based on the current deformation relative to the previous maximum and minimum deformations. C_{wc} equals to 1 if the deformation exceeds the previous extreme values, and less than 1 otherwise. With $\theta_{m,max}$ and $\theta_{m,min}$ denoting the maximum and minimum rotations at spring $m=i,j$, the cyclic degradation coefficient is defined as:

$$C_{wc,m}=\begin{cases}1 & \text{if } \theta_m<\theta_{m,\min} \text{ or } \theta_m>\theta_{m,\max}\\ 0\le C_{wc,m}\le 1 & \text{if } \theta_{m,\min}\le\theta_m\le\theta_{m,\max}\end{cases}\qquad (m=i,j) \tag{4.46}$$

$C_{cd,i}^{\pm}$ and $C_{cd,j}^{\pm}$ are the damage coupling coefficients that govern the effect of the response in one loading direction on the damage accumulation in the other direction. $C_{i,i}^{\pm}$ and $C_{i,j}^{\pm}$ are the axial-flexure interaction coefficients that govern the effect of the axial response on the damage accumulation.

Then, the total energy variables $\psi^{\pm}$ consist of the contribution from the axial response $\psi_a^{\pm}$ and the flexural response $\psi_f^{\pm}$:

$$\psi_m^{\pm} = \psi_{a,m}^{\pm} + \psi_{f,m}^{\pm} \qquad (m = i, j) \tag{4.47}$$

It is noteworthy that only the axial compression $\bar{N}^{-}$ contributes to the energy variables $\psi^{\pm}$ to account for the strength degradation due to buckling of steel members under high compression. It is also worth pointing out that in the element formulation, the energy variables $\psi^{\pm}$ depend on the plastic hinge deformation θ. This is different than the 1d damage formulation in Chapter 2 in which the energy dissipation ψ depends on the total deformation e.

The damage formulation requires the energy threshold variables $\tilde{\psi}_m^{\pm}$ to initiate the damage growth and defined as the previous maximum energy dissipation $\psi_m^{\pm}$:

$$\tilde{\psi}_m^{\pm}(t) = \max \psi^{\pm}(\tau) \qquad t_0 \leq \tau < t \qquad (m = i, j) \tag{4.48}$$

Finally, four damage loading functions for the two plastic hinges $g_i^{\pm}$ and $g_j^{\pm}$ are given as:

$$g_m^{\pm} = \psi_m^{\pm} - \tilde{\psi}_m^{\pm}, \qquad (m = i, j) \tag{4.49}$$

4.2.1.3 Damage evolution law

The damage evolution law evaluates four damage variables, d_i^{+} and d_i^{-} for the positive and negative moments at spring i, and d_j^{+} and d_j^{-} for the positive and negative moments at spring j, based on the energy dissipation variables $\psi^{\pm}$ in Equation (4.47). The damage evolution law of the column element is similar to the 1d damage formulation in Chapter 2 and the damage-plasticity beam model in Chapter 3. The following highlights the key aspects of the formulation.

The evolution law requires a definition of the energy thresholds $\bar{\psi}_{d0}^{\pm}$ corresponding to an undamaged state and the energy limits $\bar{\psi}_{d1}^{\pm}$ corresponding to a complete loss of strength. These energy variables are expressed as multiples of the yield energy $\boldsymbol{\psi}_y$ of a cantilever column without axial force:

$$\psi_{y,m} = \frac{M_{p,m}^2 L}{6EI} \tag{4.50}$$

where M_p is the nominal plastic flexural capacity, EI is the element flexural stiffness, and L is the element length.

With C_{d0} and C_{d1} denoting the damage threshold coefficient and the damage limit coefficient, the energy thresholds $\psi_{d0}^{\pm}$ and the energy limits $\psi_{d1}^{\pm}$ are given as:

$$\psi_{d0,m}^{\pm} = C_{d0,m}^{\pm} \psi_{y,m} \tag{4.51}$$

$$\psi_{d1,m}^{\pm} = C_{d1,m}^{\pm} \psi_{y,m} \tag{4.52}$$

The energy variables $\psi_i^{\pm}$ and $\psi_j^{\pm}$ in Equation (4.47) are normalized with respect to the threshold and the limit energy variables ψ_{d0} and ψ_{d1}:

$$\hat{\psi}_m^{\pm} = \frac{\psi_m^{\pm} - \psi_{d0,m}^{\pm}}{\psi_{d1,m}^{\pm} - \psi_{d0,m}^{\pm}} \tag{4.53}$$

Similar to the damage-plasticity beam formulation, the damage variables can be evaluated with two evolution functions. The first evolution function adopts the cumulative distribution function (CDF) of the beta distribution. The function modifies the original parameters of the CDF of the beta distribution and introduces two parameters d_{p1} and d_{p2}, same as the damage model in Chapter 2 and Chapter 3.

$$d_m^{\pm} = F_B\left(\hat{\psi}_m^{\pm}, \beta_{1,m}^{\pm}, \beta_{2,m}^{\pm}\right) \tag{4.54}$$

where F_B denotes the CDF of the beta distribution and β_1 and β_2 are the parameters of the CDF. Similar to the 1d damage formulation Chapter 2, to better identify the effect of the parameters on the damage evolution, the damage evolution law introduces two damage evolution parameters d_{p1} and d_{p2} defined as the ratio and the smaller of the two original parameters β_1 and β_2.

The second evolution law is a composite function similar to the formulation in Section 2.7. This evolution function accommodates sudden strength degradation due to brittle failure.

$$d_m^{\pm} = \begin{cases} F_B\left(\hat{\psi}_m^{\pm}, \beta_1, \beta_2\right), & 0 \le \hat{\psi}_m^{\pm} \le \hat{\psi}_f \\ F_B\left(\hat{\psi}_f, \beta_1, \beta_2\right) + \dfrac{1 - F_B\left(\hat{\psi}_f, \beta_1, \beta_2\right)}{\hat{\psi}_u - \hat{\psi}_f}\left(\hat{\psi}_m^{\pm} - \hat{\psi}_f\right), & \hat{\psi}_f < \hat{\psi}_m^{\pm} \le \hat{\psi}_u \\ 1, & \hat{\psi}_u < \hat{\psi}_m^{\pm} \le 1 \end{cases} \tag{4.55}$$

While the axial force N is equal to the value in the effective space $\bar{N}$, the true moments M_i and M_j result from linear combinations of the positive and negative effective moments and the damage variables:

$$M_m = \left(1 - d_m^{+}\right)\bar{M}_m^{+} + \left(1 - d_m^{+}\right)\bar{M}_m^{-} \qquad m = i, j \tag{4.56}$$

The true force $\mathbf{q}$ at the element ends are obtained from an extrapolation of the true spring force $\mathbf{q}_h$:

$$\mathbf{q} = \mathbf{b}_p^{-1}\mathbf{q}_h \tag{4.57}$$

4.2.2 Implementation

The state determination of the damage-plasticity column model is summarized in Tables 4.1–4.2.

Given: end deformations $\mathbf{v}_n$ and history variables at step $n-1$
Required: state variables at step n

1. State determination in effective space:
Procedure for the series beam model in Tables 4.1–4.2
Outputs: $\bar{\mathbf{q}}_n$, $\mathbf{v}_{p,n}$, $\boldsymbol{\alpha}_n$, $\mathbf{q}_{b,n}$, $\bar{\mathbf{q}}_h$, $\mathbf{v}_h$
2. Decomposition of $\bar{\mathbf{q}}_h$ into $\bar{\mathbf{q}}_h^+$ and $\bar{\mathbf{q}}_h^-$
3. Energy variables $\psi_{i,n}^{\pm}$ and $\psi_{j,n}^{\pm}$ with contribution from the *axial term*
4. Damage loading functions:
Evaluate the energy threshold $\tilde{\psi}_{i,n}^{\pm}$ and $\tilde{\psi}_{j,n}^{\pm}$
Evaluate damage loading functions $g_i^{\pm}$ and $g_j^{\pm}$
5. Check of damage for each of the four damage loading functions:
IF $g \leq 0$, THEN
Damage unloading, go to 6a
ELSE
Damage loading, go to 6b
6a. Damage unloading:
Update $d_{i,n}^{\pm} = d_{i,n-1}^{\pm}$ and $d_{j,n}^{\pm} = d_{j,n-1}^{\pm}$
Update $\tilde{\psi}_{i,n}^{\pm} = \tilde{\psi}_{i,n-1}^{\pm}$ and $\tilde{\psi}_{j,n}^{\pm} = \tilde{\psi}_{j,n-1}^{\pm}$
Go to 7
6b. Damage loading:
Compute normalized energy $\hat{\psi}_i^{\pm}$ and $\hat{\psi}_j^{\pm}$
Evaluate $d_{i,n}^{\pm}$ and $d_{j,n}^{\pm}$
Update $\tilde{\psi}_{i,n}^{\pm} = \psi_{i,n}^{\pm}$ and $\tilde{\psi}_{j,n}^{\pm} = \psi_{j,n}^{\pm}$
Go to 7
7. End forces and tangent stiffness:
Update the hinge force $\mathbf{q}_h$ from $\bar{\mathbf{q}}_h^{\pm}$
Update the end forces $\mathbf{q}_n$ from $\mathbf{q}_h$
Evaluate the tangent stiffness $\mathbf{k}_t$

Table 4.4: State determination algorithm of damage-plasticity column model

4.2.3 Model parameters

Parameters of the damage-plasticity column model are classified into two main categories:

(i) *Parameters of the effective constitutive relation*: These parameters vary with the element model in the effective space. In this study we select the NMYS column element with the following parameters: Young modulus E, cross-sectional area A, moment of inertia I, plastic axial capacity N_p, plastic flexural capacity M_p, kinematic hardening ratio H_{kr}, isotropic hardening parameter H_{ip}. The first 5 parameters depend on the geometry and material properties and do not require calibration.

(ii) *Damage parameters*: threshold coefficient C_{d0}, limit coefficient C_{d1}, evolution parameters d_{p1} and d_{p2}, cyclic degradation coefficient C_{wc}, coupling coefficient C_{cd}, axial-flexure interaction coefficient C_i. For each damage parameter, 4 different values can be specified for the response under positive and negative forces at spring i and j. The first 6 parameters are also present in the damage-plasticity beam model in Chapter 3, and only the last parameter is unique for the column model. The subsequent sections focus on the axial-flexure coefficient C_i and its effect on the strength and stiffness degradation under a combined axial and flexural action.

4.3 Illustrative Example

The following example studies the response of a W24x131 cantilever column in Figure 4.16 under a constant or variable axial force in combination with a monotonic or cyclic lateral displacement history at the free end. The objective is two-fold: (1) to illustrate the capabilities of the damage-plasticity column element, and (2) to investigate the effect of the axial-flexure interaction coefficient C_i on the strength and stiffness degradation. The column is modeled by one damage-plasticity column element with the following parameters: $c_1 = 2$, $c_2 = 2$, $c_3 = 3.5$, $c_4 = 2$, $c_5 = 2$; $H_{kr} = 0.02$, $H_{ip} = 1.5\text{e}{-4}$; $C^{\pm}_{d0} = 0$, $C^{\pm}_{d1} = 200$, $[d^{\pm}_{p1}, d^{\pm}_{p2}] = [2.8, 1.3]$, $C^{\pm}_{wc} = 0.1$, $C^{\pm}_{cd} = 0.3$, $C_i = 2$.

4.3.1 Monotonic response

First the column is subjected to a monotonic lateral displacement history and five separate cases of constant axial force $N/N_p = 0, -0.2, -0.4, -0.6, +0.4$. The moment-rotation relation in Figure 4.17(a) shows that the strength deterioration is the least severe under tension $N/N_p = +0.4$ and most severe under high compression $N/N_p = -0.8$. As the axial compression increases, (i) yielding initiates at a smaller moment, and (ii) the strength degradation is more severe. The yield strength reduction directly stems from the N-M interaction envelope. The more severe degradation results from an increase in the energy variable ψ in Equation (4.47), with the superscript '+' dropped for brevity. As the axial compression increases, the increase in the axial energy ψ_a overcomes the decrease in the flexural energy ψ_f and leads to an overall increase in the total energy ψ.

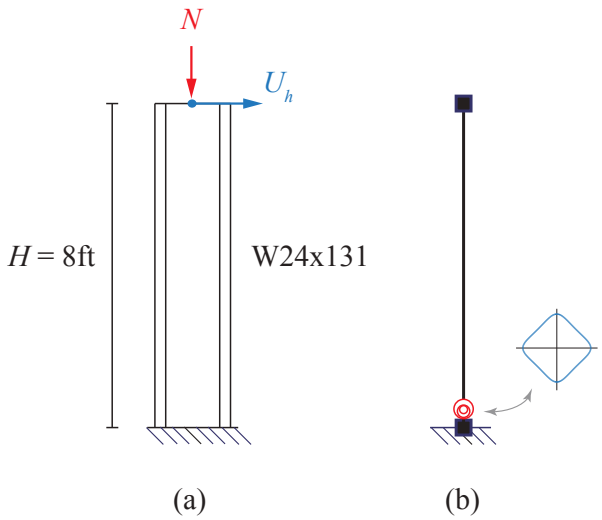

Figure 4.16: Cantilever column: (a) Structure and loading, (b) Idealized model

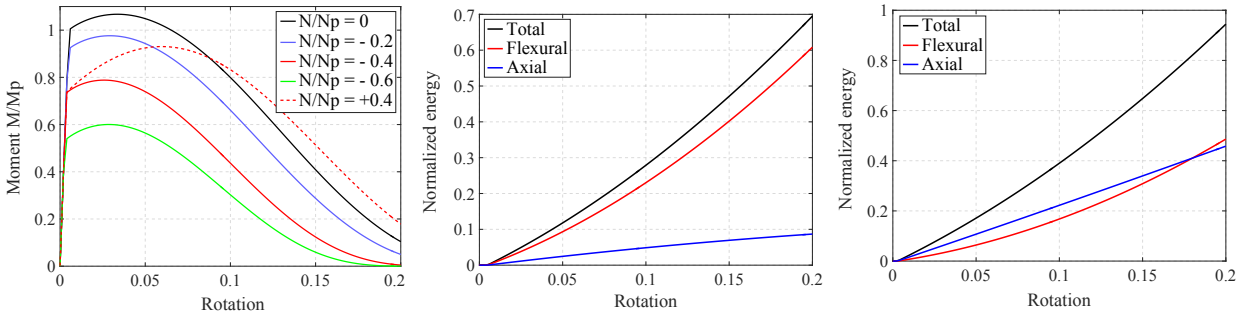

(a) Moment-rotation (b) $N/N_p = -0.2$ (c) $N/N_p = -0.6$

Figure 4.17: Monotonic response of cantilever column under different levels of axial force

Under the constant axial tension $N/N_p = +0.4$, the column yields at the same strength as under the compression $N/N_p = -0.4$ because of the symmetry in the N-M yield envelope. The column under tension, however, exhibits higher ductility than the other cases because the axial energy variable ψ_a neglects the tensile force N^+ and only considers the compressive force N^- in Equation (4.44).

The evolution of the total energy ψ and the contributions from the axial and the flexural response are demonstrated in Figure 4.17(b)-(c). The contribution from the axial response increases with the level of axial compression and $\psi_a \approx \psi_f$ under $N/N_p = -0.6$. It is clear in Equation (4.47) that ψ_a is proportional to the axial-flexure interaction coefficient C_i. A higher value of C_i leads to a higher value of ψ_a and, consequently, more severe strength deterioration. C_i must be selected properly to avoid excessive strength deterioration due to a high value of C_i as well as an unrealistic increase in ductility under a higher axial

compression due to a low value of C_i.

4.3.2 Cyclic response

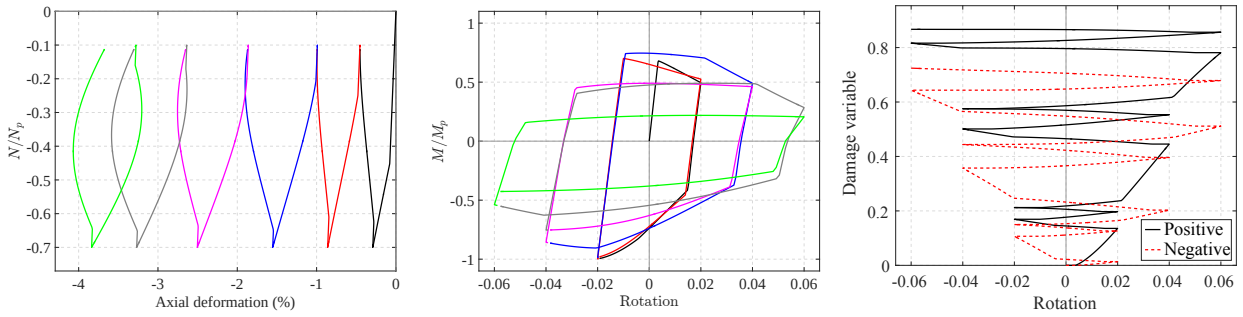

(a1) Axial force - deformation (a2) Moment - rotation (a3) Damage evolution

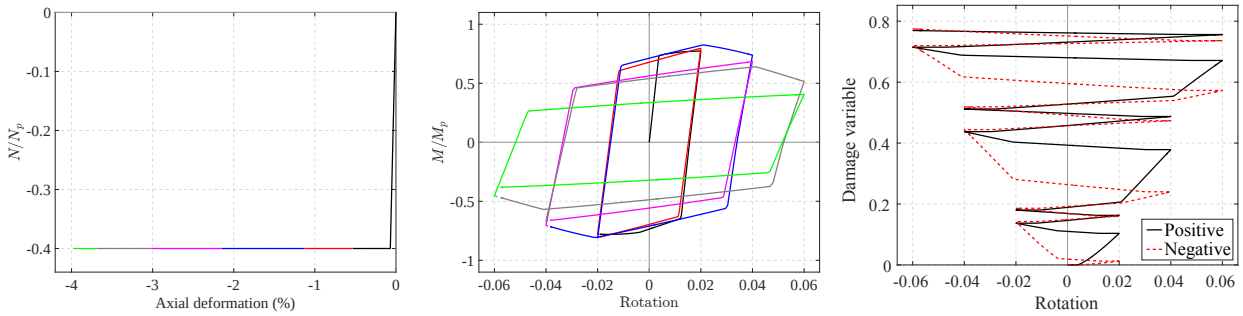

(b1) Axial force - deformation (b2) Momoment - rotation (b3) Damage evolution

Figure 4.18: Cyclic response comparison: (a) variable axial force $N/N_p = -0.4 \mp 0.3$, (b) constant axial force $N/N_p = -0.4$

The same cantilever column is subjected to a cyclic lateral displacement history at the free end and two separate axial load scenarios. The lateral displacement follows a cyclic pattern with drift ratios of 2%, 4%, 6%, in which the cycles are repeated once at each drift ratio. In the first axial load case, the axial compression remains constant $N/N_p = -0.4$. In the second load case, the column is subjected to a variable axial load history. The column is first subjected to an axial compression of $N/N_p = -0.4$, then a variable quantity $\mp 0.3 N_p$ is superimposed to represent the overturning effect in multi-story frames. The axial compression and lateral displacement are in-phase, that is, the axial force varies from $N/N_p = -0.7$ at the maximum positive drift to $N/N_p = -0.1$ at the maximum negative drift in each load cycle.

Figure 4.18 compares the column response in the two load patterns. Under the variable axial load, yielding takes place under a higher axial force than in the constant axial force scenario. Consequently, the yield moment is slightly lower, as Figures 4.18(a2)-(b2)

show. While the moment-rotation relation is relatively symmetrical under the constant axial force, the response is asymmetrical in the variable load pattern. The higher axial compression under positive rotations leads to more pronounced strength and stiffness degradation. The asymmetrical degrading behavior is also reflected in the damage evolution in Figures 4.18(a3)-(b3). The constant axial load gives comparable positive and negative damage variables d^+ and d^-, whereas under the variable axial load, the positive damage variable d^+ is higher. The positive damage variable d^+ in the variable load case exceeds both the damage variables d^+ and d^- under constant compression, which implies that it is important to account for the variable axial forces for more accurate damage assessment of steel columns.

It is noteworthy that with a higher value of C_i, the effect of axial compression would be amplified and the asymmetry in the moment-rotation relation and the damage evolution under variable axial forces would become more pronounced.

4.4 Comparison with Other Column Models

This section uses the same cantilever column in the Section 4.3 to compare the response of the damage-plasticity column element with two other column models commonly used in practice. Figure 4.19 illustrates the three modeling approaches in this comparison study: (i) Model CP with the proposed damage-plasticity column element, (ii) Model CP0 with a concentrated plasticity element without N-M interaction, and (ii) Model DP with a distributed plasticity element.

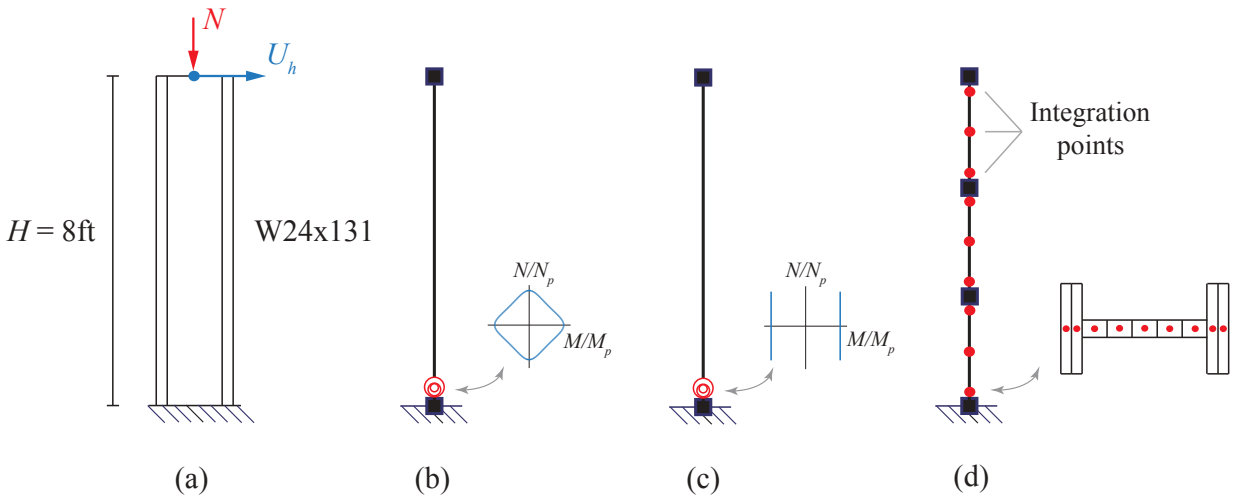

Figure 4.19: Modeling approaches for response simulation of a cantilever column: (a) Structure and loading, (b) Model CP, (c) Model CP0, (d) Model DP

Model CP0 assumes the axial force-deformation relation is linear elastic and the axial response is uncoupled from the flexural response, that is, the axial force does not affect the

yield strength and the strength deterioration. In this study, the damage-plasticity beam element in Chapter 3 is selected to represent this modeling approach. Model CP0 adopts the damage loading function and the evolution law in Chapter 3 to describe the strength softening in the stress-resultants.

Model DP uses 3 displacement-based distributed plasticity beam-column element to represent the cantilever column. Each element monitors the response at three sections along the element length, each of which is, in turns, discretized into 9 fibers: 2 in each flange and 5 in the web. The discretization scheme is calibrated a-priori to give consistent solutions with an equivalent model with one force-based element. The model adopts the 1d hysteretic damage model in Chapter 2 with a bilinear elastic-plastic model for the stress-strain relation the effective space [92].

4.4.1 Concentrated plasticity without N-M interaction

In the first example, the column assumes an elasto-plastic behavior in the effective space and is subjected to a variable axial force $N/N_p = -0.2 \mp 0.3$ and a cyclic displacement pattern with lateral drift ratios of $+1\%$, -2%, $+4\%$, -6% at the end of the half cycles. The same damage parameters are specified in the two models. Figure 4.20(a)-(b) compares the flexural response in the two models with and without damage. Due to the axial force, the yield moment is smaller in model CP than in model CP0. The variable axial force pattern results in the asymmetrical moment-rotation relation under positive and negative rotations in model CP, whereas the response in model CP0 is relatively symmetrical. Figure 4.20(c)-(d) compare the load path in both the effective space and the true space on an N-M interaction diagram defined by the yield surface parameters $c_1 = 2$, $c_2 = 2$, $c_3 = 3.5$, $c_4 = 2$, $c_5 = 2$. In the effective space, while model CP describes consistently the variation in the yield strength under variable axial forces and the load path remains on the envelope as plastic flow occurs, model CP0 does not capture the strength reduction and the load path penetrates the envelope. In both models, strength degradation shifts the load path horizontally toward the y-axis while maintaining the axial force to preserve equilibrium.

In the second example, the column assumes a linear kinematic hardening response and is subjected to a cyclic lateral displacement history with drift ratio amplitude of 2% and 4% and a variable axial load $N/N_p = -0.3 \pm 0.4$. The axial force ranges from $N/N_p = +0.1$ at the end of a half cycle in the negative direction to $N/N_p = -0.7$ in the positive direction. The modification factor $\lambda = 0.76$ is adopted to represent the constant strength reduction in model CP0 to match model CP at the first yield initiation, which correponds to $N/N_p = -0.38$ and $M/M_p = 0.76$.

Figure 4.21 compares the column response with and without damage in the two models. In model CP, the effect of the variable axial force on the effective response is evident in Figure 4.21(a) with the smaller moment under positive rotations due to the higher axial compression. Model CP0 fails to capture the variable axial force and gives a symmetrical effective response. The response comparison with damage in Figures 4.21(c)–(d) emphasizes

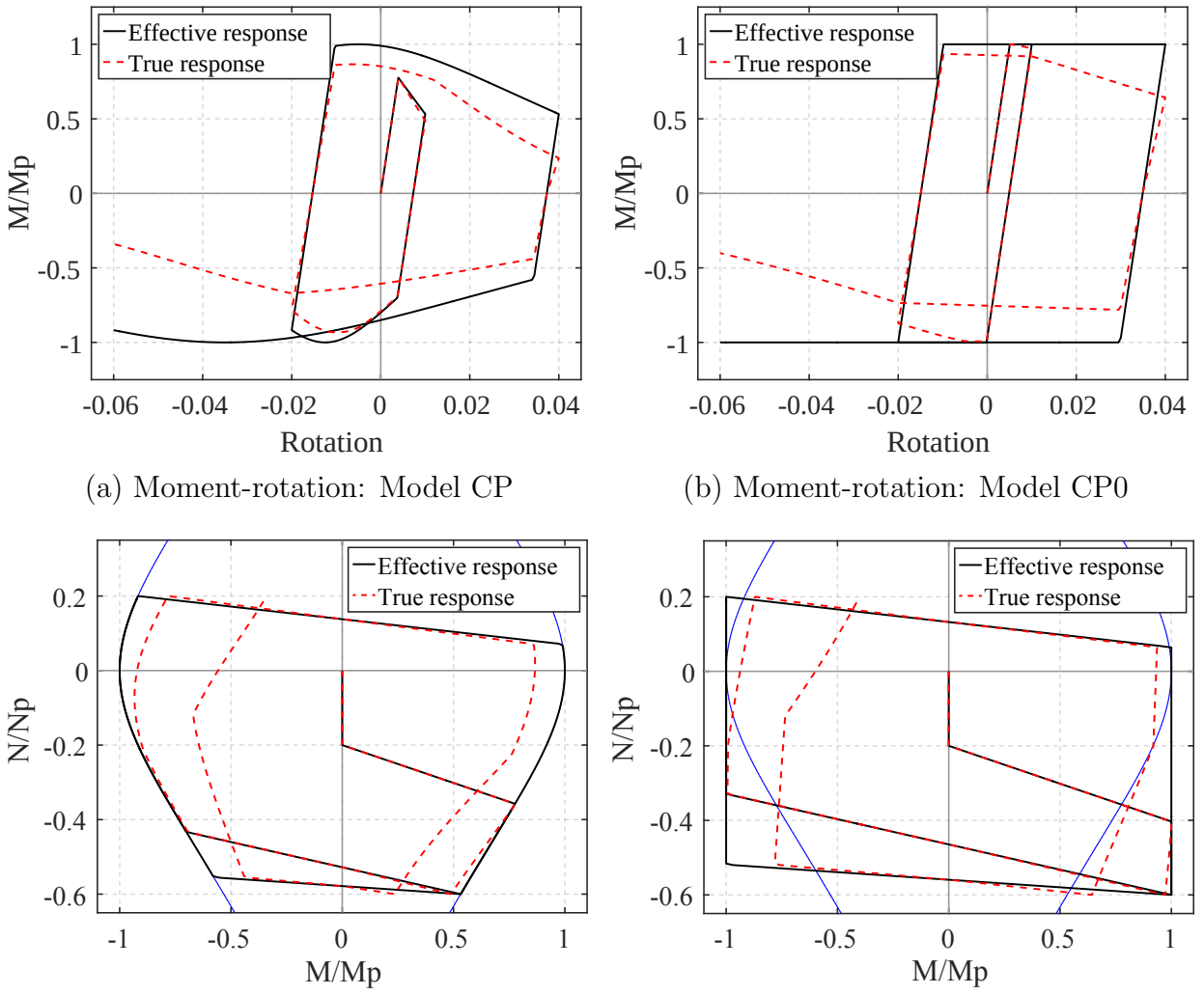

(a) Moment-rotation: Model CP

(b) Moment-rotation: Model CP0

(c) Load path: Model CP

(d) Load path: Model CP0

Figure 4.20: Response comparison of model CP and model CP0

the limitation of the model without the N-M interaction. Model CP0 overestimates the strength under positive rotations and underestimates the strength under negative rotations.

4.4.2 Distributed plasticity

In this case study, the cantilever column is subjected to a cyclic displacement history with drift ratios +2%, −2%, +4%, −4%, +6%, −6%, in which each amplitude is repeated once. Two levels of constant axial force are considered: $N/N_p = 0$ (no axial force) and $N/N_p = -0.2$. In contrast to the elasto-plastic effective response in the previous case study,

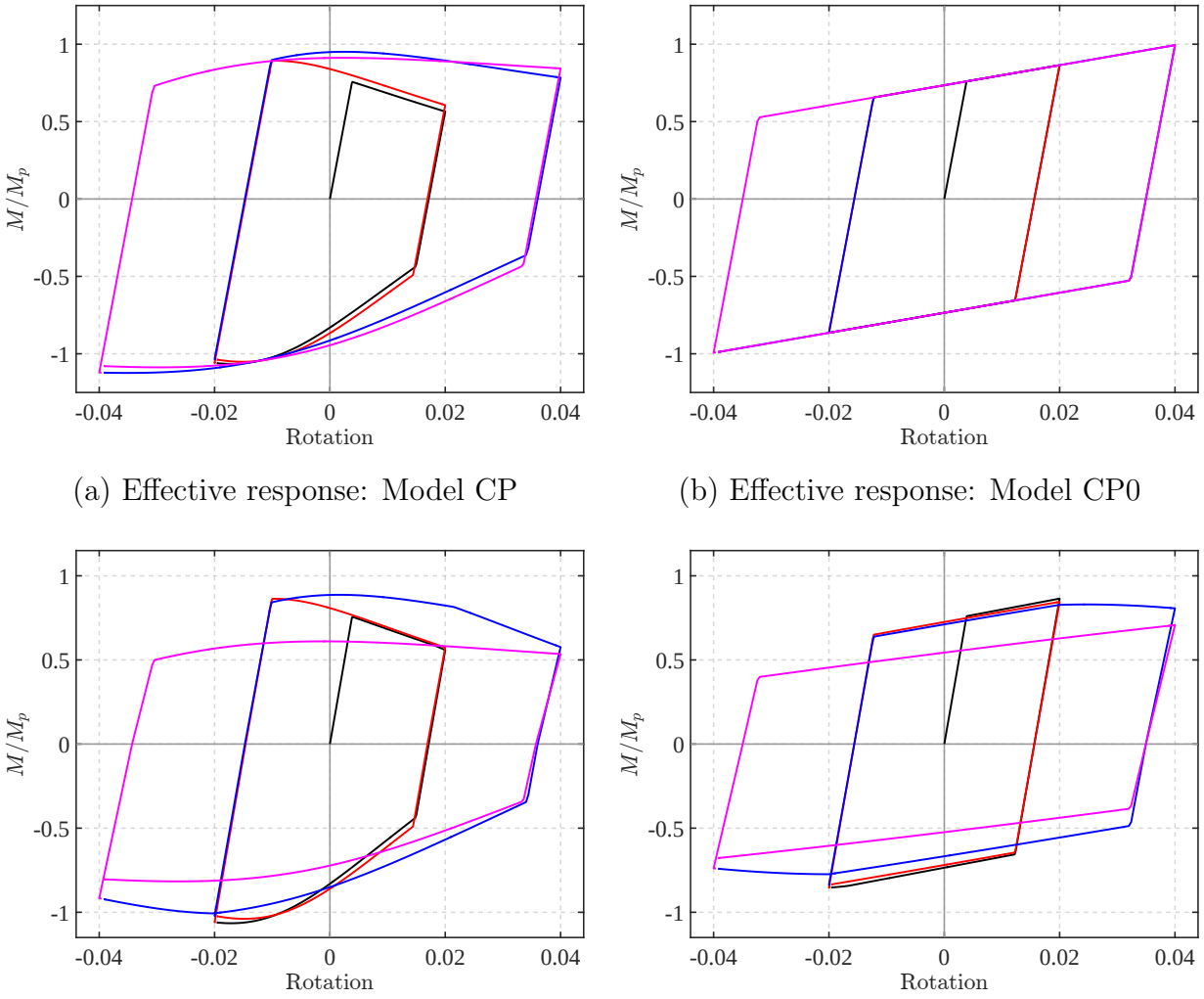

(a) Effective response: Model CP

(b) Effective response: Model CP0

(c) Degrading response: Model CP

(d) Degrading response: Model CP0

Figure 4.21: Comparison of cyclic response with variable axial compression

this example assumes a post-yield linear hardening behavior.

The following parameters are specified in model CP: $H_{kr} = 0.018$, $H_{ip} = 1.5\text{e}{-4}$, $\chi = 0$, $C_{d0}^{\pm} = 10$, $C_{d1}^{\pm} = 300$, $[d_{p1}^{\pm}, d_{p2}^{\pm}] = [2.5,\ 1.5]$, $C_{wc}^{\pm} = 0.12$, $C_{cd}^{\pm} = 0.3$, and $C_i = 4$. In model DP, the parameters of the effective response are the yield stress $s_y = 50$ ksi, kinematic hardening modulus $H_k = 2.2\%E$, and isotropic hardening modulus $H_i = 0.15\%E$. The damage parameters are $C_{d0}^{\pm} = 10$, $[C_{d1}^{+}, C_{d1}^{-}] = [650;\ 380]$, $[d_{p1}^{\pm}, d_{p2}^{\pm}] = [2.5,\ 1.5]$, $C_{wc}^{\pm} = 0.12$, $C_{cd}^{\pm} = 0.3$. A smaller value is specified for the negative limit coefficient, $C_{d1}^{-} < C_{d1}^{+}$, to represent a more rapid degradation in the fiber stress-strain relation due to local buckling under high compressive stresses. Figure 4.22 shows a sample cyclic stress-strain relation.

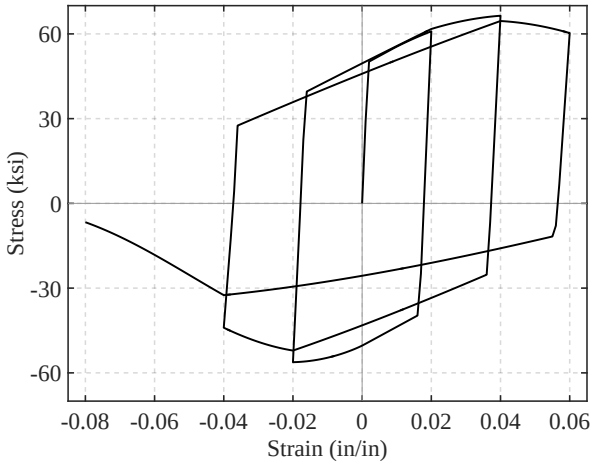

Figure 4.22: Sample stress-strain relation

Figure 4.23 shows that model CP replicates very well the response of model DP under $N/N_p = 0$. Model CP underestimates the increase in the bending moment from cyclic hardening in the early cycles under $N/N_p = -0.2$. The description of the hardening behavior can be improved with a plastic hinge offset from the column base to modify the yield strength. However, this is not pursued further in this study. Nonetheless, model CP captures rather well the strength and stiffness deterioration in the column response in both load scenarios.

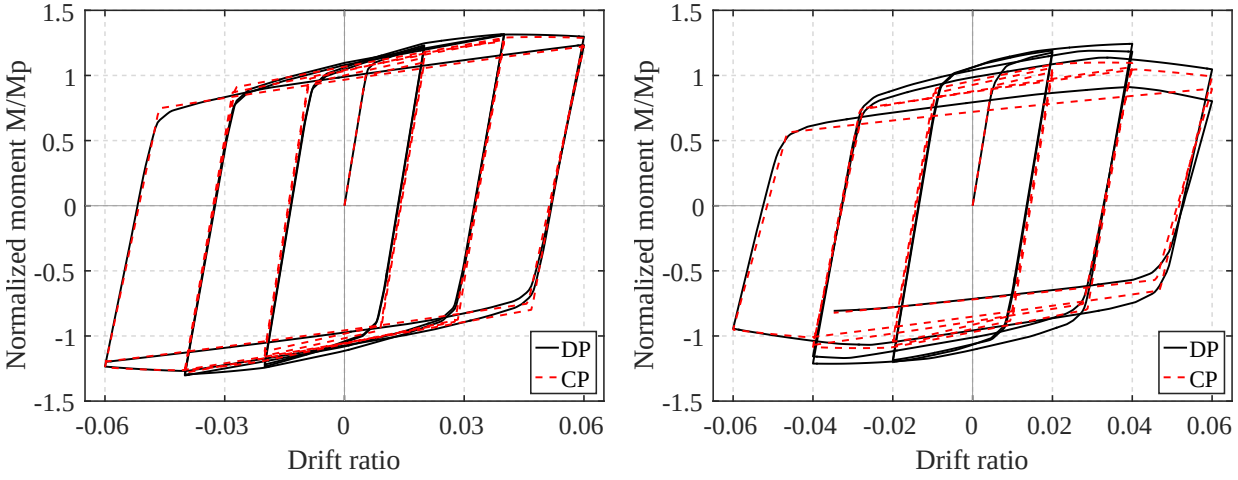

(a) $N/N_p = 0$ (b) $N/N_p = -0.2$

Figure 4.23: Comparison of cyclic response of cantilever column

It is noteworthy that similar values for $C_{d0}^{\pm}$, $C_{wc}^{\pm}$, $C_{cd}^{\pm}$, $d_{p1}^{\pm}$, $d_{p2}^{\pm}$ are used in both models, while the values for the limit coefficient $C_{d1}^{\pm}$ are different. The key distinction in the two

models is that while the parameters of model CP describe directly the force-deformation relation of the 'global' stress-resultants, the parameters of model DP describe the stress-strain relation of the 'local' fibers, which are then integrated in the sections and along the element length to evaluate the 'global' response. For a direct comparison of the damage evolution, a single 'damage index' is derived for each model to represent the level of strength and stiffness deterioration at the base of the cantilever column.

Model CP defines the damage index D_{CP} as a combination of the two damage variables d^+ and d^- that represent the strength and stiffness deterioration under positive and negative moments.

$$D_{CP} = \frac{d^+ w^+ + d^- w^-}{w^+ + w^-} \tag{4.58}$$

where the integration weights $w^\pm$ are equal to the corresponding damage variables $d^\pm$.

In model DP, the following notations are defined: the *fiber* damage variables $d_f^\pm$, the *section* damage variables $d_s^\pm$, and the *element* damage variables $d_e^\pm$. The fiber damage variables $d_f^\pm$ are readily available from the material state determination, while the section damage variables $d_s^\pm$ and the element damage variables $d_e^\pm$ are given by integration of the fiber response, as Figure 4.27 illustrates. Figure 4.24 illustrates the section discretization at the column base.

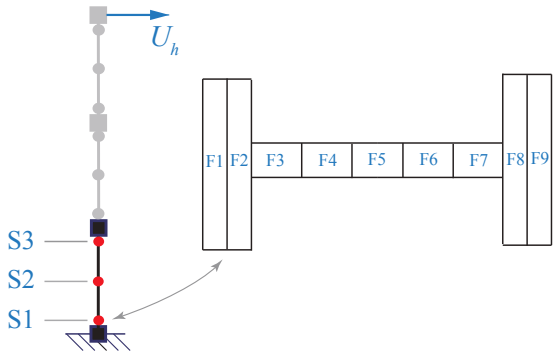

Figure 4.24: Numbering of fibers in cross-section of DP model

Figure 4.25 and Figure 4.26 plot representative stress-strain relation and the fiber damage variables d_f in fiber F1, F4, F9 at the column base without axial force $N/N_p = 0$ and with axial force $N/N_p = -0.2$, respectively. In the former scenario, the strain history is relatively symmetric, whereas in the latter case, the initial compression leads to an asymmetric strain history biased toward the compression side. With the axial compression, the fiber damage state is asymmetric with higher strength and stiffness deterioration under compressive stresses. These observations highlight that the axial compression has a tremendous impact on the fiber behavior as well as the global response.

Let nIP denote the number of fibers in a section and $w_f^\pm$ the integration weights representing the contribution of each fiber to the section damage variables $d_s^\pm$. The section

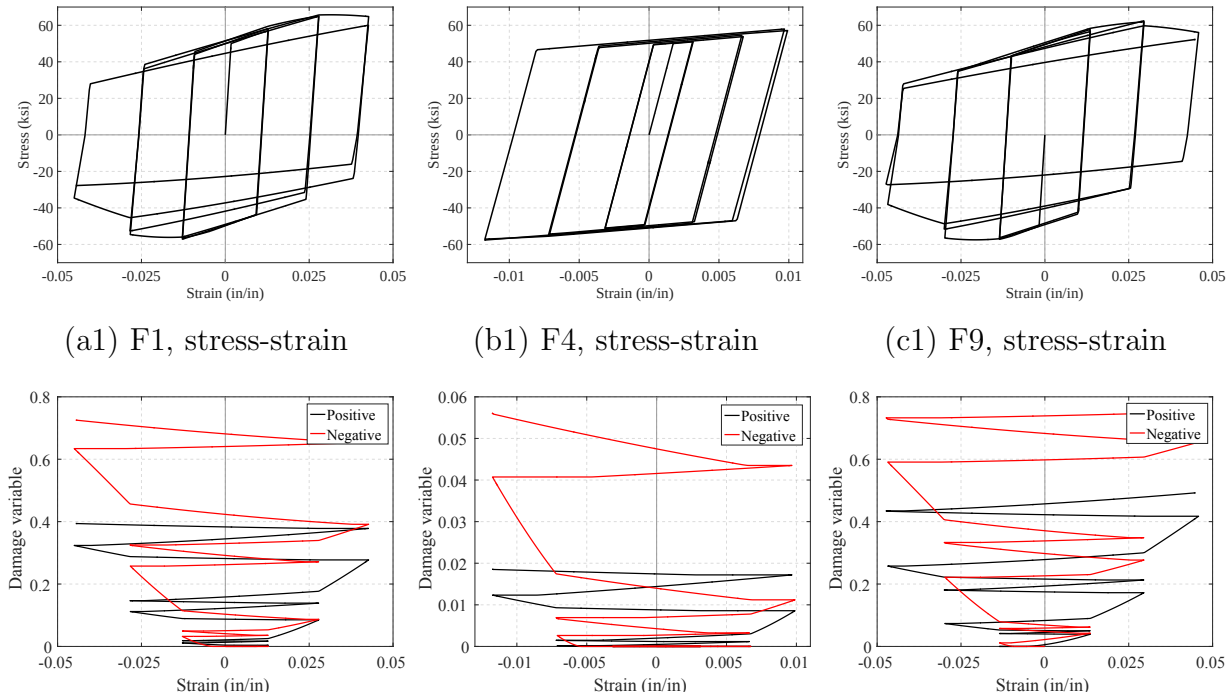

(a1) F1, stress-strain (b1) F4, stress-strain (c1) F9, stress-strain

(a2) F1, damage evolution (b2) F4, damage evolution (c2) F9, damage evolution

Figure 4.25: Sample fiber response under $N/N_p = 0$

damage variables $d_s^{\pm}$ are defined as weighted averages of the fiber damage:

$$d_s^+ = \frac{\sum_{f=1}^{nIP} d_f^+ w_f^+}{\sum_{f=1}^{nIP} w_f^+} \qquad d_s^- = \frac{\sum_{f=1}^{nIP} d_f^- w_f^-}{\sum_{f=1}^{nIP} w_f^-} \tag{4.59}$$

where $w_f^{\pm} = 1$ is assumed in this study to imply equal contributions from the fibers.

The element damage variables $d_e^{\pm}$ are defined as weighted averages of the section damage variables along the element length. Let $w_s^{\pm}$ denote the integration weights representing the contribution of each section to the element damage $d_e^{\pm}$. To account for the damage localization in a particular section, the coefficients $w_s^{\pm}$ are assumed equal to $d_s^{\pm}$ to assign more weights to the heavily damaged sections.

$$d_e^+ = \frac{\sum_{s=1}^{nIP} d_s^+ w_s^+}{\sum_{s=1}^{nIP} w_s^+} \qquad d_e^- = \frac{\sum_{s=1}^{nIP} d_s^- w_s^-}{\sum_{s=1}^{nIP} w_s^-} \tag{4.60}$$

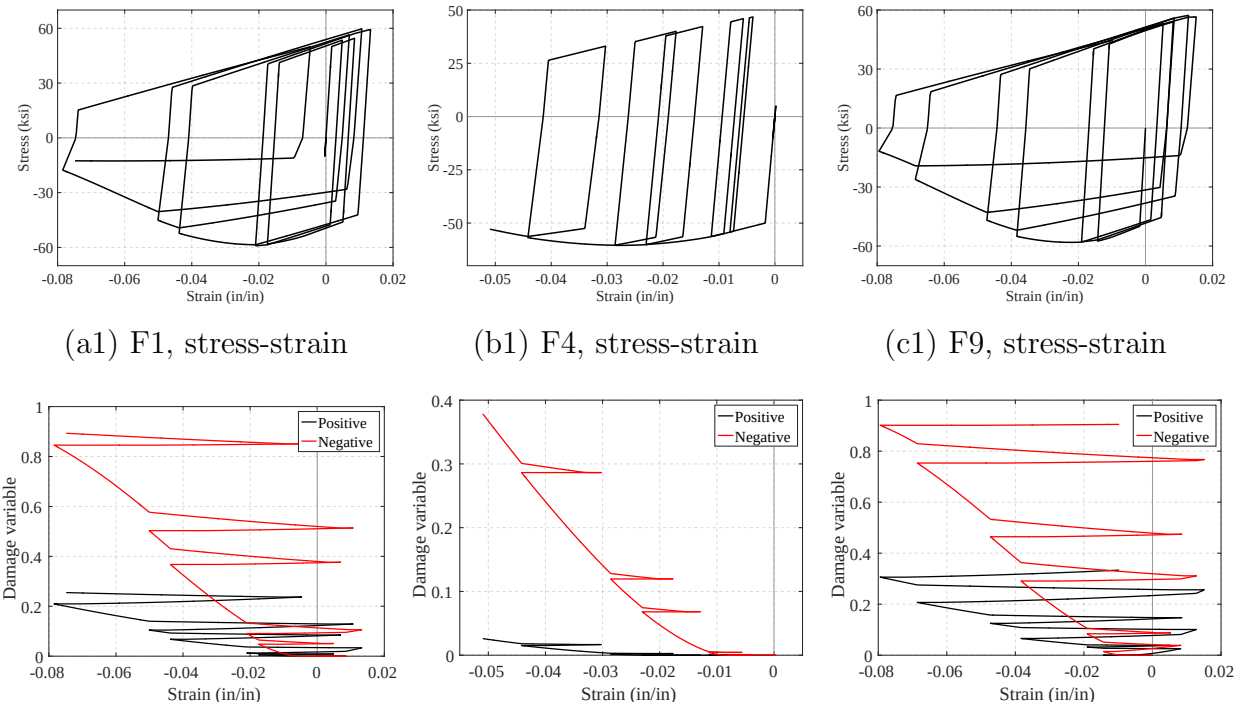

(a1) F1, stress-strain (b1) F4, stress-strain (c1) F9, stress-strain

(a2) F1, damage evolution (b2) F4, damage evolution (c2) F9, damage evolution

Figure 4.26: Sample fiber response under N/N_p = -0.2

The damage indices $D_{DP}^{\pm}$ are weighted averages of the element damage variables $d_e^{\pm}$ among all ne elements:

$$D_{DP}^{+} = \frac{\sum_{e=1}^{ne} d_e^{+} w_e^{+}}{\sum_{e=1}^{ne} w_e^{+}} \qquad D_{DP}^{-} = \frac{\sum_{e=1}^{ne} d_e^{-} w_e^{-}}{\sum_{e=1}^{ne} w_e^{-}} \tag{4.61}$$

where $w_e^{\pm}$ denote the integration weights of the positive and the negative response. The weights are assumed equal to the corresponding damage variables, $w_e^{+} = d_e^{+}$ and $w_e^{-} = d_e^{-}$.

Finally, a single global damage index D_{DP} is defined by combining the positive and the negative variables $D_{DP}^{\pm}$.

$$D_{DP} = \frac{D_{DP}^{+} w_{DP}^{+} + D_{DP}^{-} w_{DP}^{-}}{w_{DP}^{+} + w_{DP}^{-}} \tag{4.62}$$

where $w_{DP}^{\pm}$ denotes the integration weights of the positive and the negative damage variables and are set equal to the corresponding damage variables.

Figure 4.27 illustrates the relation between the global and local damage variables in model DP, with the superscript $\pm$ of the damage variables and integration weights dropped for brevity.

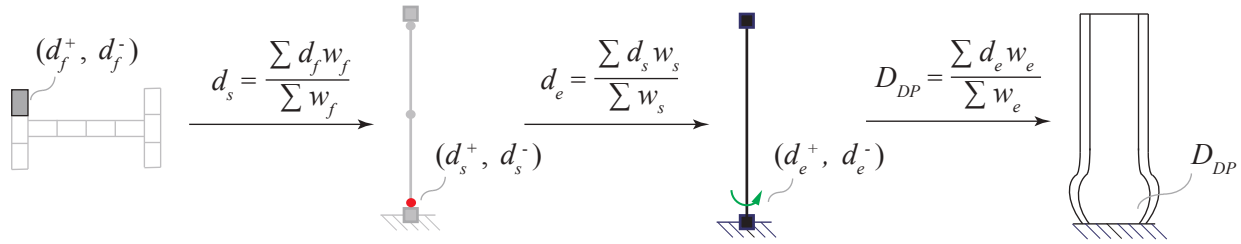

Figure 4.27: Damage measures of DP model

Figure 4.28 shows the same trend in the evolution of the damage indices D_{DP} and D_{CP}. Both exhibit several instants with rapid 'jumps' as well as those with slower damage accumulation. The former correspond to the primary cycles in which the previous minimum or maximum deformation is exceeded and the latter correspond to the follower cycles with the current deformation bounded by the previous minimum or maximum values. The excellent agreement in Figure 4.28 implies the equivalence in the damage description in the two models and justifies the use of damage mechanics for stress-resultants.

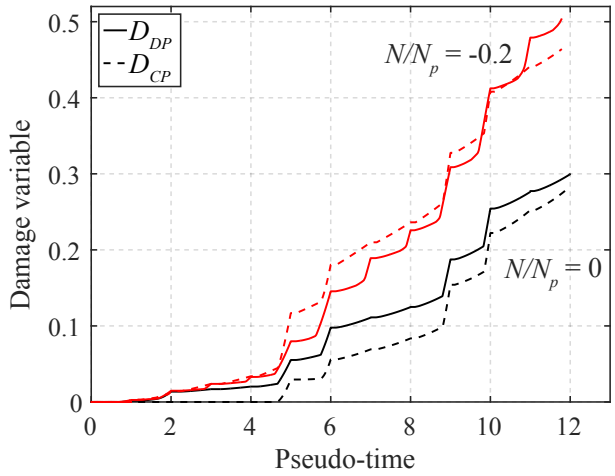

Figure 4.28: Comparison of damage variables D_{CP} and D_{DP}

It is noteworthy to point out that the goal of this example is to showcase the capability of the proposed model to replicate the response of a more sophisticated model widely used in practice. The comparison, however, does not strive to prove or disprove the validity of the proposed model based on the advantages or the limitations of the distributed plasticity models. A detailed study of the distributed plasticity models is beyond the scope of this study. The validation of the proposed model is discussed in the next section through calibrations against experimental measurements of steel columns.

4.5 Validation Studies

This section presents three case studies to validate the proposed damage-plasticity column element against experimental results of steel column components. The simulations investigate the model's ability to describe the effect of the axial load variation on the strength and stiffness degradation as well as on the axial shortening. In all three cases, the test configuration involves wide-flange steel columns that are restrained at one or both ends and sufficiently supported to prevent out-of-plane movement. The columns are subjected to constant or variable axial compression and cyclic lateral displacements at one end. The case studies do not strive for exhaustive accuracy in the simulations but attempt to convey to the readers the new element model's potential to capture sufficiently the unique hysteretic behaviors of steel columns up to failure.

4.5.1 Columns by Lignos [56]

Two sets of cantilever column specimens, W14x82 and W16x89, from the experimental campaign by Lignos et al. [56] are selected in this case study. The parameters used in the simulations of the W16x89 column are: $c_1 = 2$, $c_2 = 2$, $c_3 = 2.95$, $c_4 = 2$, $c_5 = 1.33$, $H_{kr} = 0.01$ and $H_{ip} = 5e-4$, $\chi = 0$, $C_{d0} = 15$, $C_{d1} = 200$, $C_{wc} = 0.15$, $C_{cd} = 0.6$, $[d_{p1}, d_{p2}] = [3.5, 1.5]$, $C_i = 2.75$. Same damage parameters are used to simulate the response of the W14x82 column, except for the limit coefficient $C_{d1} = 205$ and the axial-flexure interaction coefficient $C_i = 2.5$.

4.5.1.1 Monotonic response

Figure 4.29 compares the monotonic moment-rotation of the two column sections under different level of constant axial compression. The numerical solutions are shown in dashed lines and the experimental results are in solid lines.

The column model is able to capture the yield strength of different column sections and under different axial load levels. Under the same compression $N/N_p = -0.3$, the W14x82 column has a smaller yield strength than the W16x89 column due to the section geometry. For the same W16x89 column section, the yield strength decreases as the axial compression increases from $N/N_p = -0.3$ to $N/N_p = -0.5$. This is captured well by the N-M yield envelope.

The model describes well the different ductility capacities of the W14x82 and W16x89 columns under the same axial compression $N/N_p = -0.3$. This results from the fact that the W14x82 section is more compact than the W16x89 section. This is captured with a higher value of the limit coefficient C_{d1} and a lower value of the axial-flexure interaction coefficient C_i for the W14x82 specimen.

For the W16x89 column, the axial-flexure interaction coefficient $C_i = 2.75$ captures quite well the strength reduction due to the increase in axial compression. In the softening range, however, the numerical model underestimates the damage under $N/N_p = -0.5$. This suggests

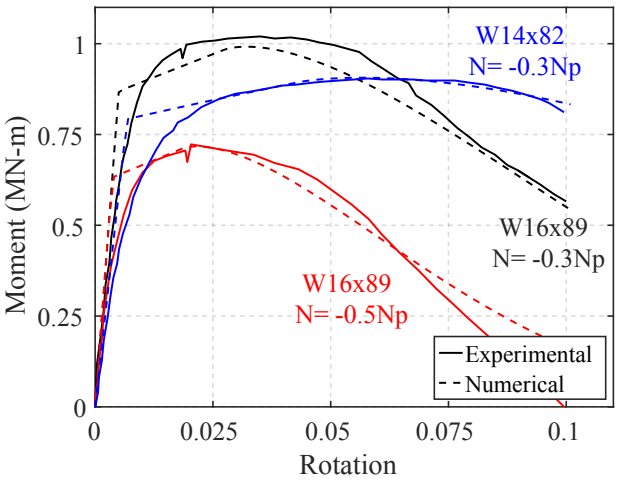

Figure 4.29: Response under constant axial compression and monotonic lateral displacement

that to improve the result, instead of specifying a constant value for C_i, the parameter could be defined as a function of the axial response, for instance, C_i increases under higher axial compression. This is not pursued further and left for future investigation. As expected, the numerical solutions also show discrepancies in the transition from the elastic to the plastic range, which is a typical limitation of the linear hardening assumption. This can be addressed by introducing a nonlinear hardening rule, such as with generalized plasticity [7].

4.5.1.2 Effect of axial load level on damage

The W14x82 column is subjected to a cyclic lateral displacement history under two separate cases of constant axial compression: $N/N_p = -0.5$ and $N/N_p = -0.75$. The same parameters in the monotonic cases are used for the simulations. The yield surface coefficients capture the yield strength reduction with increasing axial compression. The significant post-yield cyclic hardening in the first few cycles in both load cases are simulated relatively well by the isotropic hardening parameter H_{ip} and the damage threshold coefficient C_{d0} to delay the onset of strength deterioration. The axial-flexure interaction coefficient C_i allows the model to sufficiently distinguish the ductility capacity in the two load scenarios.

Although the numerical solutions do not capture exactly the strength at some load reversals, the unloading stiffness in the last few cycles, and the brittle failure in the last cycle, overall the damage-plasticity column model represents well the main characteristics of the response in Figure 4.30. To simulate the sharp strength reduction in the last half cycle, the damage evolution law could be modified to accommodate the sudden damage increment due to the brittle failure. This is, however, beyond the scope of this study.

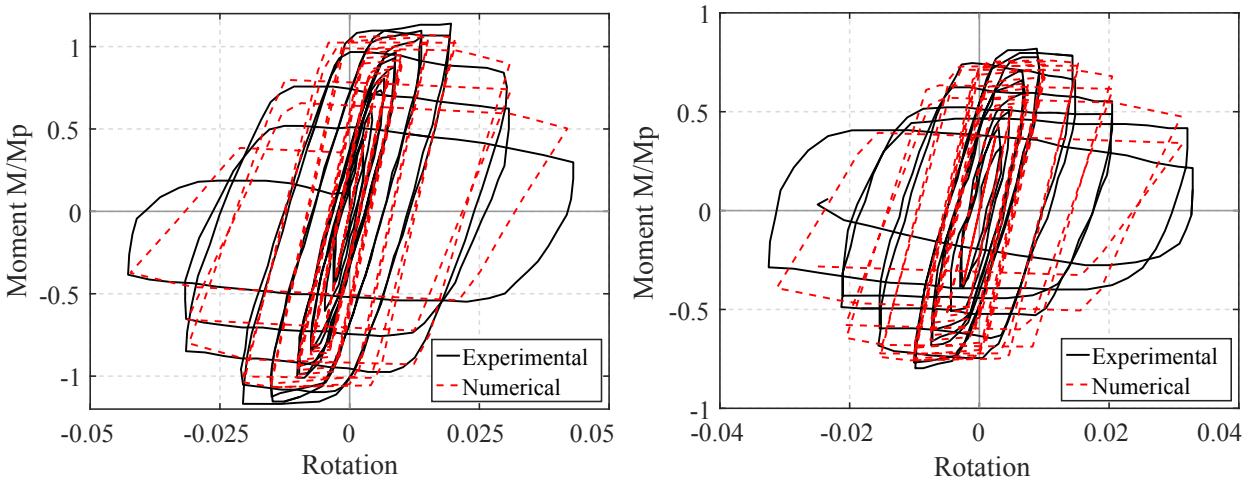

(a) W14x82, $N/N_p = -0.5$ (b) W14x82, $N/N_p = -0.75$

Figure 4.30: Effect of axial load level on cyclic response of steel column

4.5.1.3 Effect of axial load history on damage

The W16x89 column is subjected to two separate axial load patterns: (1) the axial compression remains constant throughout the load history at 50% the plastic axial capacity $N/N_p = -0.5$, and (2) the column is first subjected to the same axial compression $N/N_p = -0.5$, then the compression varies from 25% the plastic capacity $N/N_p = -0.25$ to 75% the capacity $N/N_p = -0.75$.

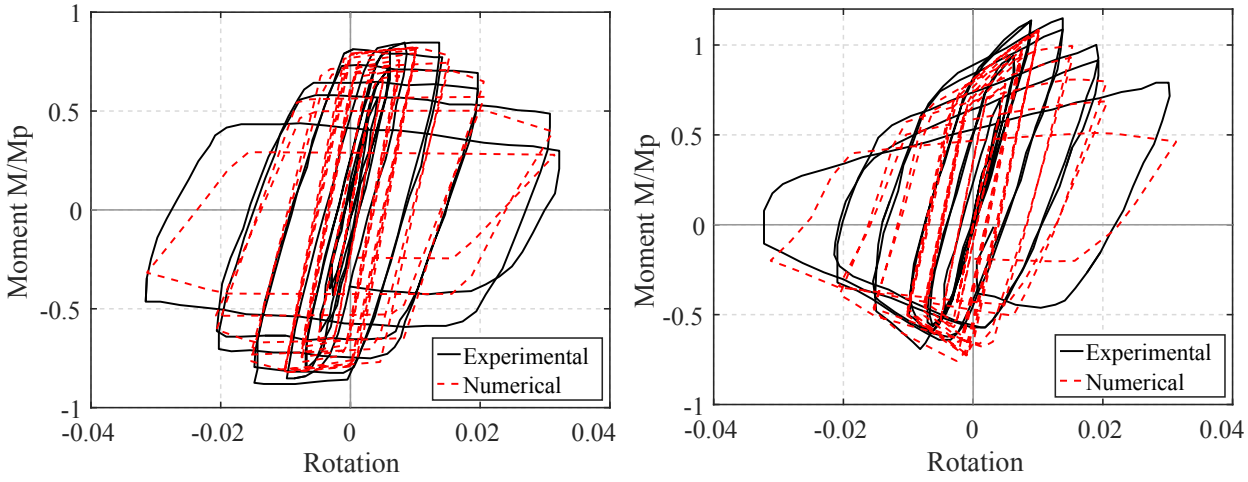

(a) W16x89, $N/N_p = -0.5$ (b) W16x89, $N/N_p = -0.5 \pm 0.25$

Figure 4.31: Effect of variable axial load on cyclic response of steel column

Figure 4.31 compares the moment-rotation relation in the two load scenarios. The numerical solution simulates rather well the asymmetrical response under the variable axial force. Compared to the constant load case in Figure 4.31(a), the response under variable axial force shows less degradation under positive rotations and more degradation under negative rotations.

The model, however, underestimates the positive moments in the variable load pattern. This observation implies that under positive rotations, the model overestimates the axial contribution ψ_a^+ to the total energy dissipation ψ^+, and in turns, overestimates the positive damage variable d^+. As recommended in the monotonic load case, to enhance the accuracy, the interaction coefficient C_i may be defined as an evolutionary function of the axial force level.

4.5.1.4 Axial shortening

The axial shortening has a tremendous impact on the column strength and stiffness deterioration as well as the global stability [60, 97]. The plastic axial deformation contributes to the axial energy, and ultimately affects the total energy and the damage variables. Figure 4.32 shows the axial shortening of the W14x82 column under a relatively high axial compression $N/N_p = -0.75$.

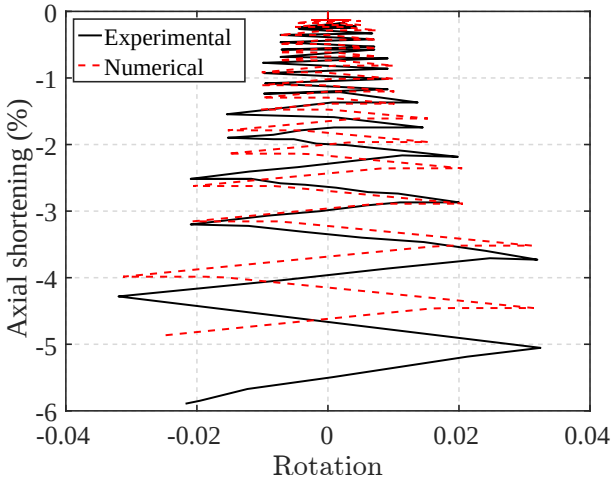

Figure 4.32: Axial shortening of steel column under constant axial load

The numerical solution captures very well the experimental response up to a rotation of 0.02 and underestimates the axial deformation in the last two half cycles, in which the column exhibits substantial shortening at the onset of fracture. The discrepancies in the axial shortening at the end of the load history is approximately 1% the column height, which is relatively minor.

4.5.2 Columns by MacRae [59]

This case study investigates the cyclic response of the steel cantilever columns from the experimental campaign by MacRae [59]. Four axial compression levels are selected for the simulations: $N/N_p = -0.3, -0.5, -0.6, -0.8$. The columns are referred to as C3, C5, C6, C8, which correspond to the axial compression level.

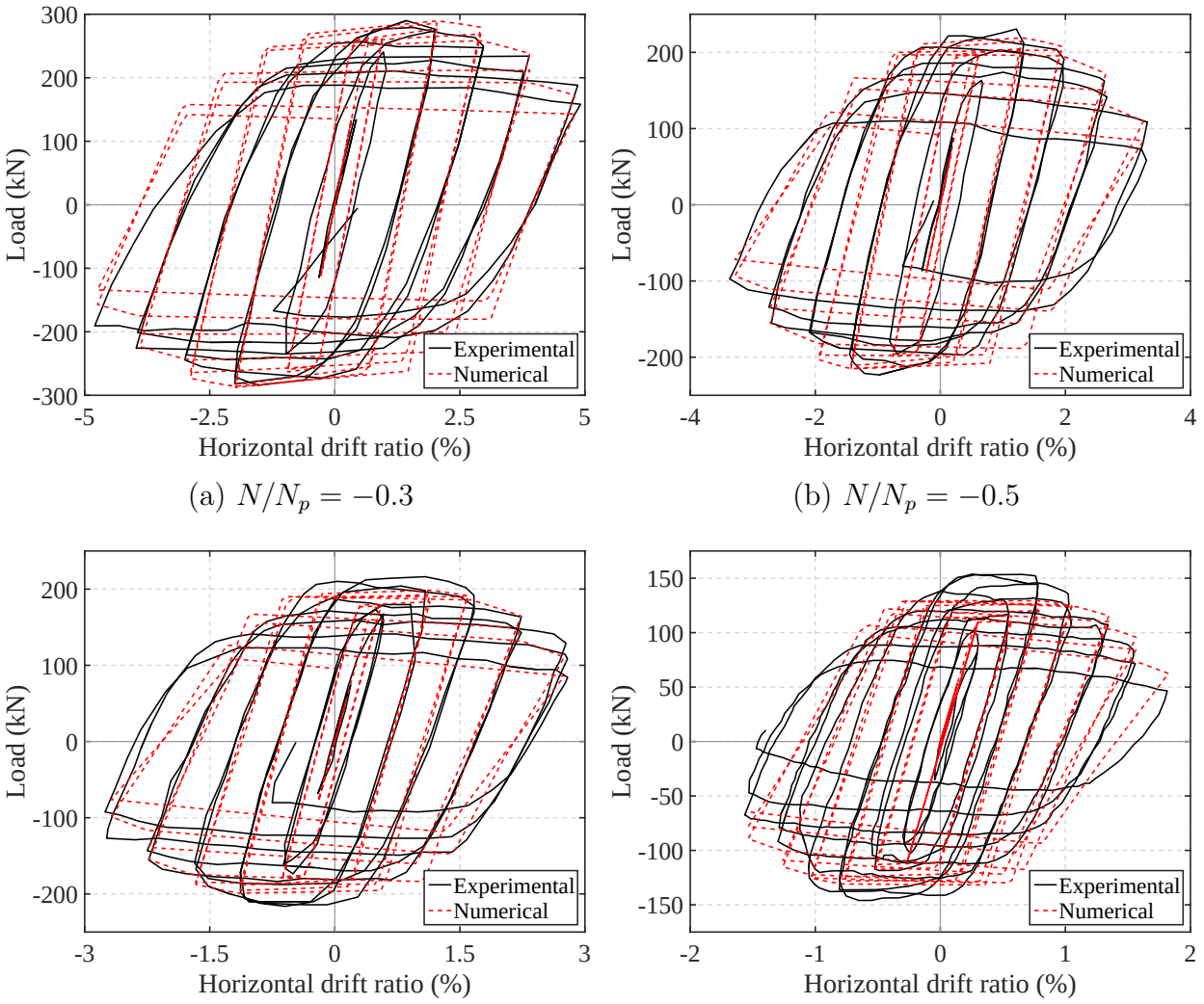

(a) $N/N_p = -0.3$ (b) $N/N_p = -0.5$

(c) $N/N_p = -0.6$ (d) $N/N_p = -0.8$

Figure 4.33: Cyclic response of steel columns under constant axial load

The following parameters are used to simulate the response of the four specimens: $c_1 = 2$, $c_2 = 3$, $c_3 = 4$, $c_4 = 2$, $c_5 = 2.5$, $H_{kr} = 0.02$, $H_{ip} = 2e-4$, $\chi = 0$, $C_{d0} = 10$, $C_{d1} = 175$, $C_{wc} = 0.15$, $C_{cd} = 0.5$, $C_i = 3$. Figure 4.33 plots the load-drift relation for the four load cases. Overall, the element model captures the reduction in strength, stiffness,

and displacement ductility with increasing axial compression with reasonable accuracy. The post-yield cyclic hardening behavior in early cycles prior to softening is represented better in the cases with lower axial compression. The model predicts particularly well the peak strength under $N/N_p = -0.3$ and $N/N_p = -0.5$, but underestimates the peak positive load under high axial compression $N/N_p = -0.8$. The discrepancies in the case of high axial compression $N/N_p = -0.8$ supports the earlier suggestion to specify the damage parameters as evolutionary functions of the damage states instead of as constants.

Figure 4.34(a) plots the evolution of the positive damage variable d^+ under $N/N_p = -0.3$. The red dashed lines in Figure 4.34(a) represent two envelopes for the damage variables. The envelope on the right indicates the maximum values for the positive damage variable d^+ and the envelope on the right corresponds to the maximum values for the negative damage variable d^-. The envelopes show two distinct characteristics in primary and follower cycles. In primary cycles, damage evolves as the cumulative maximum or minimum drift ratios increase, which is reflected in the diagonal segments of the damage envelopes. In follower cycles, damage evolves as the cumulative maximum or minimum drift ratios remain unchanged, which is reflected in the vertical segments of the damage envelopes. The damage increment in each vertical segment represents the amount of cyclic degradation due to repeated load cycles.

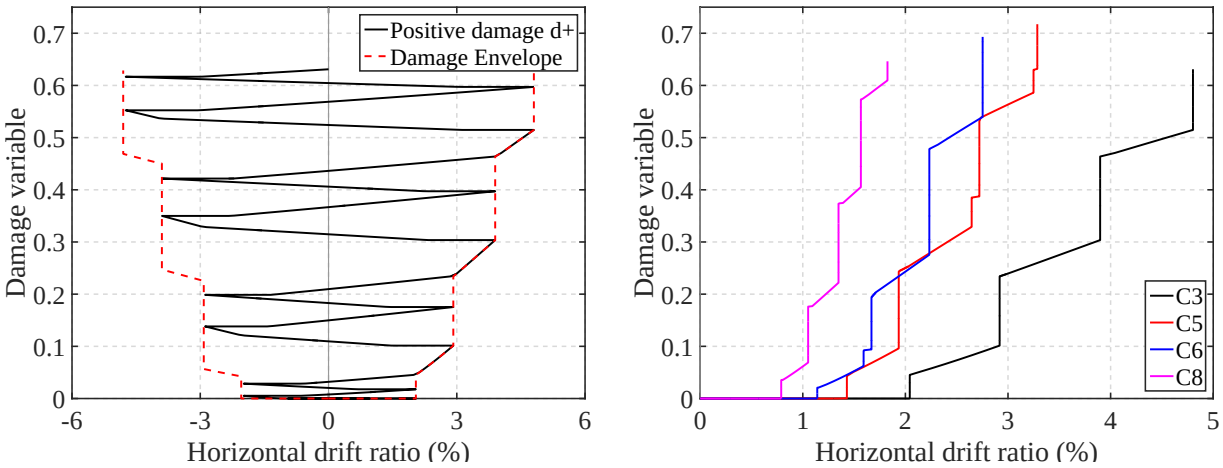

(a) Damage envelopes of specimen C3 (b) Comparison of damage evolution

Figure 4.34: Damage evolution of steel column specimens

Figure 4.34(b) compares the positive damage envelope in the four load patterns. Under the same drift ratio, the higher axial compression induces more severe damage. Alternatively, to reach the same damage level, the column under a smaller axial compression can withstand a higher drift ratio. This implies a more gradual degradation and higher ductility capacity under smaller axial forces. It is noteworthy that the column failure when the experiments terminated corresponds to a damage value of approximately 0.6 in all four specimens. This suggests a possible damage threshold to represent the failure of steel columns.

4.5.3 Columns by Newell and Uang [66]

This example studies the strength and stiffness deterioration in stockier columns. Two column sections W14x176 and W14x233 from the experimental program by Newell and Uang [66] are selected for illustration. Both column ends are restrained with base plates and strengthened by haunch stiffeners. First, a compression of $N/N_p = -0.15$ is imposed to represent the effect of gravity loading. Then, the lateral drift and variable axial force are applied in-phase to reach a target axial force. The specimens are designated by the cross section size and the target axial load. For instance, W14x176-55 refers to the W14x176 column under a variable axial force pattern with the maximum target of 55% the plastic axial capacity: $N/N_p = -0.15 \pm 0.4$.

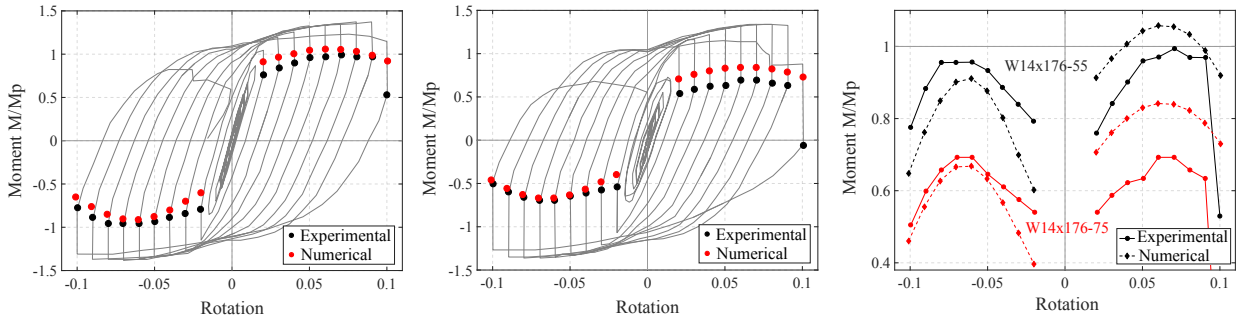

(a1) W14x176-55 (b1) W14x176-75 (c1) W14x176

(a2) W14x233-35 (b2) W14x233-55 (c2) W14x233

Figure 4.35: Cyclic response of steel column under variable axial compression

It was reported that during the tests, the load pattern was modified because the axial force and the lateral drift were not applied in-phase due to limitations of the experimental setup. It was verified analytically, however, that both the modified and the original protocols give comparable response at the end of each half cycle when the target axial force and drift are obtained [66]. In this study, the original protocol is adopted. Due to the discrepancies in the load patterns, only the force at the end of each half cycle is relevant for comparison. The following parameters are used in the simulations: $H_{kr} = 0.05$, $H_{ir} = 3\text{e}{-5}$, $\chi = 0$,

$C_{d0} = 10$, $[d_{p1}, d_{p2}] = [3, 1.5]$, $C_{cd} = 0.6$, $C_{wc} = 0.15$. For specimen W14x176, $C_{d1} = 220$ and $C_i = 1.5$, and for specimen W14x233, $C_{d1} = 270$ and $C_i = 1$. Figures 4.35(a)-(b) compare the bending moment at the end of each half cycle for the four specimens. Figure 4.35(c) highlight the magnitude of the moment under positive and negative drift ratios normalized by the corresponding plastic capacity.

The comparison gives rise to three observations. First, the strength reduction due to the higher axial compression is less pronounced in stockier columns with a more compact cross section. This is evident in Figure 4.35(c) as the black curves are above the red curves for both specimens and the deviation between the two is smaller for the W14x233 specimens. The model captures this feature with a higher limit coefficient C_{d1} and a smaller axial-flexure interaction coefficient C_i for the W14x233 specimens. Second, the different ductility capacity in the two columns is captured sufficiently by the model. While the W14x176 columns reach the peak strength and exhibit strength softening at drift ratio of 0.07, the W14x233 columns do not show strength reduction even at large drift ratios. Third, the asymmetrical response due to the variable axial load history is less pronounced than observed in the previous case studies, implying that the effect of axial forces on the strength deterioration is less significant in stockier columns. This is reflected in the relatively low values of the axial-flexure interaction coefficient C_i. The numerical solutions, however, slightly underestimate the negative moments and overestimate the positive moments. This suggests that separate coefficients C_i^+ and C_i^- for the response under positive and negative moments may be worthwhile.

4.5.4 Remarks on parameter C_i

The section concludes with a discussion on the axial-flexure interaction coefficient C_i. Table 4.5 lists the parameter values and summarizes the relevant properties of the column specimens in the previous simulations.

Section	$\mathbf{b_f/2t_f}$	$\mathbf{h/t_w}$	$\mathbf{L_b/r_y}$	$\mathbf{C_{d1}}$	$\mathbf{C_i}$
W14x233	4.6	10.7	43.9	270	1
W14x176	6.0	13.7	44.8	220	1.5
W14x82	5.9	22.4	59.5	205	2.5
W16x89	5.9	27	59.3	200	2.75
W10x49	8.9	23.1	34.1	185	3

Table 4.5: Comparison of C_i and C_{d1} in column simulations

The validation studies show that the effect of the axial response on the element damage varies with the cross sections and the geometry of the column specimens. Stocky columns with more compact cross sections appear to be less affected by the axial compression. It is evident that the value of C_i is higher for a less compact section and for a more slender column. This observation suggests that the axial-flexure interaction coefficient C_i is closely related to the limit coefficient C_{d1}, which governs the ultimate ductility capacity of the column element.

A regression analysis is performed to relate the two parameters and suggests the following relation:

$$\ln(C_i) = 17.383 - 3.114 \ln(C_{d1}) \tag{4.63}$$

with an R-value of 0.939, which ensures sufficient confidence in the correlation.

The relation in Equation (4.63) is derived from the calibration of 5 column specimens under monotonic and cyclic displacement patterns in combination with constant and variable axial forces. It is instructive to extend the correlation studies to cover a broader range of column specimens and load histories. Nonetheless, Equation (4.63) allows for the first estimate of the model parameters, which are in satisfactory agreement with the available test data.

Chapter 5

Case Study: 8-story Steel Moment Frame

In this chapter, the damage-plasticity beam and column elements in the preceding chapters are deployed in an analysis framework for the large-scale simulation and collapse assessment of structural systems. The capabilities of the modeling approach are demonstrated with the case study of an 8-story 3-bay special moment-resisting steel frame that investigates various aspects of the structural collapse behavior, including the global and local response under element strength and stiffness deterioration, the magnitude and distribution of the local element damage variables, and the different types of collapse mechanism. The chapter is organized as follows. First, the archetype structure and its idealized numerical model are described. The static and dynamic behaviors of the structure are discussed, with a focus on the continuous element strength deterioration and the response redistribution due to damage accumulation. The study proposes new local and global damage indices, which are better suitable for the collapse assessment of structures than existing engineering demand parameters like the maximum story drift. The incremental dynamic analysis of the 8-story moment frame under a suite of earthquake ground motions highlights the benefits of the proposed damage indices for the collapse assessment of structures. The study shows that an aftershock as strong as the main shock increases the collapse margin ratio by as much as 30% and requires more stringent design criteria for protecting the building from collapse that currently specified. Finally, the study compares different modeling aspects for the archetype building to highlight the benefits of the proposed beam-column elements.

5.1 Archetype Building

This study examines the static and dynamic behavior of an eight-story three-bay steel special moment frame (SMF). The frame is adapted from the PG-2RSA performance group in the NIST evaluation of the FEMA P-695 methodology [68]. Figure 5.1 shows the plan view and the elevation view of the SMF. The columns and girders are wide-flange sections

with the dimensions summarized in Table 5.1. The sections are designed for the seismic design category (SDC) D_{max} in accordance the AISC 341-05 strength requirements [5] and the ASCE/SEI 7-05 seismic requirements [1]. Reduced beam section (RBS) connections are used in the girders following the AISC 358-05 recommendations [6]. The fundamental period from eigenvalue analysis of the SMF is 2.29 sec [68], which seems rather high for a mid-rise structure. To be consistent with the design specified in the NIST report, this value is adopted in the subsequent analyses.

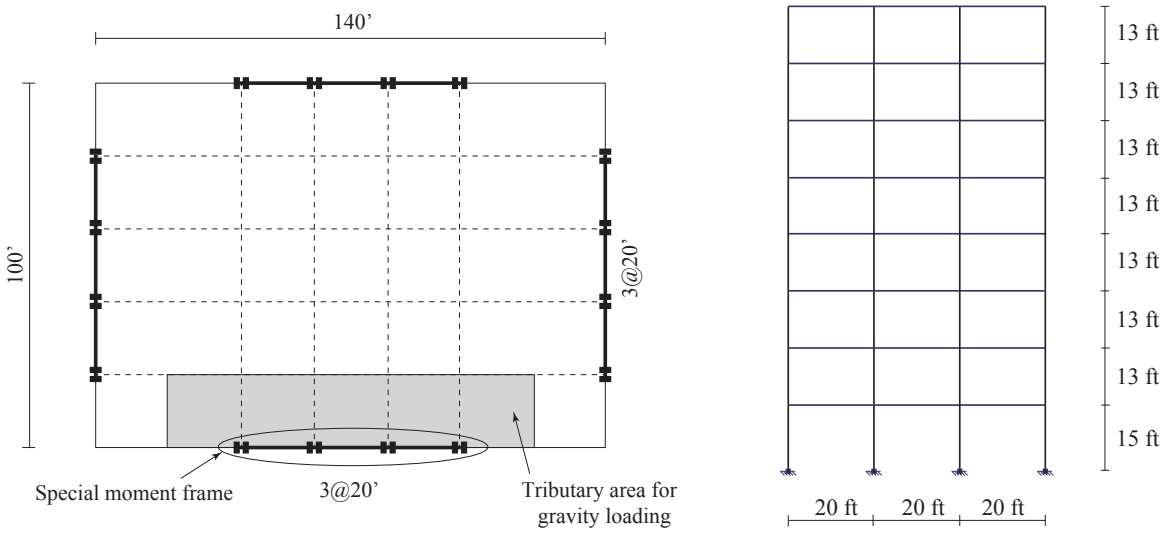

(a) Plan view of archetype building (b) Frame elevation view

Figure 5.1: Archetype eight-story three-bay special moment frame

Story	Elevation (in.)	Beam Size	Exterior Column Size	Interior Column Size
1	166.55	W30x108	W24x131	W24x162
2	322.55	W30x116	W24x131	W24x162
3	478.55	W30x116	W24x131	W24x162
4	634.55	W27x94	W24x131	W24x162
5	790.55	W27x94	W24x131	W24x131
6	946.55	W24x84	W24x131	W24x131
7	1102.55	W24x84	W24x94	W24x94
8	1258.55	W21x68	W24x94	W24x94

Table 5.1: Member sizes for eight-story three-bay moment resisting frame

5.2 Structural Model

5.2.1 Element models

5.2.1.1 Girder model

Each girder is modeled with the beam element based on damage-plasticity in Chapter 3. Plastic hinge offsets are specified and the yield strength at the reduced sections is lower than the nominal value to simulate the response of RBSs. Table 5.2 summarizes the strength reduction factor λ and the hinge offset ratio χ at the reduced sections used in the analysis. The kinematic hardening ratio $H_{kr} = 0.025$ and the isotropic hardening ratio $H_{ir} = 0.002$ are used. The damage parameters are specified based on the section compactness h/t_w and b_f/t_f and the member slenderness L_b/r_y in accordance with the guidelines for the parameter identification in Chapter 3.

Beam Size	**Strength reduction, λ**	**Hinge offset, χ**
W30x116	0.805	0.074
W30x108	0.808	0.074
W27x94	0.802	0.068
W24x84	0.798	0.061
W21x68	0.797	0.055

Table 5.2: Parameters of reduced beam sections

5.2.1.2 Column model

Each column is modeled with the column element based on damage-plasticity in Chapter 4 to capture the effect of variable axial forces on the yielding and deterioration in the flexural response. The kinematic hardening ratio $H_{kr} = 0.025$ and the isotropic hardening parameter $H_{ip} = 1.5\text{e}{-4}$ are specified. The parameters c_1, c_2, c_3, c_4, c_5 are calibrated to match the yield envelope given by an equivalent distributed plasticity model. For the W24 column sections, the following values give sufficient accuracy $c_1 = 2.1$, $c_2 = 2$, $c_3 = 2.95$, $c_4 = 2$, $c_5 = 1.335$. The damage parameters are specified in accordance with the guidelines for the parameter identification in Chapter 3 and Chapter 4.

5.2.1.3 Assumptions

To simplify the graphical illustration, a single damage variable $d = \max(d^+, d^-)$ is used to represent the strength and stiffness deterioration in each plastic hinge of a beam-column element. The damage variable d is cumulative over the range [0, 1] and has similar characteristics as the two damage variables d^+ and d^-. Other combinations of the two damage variables d^+ and d^- may be worthwhile exploring in future studies.

The primary focus of this study is on modeling of the deterioration in the columns and girders, and thus, other contributions to the global strength and stiffness deterioration are not accounted for. For instance, the panel zones are assumed to induce negligible shear deformations and strength deterioration. The effect of floor slabs on the element yield strength and flexural stiffness is also neglected. Figure 5.2 illustrates the model of a typical floor. Rigid joint offsets are specified to account for the member clear span.

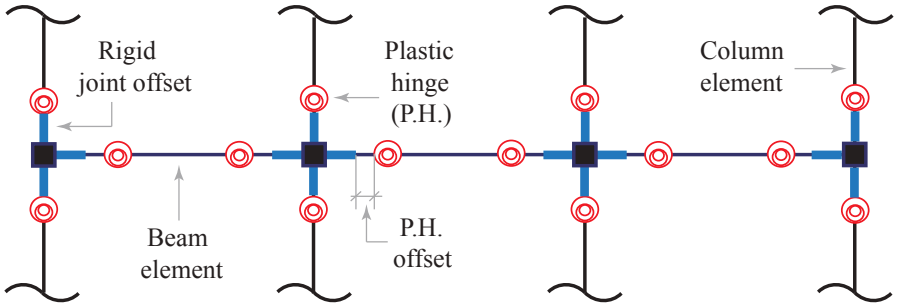

Figure 5.2: Typical floor model of the eight-story three-bay moment frame

5.2.2 Mass, damping, nonlinear geometry

A lumped mass model is adopted for the subsequent dynamic analyses. Rayleigh damping is used with the damping matrix proportional to the constant mass matrix and the tangent stiffness matrix for a damping ratio of 2.5%. The corotational formulation is used to account for the nonlinear geometry effect. Inflexible leaning columns are specified adjacent to the SMF to capture the P-Δ effect from the additional tributary gravity on the perimeter frame.

5.2.3 Member naming convention

The same naming convention as Section 4.1.6 is used. For example, C-3-1-T refers to the top end of the 3rd story exterior column on the left, G-1-2-R refers to the right end of the 1st floor girder in the second bay from the left.

5.3 Static Response

A pushover analysis is conducted under the factored gravity loads and the monotonically increasing lateral forces with distribution proportional to the fundamental mode shape, as Figure 5.3(a) shows. Figure 5.3(b) plots the base shear normalized by the weight of the structure against the average roof drift. The limited ductility capacity is evident in the relatively rapid strength reduction over a small range of drift ratio values.

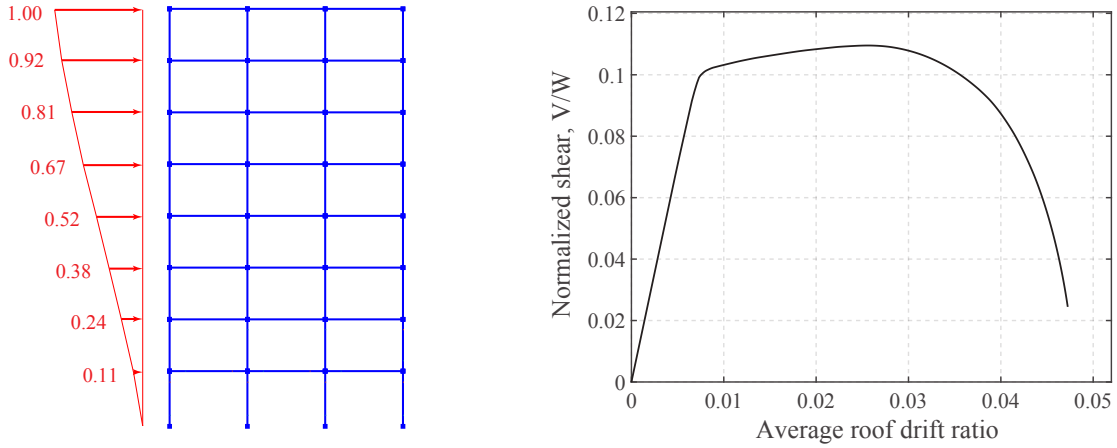

(a) Lateral load distribution (b) Pushover curve

Figure 5.3: Pushover response: load distribution and normalized base shear vs roof drift

The story drift distribution over the height of the building at different roof drift levels in Figure 5.4(a) identifies the collapse mechanism of the structure. Between $RD = 0.03$ and $RD = 0.04$, plastic hinges form at the top ends of all the 2nd-story columns to initiate a 2-story mechanism. The mechanism slightly reduces the drift in stories 3 to 8 while increases the drift in the bottom two stories. Beyond $RD = 0.04$, plastic hinges form at the top ends of all the 1st-story columns and the structure transitions into a 1-story mechanism. The new mechanism reduces the drift in the 2nd story while further increasing the 1st story drift. The two collapse mechanisms are also reflected in the story shear distribution in Figure 5.4(b). As the roof drift increases, the story shear-drift relation in the upper stories 'unloads' while it continues increasing and exhibits evident strength deterioration in the lower stories where the weak-story mechanism occurs.

Figure 5.5 shows the distribution of element damage at roof drift ratio $RD = 0.045$. The 1-story collapse mechanism concentrates damage mostly in the 1st story columns and girders. On the same story and floor, higher damage is observed in the columns on the right and in the girders on the left due to the pronounced overturning effect. The excessive damage values indicate severe local buckling in the right exterior column C-1-4.

5.4 Ground motions

This study adopts the suite of far-field ground motions in FEMA P695 [4]. The set consists of 21 ground motion records from sites located at distances greater than or equal to 10 km from the fault rupture. No more than two records are taken from the same earthquake to avoid the record-to-record bias. Criteria for the record selection are described in [4].

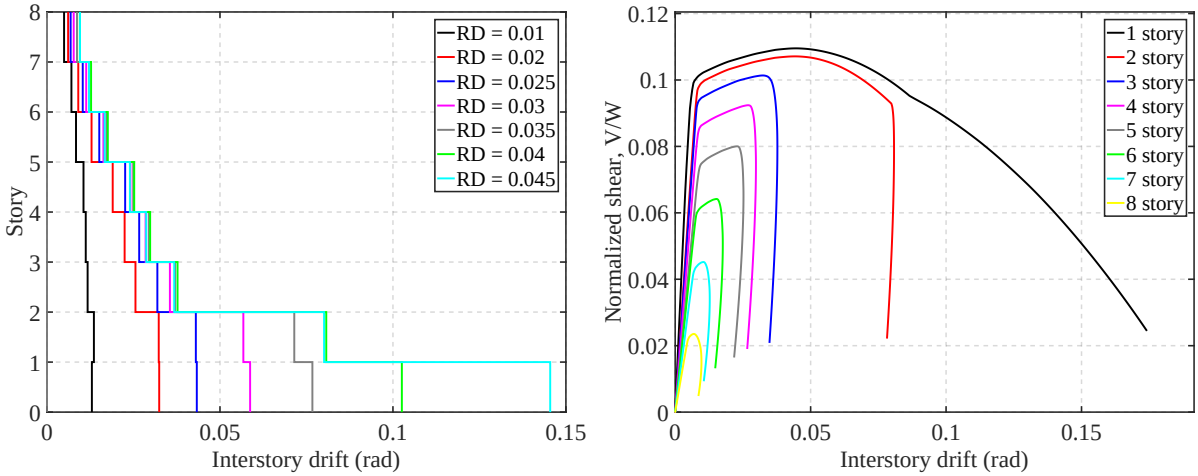

(a) Story drift distribution (b) Story shear distribution

Figure 5.4: Story drift and shear distribution

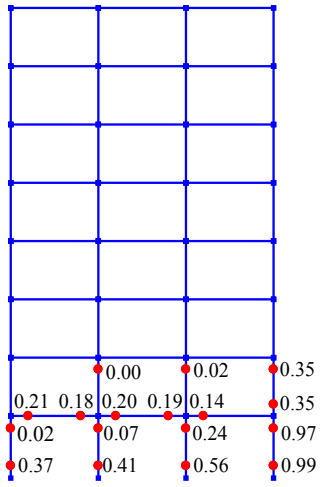

Figure 5.5: Damage distribution at $RD = 0.045$

Table 5.3 summarizes the main properties of the 21 far-field ground motions from the PEER database [14], including the record name, year, and station, the magnitude M_w, and the peak ground acceleration PGA.

Figure 5.6 plots the elastic response spectrum for the 21 ground motion records with 2.5% damping ratio. The median of the pseudo-acceleration on the spectrum is also highlighted in the figure.

ID	Name	Year	M_w	Station	PGA(g)
FF1	Northridge	1994	6.7	Beverley Hills - Mulhol	0.52
FF2	Northridge	1994	6.7	Canyon County - WCL	0.48
FF3	Duzce, Turkey	1999	7.1	Bolu	0.82
FF4	Hector Mine	1999	7.1	Hector	0.34
FF5	Imperial Valley	1979	6.5	Delta	0.35
FF6	Imperial Valley	1979	6.5	El Centro Array #11	0.38
FF7	Kobe, Japan	1995	6.9	Nishi-Akashi	0.51
FF8	Kobe, Japan	1995	6.9	Shin-Osaka	0.24
FF9	Kocaeli, Turkey	1999	7.5	Duzce	0.36
FF10	Kocaeli, Turkey	1999	7.5	Arcelik	0.22
FF11	Landers	1992	7.3	Yermo Fire Station	0.24
FF12	Landers	1992	7.3	Coolwater	0.42
FF13	Loma Prieta	1989	6.9	Capitola	0.53
FF14	Loma Prieta	1989	6.9	Gilroy Array #3	0.56
FF15	Manjil, Iran	1990	7.4	Abbar	0.51
FF16	Superstition Hills	1987	6.5	El Centro Imp. Co.	0.36
FF17	Superstition Hills	1987	6.5	Poe Road	0.45
FF18	Chi-Chi, Taiwan	1999	7.6	CHY101	0.44
FF19	Chi-Chi, Taiwan	1999	7.6	TCU045	0.51
FF20	San Fernando	1971	6.6	LA - Hollywood	0.21
FF21	Friuli, Italy	1976	6.5	Tolmezzo	0.35

Table 5.3: Far-field ground motion information

5.5 Dynamic Response

This section investigates the dynamic behavior of the archetype SMF subjected to the 21 ground motions magnified by a scale factor SF. This study uses a collapse criteria based on the maximum story drift DR. Because there are cases in which the structure stabilizes after it experiences an excessive story drift, global collapse initiates when the maximum story DR exceeds 10% and continues to grow thereafter. In the following discussion, the displacements and accelerations are measured relative to the ground.

5.5.1 Local damage distribution

The location and the magnitude of the damage variables within the structure indicate where severe damage concentrates and offer insight into the collapse mechanisms. In particular, the symmetry of the damage distribution is indicative of the overturning effect due to the relative motion of the structure. For illustration, this section examines the local response of the members on the first story where damage is most severe: the exterior columns

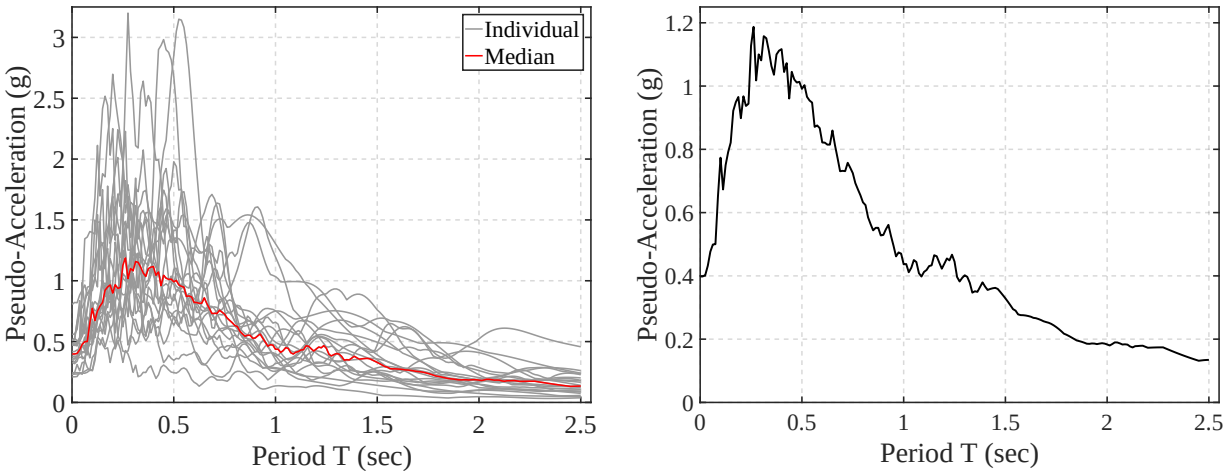

(a) Individual records (b) Median value

Figure 5.6: Elastic response spectrum of the far-field ground motions, $\xi = 2.5\%$

C-1-1 and C-1-4, and the girders G-1-1 and G-1-3. The following subsections compare two scenarios with a nonsymmetric and a symmetric damage evolution in the exterior columns and discuss the damage distribution in the girders.

5.5.1.1 Nonsymmetric column damage

A nonsymmetric damage distribution results from the considerable discrepancies in the plastic energy dissipation in the columns of the same story. Such discrepancies are typically due to the larger drift in one direction that amplifies the overturning effect and induces more plastic axial deformations in the columns on one side than on the other. In a special case, the structure initiates a weak-story mechanism and permanent deformations in one dominant direction, which exacerbates the discrepancies in the column plastic axial deformations, and in turn, leads to a nonsymmetric damage distribution.

Figure 5.7 shows the response under the Hector Mine record at Hector station (FF4) with scale factor $SF = 6.6$. A large pulse at $t = 7$ sec initiates a 2-story mechanism, as evident in the excessive drifts in the bottom two stories in Figure 5.7(a), and leads to a one-sided relative motion in the positive direction. The damage distribution is highly nonsymmetric with higher damage on the right side of the structure. The high damage value at the base of C-1-4 indicates severe local buckling in the column. It is noteworthy that the damage in the interior columns is relatively mild because of the higher ductility of the larger section size. Moreover, damage in the interior columns is more symmetric due to the reduced effect of the overturning moment.

Figure 5.8 compares the response at the base of the 1st story exterior columns C-1-1 on the left and C-1-4 on the right. The comparison of the moment-rotation relation in Figure 5.8(a)

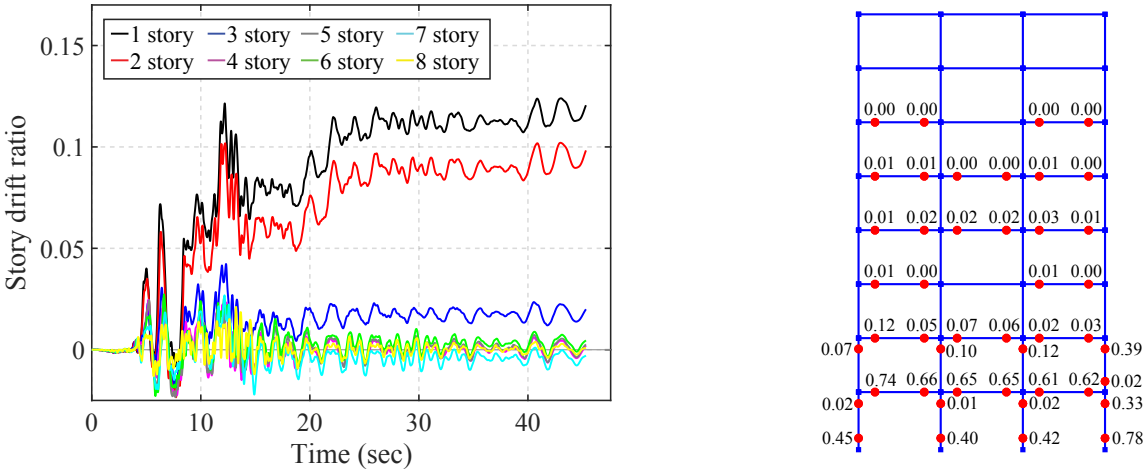

(a) Story drift distribution (b) Final damage profile

Figure 5.7: Response distribution and deformed shape (FF4, SF = 6.60)

leads to two observations: (1) the columns accumulate similar flexural deformations, and (2) the strength and stiffness deterioration is more pronounced in C-1-4 than in C-1-1. The first observation suggests that the axial deformations govern the discrepancies in the column response. Due to the relative motion of the structure causing permanent deformations in the positive direction, the overturning effect induces higher compression and more excessive plastic axial deformations on C-1-4, as Figure 5.8(b) shows. The evolution of the plastic axial deformations in Figure 5.8(b) correlates well with the damage evolution in Figure 5.8(c). After the large pulse at $t = 7$ sec triggers the weak-story mechanism, the accumulation of plastic axial deformations in C-1-4 accelerates due to the overturning effect and leads to higher damage increments than in C-1-1.

5.5.1.2 Symmetric column damage

A symmetric damage distribution results from the negligible discrepancies in the plastic energy dissipation in the columns when the ground motion induces relatively equal large drifts in both directions. Two scenarios resulting in a symmetric damage distribution are: (1) the ground motion has relatively small intensity that induces minor discrepancies in the column plastic deformations, and (2) the impact of axial forces from the overturning effect on the column response is relatively small, which is typical in low-rise to mid-rise structures.

Figure 5.9 shows the response under the Northridge record at Beverly Hills station (FF1) with a scale factor $SF = 5.0$. The evolution of the story drifts in Figure 5.9(a) indicates comparable drifts in the two directions, with the maximum positive drift ratio of 0.06 and the maximum negative drift ratio of -0.07. The damage distribution in Figure 5.9(b) is rather symmetric, with the damage in C-1-4 ($d = 0.51$) practically equal to the damage in C-1-1

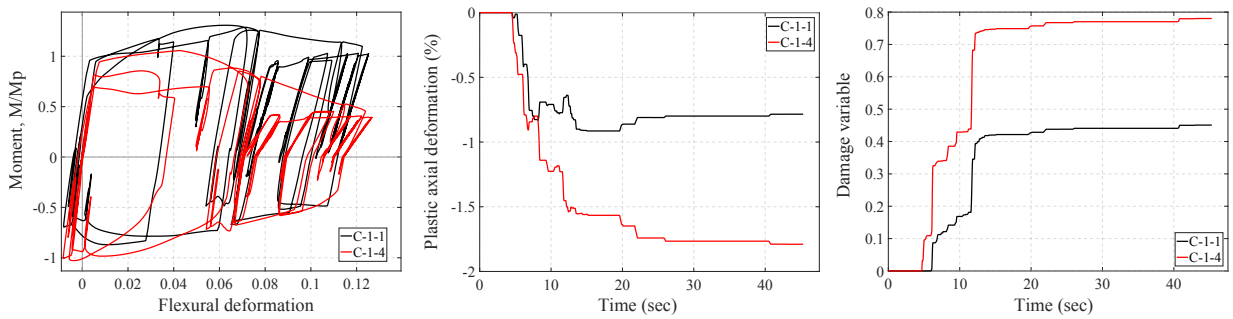

(a) (b) (c)

Figure 5.8: Response of 1st story exterior columns (FF4, SF = 6.60): (a) Flexural response at base, (b) Plastic axial deformation, (c) Damage evolution

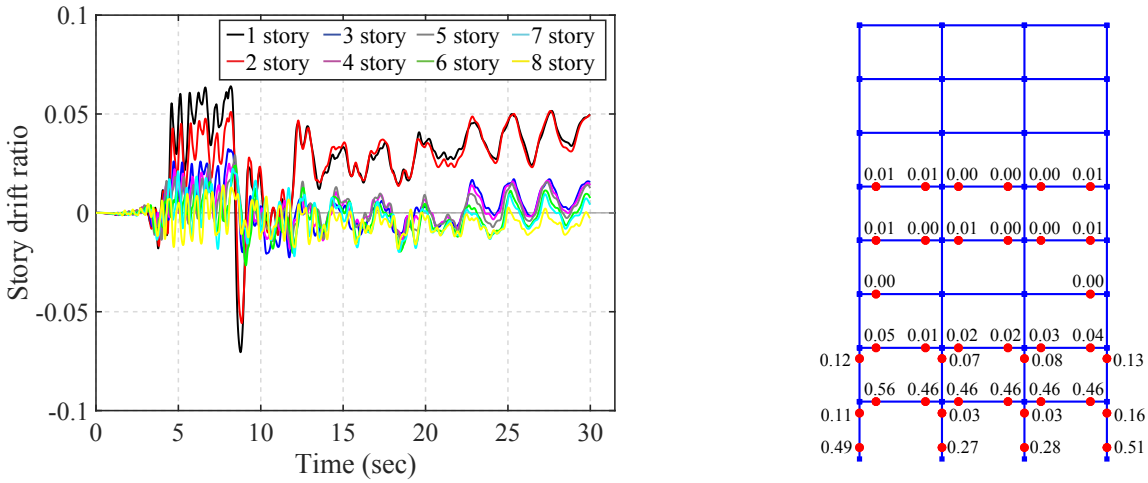

(a) Story drift distribution (b) Final damage profile

Figure 5.9: Response distribution and deformed shape (FF1, SF = 5.00)

($d = 0.49$). Even though the maximum drift is smaller in the positive direction, the right column is slightly more damaged because the structure develops permanent deformations in the positive direction and accumulates more plastic energy in the later follower cycles.

The symmetric damage distribution is reflected in the similar moment-rotation relation at the base of the exterior columns in Figure 5.10(a). The evolution of the plastic axial deformation in Figure 5.10(b) and the damage variables in Figure 5.10(c) correlate well with the 1st story drifts in Figure 5.9. The large positive drift at t = 5-8 sec gives rise to rapid increments in the plastic axial deformations and damage in C-1-4. At t = 8-9 sec, the large negative drift induces significant increases in the plastic axial deformations and damage in C-1-1, and the damage in the two columns becomes practically equal. Thereafter, as the

structure forms a 2-story mechanism and leans permanently to the right, C-1-4 gradually accumulates more plastic axial deformations and exceeds slightly the damage in C-1-1 at the end of the ground motion. The discrepancies, however, are negligible in this case.

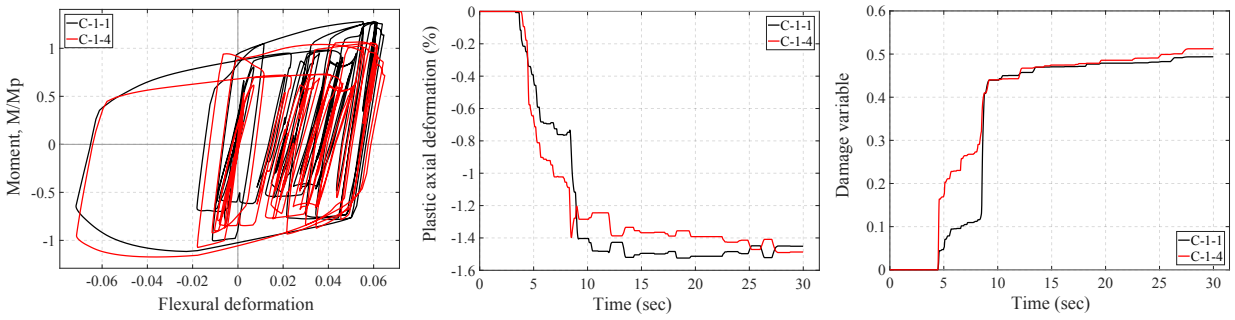

(a) (b) (c)

Figure 5.10: Response of 1st story exterior columns (FF1, SF = 5.0): (a) Flexural response at base, (b) Plastic axial deformation, (c) Damage evolution

5.5.1.3 Girder damage

Since the axial forces in the girders are relatively small, girder damage depends entirely on the flexural response, and in particular, on the plastic flexural deformations. If the columns on the same story experience similar axial deformations, which typically leads to a symmetric column damage pattern, the plastic flexural deformations in the adjacent girders are comparable and the girder damage distribution is symmetric. Otherwise, if the differential plastic axial deformations in the columns are significant, the floor rotation imposes different rotation demand on the adjacent girders and results in a nonsymmetric damage pattern. In general, however, the damage discrepancies in girders on the same floor are less pronounced than in the columns due to the relatively small differences in the plastic flexural deformations.

Figure 5.11 illustrates a slightly nonsymmetric girder damage distribution between G-1-1-L and G-1-3-R under FF4 with $SF = 6.6$. The global response and local response in the 1st-story columns are shown in Figure 5.7 and Figure 5.8. Since more plastic deformations are accumulated in C-1-4 than in C-1-1, less plastic deformations are developed in G-1-3 than in G-1-1, and as a result, the strength deterioration in G-1-3 is less pronounced, as evident in the moment-rotation relation in Figure 5.11(a).

5.5.2 Collapse mechanism

For all 21 ground motions, the structure forms either a 1-story or a 2-story collapse mechanism. The deformed shape with fivefold magnification in Figure 5.12 shows a 1-story

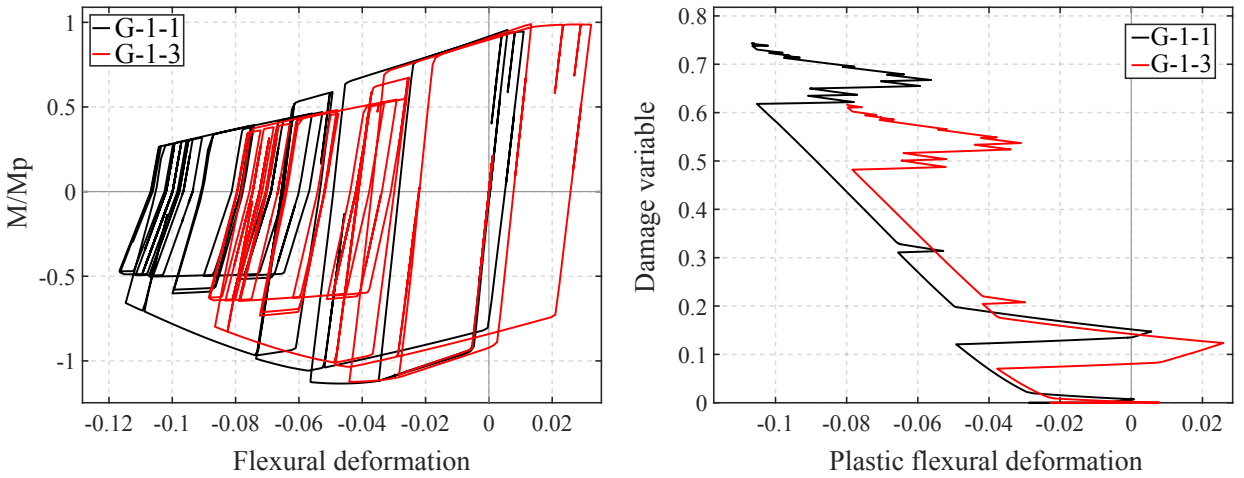

(a) Flexural response (b) Damage evolution

Figure 5.11: Girder response of 1st floor girders (FF4, SF = 6.6)

mechanism under the Loma Prieta record at Gilroy Array station (FF14) with scaled factor $SF = 9.0$, and a 2-story mechanism under the Northridge record at Beverly Hills station (FF1) with scaled factor $SF = 5.6$. In addition to the local damage variables discussed in the preceeding section, the following examines two global variables that are indicative of a weak-story collapse mechanism: the story drifts and the floor rotations.

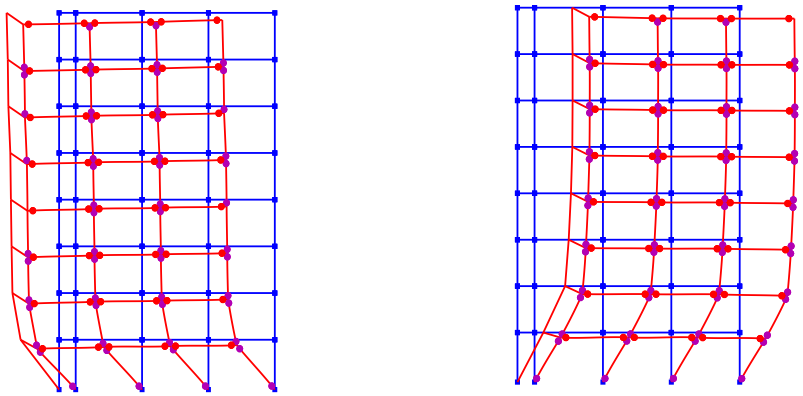

(a) One-story mechanism (b) Two-story mechanism

Figure 5.12: Deformed shape with weak-story collapse mechanism: (a) FF14, SF = 9.0, (b) FF1, SF = 5.6

Figure 5.13(a) plots the evolution of the story drifts under FF14, $SF = 9.0$. The 1st story drift ratio increases drastically near the end of the ground motion and is well-separated from

the other stories, which is indicative of a 1-story collapse mechanism. The 1-story mechanism induces significant damage to the structural members in the 1st story and negligible damage in the upper stories. This is reflected in the more pronounced deterioration in the 1st story shear in Figure 5.13(b) relative to the 2nd story shear in Figure 5.13(c).

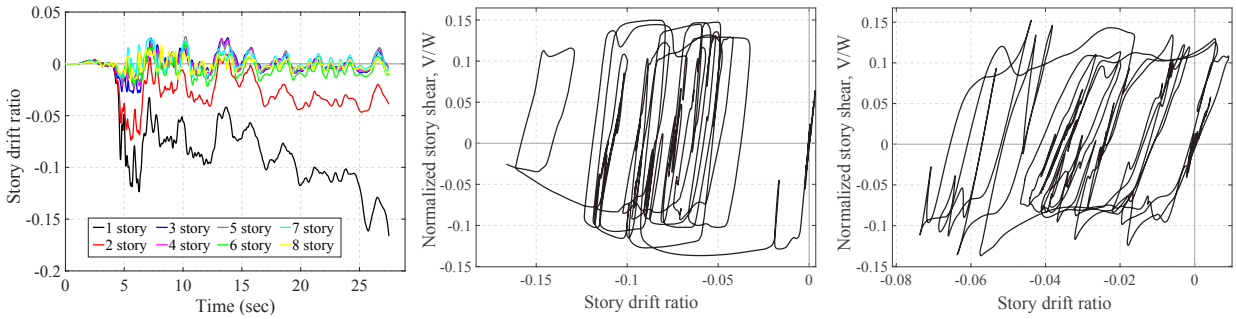

(a) Story DR distribution (b) 1st story shear vs DR (c) 2nd story shear vs DR

Figure 5.13: Story DR and shear distribution of a one-story mechanism (FF14, SF = 9.0)

The floor rotation results from the difference in the column axial deformations on the same story and adopts a positive convention for the counter-clockwise direction. Figure 5.14 shows two distinct trends in the distribution of the average floor rotation. In the first case, the floor rotation distribution under FF4 with $SF = 6.6$ in Figure 5.14(a) gives rise to two observations. First, all floor rotations remain negative and gradually increase in magnitude. This behavior implies that the structure undergoes permanent relative motion to the right until collapse. Second, the rotations from the 2nd floor to the 8th floor are practically the same and well-separated from the 1st floor. Since rotations are cumulative as elevation increases, the difference in the rotation between adjacent floors is the relative rotation due to diffential shortening in the columns between the floors. This suggests that the overturning effect is significant in the bottom two stories and negligible in the upper stories, which implies a 2-story mechanism consistent with the observation from the dynamic analysis.

The second case in Figure 5.14(b) examines the floor rotations under FF1 with $SF = 3.2$. In contrast to the first case, the floor rotations alternate in signs with relatively small magnitude and remain stable until the end of the ground motion. This behavior implies that the structure oscillates in both directions and does not collapse. The rotations on different floors are more evenly distributed, which implies that the stories contribute similarly to the total roof rotation and a weak-story mechanism is not likely.

5.5.3 Other response distribution

5.5.3.1 Plastic hinges

In contrast to the pushover analysis, the dynamic analysis indicates a wider spread of plastic hinges in almost all elements up to the roof level. This observation leads to two

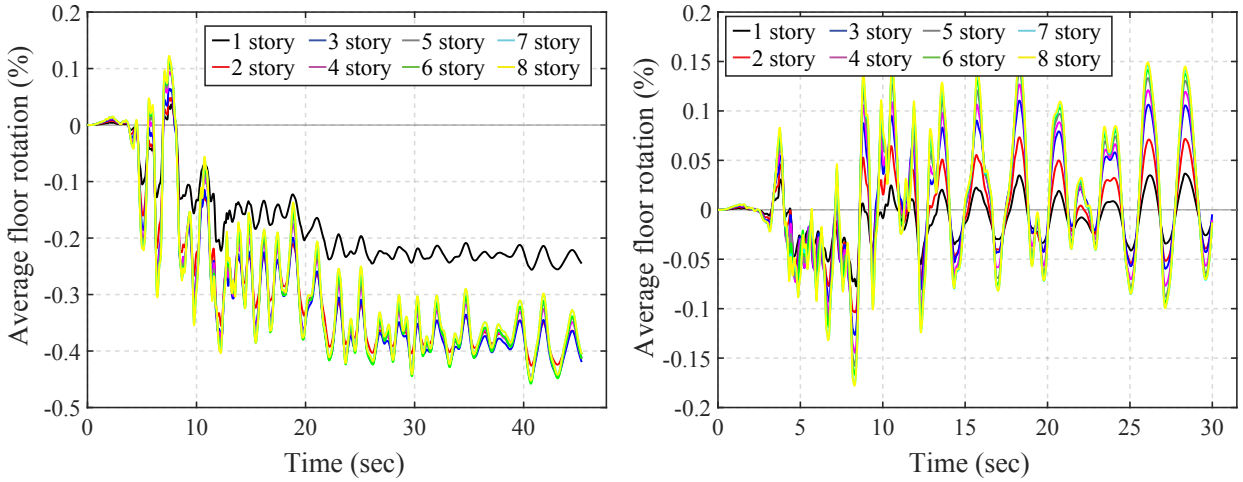

(a) FF4, SF = 6.60 (b) FF1, SF = 3.20

Figure 5.14: Time history of the average floor rotations

implications: (1) for flexible structures, which is typically the case for most tall buildings, the higher mode effect is important, and (2) the constant lateral force distribution proportional to the fundamental mode shape in pushover analysis might not represent sufficiently the force distribution in the dynamic analysis.

5.5.3.2 Lateral inertial forces

As opposed to a constant load pattern in the pushover analysis, the lateral force distribution varies in the dynamic analysis. To illustrate some commonly observed patterns, Figure 5.15 plots the distribution of the average lateral floor acceleration at various instants for 3 different ground motions.

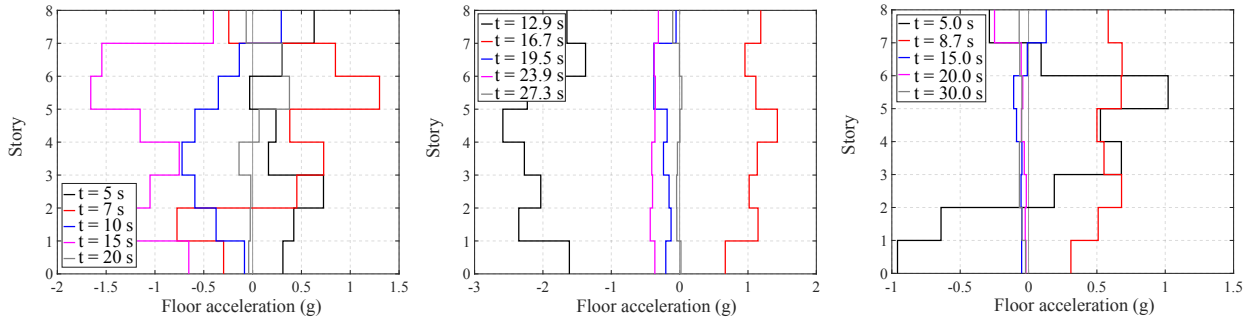

(a) FF17, SF = 9.40 (b) FF12, SF = 8.10 (c) FF1, SF = 3.20

Figure 5.15: Distribution of floor acceleration

In the first case in Figure 5.15(a), the inertial force distribution is rather irregular. Location of the maximum acceleration varies and the sign alternates with increasing elevation. This pattern emphasizes the impact of the higher modes. In the second case in Figure 5.15(b), the distribution is relatively uniform over the building height. In the third case in Figure 5.15(c), the inertial force distribution is a combination of the two: irregular with alternating signs in the beginning and more uniform as the ground motion progresses.

The magnitude of the inertial forces reduces toward the end of shaking due to two reasons: (1) the reduction in the ground motion intensity near the end, and (2) the damage localization in the structure due to the strength deterioration in the element response.

5.5.4 Further remarks

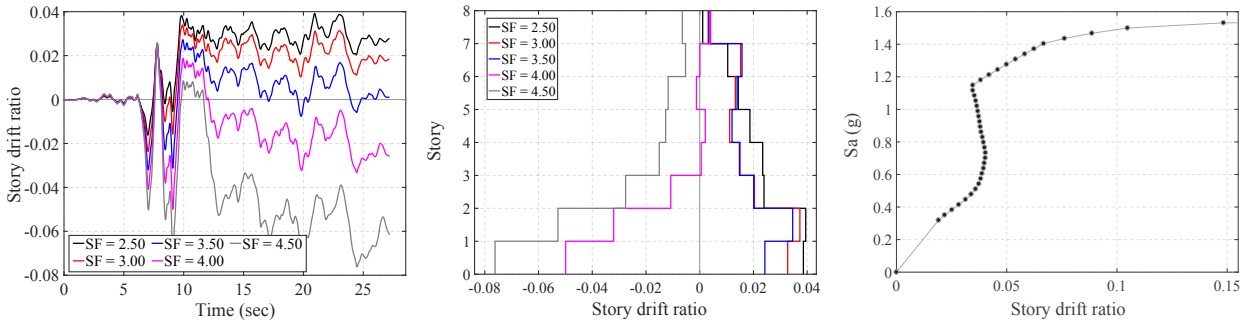

(a) 1st story drift (b) Distribution at max drift (c) IDA curve

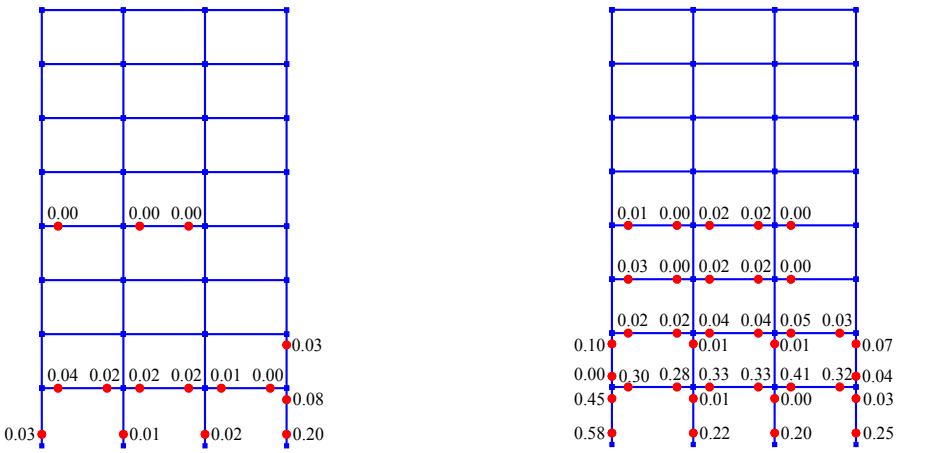

(d) Damage profile, SF = 2.5 (e) Damage profile, SF = 4.5

Figure 5.16: Dynamic response under FF9

This section examines the story drifts and damage distribution under the same ground motion with different scale factors to investigate the effect of ground motion intensity on

the dynamic behavior. The response under the Kocaeli record at Duzce station (FF9) with scale factor SF ranging from 2.5 to 4.5 is selected for illustration. The time history of the 1st story drift in Figure 5.16(a) shows that the permanent deformation changes direction as the scale factor varies. Figure 5.16(b) plots the drift distribution when the maximum value is attained. Two important observations arise: (1) for the same ground motion, the story where the highest drift value is attained varies with the ground motion intensity, and (2) the maximum drift does not increase monotonically with the ground motion intensity. The second remark is shown in the relation of the maximum drift and the spectral acceleration S_a in Figure 5.16(c). The change in the relative motion direction leads to the nonmonotonic relation and explains the 'resurrection' phenomenon observed in the literature in which the structure regains stability as the ground motion intensity increases.

Figures 5.16(d)–(e) highlights the effect of the ground motion intensity on the damage distribution. For $SF = 2.5$, the maximum drift is attained in the positive direction and the right columns are more damaged, whereas for $SF = 4.5$, the maximum drift is attained in the negative direction and the damage in the left columns is more severe.

5.6 Global Damage Index

The preceeding sections suggest a close correlation between the local damage variables and the global response. This section derives a global damage index from the local damage variables to assist in the assessment of the global damaged states. The section starts with the formulation of the global damage index and an example to illustrate the satisfactory correlation to the collapse mechanisms. The section proceeds with a comparison study with the maximum story drift, which is the most common Engineering Demand Parameter (EDP) for damage assessment of structures. Based on the comparison, three limit states of steel structures are identified in terms of the damage values. The section concludes with a case study to demonstrate the use of the proposed damage index in the collapse assessment of the archetype structure under an earthquake sequence.

5.6.1 Formulation

Figure 5.17 illustrates four damage indices: the column top and bottom indices, the joint indices, and the floor indices.

The column top index of the k-th story, $D_t^{(k)}$, is defined as a weighted average of the damage variables $d_t^{(el)}$ at the top end of column element el on the k-th story. Similarly, the column base index of the k-th story, $D_b^{(k)}$, is defined as a weighted average of the damage variables $d_b^{(el)}$ at the base of column element el on the k-th story.

$$D_t^{(k)} = \frac{\sum w_t^{(el)} d_t^{(el)}}{\sum w_t^{(el)}} \qquad D_b^{(k)} = \frac{\sum w_b^{(el)} d_b^{(el)}}{\sum w_b^{(el)}} \tag{5.1}$$

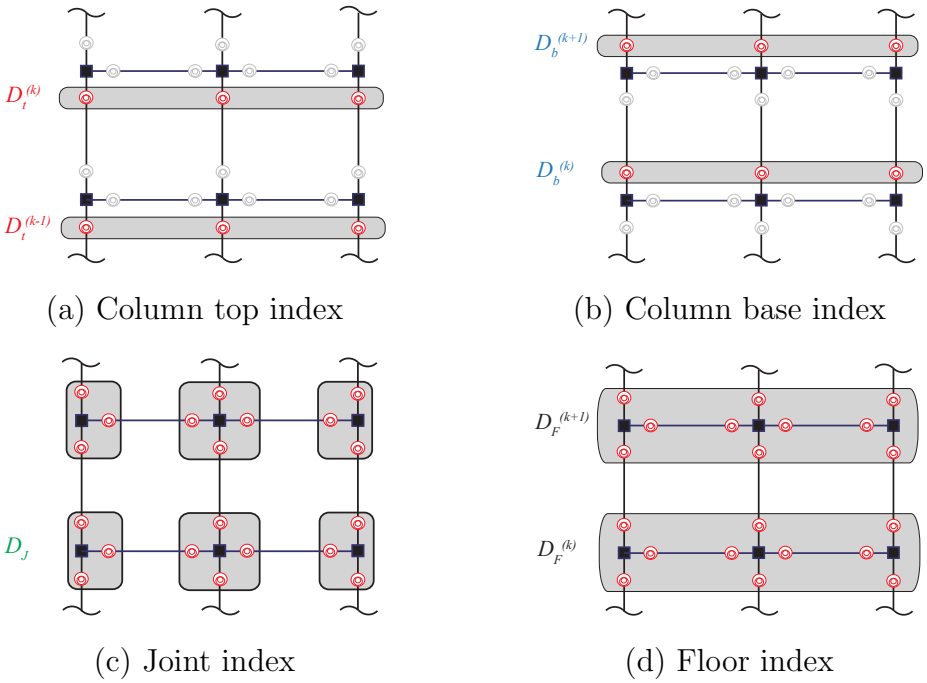

(a) Column top index (b) Column base index

(c) Joint index (d) Floor index

Figure 5.17: Illustration of column indices, joint indices, and floor indices

where $w_t^{(el)}$ serves as weight for the damage variable $d_t^{(el)}$ and $w_b^{(el)}$ is the weight for the damage variable $d_b^{(el)}$. $w_t^{(el)} = w_b^{(el)} = 1$ is adopted in this study.

The joint index at the k-th node, $D_j^{(k)}$, is defined as a weighted average of the damage variables $d^{(el)}$ at the end of element el adjacent to node k:

$$D_j^{(k)} = \frac{\sum w^{(el)} d^{(el)}}{\sum w^{(el)}} \tag{5.2}$$

where $w^{(el)}$ serves as weight for the damage variable $d^{(el)}$; $w^{(el)} = 1$ is adopted in this study, implying that the joint index is the mean of the respective local damage variables.

The floor index of the k-th floor, $D_f^{(k)}$, is defined as a weighted average of the joint indices D_j on floor k:

$$D_f^{(k)} = \frac{\sum W_j D_j}{\sum W_j} \tag{5.3}$$

where W_j serves as weight for the joint index D_j and $W_j = 1$ is adopted in this study.

Finally, the global damage index, D_G, is defined as the weighted average of the floor indices D_f:

$$D_G = \frac{W_b^{(1)} D_b^{(1)} + \sum W_f^{(k)} D_f^{(k)}}{W_b^{(1)} + \sum W_f^{(k)}} \tag{5.4}$$

where $D_b^{(1)}$ and $W_b^{(1)}$ are the 1st-story column base index and the corresponding weight, and $D_f^{(k)}$ and $W_f^{(k)}$ are the floor index and the corresponding weight. The weight is assumed equal to the respective damage index, $W_b^{(1)} = D_b^{(1)}$, $W_f^{(k)} = D_f^{(k)}$ to emphasize the contribution of the floors with more severe deterioration.

5.6.2 Localized Damage Region

When a story mechanism initiates, the structure deforms as multiple blocks: one 'active' block with highly inelastic element behavior and several adjacent 'passive' blocks with elastic or mildly inelastic element behavior. A *localized damaged region* (LDR) is defined as the 'active' block, which is a collection of elements over one or more stories with significantly higher damage than in the other elements outside the block. The LDR is characterized by a high column top index D_t and a high column base index D_b at the upper and lower edges of the block, and relatively high floor indices D_f on the intermediate floors within the LDR.

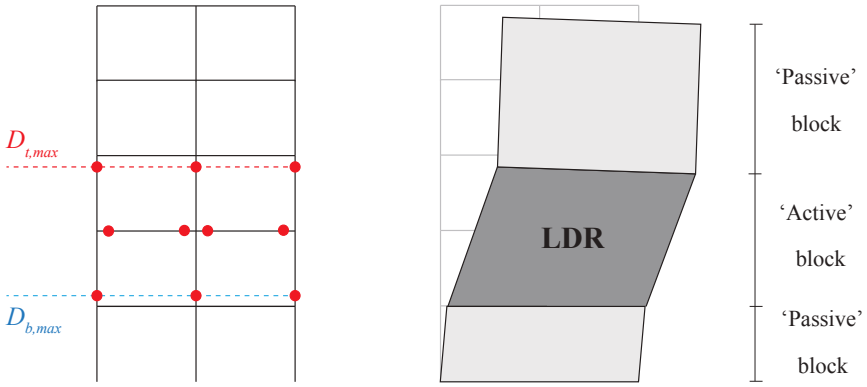

Figure 5.18: Typical configuration of a story mechanism

Figure 5.18 illustrates a possible weak-story collapse mechanism of a five-story two-bay frame. The element ends with relatively high damage and plastic deformations are shown with red circles. The LDR consists of the 2nd and 3rd stories and is restricted between the column bases with the highest damage index D_b and the column tops with the highest damage index D_t. The LDR has significant story drifts, vertical floor translations, and floor rotations due to the excessive element deformations, as opposed to the limited element deformations in the adjacent 'passive' blocks.

The following example demonstrates the correlation of the LDR and the collapse behaviors of the structure. Figure 5.19 shows the distribution of the column top and base damage indices and the floor indices for the archetype eight-story SMF under FF1 with $SF = 5.6$. It is noteworthy that the global damage indices D_t, D_b, D_f have lower values than the local element damage variables because the former are averages of the latter and account also for the undamaged element ends. The LDR consists of members in the bottom 2 stories and

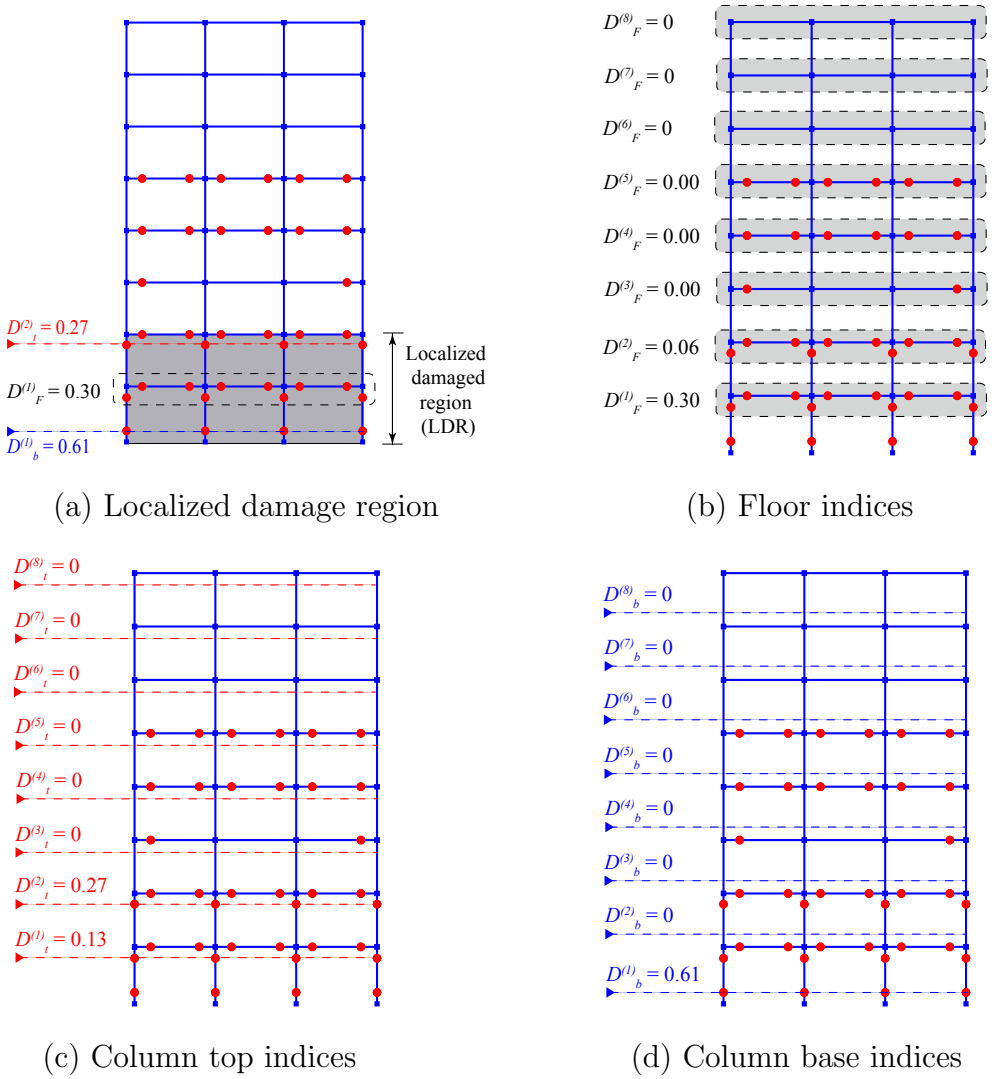

(a) Localized damage region

(b) Floor indices

(c) Column top indices

(d) Column base indices

Figure 5.19: Damage indices and localized damage region (FF1, SF = 5.6)

satisfies all three conditions: (1) the upper edge corresponds to the maximum column top index $D_t^{(2)} = 0.27$ on the 2nd story, (2) the lower edge corresponds to the minimum column base damage $D_b^{(1)} = 0.61$ on the 1st story, and (3) the floor indices between the two edges are relatively high $D_f^{(1)} = 0.3$. The LDR is consistent with the 2-story mechanism observed for this ground motion.

5.6.3 Comparison with maximum story drift

Figure 5.20(a) plots the global damage index D_G against the maximum story drift ratio DR. Each data point corresponds to a dynamic analysis under one of the 21 far-field ground motions with a scale factor SF. For clarity, lines are drawn to connect the data points from the same ground motion. The figure zooms in the response up to collapse and leaves out the data points beyond collapse in which the structure is unstable and the maximum story drift becomes unbounded. The damage index D_G initiates at $DR \approx 0.025$ and varies essentially linearly with the story drift DR up to $DR \approx 0.15$ when the structure becomes unstable. Due to the weak-story mechanism, both the story drift and the damage are excessive in the LDR, which explain the correlation of the two variables.

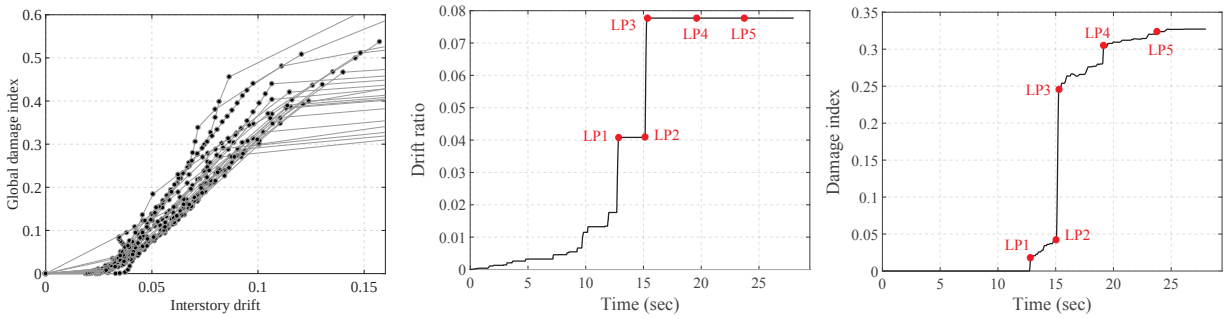

(a) D_G vs DR (b) Maximum story drift (c) Global damage index

Figure 5.20: Comparison of damage index D_G and maximum story drift

To distinguish the two variables, Figure 5.20(b)-(c) plots the evolution of the maximum story drift ratio DR and the global damage index D_G under FF12 and $SF = 6.9$. The story drift shows two significant increments at load point (LP) 1 and 3 when the previous maximum or minimum drift value is exceeded, while remains constant between LP1 and LP2 and after LP3. The maximum story drift is able to capture the large earthquake pulses that cause excessive drift increments but fails to account for the damage accumulation in follower half cycles after the maximum drift is attained. In contrast, the global damage index D_G not only predicts the rapid damage growth between LP2 and LP3, but also captures the gradual damage accumulation during the load reversal from LP1 to LP2 and during the follower cycles after LP3. The global damage index is cumulative and attains its maximum value at the end of the ground motion, which is critical for ground motions with longer duration and numerous cycles.

Figure 5.21 plots the two variables against the ground motion intensity, which is represented by the spectral acceleration S_a evaluated at the fundamental period of the archetype structure. This plot is known as the incremental dynamic analysis (IDA) curve [105] and typically used in collapse assessment of structures. It is noteworthy that the maximum story drift DR does not always vary monotonically with the ground motion intensity because it

does not account for the direction of motion. In contrast, the global damage index D_G varies monotonically with the ground motion intensity.

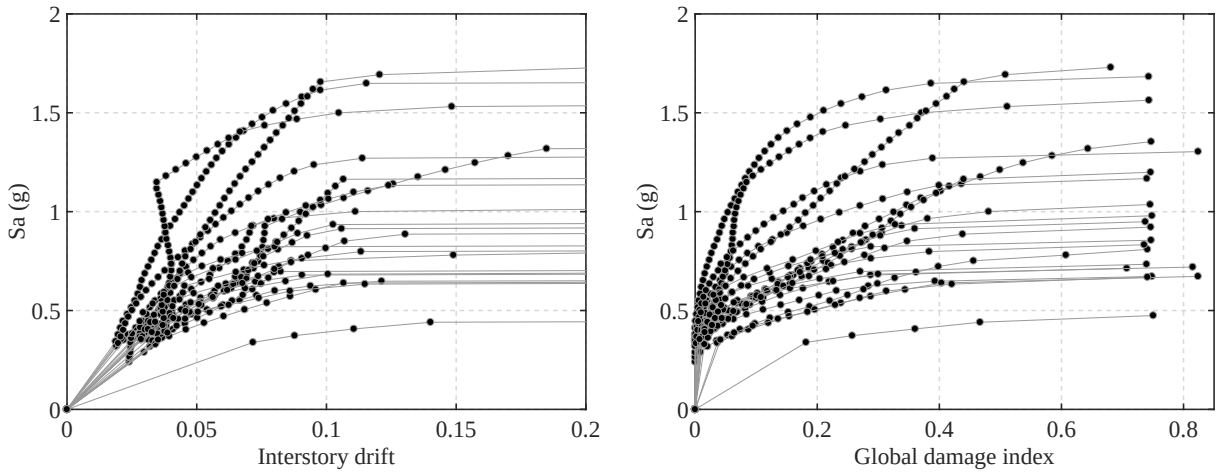

(a) Max story drift (b) Global damage index

Figure 5.21: Incremental dynamic analysis curve in terms of story drift and damage index

It is noteworthy that the proposed global and local damage measures correlate well with both the global and the local response variables. In particular, the damage variables account for the plastic axial deformation, which is critical in collapse simulations but typically neglected in practice due to limitations of available column models. Therefore, the proposed damage formulation is a rational way to bridge from the local to the global response and avoids separate limit state checks that are commonly used in practice.

5.6.4 Damage-base limit states

This subsection calibrates the global damage index D_G against the maximum story drift ratio DR to define three limit states of the archetype structure in terms of damage: life safety (LS), collapse prevention (CP), and collapse (CL). FEMA 356 [3] associates the LS limit state with a story drift value $DR = 0.025$ and the CP limit state with $DR = 0.05$. A drift ratio between $DR = 0.1$ and $DR = 0.15$ has been widely adopted for the CL limit state [4]. These story drift values correspond to the following damage thresholds at the limit states of the 8-story frame:

(1) *Life safety (LS):* $D_G = 0.01$. Damage initiates in several elements after sufficient plastic deformations. The story drift is relatively small and a story mechanism is not present.

(2) *Collapse prevention (CP):* $D_G = 0.1$. Significant plastic deformations are accumulated in several elements and the strength and stiffness deterioration is moderate, especially

in the 1st and 2nd stories. The structure forms a localized damage region (LDR) and initiates a weak-story mechanism.

(3) *Collapse (CL):* $D_G = 0.4$ Elements in the LDR undergo significant plastic deformations and severe damage due to local buckling and/or brittle failure. Differential column shortening results in considerable floor rotations. The weak-story mechanism is pronounced with significant story drifts.

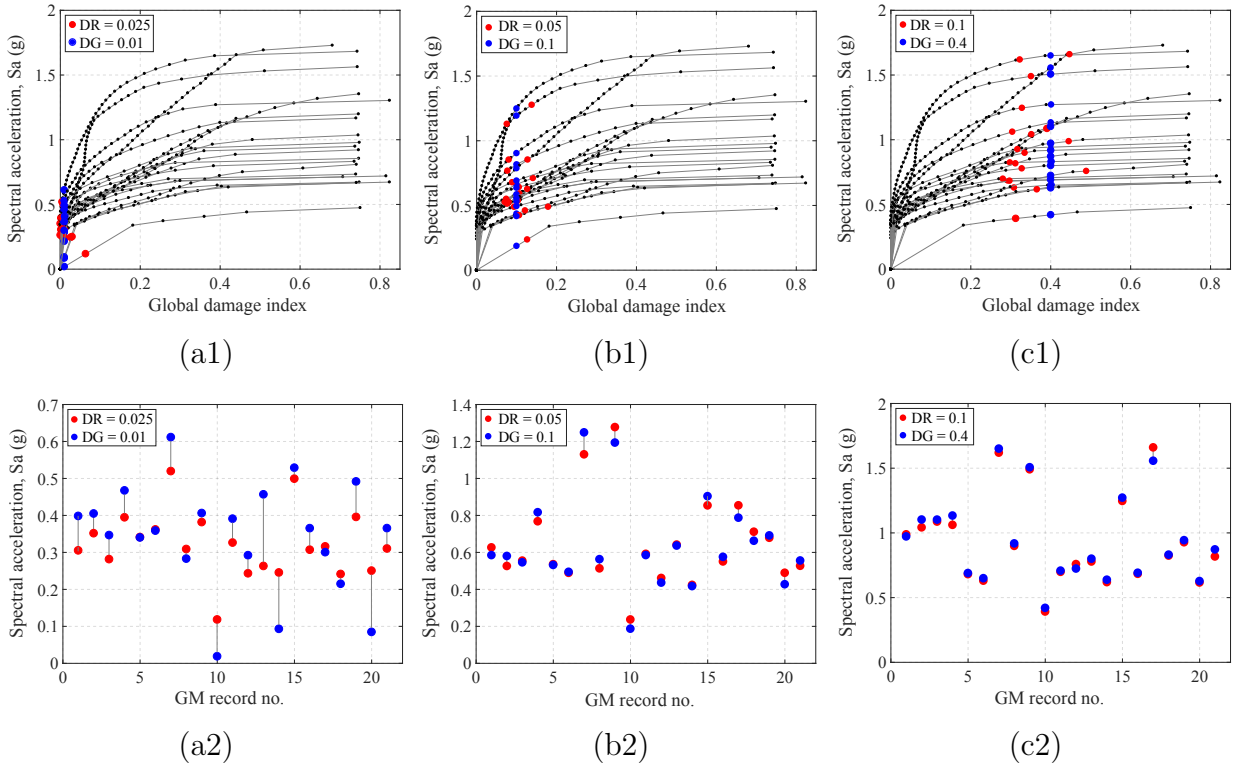

Figure 5.22: Comparison of max drift ratio DR and damage index D_G at different limit states: (a) Life safety, (b) Collapse prevention, (c) Collapse

Figures 5.22(a)–(c) compare the damage index D_G and the maximum story drift ratio DR at the three limit states on the IDA curves in terms of the damage index D_G. Figure 5.22(d)–(e) compare the ground motion intensity at the three limit states defined by the two response variables. The red circles correspond to the limit states in terms of the story drift and the blue circles in terms of the damage index. The slight discrepancies in the spectral acceleration S_a at the LS limit state suggest that a smaller damage threshold may provide a more consistent result, and indeed, $D_G = 0.075$ gives better agreement. However, this is not pursued here because the small damage value implies an impractical level of accuracy. The value $D_G = 0.01$ is selected to represent an arbitrary small threshold when the global

damage index D_G begins to accumulate. At the CP and the CL limit states, the agreement between the two criteria is satisfactory.

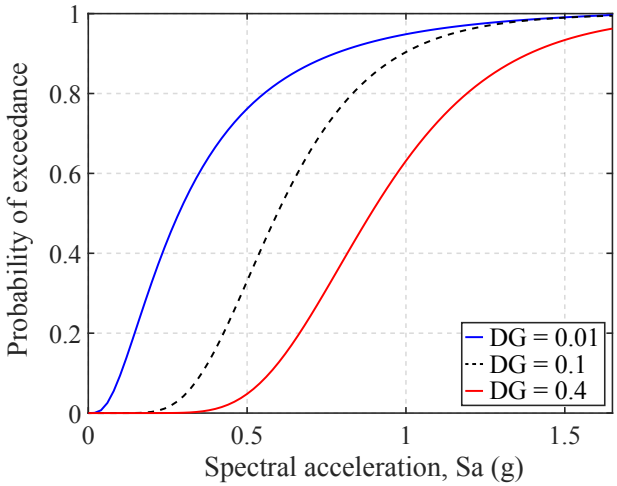

Figure 5.23: Probability of different damage limit states

Figure 5.23 compares the fragility curves for the three limit states defined in terms of the proposed damage index. The curves are constructed from the IDA results and assume that the fragility function follows the cumulative distribution function of the log-normal distribution. The fragility curves permits an estimation of the structural damage state for a given ground motion intensity so that measures for damage mitigation can be undertaken.

5.6.5 Case study: collapse assessment with aftershocks

The following case study illustrates an application of the proposed global damage index in the damage assessment of structures in the event of aftershocks. The archetype 8-story frame is subjected to a series of ground motions consisting of a main shock and an aftershock. An incremental dynamic analysis is performed and the global damage index is used to assess the change in the damaged states and the collapse fragility of the structure with consideration of aftershocks.

5.6.5.1 Ground motions

Characterization of aftershocks involves two major sources of uncertainties: the probable intensity and the location of the aftershock relative to the main shock. Both can create different damaging effects to the structure. Another critical aspect is when the aftershock occurs after the main shock. This has an important implication in repair of damaged buildings, that is, whether it is more practical to repair immediately after the main shock and perhaps again following the aftershock, or to repair after the aftershock provided that the structure survives the main shock. These complex issues are beyond the scope of this study.

For this preliminary study, the following assumptions are made: (1) the main shock is among the 21 far-field ground motions in the preceeding sections; (2) the aftershock is identical to the main shock, and consequently, has the same spectral shape and energy content; (3) the effect of free vibration after the MS is neglected and the aftershock follows the main shock immediately; (4) the effect of the aftershock location is not accounted for; and (5) the ground motions are scaled by the same factor in the main shock and the aftershock for the incremental dynamic analysis.

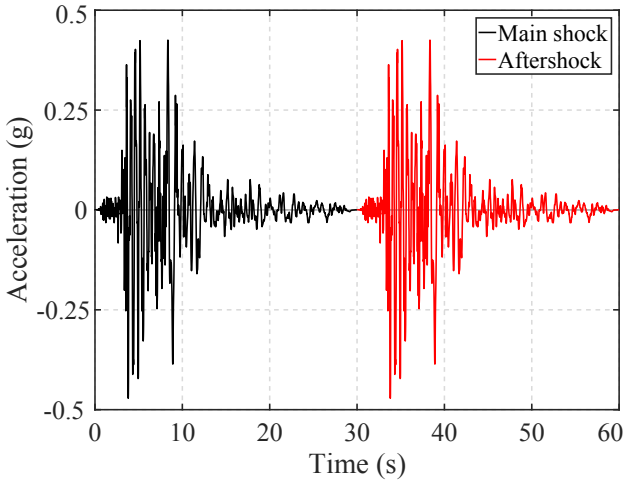

Figure 5.24: Acceleration history of FF1 record with aftershock

The simplifications, in particular (2)-(5), might not give the most realistic representation of the AS; however, they are sufficient for the current study. Moreover, the selection of the aftershock as large as the main shock has been done in design practice and found to give confidence to engineers, public officials, and owners as they already have a clear idea of what the structure undergoes in the main shock. Figure 5.24 illustrates the ground acceleration history of the MS and aftershock sequence, in which the MS is the FF1 record with $SF = 1$.

5.6.5.2 Collapse probability

Figures 5.25(a)–(b) plot the collapse probability against a ground motion intensity measure and a target demand parameter, respectively, in two cases: (1) if only the main shock is considered (MS), and (2) both the main shock and the aftershock are considered (MS + AS).

The fragility curves in Figure 5.25(a) suggest that under the same spectral acceleration S_a, the aftershock leads to a considerable increase in the collapse risk: from 20% under MS to 45% under MS + AS, 40% under MS to 75% under MS + AS. The aftershock also results in a roughly 30% increase in the collapse margin ratio, which is proportional to the ground motion intensity corresponding to a 50% collapse probability [4].

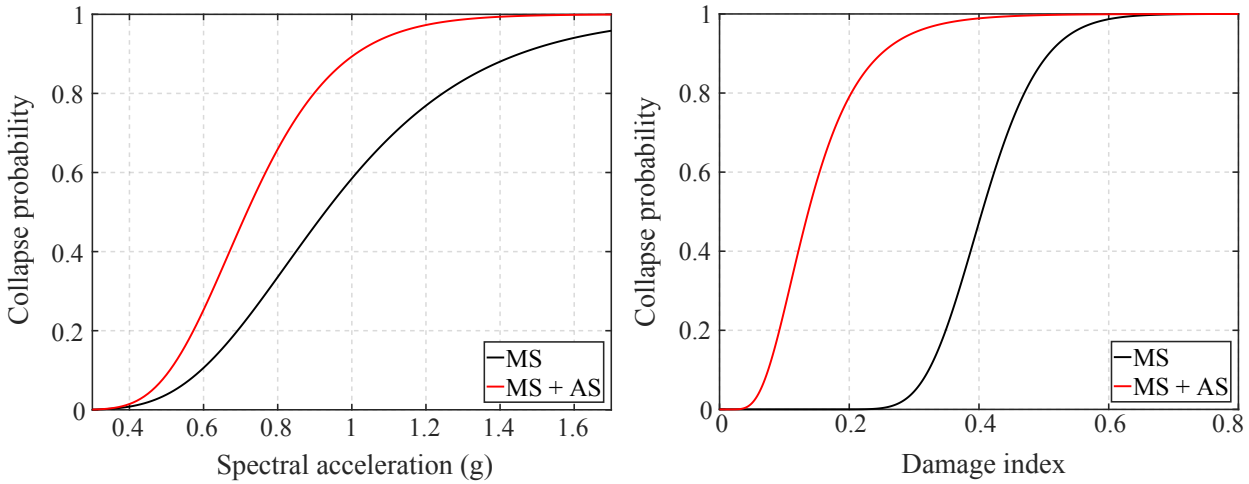

(a) Ground motion intensity (b) Damage index after main shock

Figure 5.25: Collapse probability with and without consideration of aftershocks

Figure 5.25(b) implies a substantial increase in the collapse risk if an aftershock follows. For example, the structure does not collapse with $D_G = 0.2$ at the end of the main shock; however, if an aftershock follows, the collapse risk increases significantly with a 80% probability. In another example, the threshold $D_G = 0.4$ at the end of the main shock is the median damage level corresponding to a 50% collapse probability if only the main shock is accounted for; however, if an aftershock follows, this damage level almost ensures collapse with a 98% probability. Figure 5.25(b) suggests that to target a 50% collapse probability, the structure is designed for a damage threshold $D_G = 0.4$ if only the main shock is accounted for. However, if the aftershock is also considered, the target damage threshold becomes $D_G = 0.13$, which implies that the structure is designed for the CP limit state instead of the CL limit state at the end of the main shock. Due to the substantial increase in the collapse probability and the more stringent requirements of the allowable damage when aftershocks are present, the study recommends that aftershocks should be considered in the dynamic analysis and design of structures. The structure should be 'red-tagged' once the damage index exceeds the CP limit state threshold $D_G = 0.1$ to account for the possible following aftershock.

It is instructive to compare the collapse fragility of the structure under aftershocks using other commonly used damage measures, such as the maximum story drift and the residual story drift. This task will be pursued in future studies.

5.7 Effect of Modeling Assumptions

The proposed damage-plasticity element models account for three characteristic features that capture complex global and local behavior up to collapse: (1) the strength and stiffness deterioration of the element response, (2) the plastic hinge offsets, and (3) the inelastic axial force-deformation relation and the effect of variable axial forces on the flexural behavior. In practice, one or several aspects are often neglected in the simulations due to limitations of available models. In this section, the structural model in the preceeding sections is used as a reference (model R) to compare against three alternatives that represent commonly-used existing models:

- *Model A*: same as Model R, but the element response does not account for damage. The element behavior is linear elastic with linear kinematic and isotropic hardening.
- *Model B*: same as Model R, but no plastic hinge offset is specified. The model does not explicitly simulate the RBS connections.
- *Model C*: same as Model R, but the column response does not account for the inelastic axial behavior and the axial-flexural interaction. To replicate this behavior, the damage-plasticity beam element in Chapter 3 is used to model the columns.

The comparison addresses two objectives: (1) to evaluate the change in the dynamic response of the archetype SMF in the absence of the aboved features in the element models, (2) to identify potential limitations of the existing element models and highlight the advantages of the proposed models in collapse assessment of SMFs.

5.7.1 Effect of element damage

The response under the Loma Prieta record at Gilroy Array station (FF14) is used to distinguish model R and model A. With the strength and stiffness deterioration, the structure collapses at $SF = 9.0$ compared to $SF = 12.15$ if no element damage is accounted for. Figure 5.26 compares the global and local response of the two models under the same ground motion intensity $SF = 9.0$. The average lateral roof drifts are almost identical up to $t = 15$ sec whereas the 1st story drifts deviate substantially after $t = 5$ sec. In contrast to model A, model R shows a drastic increase in the 1st story drifts and indicates the loss of global stability. The residual story drift distribution in Figure 5.26(c) implies a 1-story collapse mechanism with excessive 1st story drift in model R and a stable structure with negligible deformations in model A.

Figures 5.26(d)-(f) highlight the local response of the members in the 1st story. Model A captures well the yield strength and the response prior to softening because both models use the same elements to describe the nondegrading response, but misses the strength and stiffness deterioration under cyclic loading. Without the strength and stiffness deterioration, less plastic axial deformation is accumulated in the columns, as evident in the axial response

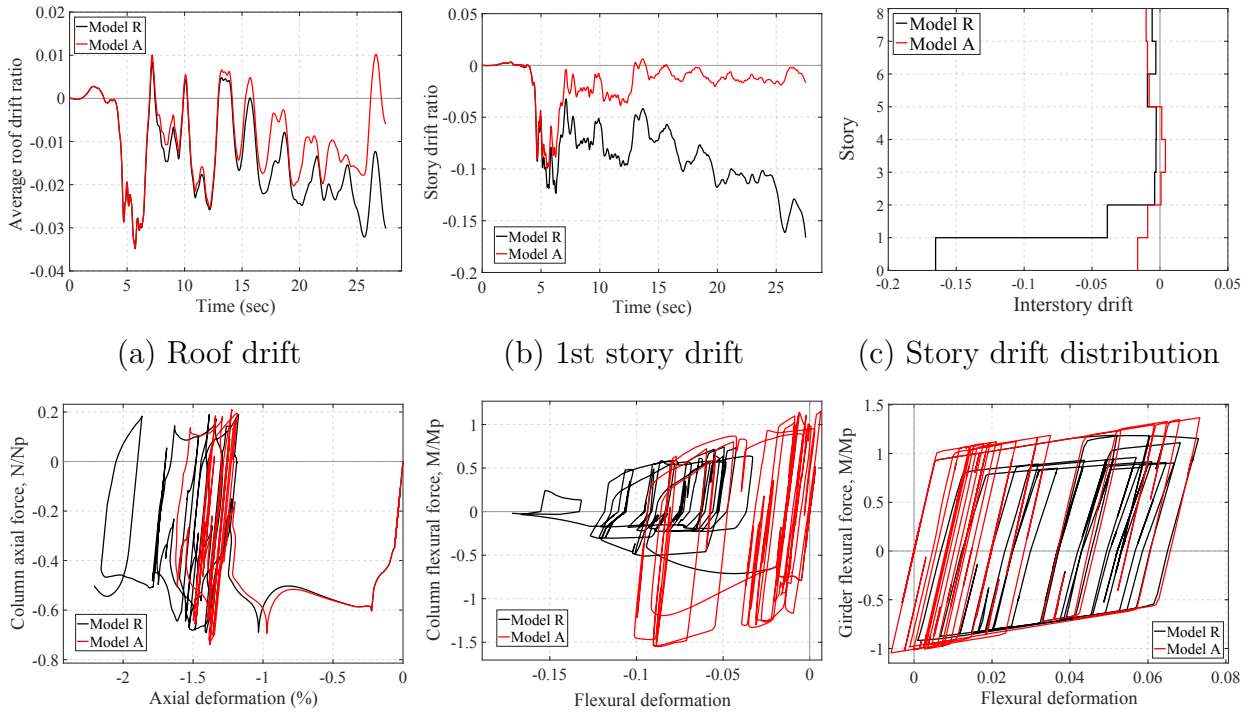

(a) Roof drift (b) 1st story drift (c) Story drift distribution

(d) C-1-1 axial response (e) C-1-1-B flexural response (f) G-1-3-R flexural response

Figure 5.26: Comparison of dynamic response in model R and model A

of C-1-1 in Figure 5.26(d). Model A gives stable hysteresis loops for the column moment-rotation relation and overlooks the severe strength reduction in C-1-1, as Figure 5.26(e) shows. Discrepancies in the girder response are less pronounced in Figure 5.26(f) because the damage in the girders is relatively mild.

Figure 5.27 shows the response of model A at $SF = 12.15$ to demonstrate the different collapse behavior when element damage is not accounted for. The story drift distribution in Figure 5.27(a) suggests that the structure is subjected to a large pulse at $t = 5$ sec leading to a 2-story mechanism with excessive drifts in the bottom two stories. In contrast to the collapse behavior of model R at $SF = 9.0$, the structure does not lose stability but stabilizes with smaller story drifts as the ground motion progresses. Figure 5.27(b) compares the story drift distribution at the instant of maximum story drift and at the end of the ground motion to highlight the structural stability in the absence of element damage. The global response is also reflected in the floor rotation distribution in Figure 5.27(c), which shows large positive rotations with the bottom two floors in the early cycles followed by stable oscillations with small amplitudes in later cycles.

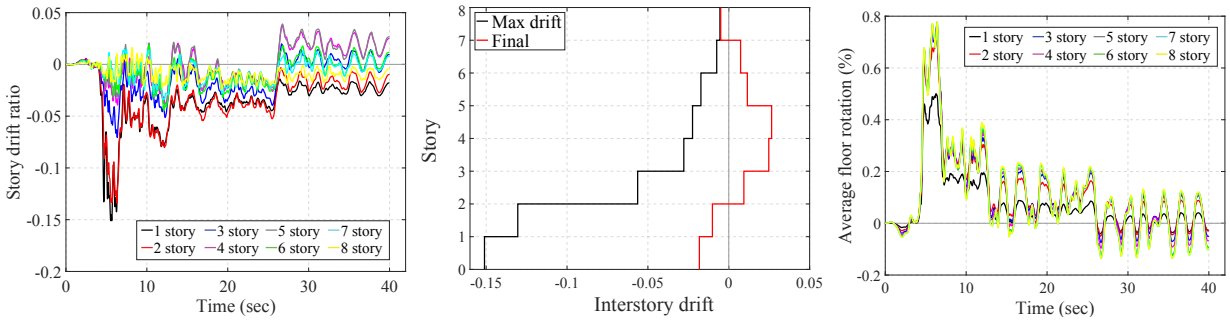

(a) Story drift ratio (b) Story drift distribution (c) Average floor rotation

Figure 5.27: Dynamic response without element damage (FF14, SF = 12.15)

5.7.2 Effect of plastic hinge offsets

Model B uses the same beam and column elements as the reference model R but does not explicitly simulate the RBS connections. No plastic hinge offset is specified in the girders: the offset parameter $\chi = 0$ and the section strength factor $\lambda = 1$. To investigate the impact of the plastic hinge offsets, this section compares the two models using three representative ground motions: (1) Imperial Valley record at Delta station (FF5) with scale factor $SF = 2.7$, (2) San Fernando record at LA-Hollywood station (FF20) with scale factor $SF = 6.84$, (3) Duzce record at Bolu station (FF3) with scale factor $SF = 6.12$.

Global response

Figure 5.28 compares the average roof translation and suggests moderate discrepancies between the two models. The RBSs enhance the structural performance by reducing the roof drift under FF5 but show no benefit under FF20 and FF3.

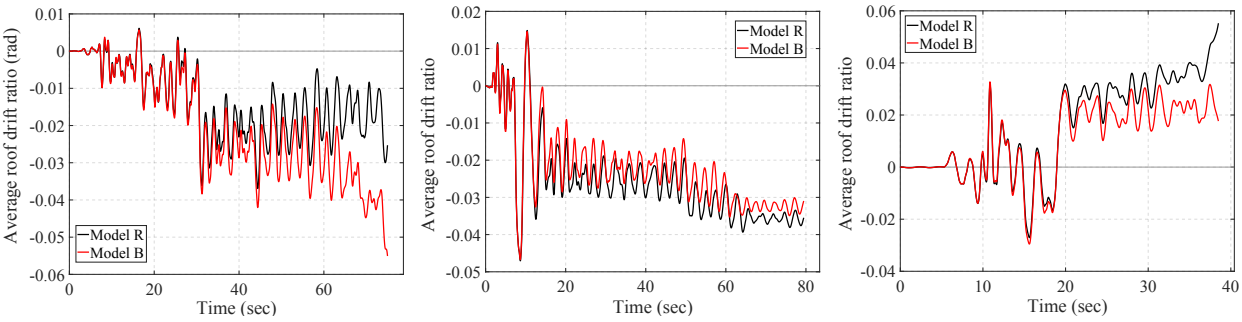

(a) FF5, SF = 2.7 (b) FF20, SF = 6.84 (c) FF3, SF = 6.12

Figure 5.28: Comparison of model R and model B: average roof translation

The 1st story drift in Figure 5.29 offers further insight of the model response. Under

FF5, the plastic hinge offsets in model R strengthen the structure and avoid the rapid story drift increments that lead to instability in model B. Under FF20, the offsets also improve the global response by reducing the story drift. Conversely, under FF3, the offsets weaken the structure and cause excessive 1st story drifts.

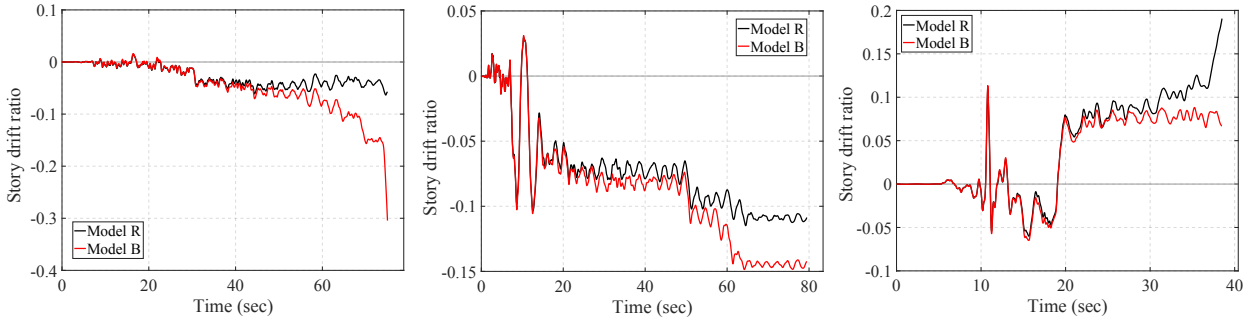

(a) FF5, SF = 2.7 (b) FF20, SF = 6.84 (c) FF3, SF = 6.12

Figure 5.29: Comparison of model R and model B: 1st story drift

The story drift time history suggests that the roof drift alone is insufficient to capture the complex behavior of structures under extreme loads. Additional response variables in the stories and elements are necessary to evaluate the response at a more local level, especially when the inelastic behavior is localized in a small portion of the structure in an event of a weak-story mechanism.

Collapse mechanism

The residual story drift distribution in Figure 5.30 compares the collapse mechanisms predicted by the models. Among the three cases, the plastic hinge offsets are the most effective under the FF5 record with $SF = 2.7$: model R remains stable while model B collapses in a 1-story mechanism. Under the FF20 record with $SF = 6.84$, both models show excessive story drifts but indicate different collapse mechanisms: model R forms a 2-story mechanism with $DR = 0.11$ whereas model B initiates a 1-story mechanism with $DR = 0.14$. In this case, although both models collapse, the plastic hinge offsets improve the global behavior with smaller drifts and a slightly less catastrophic collapse mechanism. Under the FF3 record at $SF = 6.12$, model R collapses with a 2-story mechanism while model B remains stable. This is in agreement with the story drift evolution and suggests that the RBSs appear to be counter-effective.

Damage distribution

Figure 5.31 compares the final damage profiles of the two models. The plastic hinge offsets accumulate more plastic deformations and damage at the reduced sections in the girders to protect the adjacent column ends from severe deterioration. Due to the response redistribution, damage initiates in the girder earlier and spreads among more members in model R than model B.

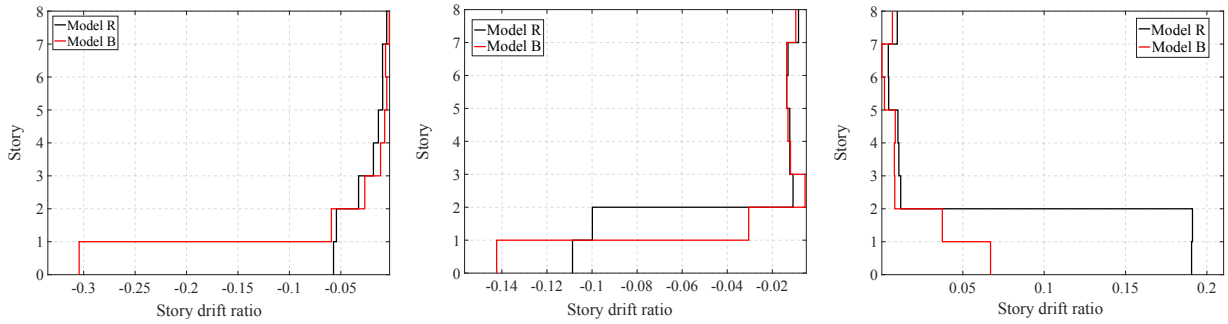

(a) FF5, SF = 2.7 (b) FF20, SF = 6.84 (c) FF3, SF = 6.12

Figure 5.30: Comparison of model R and model B: collapse mechanisms

Under FF5, in model R, only the base of C-1-1 is significantly damaged while the damage in other members are relatively mild. The damage profile suggests that no member fails from severe local buckling and the structure does not initiate a weak-story collapse mechanism. In contrast, damage in model B localizes at both ends of all the 1st story columns and is relatively negligible elsewhere. The high damage values imply severe local buckling that leads to column failure, and subsequently, a 1-story collapse mechanism.

Under FF20, in model R, the highest damage locates at the base of the 1st story columns, the top end of the 2nd story columns, and the 1st floor girders. On the other hand, in model B, damage concentrates at the top and bottom of the 1st story columns. The damage profiles are consistent with the collapse mechanisms observed in the two models: a 2-story mechanism in model R and a 1-story mechanism in model B.

Under FF3, in model R, the highest damage concentrates at the base of the 1st story columns, the top of the 2nd story columns, and the 1st floor girders. The high damage values indicate severe local buckling at these locations and a 2-story collapse mechanism. Damage in model B localizes at the base of the 1st story columns, the top of C-1-4, and the 1st floor girders. The damage distribution indicates a potential 1-story mechanism. It is noteworthy that in contrast to the first two ground motions, in this case the column damage in model R is higher because the excessive girder damage leads to the weak-story collapse mechanism, which in turns accelerates the damage accumulation in these columns.

5.7.3 Axial-flexure interaction

To further investigate the effect of variable axial forces on the strength and stiffness deterioration in the flexural response, two variations of model C are examined:

- **Model CA**: no strength reduction in the columns.
- **Model CB**: the column strength is reduced based on the FEMA P695 recommendations [4]. The strength reduction in a column is determined from the axial-flexure

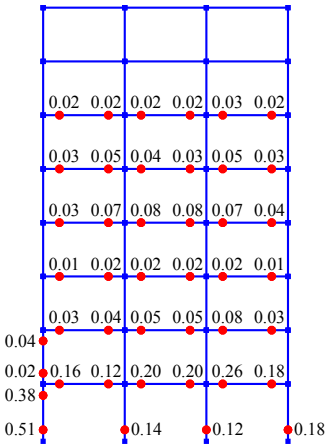

(a) FF5, SF = 2.7: Model R

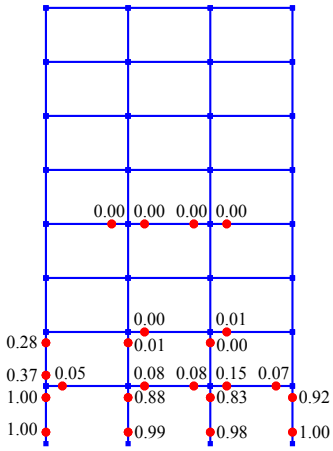

(b) FF5, SF = 2.7: Model B

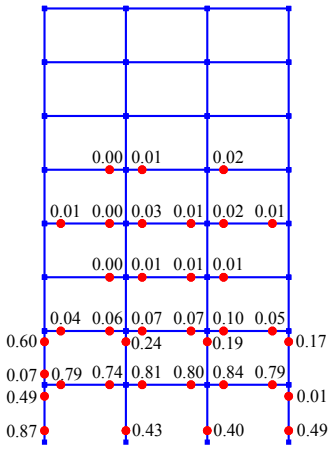

(c) FF20, SF = 6.84: Model R

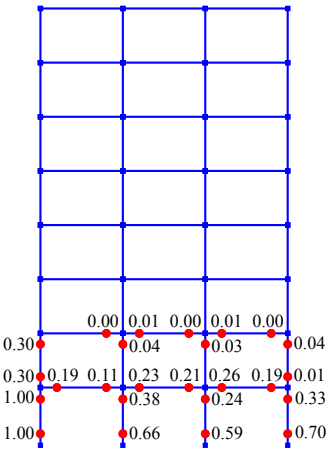

(d) FF20, SF = 6.84: Model B

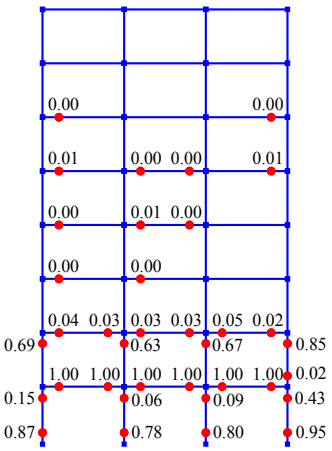

(e) FF3, SF = 6.12: Model R

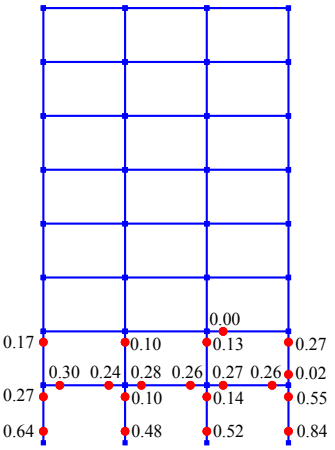

(f) FF3, SF = 6.12: Model B

Figure 5.31: Comparison of model R and model B: damage distribution

interaction envelope for a constant axial force $P_{grav} + 0.5P_E$, where P_{grav} is the gravity load and P_E is the maximum axial force imposed on the column that results from the lateral forces in pushover analysis.

Model CB gives rise to two important observations: (1) theoretically the calibration shall be performed for each individual column because the column axial force varies between stories as well as among members on the same story due to the overturning effect, (2) since the lateral forces are applied in one direction in the pushover analysis, the overturning effect exerts higher axial forces and implies higher strength reduction to the columns of one side of the building. Conversely, the lateral force direction in dynamic analysis varies, and thus, the assumption of the direction in pushover analysis could result in inaccurate estimation of the column strength. To account for the variable load direction, on each floor, the strength reduction in the exterior columns is conservatively selected based on the higher axial force among the two, and the same procedure applies to the interior columns. With these two remarks, model CB requires preprocessing to calibrate the column strength 16 times, i.e. for one exterior and one interior column on each story.

The following discussion highlights the dynamic response of the models in comparison to the reference model.

Model CA

The response under FF17 with $SF = 9.4$ highlights the key differences in model R and model CA. Figure 5.32 plots the evolution and the distribution of the story drifts. The evolution of the drift in the 1st story and at the roof level indicates that model CA remains stable while model R loses stability. The residual deformations in model CA are relative small and do not initiate a weak-story mechanism whereas model R collapses in a 2-story mechanism with considerable drifts in the bottom 2 stories.

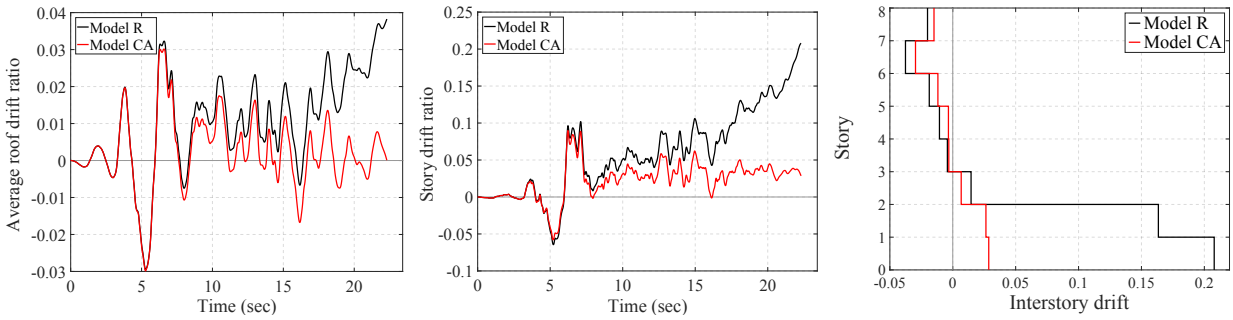

(a) Average roof translation (b) 1st story drift (c) Story drift distribution

Figure 5.32: Comparison of model R and model CA: story drift and deformed shape (FF17, SF = 9.40)

In addition to the excessive lateral drifts, the inelastic axial response allows model R to simulate the significant shortening when the columns are severely damaged, and in turns, the

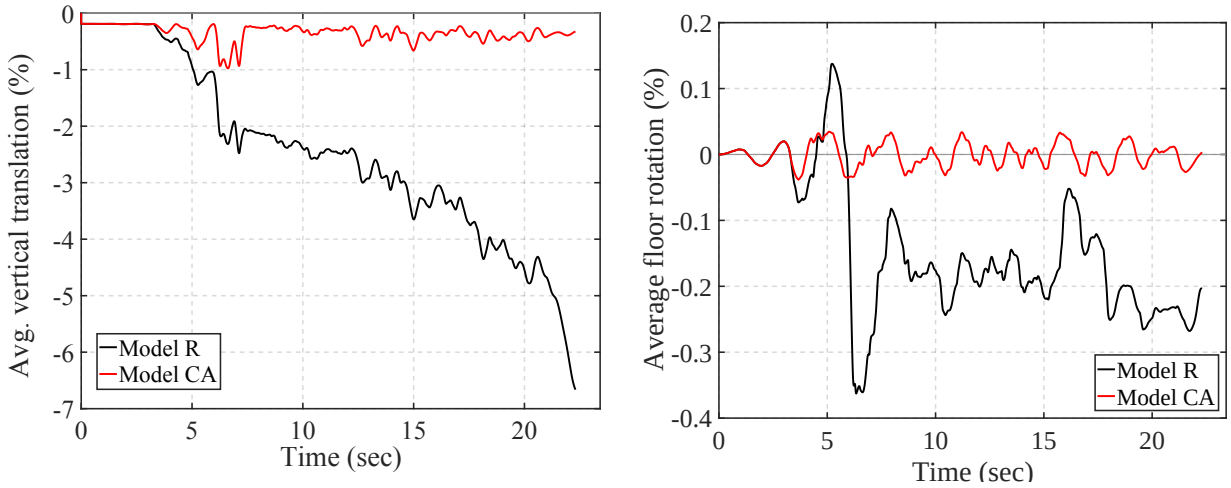

(a) Average 1st floor vertical translation (b) Average 1st floor rotation

Figure 5.33: Comparison of model R and model CA: effect of column shortening (FF17, SF = 9.40)

considerable vertical floor displacement and floor rotation, as illustrated in Figures 5.33(a)-(b). The vertical translation shown in Figure 5.33(a) is given as the average displacements at the top end of the columns on the same story normalized by the column height. Model CA does not capture the plastic axial deformation in the columns and only accounts for the elastic axial deformation, which is relatively negligible, and thus, fails to describe the floor vertical translations as observed in model R. Consequently, the differential axial deformations in model CA are relatively small and lead to insignificant floor rotations. Variations in the floor rotation with alternating signs and small amplitudes imply that the structure oscillates about the undeformed configuration without initiating permanent relative displacements in one dominant direction or a weak-story mechanism.

Figure 5.34 shows the response of left exterior column in the 1st story. Figure 5.34(a) shows the load path at the column base during the first 3 inelastic half cycles in which the column yields and accumulates plastic deformations. The axial and flexural forces are normalized by the respective plastic capacities and superimposed on the initial yield envelope. At the first instant, model R yields at $0.8M_p$ due to an axial compression $-0.25N_p$, whereas model CA yields at the nominal strength M_p. At the second instant, both models yield at a similar strength $-0.9M_p$ under practically no axial force. After several elastic load reversals the models yield the third time, at which model R yields at $-0.7M_p$ under an axial compression $-0.5N_p$ and model CA yields at a slightly higher strength than M_p. It is evident that under a small axial force, model CA gives reasonable approximations of the column yield strength while it overestimates the strength as the axial force increases.

Figures 5.34(b)-(e) compare the flexural and axial response of C-1-1. Model CA fails to capture the excessive strength and stiffness deterioration in the column hysteretic behavior

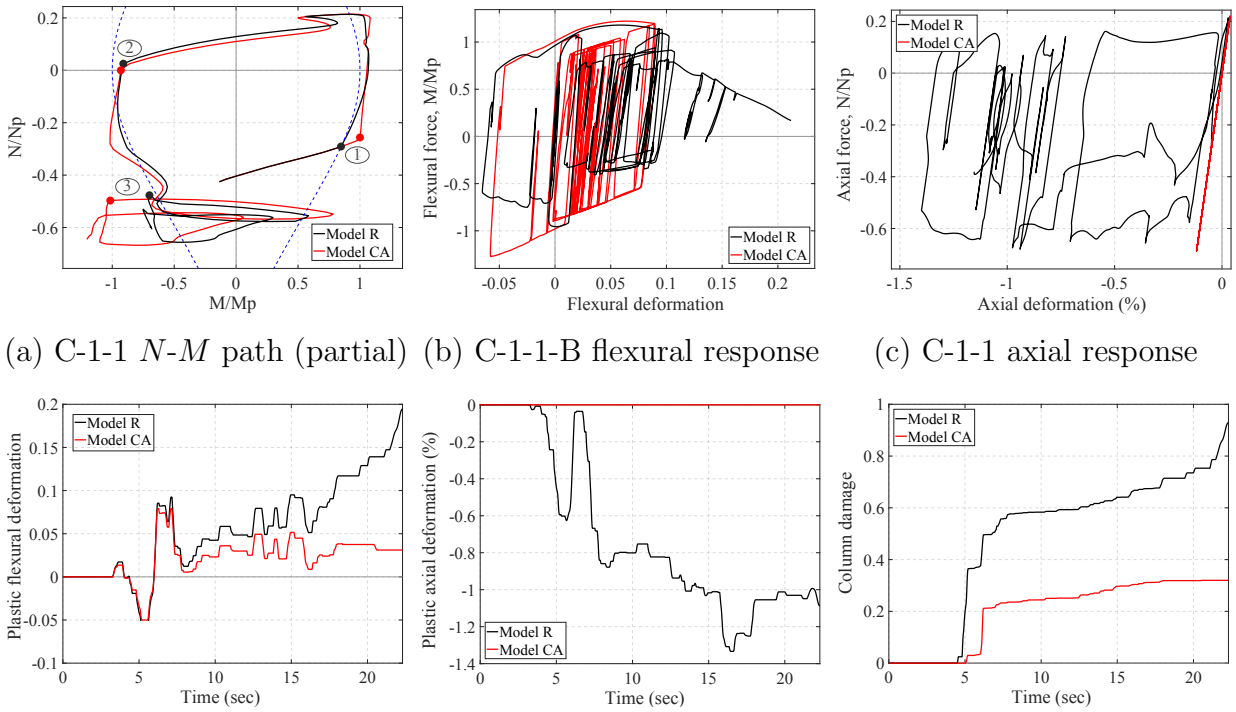

(a) C-1-1 N-M path (partial) (b) C-1-1-B flexural response (c) C-1-1 axial response

(d) C-1-1-B plas. flexural def. (e) C-1-1-B plas. axial def. (f) C-1-1-B damage evolution

Figure 5.34: Comparison of model R and model CA: local column response (FF17, SF = 9.40)

and the significant increments in the flexural deformation near the end of the ground motion. As expected, the two models differ significantly in the axial response. While model CA gives a linear elastic response with limited axial deformations, model R captures the accumulation of the plastic axial deformations as the column yields. The differences in the plastic deformations are reflected in the evolution of the damage variables in the two models, as Figure 5.34(f) shows.

The damage distribution at the end of the ground motion in Figures 5.35(a)-(b) are consistent with the global and the local response. While model R indicates a 2-story mechanism with damage concentration in the members of the lower two stories, model CA suggests a different mechanism with damage localized in the girders. The symmetry of the damage distribution also distinguishes the two models and emphasizes the effect of the axial force on the element damage. In model CA, without the inelastic axial behavior, damage in the columns depends solely on the flexural response. On the same floor, the elements accumulate the same plastic flexural deformations, and thus, leading to the symmetric damage pattern. The inelastic axial response and the axial-flexural interaction allow model R to capture the nonsymmetric damage distribution due to the considerable overturning effect.

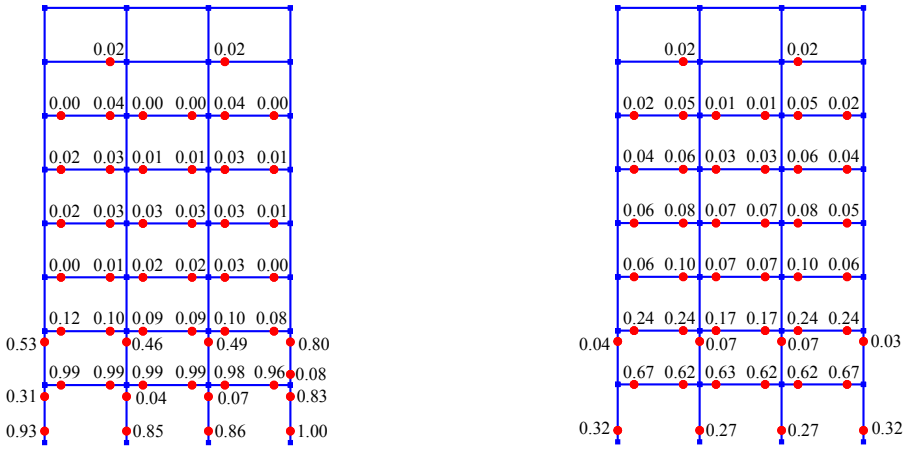

(a) Damage profile: Model R (b) Damage profile, Model CA

Figure 5.35: Comparison of model R and model CA: damage distribution (FF17, SF = 9.40)

Model CB

With the modification based on the FEMA P695 recommendations [4], in contrast to model CA, model CB overestimates the yield strength reduction and the element damage. For all ground motions, model CB requires a lower scale factor SF to trigger collapse, which implies that the model overestimates the collapse fragility of the SMF. The response under the Northridge record at Canyon County station (FF2) is representative of the ground motion suite and distinguishes well the two models. Figure 5.36 plots the roof drift and the 1st story drift as well as the residual deformed shape under FF2 with $SF = 7.92$. The drifts are almost identical up to $t = 7$ sec then start to deviate. Near the end of the ground motion, the 1st story drift in model CB grows rapidly and leads to a 1-story collapse mechanism, as evident in the deformed shape at $t = 12$ sec in Figure 5.36(d). In contrast, in model R, the structure remains stable and does not initiate a weak-story mechanism. It is noteworthy that the deformed shape in model CB shows significant vertical translation of the floors, which results from the excessive lateral story drifts. In each story, the column axial deformations are uniform and the floor remains practically horizontal. In contrast, in model R, even though the vertical translation is less pronounced, the floor rotation is evident due to the discrepancies in the shortening of the columns in a story.

Figure 5.37 shows the response of C-1-1 and the damage distribution to further distinguish the two models. Figure 5.37(a) shows the load path at the column base during the first 3 inelastic half cycles in which the column yields and accumulates plastic deformations. The axial and flexural forces are normalized by the respective plastic capacities and superimposed on the initial yield envelope. At the first instant, model R yields at $0.8M_p$ under an axial compression $-0.25N_p$. On the other hand, model CB yields at $0.6M_p$, which results from the strength reduction due to a constant axial force according to FEMA P695 recommendations.

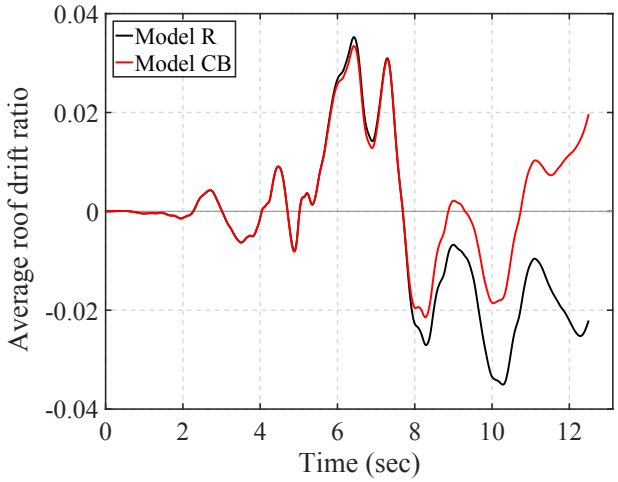

(a) Average roof translation

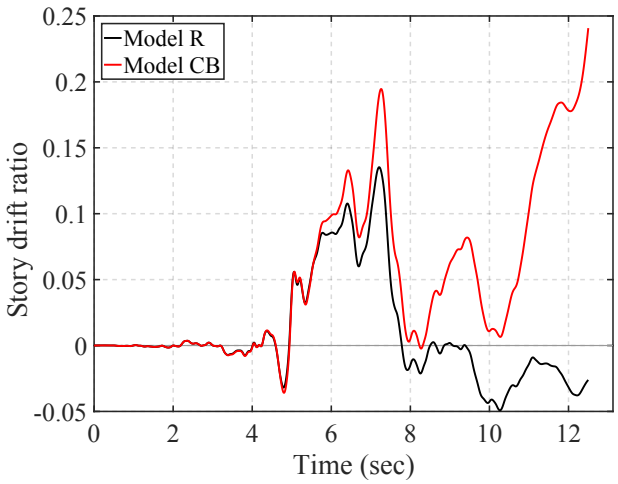

(b) 1st story drift

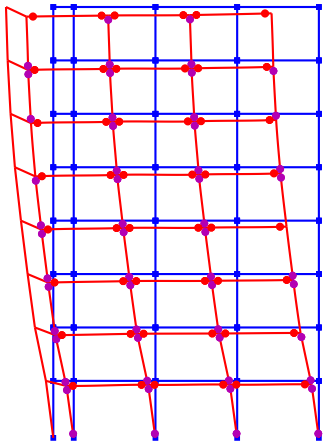

(c) Deformed shape: Model R

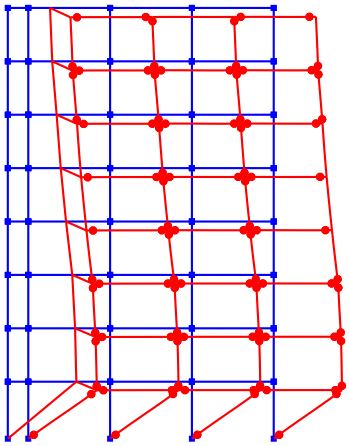

(d) Deformed shape, Model CB

Figure 5.36: Comparison of model R and model CB: story drift and deformed shape (FF2, SF = 7.92)

At the second instant, model R yields at a strength slightly lower than M_p under a small axial compression $-0.05N_p$, while model CB again yields at roughly $0.6M_p$. At the third instant, model R yields under a negative moment with a slightly smaller magnitude than $-M_p$ at axial force $-0.12N_p$, whereas model CB yields at $-0.6M_p$. It is evident that the constant axial force $P_{grav} + 0.5P_E$ underestimates the column yield strength under the effect of variable axial force.

Figures 5.37(b)-(e) compare the flexural and axial response of C-1-1. Model CB overestimates the element damage and shows excessive strength and stiffness deterioration in

the column hysteretic behavior. The flexural deformation grows drastically near the end of the ground motion implying the loss of column stability. As expected, the two models differ tremendously in the axial response. While model CB gives a linear elastic response with limited axial deformation, the damage-plasticity element in model R captures the plastic axial deformations accumulated as the column yields. In model R, the plastic axial deformations are different in the members on the two sides of the structure and lead to the floor rotations as shown in the deformed shape in Figure 5.36(c). The discrepancies in the models are reflected in the damage evolution in the column. Figure 5.37(f) plots the damage variable d defined as the higher of the positive and the negative damage variables d^+ and d^- at the base of the column.

As expected, model CB shows more severe damage in the 1st story columns than model R. In contrast, the damage in the 1st floor girders is higher in model R, which implies different load redistribution mechanisms in the two models. In model CB, the high damage values indicate severe local buckling at both ends of the 1st story columns and leads to a 1-story collapse mechanism. Model R shows severe local buckling at the base of the 1st story exterior columns and the 1st floor girders, moderate damage at the base of 1st story interior columns, and mild to no damage in other members. This damage distribution suggests a possible 2-story mechanism, however, the damage values at the top end of the 2nd story columns are relatively small to trigger a weak story mechanism. It is evident that the column strength modification in model CB weakens the structure and concentrates damage in a smaller region. Moreover, without the inelastic axial behavior, the column damage in model CB depends solely on the flexural response. On the same floor, the same plastic flexural deformations result in a symmetric damage pattern. In contrast, the inelastic axial response and the axial-flexure interaction allow model R to capture the nonsymmetric damage distribution to better identify the more vulnerable locations within the structure.

5.8 Consideration of Element Brittle Failure

5.8.1 Background

Due to software limitations, the FEMA P695 methodology [4] does not explicitly simulate the sudden strength deterioration in the element behavior, and instead, uses component limit checks to account for the non-simulated modes. FEMA recommends that if the plastic rotation in any plastic hinge exceeds $\theta_p = 0.063$, the component is assumed to fracture. FEMA P695 recommends that global collapse takes place if fracture occurs in any element or the story drift exceeds the collapse limit, whichever occurs first. One limitation of this methodology is that it overestimates the true collapse probability because failure of one element does not necessarily result in global collapse. Moreover, the method does not address the response redistribution in the structure in the event of an element failure, which is a very important characteristic of the structural behavior. To address these limitations, another structural model of the eight-story SMF, so-called model D, is developed using the same

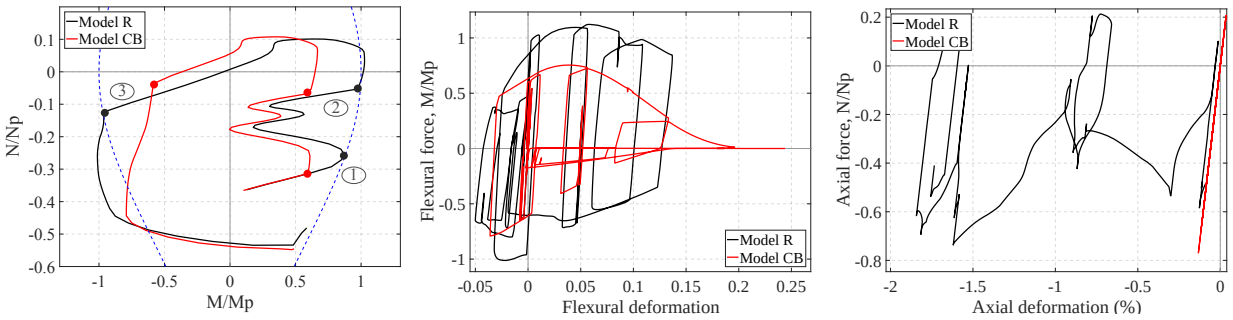

(a) C-1-1 N-M path (partial) (b) C-1-1-B flexural response (c) C-1-1 axial response

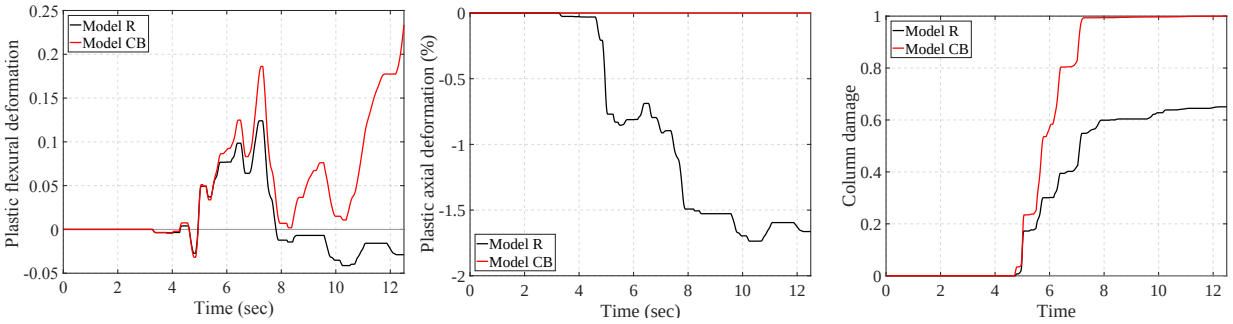

(d) C-1-1-B plas. flexural def. (e) C-1-1-B plas. axial def. (f) C-1-1-B damage evolution

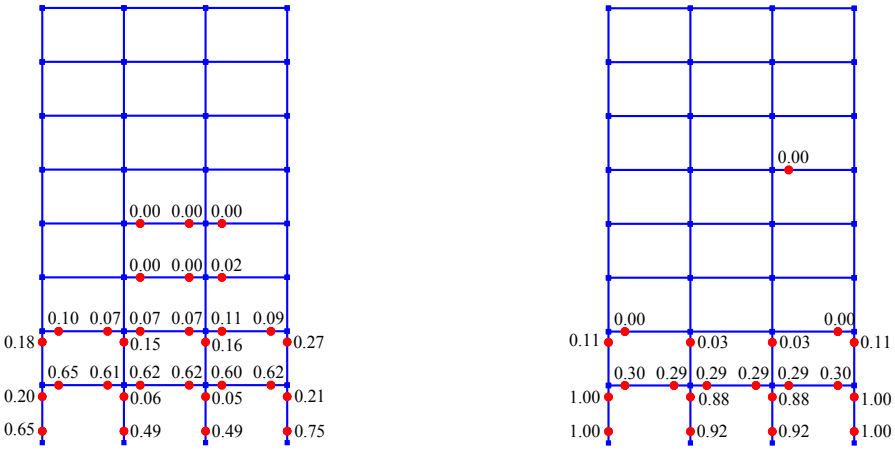

(g) Damage profile: Model R (h) Damage profile, Model CB

Figure 5.37: Comparison of model R and model CB: local column response and damage distribution (FF2, SF = 7.92)

elements as in model R, but the damage evolution is modified to account for the sudden strength deterioration in the element response.

5.8.2 Calibration of model parameters

To describe the sudden strength reduction in the element response, the composite damage evolution function in Section 2.7 is adopted. The following values are specified for the evolution law: the normalized fracture energy $\hat{\psi}_f = 0.14$ and the normalized ultimate energy $\hat{\psi}_u = 0.18$. These values are calibrated so that the plastic energy at the onset of brittle failure $\tilde{\psi} = \hat{\psi}_f$ corresponds to the target plastic rotation $\theta_p = 0.063$ under a constant axial compression of $0.3N_p$. This axial force level is chosen to match the median axial force level in the columns of the SMF subjected to the ground motion suite.

5.8.3 Pushover analysis

Figure 5.38(a) compares the base shear in model D and model R. It is noteworthy that the pushover curve of model D is jagged with sudden reduction in the base shear. Each drop corresponds to an instant of element fracture, and the relatively flat plateaus between the drops indicate the force redistribution after the element failure. Four important events are identified on the pushover curve of model D. The first event A corresponds to the first fracture at the base of C-1-4. Up to this point, both models have identical response, and thus, the same maximum base shear $V_{\max}$. Thereafter, due to the accelerated element strength reduction, the normalized base shear in model D remains smaller. The second event B takes place shortly after A and corresponds to the onset of fracture at the top end of C-1-4. The third event C occurs at a roof drift ratio of 0.035 when the base of C-1-3 fractures and leads to the rapid drop in the base shear. The fourth event D follows almost immediately as fracture initiates at the base of C-1-1 and C-1-2. The roof drift reaches its maximum value of 0.036 then slightly decreases as the structure loses stability and the base shear quickly drops to zero.

The fracturing sequence is confirmed in the response of the 1st story columns in Figure 5.38(b). Fracture of an element leads to a significant drop in the column moment. As fracture progresses among the 1st story columns, the forces redistribute and lead to slight increases in the force demand in the top ends of C-1-1, C-1-2, C-1-3 as Figure 5.38(b) shows.

5.8.4 Dynamic analysis

Model D is subjected to the same 21 far-field ground motions with increasing intensity until collapse. Response under the following two representative cases illustrate the effect of element sudden strength deterioration: (1) the Landers record at Coolwater station (FF12) with scale factor $SF = 5.4$, and (2) the Superstition Hills record at Poe Road station (FF17) with scale factor $SF = 7.2$.

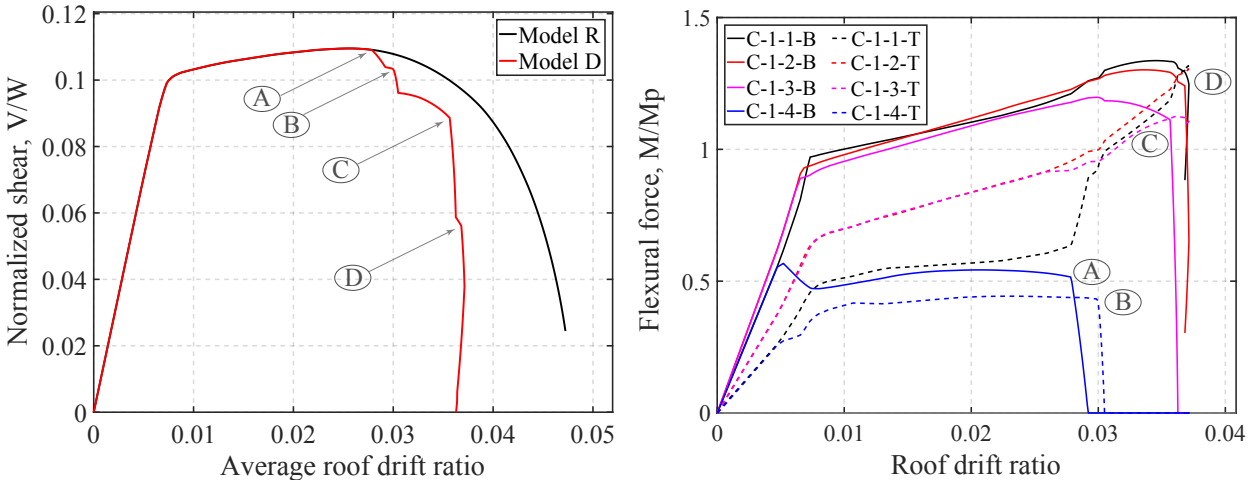

(a) Pushover curve

(b) 1st story column response

Figure 5.38: Pushover analysis response with sudden strength deterioration

Global response

Figure 5.39 compares the 1st story drifts in the two models. The 1st story is selected because most inelastic phenomena are expected to localize in this region. For each ground motion, the instants of element fracturing are identified, which correspond to the damage variable d exceeding the threshold 0.6. Model D exhibits many similar behaviors under the two ground motions. In both cases, the drifts become excessive and indicate the loss of global stability. The first fracture occurs at the base of the exterior column under higher axial compression. Subsequent cycles lead to failure of both exterior columns, excessive story drifts, and then failure at the base of the interior columns. The structure technically collapses at this point as it is no longer able to resist lateral forces at the base. Failure at the top of the 1st story columns follows shortly and accentuates the 1-story mechanism. Conversely, under both ground motions, model R suggests a stable structure without a weak-story mechanism.

The two cases FF12 and FF17, however, differ in the relative motion history of the structure. After the first event, under FF12, the structure switches direction and leans permanently to the right, whereas under FF17, the structure maintains in the same direction. Under FF12, as the structure deforms in the opposite direction after the first exterior column fractures, the overturning effect imposes higher axial compression on the remaining 1st story exterior column, making it more susceptible to fracture. The load reversal with a large drift amplitude in FF12 accentuates the strength deterioration in the exterior columns and initiates collapse faster than in FF17.

Local response

Figures 5.40(a)-(b) show the response of the exterior column C-1-1 and the interior column C-1-2 under FF12. The two models give identical response up to the first event because

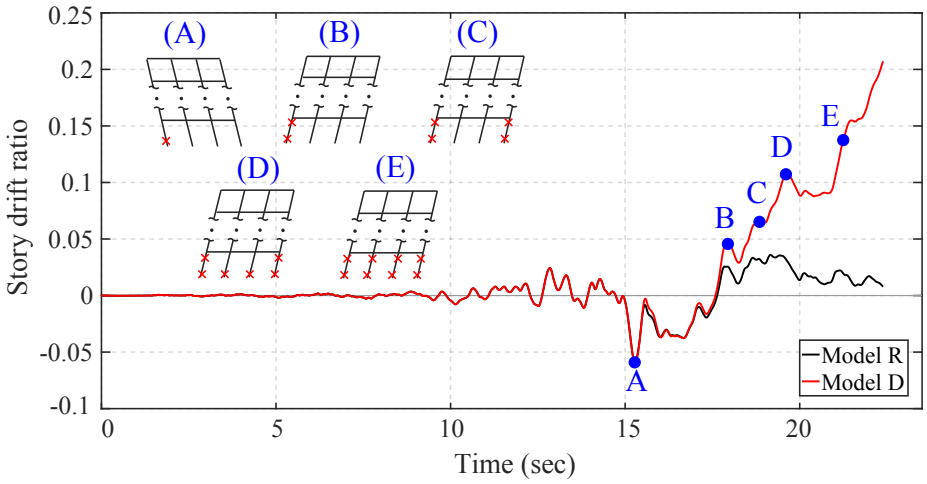

(a) FF12, SF = 5.4

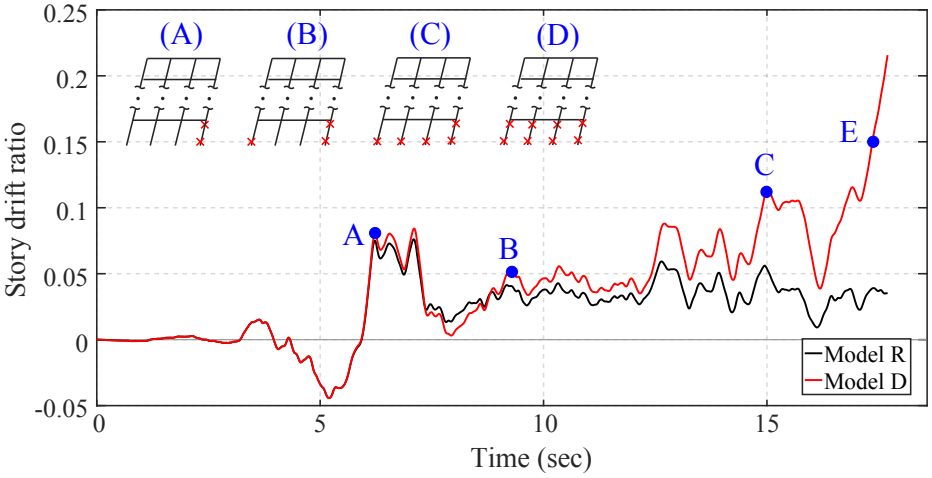

(b) FF17, SF = 7.2

Figure 5.39: Comparison of model R and model D: 1st story drift

the damage evolution is the same until the plastic energy $\tilde{\psi}$ reaches the fracture plastic energy limit ψ_f and initiates the brittle failure. In model D, both the exterior and interior columns experience a sharp strength reduction due to excessive plastic deformations during primary half cycles, in which the deformation exceeds the previous maximum value. The exterior column fails at a smaller plastic flexural deformation amplitude than the interior column due to the higher axial compression and plastic axial deformations from the overturning effect.

Figures 5.40(c)-(d) compare the response of the two exterior columns C-1-1 and C-1-4 under FF17. In model D, both columns fracture and lose all the strength capacity, but in slightly different manners due to the relative motion of the structure. The high axial force and

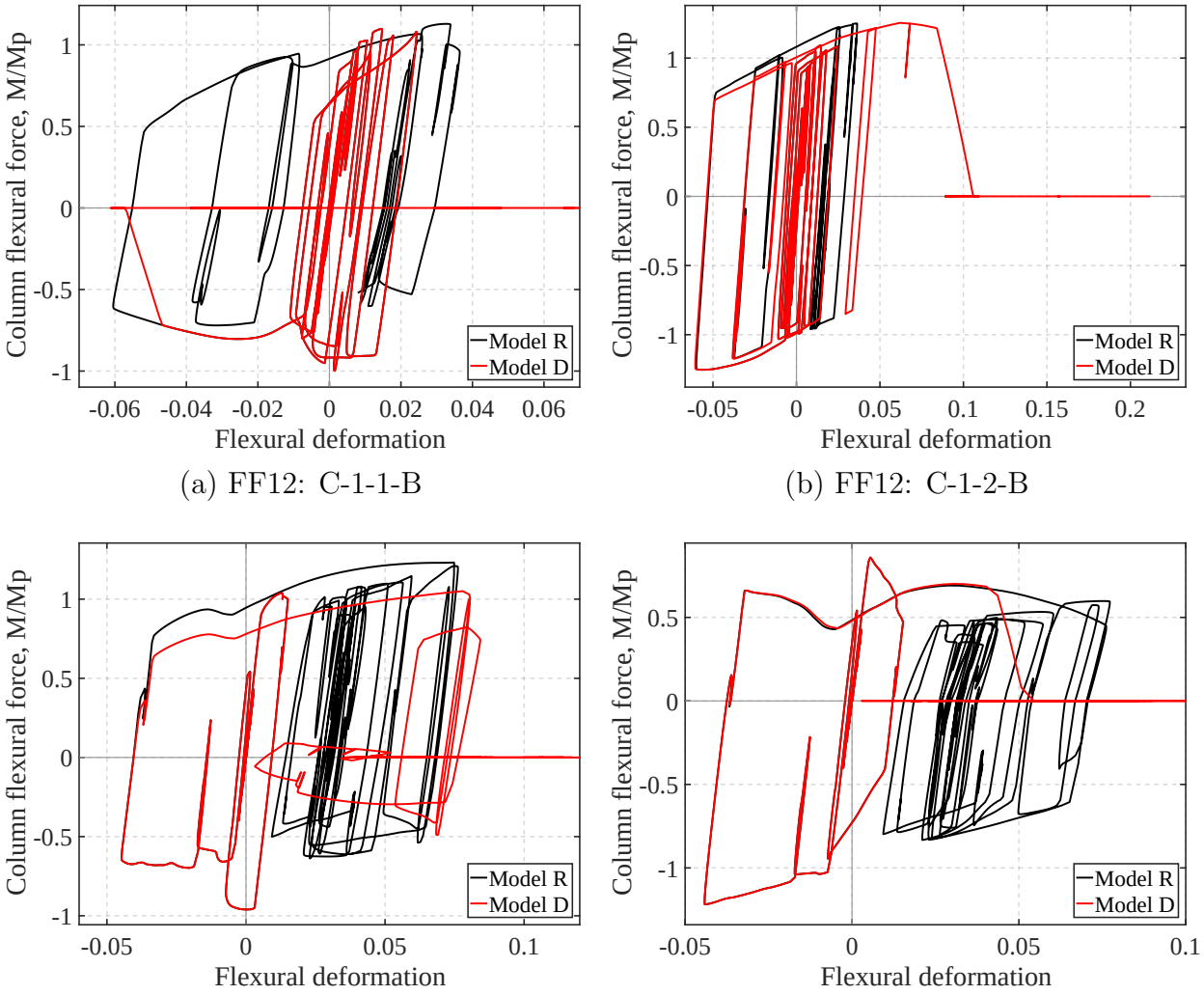

(a) FF12: C-1-1-B

(b) FF12: C-1-2-B

(c) FF17: C-1-1-B

(d) FF17: C-1-4-B

Figure 5.40: Comparison of model R and model D: 1st story column response

plastic deformations accelerate the damage growth in C-1-4, and the column undergoes rapid damage increments within a single primary cycle. On the other hand, C-1-1 is subjected to a lower axial demand and the damage accumulation is relatively more gradual. The strength reduction occurs in multiple subsequent follower half cycles, which explains the longer duration to trigger global collapse in FF17 than FF12.

The case studies highlight the limitations in the FEMA P695 recommendation of the plastic rotation limit $\theta_p = 0.063$ for the non-simulated collapse mode. First, the criteria does not account for the plastic axial deformations and fails to distinguish the failure modes of the columns from the girders. Second, the constant plastic rotation limit θ_p does not account

for the effect of cyclic degradation, which causes the substantial low-cycle fatigue behavior in follower half cycles. Therefore, the proposed element model addresses the limitations of the FEMA P695 criteria and offers a more rational and consistent approach to capture the non-simulated collapse mode.

5.8.5 Further remarks

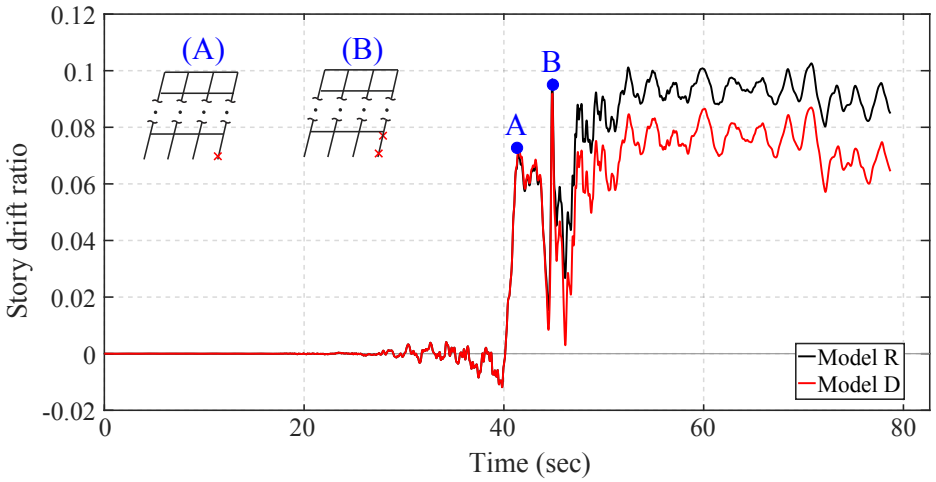

Figure 5.41: 1st story drift ratio under FF19, $SF = 6.93$

The study concludes with an example to illustrate the complex dynamic response with brittle failure in one or several elements. The 1st story drift under the Chi-Chi record at TCU045 station (FF19) with scale factor $SF = 6.93$ is shown in Figure 5.41. It is interesting that even with column failure, model D gives smaller drifts than model R. Only two major events occur in model D: fracture at the base of C-1-4 at roughly $t = 40$ sec and then at the top end of C-1-4 at $t = 45$ sec. The frame then undergoes a large number of cycles without severe damage in other members. The structure does not lose both exterior columns under this ground motion, which is the key driver for the instability under FF12 and FF17.

The local element response and the damage distribution in Figure 5.42 offer further insight of the dynamic behavior. The response of C-1-4 in Figure 5.42(a) is vastly different in the two models. Model D shows a significant strength reduction in a primary half cycle, whereas model R shows relatively less severe damage. In contrast, the response of C-1-1 in Figure 5.42(b) is very similar in the two models with only a slight discrepancy in the damage value at the base: $d = 0.3$ in model R and $d = 0.4$ in model D. The response of G-1-1 in Figure 5.42(c) shows more plastic deformations and damage in model R. The damage profile of model D indicates higher damage in the 1st story columns and lower damage in the other members relative to model R. In this case, the girder damage governs the global behavior and leads to an unfavorable response in model R.

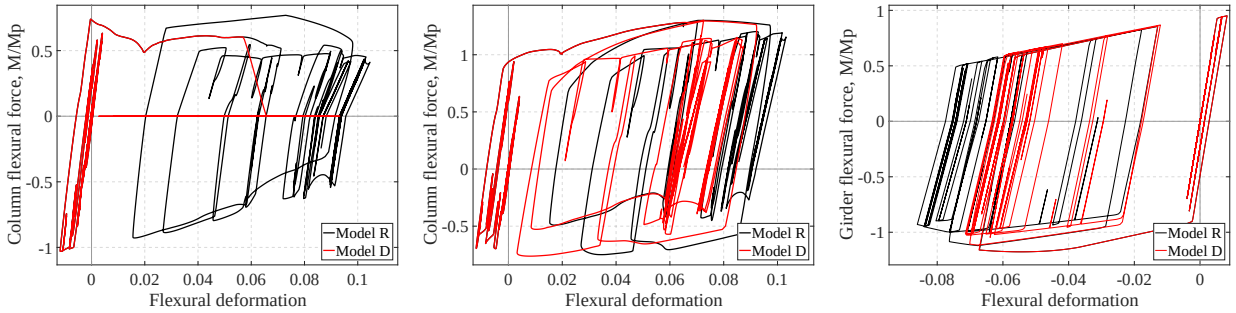

(a) C-1-4-B (b) C-1-1-B (c) G-1-1-L

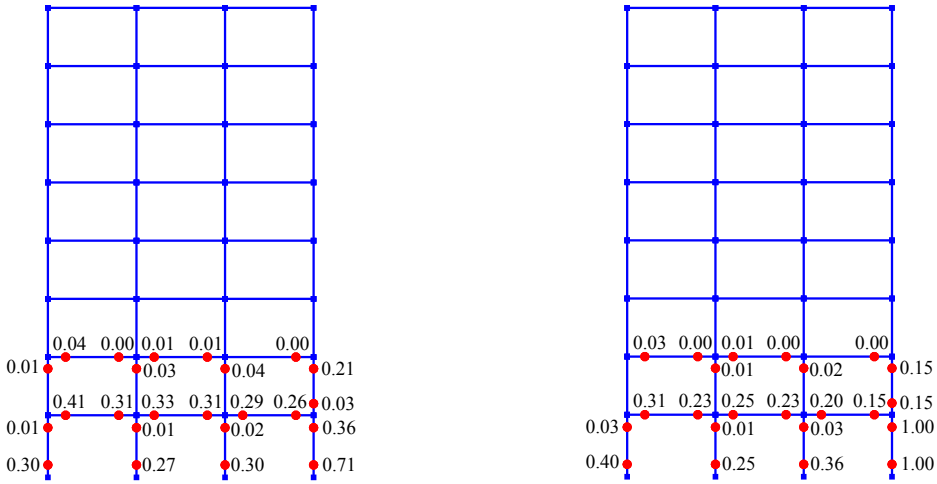

(d) Model R (e) Model D

Figure 5.42: Local response and damage distribution under FF19, $SF = 6.93$

Discrepancies in the local response are attributed to the force redistribution among the members. As fracture progresses, additional forces are exerted on the adjacent members. The simulation result suggests as that as C-1-4 fractures in model D, the additional demand is mainly distributed to the adjacent 1st story columns instead of the 1st floor girders. Further study is required to examine alternative load paths, such as to distribute the response partially to both the columns and the girders.

Chapter 6

Concluding Remarks

6.1 Summary

The objective of this dissertation is the development of a family of beam-column element models which are based on damage-plasticity and are suitable for the damage assessment and the collapse simulation of structures.

First, a new hysteretic damage model based on damage mechanics is developed that relates any two work-conjugate response variables such as force-displacement, moment-rotation or stress-strain. The strength and stiffness deterioration is described by a damage variable with continuous evolution. The formulation uses a criterion based on the hysteretic energy and the maximum absolute deformation value for the damage initiation with a cumulative probability distribution function for the damage evolution. The damage evolution function is extended to accommodate the sudden strength and stiffness degradation of the force-deformation relation due to brittle fracture. The model shows excellent agreement with the hysteretic response of an extensive set of reinforced concrete, steel, plywood, and masonry specimens. In this context it is possible to relate the model's damage variable to the Park-Ang damage index so as to benefit from the extensive calibration of the latter against experimental evidence.

The 1d damage model is then extended to the development of beam-column elements based on damage-plasticity. In these models the non-degrading force-deformation relation in the effective space is described by a linear elastic element in series with two rigid-plastic springs with linear kinematic and isotropic hardening behavior. The first model, the series beam element, assumes that the axial response is linear elastic and uncoupled from the flexural response. The second model, the NMYS column element, uses an axial-flexure interaction surface for the springs to account for the inelastic axial response and capture the effect of a variable axial load on the flexural response. A novel aspect of the beam-column formulation is that the inelastic response is monitored at two locations that are offset from the element ends to account for the spread of inelasticity for hardening response and the size of the damage zones for softening response. The plastic hinge offsets account for the

response coupling between the two element ends. The proposed models assume that damage is governed by the plastic energy dissipation and the maximum absolute deformation values in the plastic hinges. In the column model, the plastic energy dissipation accounts for the interaction between the axial and the flexural response during the degrading hysteretic behavior. The excellent accuracy of the proposed models is confirmed with the agreement with experimental results from more than 50 steel specimens under monotonic and cyclic loading. The models are able to describe accurately the main characteristics of steel members, including the accumulation of plastic deformations, the cyclic strength hardening in early cycles, the low-cycle fatigue behavior, and the different deterioration rates in primary and follower half cycles.

The proposed damage-plasticity frame elements are deployed in an analysis framework for the large-scale simulation and collapse assessment of structural systems. Pushover analysis and dynamic analyses under a suite of 21 far-field ground motions are performed on an 8-story, 3-bay moment resisting steel frame to investigate various aspects of the dynamic behavior of the structure under high ground motion intensity, including the local damage distribution, the distribution of various response variables, and the characteristics of the collapse mechanism. The study proposes new local and global damage indices, which are better suited for the collapse assessment of structures than existing engineering demand parameters like the maximum story drift, and culminates with the definition of key limit states for steel structures in terms of the new damage indices.

To account for the damage distribution over a portion of the structure, the Localized Damage Region (LDR) is introduced to accurately identify the most probable collapse mechanisms consistent with the observed simulated results. Then, an incremental dynamic analysis of the archetype structure under an earthquake sequence is used to highlight the consistency of the proposed damage indices for the collapse assessment of multi-story frames.

The study compares different modeling aspects for the archetype building to assess the benefits of the proposed beam-column elements, such as the ability to account for the member damage, the offset location of the plastic hinges, the inelastic axial response, the axial-flexure interaction, and the sudden strength and stiffness deterioration due to brittle fracture of the structural member.

6.2 Conclusions

6.2.1 Hysteretic damage model

- The modular formulation of the damage model accommodates any force-deformation relation for the non-degrading effective response and any function for the damage evolution law. Moreover, the proposed formulation is thermodynamically consistent.

- The correlation studies of the proposed hysteretic damage model with an extensive set of experimental data for the hysteretic behavior of steel, reinforced concrete, masonry,

and plywood specimens under different load histories demonstrate its ability to describe accurately different types of hysteretic behavior with a consistent set of parameters.

- The continuous updating of the damage variables d^+ and d^- on the basis of a continuous damage evolution law matches the continuous strength and stiffness degradation of structural members under cyclic load reversals in contrast to models with discrete updates at the end of each half cycle.

- The damage variables give an assessment of the damaged state of a structural member that is consistent with well-known damage indices and can thus benefit from the extensive calibration of the latter against a large database of experimental observations. The comparison of the damage variables with the Park-Ang damage index, in particular, under different load histories highlights the flexibility of the proposed formulation and its ability to overcome some limitations of this well known index in agreement with recent proposals for its improvement.

6.2.2 Damage-plasticity beam and column elements

- Because the series beam model and the NMYS column model account directly for the rigid-plastic behavior of the plastic hinges, they do not suffer from the numerical issues that plague existing series models that use a high elastic stiffness to simulate the rigidity of the inelastic spring before yielding. Because the series spring formulation does not require additional nodes at the interface between the zero-length inelastic spring and the elastic element, it is characterized by a better-conditioned, robust numerical response.

- The plastic hinge offsets represent well the spread of inelasticity and describe accurately the post-yield hardening response and the coupling between the response at the element ends. Moreover, the plastic hinge offsets are ideally suitable for the modeling of girders with reduced beam section (RBS) connections with a single element.

- By adopting the resultant-plasticity concept in connection with the 1d hysteretic damage model, the proposed beam and column element models are able to describe the characteristic hysteretic behavior of steel components, including the accumulation of plastic deformations, the cyclic strength hardening in early cycles, the low-cycle fatigue behavior, and the different deterioration rates in primary and follower half cycles.

- The two proposed damage evolution laws, a smooth cumulative distribution function and a composite function that includes a sudden change, capture well the most typical degrading response of steel members: the gradual deterioration captures the strength loss due to local buckling, while the sudden strength and stiffness loss captures the brittle fracture of the member or its connection.

- With the inclusion of the plastic axial energy dissipation in the damage loading function, the damage-plasticity column model captures the effect of a variable axial force on the strength and stiffness deterioration in flexure, the severe deterioration under high axial compression, the nonsymmetric response under a variable axial force, and the large plastic axial and flexural deformations near column failure.

- The correlation studies of the proposed beam-column models with data from more than 50 wide-flange steel specimens under monotonic and cyclic loading give regression equations for the selection of the damage parameters in relation to the web and flange compactness and the member slenderness.

- The proposed beam-column models compare favorably in terms of computational efficiency with more sophisticated models with fiber discretization of the cross section while achieving excellent agreement in the response description for homogeneous metallic structural components. The implementation of the damage-plasticity elements with the return-mapping algorithm ensures excellent convergence characteristics for the state determination.

- The proposed beam-column models strike a balance between accuracy and numerical efficiency to meet the challenge of large-scale simulations of steel multi-story frames under seismic excitations.

6.2.3 Damage assessment of steel moment-frames

The pilot study of an 8-story, 3-bay moment resisting steel frame leads to the following conclusions:

- The pushover analysis with a load distribution that follows the fundamental mode of vibration according to FEMA P695 gives unreliable results regarding the plastic hinge distribution and the collapse mechanism unless the influence of higher modes is included, especially for tall buildings.

- A weak-story collapse mechanism is reflected in the concentration of high plastic deformations in the element response, severe story shear deterioration, relatively large rotations of the floors above the weak stories, and excessive story drifts in one or several stories of multi-story moment resisting frames.

- The magnitude and the distribution of the element damage variables offer insight into the local element response and the global structural behavior. A nonsymmetric damage distribution, typical of a structure with a weak story mechanism, results from excessive story drifts in one dominant direction inducing higher plastic axial deformations in the columns on one side of the building. In contrast, a symmetric damage distribution is indicative of a more stable structure and occurs when the magnitude of the maximum

positive and negative story drift is about the same and the plastic axial deformations are comparable in the columns on both sides of the building.

- The proposed global and local damage indices are cumulative and monotonically increasing with the ground motion intensity. This characteristic allows the damage indices to capture more accurately the continuous damage evolution of the structure and offer several advantages over commonly used EDPs such as the maximum story drift, which only captures the maximum value. Moreover, the damage indices are highly dependent on the plastic axial deformation, which is critical in the collapse assessment of multi-story buildings but is often neglected in seismic response analyses.

- By correlating the proposed global damage index with the maximum story drift three limit states are identified for the damage evaluation of steel moment-resisting frames: life safety, collapse prevention, and collapse.

- The Localized Damage Region (LDR), which is established directly from the damage distribution, is able to identify the most probable collapse mechanism of the structure in agreement with the results of several dynamic response simulations.

- The incremental dynamic analysis of the archetype structure under an earthquake sequence demonstrates the capabilities of the damage indices and emphasizes the important influence of aftershocks in the collapse of multi-story frames. With an aftershock as strong as the main shock, the collapse margin ratio increases by as much as 30%.

- Neglecting the strength and stiffness deterioration of structural members leads to an underestimation of the collapse fragility and to the inability to predict the actual collapse mechanism.

- The plastic hinge offsets play an important role in the seismic response of the multi-story frames under high ground motion intensities. The dynamic response with offset plastic hinges for simulating RBS connections in the girders of the multi-story frame gives contradictory results: (1) On the one hand, the RBS connections improve the dynamic behavior of the structure and prevent collapse at an intensity that results in a weak-story collapse mechanism for the frame without the RBS connections; (2) On the other hand, the RBS reduces the lateral strength of the multi-story frame and leads to a significant damage accumulation in the RBS connection that leads to early global collapse.

- Neglecting the column strength reduction due to the axial-flexure interaction leads to an underestimation of the collapse fragility and an inaccurate prediction of the collapse mechanism. In contrast, the calibration of the column strength based on the constant axial force recommendation in FEMA P695 leads to an overestimation of the collapse fragility.

- Column models with linear elastic axial response fail to capture the pronounced vertical floor translations, the floor rotations, and the nonsymmetric damage distribution when a weak-story collapse mechanism arises.

- The sudden strength and stiffness deterioration due to brittle fracture of the member leads to the redistribution of forces and plastic deformations in adjacent elements, and in turn, to the progressive failure of the corresponding members of the structural model. As a result, significant damage is localized in a smaller region as the structure that initiates a weak-story mechanism and leads to higher collapse fragility.

6.3 Recommendations for Further Study

This dissertation develops an analytical framework for the large-scale simulation and collapse assessment of structural systems and showcases its potential in the pilot study of the 8-story moment frame in Chapter 5. It is recommended to extend the study to different steel structures to cover a range of building configurations common in earthquake resistant design practice. It is also recommended to explore the impact of different ground motion characteristics on the damage evolution of structures. A thorough investigation of common modeling assumptions regarding damping is also important. Finally, it is recommended to correlate the damaged variables and the associated damage states to economic losses so as to extend the study to the resilience assessment of structures under one or more extreme events in sequence.

There is, naturally, room for further investigation of the proposed hysteretic damage model and the beam-column element models. Areas of further study are:

- Different constitutive models for the force-deformation relation in the effective force space may be better suited for the variety of structural systems with materials ranging from steel and reinforced concrete to timber and masonry. Similarly, different damage evolution functions may provide a better description for the damage evolution of these materials.

- The inclusion of the damage parameter evolution in terms of non-mechanical effects, such as fire, environmental conditions, and chemical exposure, can help extend the proposed framework to the evaluation of structures under multi-hazard risk scenarios.

- The inclusion of the axial strength deterioration under significant flexural damage in the column model can improve the assessment of the collapse risk of multi-story frames under seismic excitations.

Bibliography

[1] ASCE/SEI 7-05. "Minimum design loads for buildings and other structures". In: American Society of Civil Engineers Virginia, USA. 2006.

[2] Daniela Addessi and Vincenzo Ciampi. "A regularized force-based beam element with a damage-plastic section constitutive law". In: *International Journal for Numerical Methods in Engineering* 70.5 (2007), p. 610.

[3] Federal Emergency Management Agency. *Prestandard and Commentary for the Seismic Rehabilitation of Buildings*. Tech. rep. Report FEMA 356, Federal Emergency Management Agency, Washington, D.C., 2000.

[4] Federal Emergency Management Agency. *Quantification of Building Seismic Performance Factors*. Tech. rep. Report FEMA P-695, Federal Emergency Management Agency, Washington, D.C., 2009.

[5] ANSI AISC. "AISC 341-05". In: *Seismic provisions for structural steel buildings. Chicago (IL): American Institute of Steel Construction* (2005).

[6] AISC ANSI. "Aisc 358–05 prequalified connections for special and intermediate steel moment frames for seismic applications". In: *American Institute of Steel Construction Inc., Chicago* (2005).

[7] Ferdinando Auricchio and Robert L Taylor. "Two material models for cyclic plasticity: nonlinear kinematic hardening and generalized plasticity". In: *International Journal of Plasticity* 11.1 (1995), pp. 65–98.

[8] Thomas T Baber and Mohammad N Noori. "Random vibration of degrading, pinching systems". In: *Journal of Engineering Mechanics* 111.8 (1985), pp. 1010–1026.

[9] Thomas T Baber and Yi-Kwei Wen. "Random vibration hysteretic, degrading systems". In: *Journal of the Engineering Mechanics* 107.6 (1981), pp. 1069–1087.

[10] Hakim Bechtoula, Susumu Kono, and Fumio Watanabe. "Experimental and analytical investigations of seismic performance of cantilever reinforced concrete columns under varying transverse and axial loads". In: *Journal of Asian Architecture and Building Engineering* 4.2 (2005), pp. 467–474.

[11] R Bouc. "Forced vibration of mechanical systems with hysteresis". In: *Proceedings of the Fourth Conference on Nonlinear Oscillation, Prague, Czechoslovakia*. 1967.

[12] Yousef Bozorgnia and Vitelmo V Bertero. "Damage spectra: characteristics and applications to seismic risk reduction". In: *Journal of Structural Engineering* 129.10 (2003), pp. 1330–1340.

[13] JM Bracci et al. "Deterministic model for seismic damage evaluation of reinforced concrete structures". In: *National Center for Earthquake Engineering Research, Technical Report NCEER-89-0033, State University of New York at Buffalo* (1989).

[14] Brian Chiou et al. "NGA project strong-motion database". In: *Earthquake Spectra* 24.1 (2008), pp. 23–44.

[15] Anil K Chopra and Frank McKenna. "Modeling viscous damping in nonlinear response history analysis of buildings for earthquake excitation". In: *Earthquake Engineering & Structural Dynamics* 45.2 (2016), pp. 193–211.

[16] A Cipollina, A López-Inojosa, and J Flórez-López. "A simplified damage mechanics approach to nonlinear analysis of frames". In: *Computers & Structures* 54.6 (1995), pp. 1113–1126.

[17] Ray W Clough. *Effect of stiffness degradation on earthquake ductility requirements*. Tech. rep. UCB/SESM-1966/16, Department of Civil Engineering, University of California Berkeley, Berkeley, CA, 1966.

[18] J Coleman and Enrico Spacone. "Localization issues in force-based frame elements". In: *Journal of Structural Engineering* 127.11 (2001), pp. 1257–1265.

[19] Applied Technology Council. *Effects of Strength and Stiffness Degradation on Seismic Response*. Tech. rep. Report ATC 62/FEMA P440A, Federal Emergency Management Agency, Washington, D.C., 2009.

[20] René De Borst et al. *Nonlinear finite element analysis of solids and structures*. John Wiley & Sons, 2012.

[21] Derya Deniz. "Stochastic prediction of collapse of building structures under seismic excitations". PhD thesis. University of Illinois, Urbana-Champaign, 2014.

[22] E DiPasquale and AS Cakmak. "Detection of seismic structural damage using parameter-based global damage indices". In: *Probabilistic Engineering Mechanics* 5.2 (1990), pp. 60–65.

[23] Edmondo DiPasquale and Ahmet S Cakmak. *Identification of the serviceability limit state and detection of seismic structural damage*. National Center for Earthquake Engineering Research, 1988.

[24] Sherif El-Tawil and Gregory G Deierlein. "Stress-resultant plasticity for frame structures". In: *Journal of engineering mechanics* 124.12 (1998), pp. 1360–1370.

[25] MD Engelhardt and Thomas A Sabol. "Testing of welded steel moment connections in response to the Northridge earthquake". In: *Northridge Steel Update* 1 (1994).

[26] J Faleiro, S Oller, and AH Barbat. "Plastic-damage analysis of reinforced concrete frames". In: *Engineering Computations* 27.1 (2010), pp. 57–83.

[27] Filip C Filippou, Egor Paul Popov, and Vitelmo Victorio Bertero. *Effects of bond deterioration on hysteretic behavior of reinforced concrete joints*. Tech. rep. Report UCB/EERC-83-19, Department of Civil and Environmental Engineering, University of California, Berkeley, CA, 1983.

[28] Julio Flórez-López. "Frame analysis and continuum damage mechanics". In: *European Journal of Mechanics-A/Solids* 17.2 (1998), pp. 269–283.

[29] Kip Gatto and Chia-Ming Uang. "Effects of loading protocol on the cyclic response of woodframe shearwalls". In: *Journal of Structural Engineering* 129.10 (2003), pp. 1384–1393.

[30] Melbourne Fernald Giberson. "The response of nonlinear multi-story structures subjected to earthquake excitation". PhD thesis. California Institute of Technology, 1967.

[31] Chad S Gilton and Chia-Ming Uang. "Cyclic response and design recommendations of weak-axis reduced beam section moment connections". In: *Journal of Structural Engineering* 128.4 (2002), pp. 452–463.

[32] VS Gopalaratnam and Surendra P Shah. "Softening response of plain concrete in direct tension". In: *ACI Journal proceedings*. Vol. 82. 3. ACI. 1985.

[33] Surya Kumar V Gunturi and Haresh C Shah. "Mapping structural damage to monetary damage". In: *Structural Engineering in Natural Hazards Mitigation:* ASCE. 1993, pp. 1331–1336.

[34] Jerome F Hajjar and Brett C Gourley. "A cyclic nonlinear model for concrete-filled tubes. I: Formulation". In: *Journal of Structural Engineering* 123.6 (1997), pp. 736–744.

[35] Alex D Hanganu, Eugenio Onate, and Alex H Barbat. "A finite element methodology for local/global damage evaluation in civil engineering structures". In: *Computers & Structures* 80.20 (2002), pp. 1667–1687.

[36] TK Hasselman and JH Wiggins. "Earthquake damage to high-rise buildings as a function of interstory drift". In: *Proc. 3rd Int. Earthquake Microzonation Conf.* 1982, pp. 883–894.

[37] Said I Hilmy and John F Abel. "Material and geometric nonlinear dynamic analysis of steel frames using computer graphics". In: *Computers & structures* 21.4 (1985), pp. 825–840.

[38] Yuli Huang. "Simulating the inelastic seismic behavior of steel braced frames including the effects of low-cycle fatigue". PhD thesis. University of California, Berkeley, 2009.

[39] Luis F Ibarra, Ricardo A Medina, and Helmut Krawinkler. "Hysteretic models that incorporate strength and stiffness deterioration". In: *Earthquake Engineering & Structural Dynamics* 34.12 (2005), pp. 1489–1511.

[40] Pether Inglessis et al. "Model of damage for steel frame members". In: *Engineering structures* 21.10 (1999), pp. 954–964.

[41] LM Kachanov. "On rupture time under condition of creep". In: *Izvestia Akademi Nauk USSR, Otd. Techn. Nauk, Moskwa* 8 (1958), pp. 26–31.

[42] Griengsak Kaewkulchai and Eric B Williamson. "Beam element formulation and solution procedure for dynamic progressive collapse analysis". In: *Computers & Structures* 82.7 (2004), pp. 639–651.

[43] Makoto Kanda et al. "Analytical study on elasto-plastic hysteretic behaviors of reinforced concrete members". In: *Transactions of the Japan Concrete Institute* 10.1 (1988), pp. 257–264.

[44] AM Kanvinde and GG Deierlein. "Cyclic void growth model to assess ductile fracture initiation in structural steels due to ultra low cycle fatigue". In: *Journal of Engineering Mechanics* 133.6 (2007), pp. 701–712.

[45] I Demir Karsan and James O Jirsa. "Behavior of concrete under compressive loadings". In: *Journal of the Structural Division* (1969).

[46] Kazuhiko Kasai, Tran-Tuan Nam, and Bruce F Maison. "Structural collapse correlative analysis using phenomenological fiber hinge elements to simulate two-directional column deteriorations". In: *Earthquake Engineering & Structural Dynamics* 45.10 (2016), pp. 1581–1601.

[47] Warner Tjardus Koiter. *General theorems for elastic-plastic solids*. North-Holland Amsterdam, 1960.

[48] Svetlana M Kostic, Filip C Filippou, and Biljana Deretic-Stojanovic. "Generalized plasticity model for inelastic RCFT column response". In: *Computers & Structures* 168 (2016), pp. 56–67.

[49] WB Krätzig, IF Meyer, and K Meskouris. "Damage evolution in reinforced concrete members under cyclic loading". In: *Structural Safety and Reliability*. American Society of Civil Engineers. 1989, pp. 795–804.

[50] Helmut Krawinkler. "Loading histories for cyclic tests in support of performance assessment of structural components". In: *The 3rd International Conference on Advances in Experimental Structural Engineering, San Francisco*. 2009.

[51] Helmut Krawinkler et al. *Recommendations for Experimental Studies on The Seismic Behavior of Steel Components and Materials*. 1983.

[52] Swaminathan Krishnan and Matthew Muto. "Mechanism of collapse of tall steel moment-frame buildings under earthquake excitation". In: *Journal of Structural Engineering* 138.11 (2012), pp. 1361–1387.

[53] Sashi K Kunnath, Andrei M Reinhorn, and Young J Park. "Analytical modeling of inelastic seismic response of R/C structures". In: *Journal of Structural Engineering* 116.4 (1990), pp. 996–1017.

[54] Jean Lemaitre. *A Course on Damage Mechanics*. Springer Science & Business Media, 2012.

[55] Dimitrios Lignos. *Sidesway Collapse of Deteriorating Structural Systems Under Seismic Excitations*. ProQuest, 2008.

[56] Dimitrios Lignos, Julien Cravero, and Ahmed Mohamed Ahmed Elkady. "Experimental Investigation of the Hysteretic Behavior of Wide-Flange Steel Columns under High Axial Load and Lateral Drift Demands". In: *Proceedings of the 11th Pacific Structural Steel Conference (PSSC)*. EPFL-CONF-222730. 2016.

[57] Dimitrios G Lignos and Helmut Krawinkler. "Deterioration modeling of steel components in support of collapse prediction of steel moment frames under earthquake loading". In: *Journal of Structural Engineering* 137.11 (2010), pp. 1291–1302.

[58] Judy Liu and Abolhassan Astaneh-Asl. "Moment-rotation parameters for composite shear tab connections". In: *Journal of Structural Engineering* 130.9 (2004), pp. 1371–1380.

[59] Gregory A MacRae. "The seismic response of steel frames". PhD thesis. University of Canterbury. Civil Engineering, 1989.

[60] Gregory A MacRae et al. "Axial shortening of steel columns in buildings subjected to earthquakes". In: *Bulletin of the New Zealand Society for Earthquake Engineering* 42.4 (2009), p. 275.

[61] JO Malley et al. "Modeling and Acceptance Criteria for Seismic Design and Analysis of Tall Buildings". In: *Applied Technology Council* (2010).

[62] Jacky Mazars and Gilles Pijaudier-Cabot. "Continuum damage theory-Application to concrete". In: *Journal of Engineering Mechanics* 115.2 (1989), pp. 345–365.

[63] SSF Mehanny. "Modeling and assessment of seismic performance of composite frames with reinforced concrete columns and steel beams". PhD thesis. Stanford University, 1999.

[64] SSF Mehanny and GG Deierlein. "Seismic damage and collapse assessment of composite moment frames". In: *Journal of Structural Engineering* 127.9 (2001), pp. 1045–1053.

[65] Ansgar Neuenhofer and Filip C Filippou. "Evaluation of nonlinear frame finite-element models". In: *Journal of structural engineering* 123.7 (1997), pp. 958–966.

[66] James D Newell and Chia-Ming Uang. "Cyclic behavior of steel wide-flange columns subjected to large drift". In: *Journal of structural engineering* 134.8 (2008), pp. 1334–1342.

[67] NC Nigam. "Yielding in framed structures under dynamic loads". In: *Journal of the Engineering Mechanics Division* 96.5 (1970), pp. 687–709.

[68] GCR NIST. "GCR 10-917-8 (2010) Evaluation of the FEMA P-695 Methodology for Quantification of Building Seismic Performance Factors". In: *National Institute of Standards and Technology, Gaithersburg, MD* (2011).

[69] Minoru Ohue and Nihon Konkurīto Kōgaku Kyōkai. *Behavior of RC Short Columns Failing in Splitting Bond-Shear Under Dynamic Lateral Loading*. Japan Concrete Institute, 1985.

[70] James G Orbison, William McGuire, and John F Abel. "Yield surface applications in nonlinear steel frame analysis". In: *Computer Methods in Applied Mechanics and Engineering* 33.1 (1982), pp. 557–573.

[71] YJ Park, A HS Ang, and YK Wen. "Damage-limiting seismic design of buildings". In: *Earthquake Spectra* 3.1 (1987), pp. 1–26.

[72] Young J Park, Andrei M Reinhorn, and Sashi K Kunnath. *IDARC: Inelastic damage analysis of reinforced concrete frame-shear-wall structures*. Tech. rep. NCEER-87-0008, State University of New York at Buffalo, Buffalo, NY, 1987.

[73] Young-Ji Park and Alfredo H-S Ang. "Mechanistic seismic damage model for reinforced concrete". In: *Journal of Structural Engineering* 111.4 (1985), pp. 722–739.

[74] Egor Paul Popov and Roy M Stephen. "Cyclic loading of full-size steel connections". In: *American Iron and Steel Institute* 21 (1972).

[75] Frank L Porter and Graham H Powell. *Static and dynamic analysis of inelastic frame structures*. University of California, College of Engineering, Earthquake Engineering Research Center, 1971.

[76] Graham H Powell and Paul Fu-Song Chen. "3D beam-column element with generalized plastic hinges". In: *Journal of Engineering Mechanics* 112.7 (1986), pp. 627–641.

[77] Graham Harcourt Powell. *Modeling for Structural Analysis: Behavior and Basics*. Computers and Structures, 2010.

[78] Madhwesh Raghavendrachar and Ahmet E Aktan. "Flexibility by multireference impact testing for bridge diagnostics". In: *Journal of Structural Engineering* 118.8 (1992), pp. 2186–2203.

[79] Mohsen Rahnama and Helmut Krawinkler. *Effects of soft soil and hysteresis model on seismic demands*. Tech. rep. John A. Blume Earthquake Engineering Center Report No. 108. Department of CEE, Stanford University, 1993.

[80] Tathagata Ray and Andrei M Reinhorn. "Enhanced smooth hysteretic model with degrading properties". In: *Journal of Structural Engineering* 140.1 (2012), p. 04013028.

[81] Andrei M Reinhorn et al. *IDARC2D version 7.0: A Program for the Inelastic Damage Analysis of Structures*. 2009.

[82] Filipe LA Ribeiro et al. "Deterioration modeling of steel moment resisting frames using finite-length plastic hinge force-based beam-column elements". In: *Journal of Structural Engineering* 141.2 (2014), p. 04014112.

[83] J R Rice and Dennis Michael Tracey. "On the ductile enlargement of voids in triaxial stress fields". In: *Journal of the Mechanics and Physics of Solids* 17.3 (1969), pp. 201–217.

[84] James M. Ricles et al. *Developement of seismic guidelines for deep-column steel moment connections*. Tech. rep. ATLSS Report No. 04-13, Lehigh University, Bethlehem, PA, USA, 2004.

[85] Maria Grazia Santoro and Sashi K Kunnath. "Damage-based RC beam element for nonlinear structural analysis". In: *Engineering Structures* 49 (2013), pp. 733–742.

[86] Michael H Scott and Gregory L Fenves. "Plastic hinge integration methods for force-based beam–column elements". In: *Journal of Structural Engineering* 132.2 (2006), pp. 244–252.

[87] Michael H Scott and Keri L Ryan. "Moment-rotation behavior of force-based plastic hinge elements". In: *Earthquake Spectra* 29.2 (2013), pp. 597–607.

[88] Roberto Scotta et al. "Global damage indexes for the seismic performance assessement of RC structures". In: *Earthquake Engineering & Structural Dynamics* 38.8 (2009), pp. 1027–1049.

[89] Halil Sezen and Jack P Moehle. "Shear strength model for lightly reinforced concrete columns". In: *Journal of Structural Engineering* 130.11 (2004), pp. 1692–1703.

[90] P Benson Shing. *Response of single-story reinforced masonry shear walls to in-plane lateral loads*. Tech. rep. Report No. 3.1(a)–2, Department of Eivil, Environmental and Architectural engineering, University of Colorado, Boulder, CO, 1991.

[91] J. C. Simo and J. W. Ju. "Strain- and stress-based continuum damage models: Part I - Formulation". In: *International Journal of Solids and Structures* 23.7 (1987), pp. 821–840.

[92] Juan C Simo and Thomas JR Hughes. *Computational Inelasticity*. Vol. 7. Springer Science & Business Media, 2006.

[93] Mettupalayam V Sivaselvan and Andrei M Reinhorn. "Hysteretic models for deteriorating inelastic structures". In: *Journal of Engineering Mechanics* 126.6 (2000), pp. 633–640.

[94] Jong-Keol Song and JoseA Pincheira. "Spectral displacement demands of stiffness- and strength-degrading systems". In: *Earthquake Spectra* 16.4 (2000), pp. 817–851.

[95] Enrico Spacone, Vincenzo Ciampi, and Filip C Filippou. *A beam Element for Seismic Damage Analysis*. Vol. 92. 7. Earthquake Engineering Research Center, University of California, 1995.

[96] Bozidar Stojadinovic et al. "Parametric tests on unreinforced steel moment connections". In: *Journal of Structural Engineering* 126.1 (2000), pp. 40–49.

[97] Y Suzuki and DG Lignos. "Large scale collapse experiments of wide flange steel beam-columns". In: *8th International Conference on Behavior of Steel Structures in Seismic Areas (STESSA)*. 2015.

[98] Toshikazu Takeda, Mete Avni Sozen, and N Norby Nielsen. "Reinforced concrete response to simulated earthquakes". In: *Journal of the Structural Division* 96.12 (1970), pp. 2557–2573.

[99] Hiroshi Takemura and Kazuhiko Kawashima. "Effect of loading hysteresis on ductility capacity of reinforced concrete bridge piers". In: *Journal of Structural Engineering* 43 (1997), pp. 849–858.

[100] Haruo Takizawa and Hiroyuki Aoyama. "Biaxial effects in modelling earthquake response of R/C structures". In: *Earthquake Engineering & Structural Dynamics* 4.6 (1976), pp. 523–552.

[101] Wilson H Tang and A Ang. *Probability Concepts in Engineering: Emphasis on Applications to Civil & Environmental Engineering*. Wiley, 2007.

[102] RL Taylor et al. "A mixed finite element method for beam and frame problems". In: *Computational Mechanics* 31.1 (2003), pp. 192–203.

[103] Hidetaka Umehara. "Shear strength and deterioration of short reinforced concrete columns under cyclic deformations." In: *Dissertation Abstracts International Part B: Science and Engineering[DISS. ABST. INT. PT. B- SCI. & ENG.]*. 43.3 (1982), p. 1982.

[104] P Uriz and S Mahin. "Seismic performance of concentrically braced steel frame buildings". In: *Proceedings, 13th World Congress on Earthquake Engineering*. 2004.

[105] Dimitrios Vamvatsikos and C Allin Cornell. "Incremental dynamic analysis". In: *Earthquake Engineering & Structural Dynamics* 31.3 (2002), pp. 491–514.

[106] M Venti and MD Engelhardt. *Brief report of steel moment connection test, specimen DBBW (Dog Bone–Bolted Web)*. Tech. rep. Phase 2 Report, SAC Joint Venture, 1999.

[107] SAC Joint Venture. "State of the Art Report on Past Performance of Steel Moment-Frame Buildings in Earthquakes". In: *SAC Rep. No. FEMA 355e, Federal Emergency Management Agency, Washington, DC* (2000).

[108] Yi-Kwei Wen. "Method for random vibration of hysteretic systems". In: *Journal of the Engineering Mechanics* 102.2 (1976), pp. 249–263.

[109] Martin S Williams and Robert G Sexsmith. "Seismic damage indices for concrete structures: a state-of-the-art review". In: *Earthquake spectra* 11.2 (1995), pp. 319–349.

[110] Jian Ying Wu, Jie Li, and Rui Faria. "An energy release rate-based plastic-damage model for concrete". In: *International Journal of Solids and Structures* 43.3 (2006), pp. 583–612.

[111] Qi Song Yu, Chad Gilton, and Chia-Ming Uang. *Cyclic Response of Rbs Moment Connections: Loading Sequence and Lateral Bracing Effects*. Vol. 99. 13. Dept. of Structural Engineering, Univ. of California, San Diego, 2000.

[112] Olgierd Cecil Zienkiewicz and Robert Lee Taylor. *The finite element method*. Vol. 3. McGraw-hill London, 1977.

Appendix A

Alterative Damage Evolution Functions

The wealth of cumulative distribution functions (CDFs) in statistics permits a wide range of damage evolution characteristics. Further study is necessary to evaluate the capabilities and applications of the CDFs. This appendix presents two representative functions that could be potential alternatives for the proposed damage evolution functions in this dissertation. The first function is the CDF of the beta distribution. This function is similar to the proposed function in Chapter 2 but with the original parameters of the statistical function. The second function is the CDF of the lognormal distribution, which is shown to describe well the uniaxial hysteretic behavior of concrete material.

A.1 Beta Distribution

Figure A.1 plots the damage variable d if the original CDF of the beta distribution is used to describe the damage evolution.

$$d = F_B\left(\hat{\psi}, \beta_1, \beta_2\right) \tag{A.1}$$

where F_B is the CDF of the beta distribution, $\hat{\psi}$ is the normalized energy variable in (2.10), and β_1 and β_2 are the shape parameters of the CDF.

Figure A.1(a) demonstrates the effect of β_1 for $\beta_2 = 1$ and Figure A.1(b) showcases the effect of β_2 for $\beta_1 = 1$. Similar to the damage evolution adopted in Chapter 2, $\beta_1 = \beta_2 = 1$ describes a linear damage evolution with the energy variable. $\beta_1 < 1$ gives faster deterioration rate in the early stage of the energy dissipation whereas $\beta_1 > 1$ concentrates the damage growth in the later stage. The effect of β_2 shows a similar behavior, with $\beta_2 > 1$ corresponding to faster deterioration rate in the early stage of the energy dissipation whereas $\beta_2 < 1$ representing more damage growth in the later stage.

It is noteworthy that since there exists a one-to-one conversion of the parameters in the two functions, both can describe exactly the same damage evolution. However, the

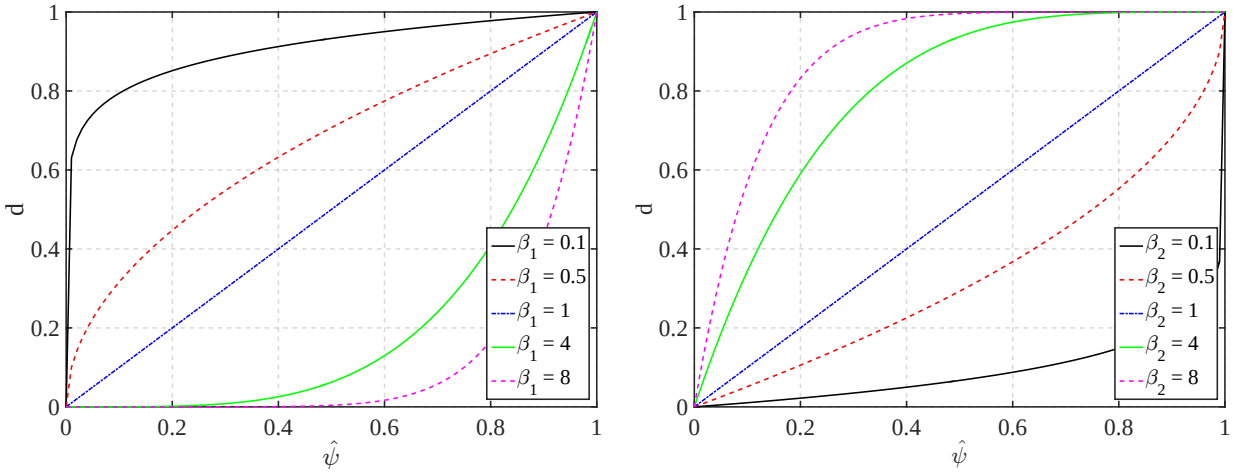

(a) Effect of β_1 for $\beta_2 = 1$

(b) Effect of β_2 for $\beta_1 = 1$

Figure A.1: Effect of β_1 and β_2 on the beta CDF

transformation in the modified CDF in Equations (2.12)−(2.13) allow the paramaters d_{p1} and d_{p2} to have distinct effects on the deterioration rate. Therefore, the parameter identification in the modified CDF is more convenient.

A.2 Lognormal distribution

The CDF of the lognormal distribution, or lognormal CDF for short, has two parameters, the location parameter μ and scale parameter σ. In contrast to the beta distribution, the domain of the lognormal CDF is $(0,+\infty)$, and thus, the normalized energy variable $\hat{\psi}$ is modified as follows:

$$\hat{\psi} = \frac{\psi - \psi_{d0}}{\psi_{d0}} \tag{A.2}$$

It is clear that $\hat{\psi}$ is positive but does not have an upperbound as when the beta distribution is utilized. The damage variable d is evaluated from the lognormal CDF, F_L, the normalized energy $\hat{\psi}$ in Equation (A.2), and the two parameters μ and σ.

$$d = F_L\left(\hat{\psi}, \mu, \sigma\right) \tag{A.3}$$

Figure A.2 illustrates the effect of μ and σ on the force-deformation relation and the damage evolution. With σ remains fixed, at the same deformation value, a higher μ gives a smaller damage value d, and as a result, a higher force value. On the other hand, for a fixed μ value, a higher σ concentrates more damage during the earlier stage and less damage during the later stage. Consequently, a higher σ leads to a smaller peak strength attained at a higher deformation value.

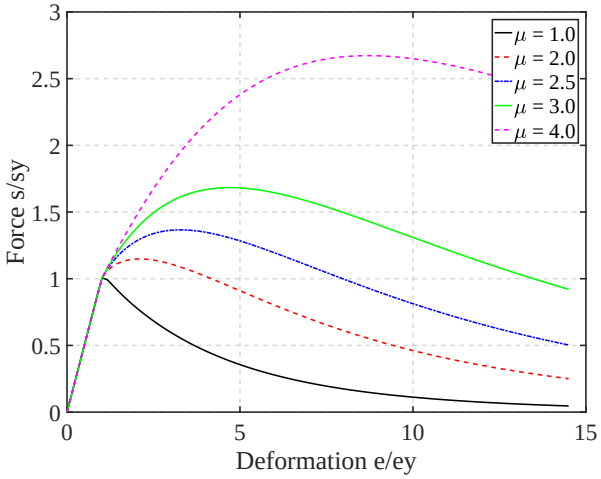

(a) Effect of μ on force-deformation

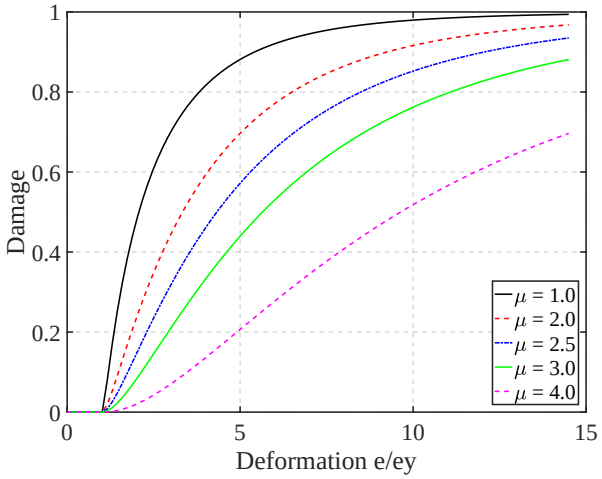

(b) Effect of μ on damage

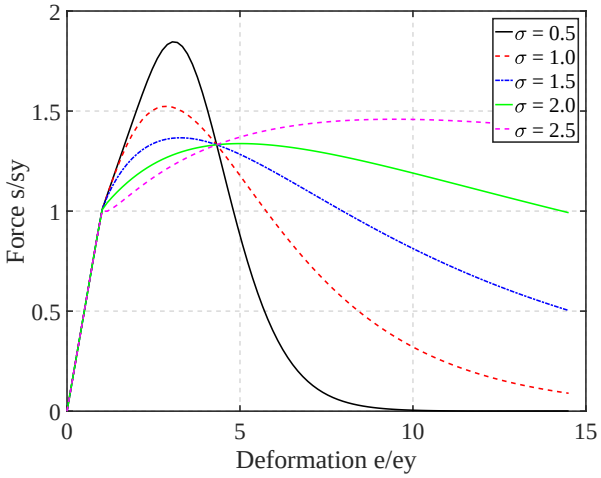

(c) Effect of σ on force-deformation

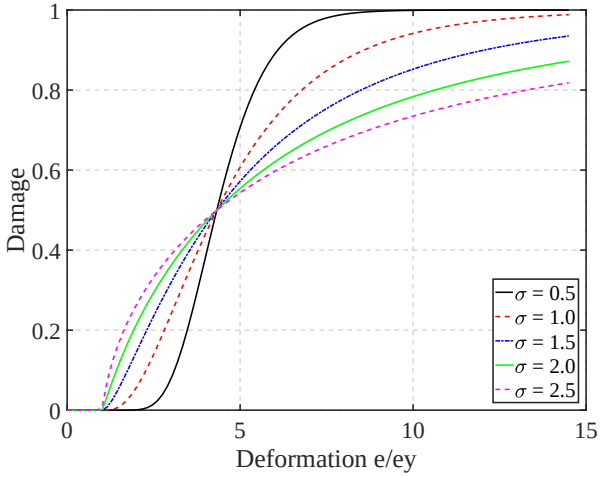

(d) Effect of σ on damage

Figure A.2: Effect of μ and σ on the lognormal CDF

It is noteworthy that the effect of parameters μ and σ of the lognormal CDF on the damage evolution resembles the parameters d_{p1} and d_{p2} in Figure 2.5. An attractive feature of the lognormal CDF is the ability to describe the 'skewness' in the force-deformation relation. This property is particularly powerful to represent the stress-strain relation in concrete material in compression. As an illustration,Figure A.3 compares the numerical response using the lognormal CDF for the damage evolution function against the experimental response of concrete in uniaxial tension [32] and in uniaxial compression [45].

The preliminary work shows excellent promise in the lognormal CDF for the response simulations of reinforced concrete structures. Further studies are necessary to calibrate

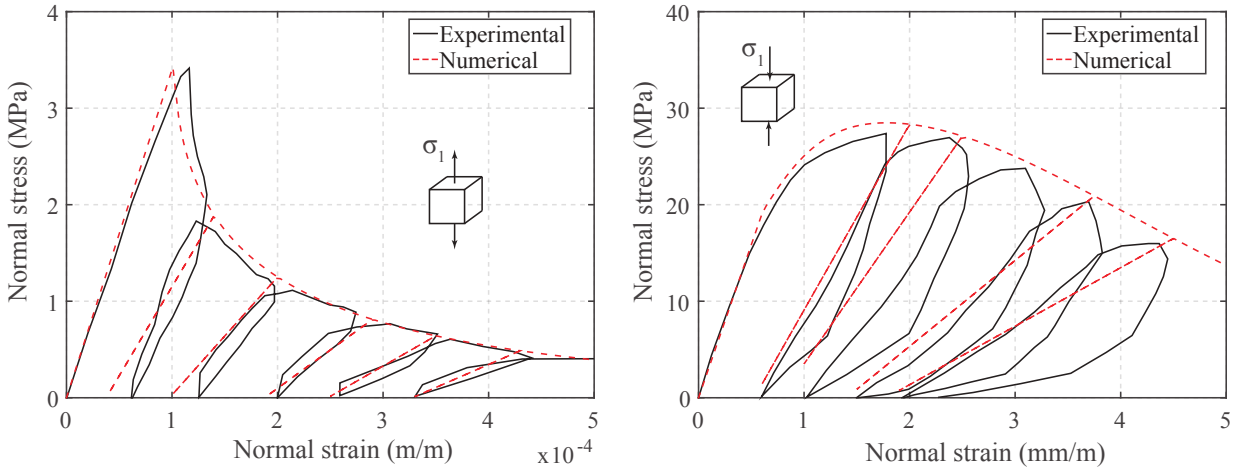

(a) Uniaxial tension (b) Uniaxial compression

Figure A.3: Simulation of concrete uniaxial response

the parameters μ and σ for various unique characteristics of concrete material, such as, the compressive strength and the respective strain value, the ductility, the strength and ductility variation due to confinement effect, among others.

Appendix B

Mathematical Derivations

B.1 Plastic Consistency Parameter

This section derives the plastic consistency parameter $\boldsymbol{\beta}$ in the return-mapping algorithm of the series beam element model state determination in Section 3.1.3. In the plastic correction at step n, the yield function $\mathbf{n}$ can be expressed in the following form:

$$\begin{aligned}\mathbf{f}_n &= \mathbf{n}^T(\mathbf{b}_p\mathbf{q}_n - \mathbf{q}_{b,n}) - (\mathbf{M}_p + \mathbf{H}_i\boldsymbol{\alpha}_n) \\ &= \mathbf{n}^T\left[\mathbf{b}_p\left(\mathbf{q}^{tr} - \mathbf{k}_e\mathbf{b}_p^T\mathbf{n}\boldsymbol{\beta}\right) - \left(\mathbf{q}_b^{tr} + \mathbf{H}_k\mathbf{n}\boldsymbol{\beta}\right)\right] - \left[\mathbf{M}_p + \mathbf{H}_i\left(\boldsymbol{\alpha}^{tr} + \boldsymbol{\beta}\right)\right] \\ &= \left[\mathbf{n}^T(\mathbf{b}_p\mathbf{q}_n^{tr} - \mathbf{q}_b^{tr}) - (\mathbf{M}_p + \mathbf{H}_i\boldsymbol{\alpha}^{tr})\right] - \left[\mathbf{n}^T\left(\mathbf{b}_p\mathbf{k}_e\mathbf{b}_p^T + \mathbf{H}_k\right)\mathbf{n} + \mathbf{H}_i\right]\boldsymbol{\beta} \qquad \text{(B.1)}\end{aligned}$$

(B.2)

Similar to the return-mapping algorithm in classical plasticity, the normals in the trial and the correction step are equal $\mathbf{n} = \mathbf{n}^{tr}$. Consequently, the term in the square bracket in Equation (B.2) gives the value of the trial yield function $\mathbf{f}^{tr}$. Finally, set the yield function $\mathbf{n}$ to its target value $\mathbf{0}$:

$$\mathbf{0} = \mathbf{f}^{tr} - \left[\mathbf{n}^T\left(\mathbf{b}_p\mathbf{k}_e\mathbf{b}_p^T + \mathbf{H}_k\right)\mathbf{n} + \mathbf{H}_i\right]\boldsymbol{\beta} \qquad \text{(B.3)}$$

one obtains the expression of the plastic consistency parameter $\boldsymbol{\beta}$ in Equation (3.38).

B.2 Algorithmic Tangent

This section derives the tangent stiffness of the series beam element and the NMYS column element.

B.2.1 Series beam model

This subsection presents the derivation of the tangent stiffness of the series beam model given in Equation (3.22). Starting with the final form of the element forces $\mathbf{q}_n$ in Equa-

tion (3.42), the tangent $\mathbf{k}_t$ is evaluated as follows:

$$\mathbf{k}_t = \frac{\partial \mathbf{q}_n}{\partial \mathbf{v}_n} = \frac{\partial \mathbf{q}^{tr}}{\mathbf{v}_n} - \mathbf{k}_e \mathbf{b}_p^T \mathbf{n} \frac{\partial \beta}{\partial \mathbf{v}_n} \tag{B.4}$$

The partial derivative of the trial force $\mathbf{q}^{tr}$ with respect to the deformation $\mathbf{v}_n$ gives the elastic stiffness $\mathbf{k}_e$ due to the assumption of a trial elastic step:

$$\frac{\partial \mathbf{q}^{tr}}{\mathbf{v}_n} = \mathbf{k}_e \tag{B.5}$$

Using the expression of the plastic consistency parameter $\boldsymbol{\beta}$ in Equation (3.38) and note that:

$$\frac{\partial \mathbf{f}^{tr}}{\mathbf{v}_n} = \mathbf{n}^T \mathbf{b}_p \frac{\partial \mathbf{q}^{tr}}{\mathbf{v}_n} = \mathbf{n}^T \mathbf{b}_p \mathbf{k}_e \tag{B.6}$$

the partial derivative of $\boldsymbol{\beta}$ with respect to the deformation $\mathbf{v}_n$ is:

$$\frac{\partial \boldsymbol{\beta}}{\partial \mathbf{v}_n} = \left[\mathbf{n}^T \left(\mathbf{b}_p \mathbf{k}_e \mathbf{b}_p^T + \mathbf{H}_k\right) \mathbf{n} + \mathbf{H}_i\right]^{-1} \mathbf{n}^T \mathbf{b}_p \mathbf{k}_e \tag{B.7}$$

The partial derivatives in Equations (B.5) and (B.7) are subtituted into (B.4), and the expression in Equation (3.22) for the tangent stiffness can be recovered.

B.2.2 NMYS column model

Diffentiating the residuals in Equation (4.28) to arrive at the following system of equations:

$$\begin{pmatrix} \mathbf{dv} \\ \mathbf{0} \\ \mathbf{0} \\ 0 \end{pmatrix} = \begin{bmatrix} \frac{\partial \mathbf{R_v}}{\partial \mathbf{q}} & \frac{\partial \mathbf{R_v}}{\partial \Delta \boldsymbol{\beta}} & \frac{\partial \mathbf{R_v}}{\partial \boldsymbol{\alpha}} & \frac{\partial \mathbf{R_v}}{\partial \mathbf{q_b}} \\ \frac{\partial \mathbf{R}_\alpha}{\partial \mathbf{q}} & \frac{\partial \mathbf{R}_\alpha}{\partial \Delta \boldsymbol{\beta}} & \frac{\partial \mathbf{R}_\alpha}{\partial \boldsymbol{\alpha}} & \frac{\partial \mathbf{R}_\alpha}{\partial \mathbf{q_b}} \\ \frac{\partial \mathbf{R_b}}{\partial \mathbf{q}} & \frac{\partial \mathbf{R_b}}{\partial \Delta \boldsymbol{\beta}} & \frac{\partial \mathbf{R_b}}{\partial \boldsymbol{\alpha}} & \frac{\partial \mathbf{R_b}}{\partial \mathbf{q_b}} \\ \frac{\partial f}{\partial \mathbf{q}} & \frac{\partial f}{\partial \Delta \boldsymbol{\beta}} & \frac{\partial f}{\partial \boldsymbol{\alpha}} & \frac{\partial f}{\partial \mathbf{q_b}} \end{bmatrix} \begin{pmatrix} \mathbf{dq} \\ \mathbf{d\Delta\beta} \\ \mathbf{d\alpha} \\ \mathbf{dq_b} \end{pmatrix} \tag{B.8}$$

The Jacobian matrix can be partitioned into four submatrices:

$$\mathbf{J} = \begin{bmatrix} \mathbf{F_{rr}} & \mathbf{F_{rc}} \\ \mathbf{F_{cr}} & \mathbf{F_{cc}} \end{bmatrix} \tag{B.9}$$

where the block matrices are:

$$\mathbf{F_{rr}} = \frac{\partial \mathbf{R_v}}{\partial \mathbf{q}} \qquad \mathbf{F_{rc}} = \left[\frac{\partial \mathbf{R_v}}{\partial \Delta\boldsymbol{\beta}}, \frac{\partial \mathbf{R_v}}{\partial \boldsymbol{\alpha}}, \frac{\partial \mathbf{R_v}}{\partial \mathbf{q_b}}\right] \tag{B.10}$$

$$\mathbf{F_{cr}} = \left[\frac{\partial \mathbf{R}_\alpha}{\partial \mathbf{q}}, \frac{\partial \mathbf{R_b}}{\partial \mathbf{q}}, \frac{\partial f}{\partial \mathbf{q}}\right]^T \qquad \mathbf{F_{cc}} = \begin{bmatrix} \frac{\partial \mathbf{R}_\alpha}{\partial \Delta\boldsymbol{\beta}} & \frac{\partial \mathbf{R}_\alpha}{\partial \boldsymbol{\alpha}} & \frac{\partial \mathbf{R}_\alpha}{\partial \mathbf{q_b}} \\ \frac{\partial \mathbf{R_b}}{\partial \Delta\boldsymbol{\beta}} & \frac{\partial \mathbf{R_b}}{\partial \boldsymbol{\alpha}} & \frac{\partial \mathbf{R_b}}{\partial \mathbf{q_b}} \\ \frac{\partial f}{\partial \Delta\boldsymbol{\beta}} & \frac{\partial f}{\partial \boldsymbol{\alpha}} & \frac{\partial f}{\partial \mathbf{q_b}} \end{bmatrix} \tag{B.11}$$

One approach to obtain the tangent stiffness $\mathbf{k}_t$ is to first find the flexibility matrix $\mathbf{f} = \partial \mathbf{v}/\partial \mathbf{q}$ and then invert the flexibility for the stiffness. The flexibility $\mathbf{f}$ is derived from static condensation of Equation (B.8):

$$\mathbf{f} = \frac{\partial \mathbf{v}}{\partial \mathbf{q}} = \left(\mathbf{F_{rr}} - \mathbf{F_{rc}}\mathbf{F_{cc}}^{-1}\mathbf{F_{cr}}\right)^{-1} \tag{B.12}$$

One drawback of this apprroach, however, is the issue of inverting a singular matrix during static condensation. For instance, in case of an elasto-plastic response with $\mathbf{H_{ip}} = \mathbf{0}$ and $\mathbf{H_{kr}} = \mathbf{0}$, then $\mathbf{F_{cc}}$ becomes singular.

An alternative to find the tangent stiffness without directly using static condensation is to adopt the Woodbury formula:

$$(\mathbf{A} + \mathbf{UCV})^{-1} = \mathbf{A}^{-1} - \mathbf{A}^{-1}\mathbf{U}\left(\mathbf{C}^{-1} + \mathbf{VA}^{-1}\mathbf{U}\right)^{-1}\mathbf{VA}^{-1} \tag{B.13}$$

The expression of the tangent stiffness matrix becomes:

$$\mathbf{k} = \frac{\partial \mathbf{q}}{\partial \mathbf{v}} = \mathbf{F_{rr}}^{-1} + \mathbf{F_{rr}}^{-1}\mathbf{F_{rc}}\left(\mathbf{F_{cc}} - \mathbf{F_{cr}}\mathbf{F_{rr}}^{-1}\mathbf{F_{rc}}\right)^{-1}\mathbf{F_{cr}}\mathbf{F_{rr}}^{-1} \tag{B.14}$$

Appendix C

Thermodynamics Framework

A free energy potential per unit volume, Φ, can be defined as a function of the elastic deformation e_e, the plastic deformation e_p, the damage variable d, and some hardening variables γ. The free energy potential is assumed to be decomposed into the elastic potential Φ_e, the plastic potential Φ_p, and the hardening potential Ω. The elastic potential Φ_e depends on the elastic deformation e_e and damage index d, while the plastic potential Φ_p is a function of the plastic deformation e_p and damage index d. The hardening potential Ω is dependent on the hardening variables γ. The elastic and plastic potentials are proportional to their counterparts in the effective space, $\bar{\Phi}_e$ and $\bar{\Phi}_p$.

$$\begin{aligned}\Phi(e_e, e_p, d, \gamma) &= \Phi_e(e_e, d) + \Phi_p(e_p, d) + \Omega(\gamma) \\ &= (1-d)\bar{\Phi}_e(e_e) + (1-d)\bar{\Phi}_p(e_p) + \Omega(\gamma)\end{aligned} \tag{C.1}$$

According to the second principle of thermodynamics, any irreversible process shall produce non-negative energy dissipation. The condition applies for all admisible process and is given by the Clausius-Dulhem inequality:

$$s\dot{e} - \dot{\Phi} \geq 0 \tag{C.2}$$

The inequality in Equation (C.2) can be rewritten as:

$$s\dot{e} - \left(\frac{\partial \Phi}{\partial e}\,\dot{e} + \frac{\partial \Phi}{\partial d}\,\dot{d} + \frac{\partial \Phi}{\partial \gamma}\,\dot{\gamma}\right) \geq 0 \tag{C.3}$$

Rearranging the terms in Equation (C.3) gives:

$$\left(s - \frac{\partial \Phi}{\partial e}\right)\dot{e} - \frac{\partial \Phi}{\partial d}\,\dot{d} - \frac{\partial \phi}{\partial \gamma}\,\dot{\gamma} \geq 0 \tag{C.4}$$

Imposing a constraint on the deformation field, the first term in equation (C.4) leads to the constitutive relation:

$$s = \frac{\partial \Phi}{\partial e} \tag{C.5}$$

The second and third terms in equation (C.4) invoke the nonnegativity of the energy dissipation:

$$-\frac{\partial \Phi}{\partial d}\,\dot{d} \geq 0 \tag{C.6}$$

$$-\frac{\partial \Phi}{\partial \gamma}\,\dot{\gamma} \geq 0 \tag{C.7}$$

In Equation (C.6), define ψ as the conjugate to the damage index d as:

$$\psi = -\frac{\partial \Phi}{\partial d} = \bar{\Phi}_e + \bar{\Phi}_p \tag{C.8}$$

Equation (C.8) suggests that ψ is an energy variable and is related to the energy dissipation in the effective space. The damage conjugate ψ, usually referred to as the energy release rate in the literature, is the key variable that governs the damage evolution. This observation is consistent with the formulation in Chapter 2, in which the energy variable is evaluated in Equations (2.2)−(2.3). Therefore, the proposed damage formulation is thermodynamically consistent.